

# **Physical and Chemical Constraints on Core - Mantle Differentiation in Terrestrial Planets**

## **Dissertation**

Fakultät für Biologie, Chemie und Geowissenschaften,  
Universität Bayreuth

**Ute Mann**

(Diplom-Geologin)

aus Senden bei Neu-Ulm

Bayreuth, Oktober 2007

Die vorliegende Arbeit wurde von Oktober 2004 bis Oktober 2007 am Bayerischen Geoinstitut, Universität Bayreuth unter Leitung von Prof. D:C: Rubie angefertigt.

Vollständiger Abdruck der von der Fakultät für Biologie, Chemie und Geowissenschaften der Universität Bayreuth genehmigten Dissertation zur Erlangung des akademischen Grades einer Doktorin der Naturwissenschaften (Dr. rer. nat.).

Datum der Einreichung der Dissertation: 23. Oktober 2007

Datum des wissenschaftlichen Kolloquiums: 13. Februar 2008

Prüfungsausschuß:

Prof. S. Peiffer, Universität Bayreuth (Vorsitzender)

Prof. D.C. Rubie, Universität Bayreuth (Erster Gutachter)

Prof. H. Keppler, Universität Bayreuth (Zweiter Gutachter)

Prof. K. Bitzer, Universität Bayreuth

Prof. J. Breu, Universität Bayreuth

# Contents

<b>Abstract</b>	<b>1</b>
<b>Zusammenfassung</b>	<b>3</b>
<b>1. Introduction</b>	<b>7</b>
1.1 The Geochemical Signature of the Earth.....	8
1.2 Core Formation Models .....	10
1.3 Geochemical Constraints from Liquid Metal - Liquid Silicate Partitioning Behaviour.....	15
1.4 Mechanical Separation Processes of Core Forming Liquids.....	18
1.5 High Pressure - High Temperature Experimental Techniques .....	19
1.6 Aims of this Study.....	25
<b>2. The Wetting Ability of Si-bearing Liquid Fe-alloys in Solid Silicate Mantle Matrix</b>	<b>27</b>
2.1 Previous Work .....	27
2.2 Experimental Setup and Analytical Techniques.....	28
2.3 Results .....	30
2.4 Discussion and Conclusions.....	34
<b>3. Liquid Metal - Liquid Silicate Partitioning of Nominally Lithophile and Weakly Siderophile Elements</b>	<b>37</b>
3.1 Introduction .....	37
3.2 Experimental Conditions .....	38
3.3 Run Products.....	41
3.4 Analytical Techniques .....	43

3.5	Results .....	45
3.5.1	Calculation of the Oxygen Fugacity .....	45
3.5.2	Metal-Silicate Partition Coefficients - Dependence on Oxygen Fugacity.....	47
3.5.3	Compositional Effects and Influence of the Capsule Material.....	51
3.5.4	Change of the Partitioning Behaviour with Pressure and Temperature .....	56
3.6	Discussion and Implications for Existing Core Formation Models.....	66
3.6.1	Testing Heterogeneous Low Pressure Core Formation Scenarios .....	67
3.6.2	Constraints on High Pressure Core Formation Models .....	72
3.7	Conclusions .....	77
<b>4.</b>	<b>Liquid Metal - Liquid Silicate Partitioning of Highly Siderophile Elements at High Pressures and High Temperatures</b>	<b>79</b>
4.1	Introduction .....	79
4.2	HSE Glass Standards for Trace Element Microanalysis and Analytical Techniques .....	82
4.2.1	Synthesis of the Glass Standards .....	82
4.2.2	Quantitative Analysis of the Glasses and Evaluation of their Suitability as Standards for HSE Microanalysis .....	84
4.3	Metal-Silicate Partitioning Experiments .....	93
4.3.1	Starting Materials and Experimental Setup .....	93
4.3.2	Run Products and Analytical Techniques .....	95
4.3.3	Results .....	102
4.4	Summary and Conclusions.....	114
<b>5.</b>	<b>Constraints on Planetary Core Formation Models - Conclusions and Outlook</b>	<b>117</b>
	<b>Acknowledgements</b>	<b>121</b>
	<b>References</b>	<b>123</b>
	<b>Appendix</b>	<b>133</b>

## Abstract

In this study a physical mechanism and geochemical parameters have been examined in high pressure and high temperature experiments in order to place constraints on the conditions and the manner by which core-mantle differentiation occurred on Earth and terrestrial planets.

The wetting characteristics of liquid Fe-Si alloys in a matrix of the respective predominating stable silicate mantle mineral (forsterite or silicate perovskite) at pressures of 2-5 and 25 GPa and temperatures of 1600-2000 °C were studied by determining the liquid metal-solid silicate contact angles. The median angle values from texturally-equilibrated samples were found to be independent of pressure, temperature, silicate mineralogy and the Si content in the metal fraction and range between 130° and 140° which is far above the critical wetting boundary of 60°. This shows that within the studied range of conditions dissolved Si does not lower the surface energies between Fe-rich liquids and silicate mantle grains. As a consequence, under reducing conditions the presence of Si in the metal phase of planetary bodies would not have induced or aided percolative flow as the metal-silicate separation process.

Liquid metal - liquid silicate partitioning experiments for the elements Ta, Nb, V, Cr, Si, Mn, Ga, In and Zn have been performed over a wide range of high-pressure and high-temperature conditions of 2 - 24 GPa, 1750 - 2600°C and at low oxygen fugacities of -1.3 to -4.2 log units below the iron wüstite buffer. The effects of pressure, temperature and oxygen fugacity on the partitioning behaviour have been separated and the derived relationships have been applied to test the respective element depletions in the mantle under various conditions suggested in core formation models. These data indicate that Nb can serve as an important constraint on oxygen fugacity and pressure for metal-silicate equilibration. Ta is less siderophile than Nb and its lack of depletion in the mantle places a hard constraint on the minimum  $f_{O_2}$  encountered during core formation. Moreover, core formation must have occurred at conditions significantly greater than 20 GPa in order for Nb not to have been massively depleted under conditions necessary to deplete the weakly siderophile element V. Moreover, our study shows that the volatile elements Mn and Ga, would experience strong fractionations in any core-mantle equilibration scenario at pressures below 60 GPa and temperatures at least as high as the peridotite liquidus, which is inconsistent with their observed near-chondritic abundances in the mantle. The same observation has been made for the elements Zn and In though to a more extreme extent such that pressures over 80 GPa may be required to explain their near-chondritic ratio in the mantle. Based on these observations we find strong support for the existence of a deep magma ocean during metal-silicate separation, which is an essential component in current polybaric multi-stage core formation models. Although these models succeed in reproducing the observed mantle abundances of many siderophile elements, and can be constrained based on the partitioning behaviour of elements such as Nb, the observed behaviour of the volatile elements Mn, Ga, Zn and In may call for an additional process. Such a process may be the late accretion of volatiles in

material that did not undergo core-mantle separation or strong fractionation processes in the condensing nebula that are reflected in the meteorite record.

In the third part of this study, the first liquid metal-liquid silicate partitioning data at high pressures up to 18 GPa and high temperatures up to 2500 °C have been obtained for the highly siderophile elements (HSE's) Ru, Rh, Pd, Re, Ir and Pt. This group of elements presents a number of experimental and analytical difficulties, mainly due to their extreme metal-silicate partition coefficients. In addition to refining the experimental technique we have also succeeded in producing suitable standards for trace analysis of these elements in quenched silicates using LA-ICP-MS. This study shows that both increasing pressure and temperature would decrease the partition coefficients of all HSE's examined in a way similar to the pressure effect observed for the siderophile elements Ni and Co. This involves two pressure regimes with a strong decrease of the partition coefficients at  $< 6$  GPa, but only a weak pressure dependence at higher pressures. This difference in pressure effect can most likely be assigned to structural changes in the silicate melt. In order for the determined partition coefficients to be used quantitatively in models for the Earth the data would have to be corrected from the wt % concentrations in the experiments to the ppm levels relevant for core forming alloys using data on HSE activities in the alloy phase. Using Rh as an example for which data exist to perform such a correction, it can be shown that the principal pressure and temperature trend does not change significantly once the correction for dilution is performed. From this we can conclude that the pressure effect would not be sufficient to decrease the partition coefficients to a degree that the mantle concentrations of the HSE's could be explained. Therefore, a process such as the accretion of an undifferentiated late veneer seems to be necessary.

## Zusammenfassung

Gegenstand dieser Arbeit war die Untersuchung eines physikalischen Prozesses und die Bestimmung verschiedener geochemischer Parameter, die dazu dienen können, die Bedingungen und Mechanismen einzugrenzen, die bei der Kernbildung der Erde und anderer terrestrischer Planeten eine Rolle spielten.

Mit der ersten Studie wurde die Benetzungseigenschaft von Fe-Si-Legierungen in verschiedener Matrix aus Mantelmineralen unter Bedingungen von 2 - 5 und 25 GPa und 1600 - 2000°C untersucht. Dies erfolgte mittels Bestimmung des Kontaktwinkels zwischen Metallschmelze und Silikat Körnern, für die, abhängig vom Druckregime, Forsterit oder Silikatperowskit verwendet wurden. In Proben, für die textuelles Gleichgewicht angenommen werden kann, wurden die Medianwerte für die jeweils beobachtete Winkelpopulation bestimmt. Mit Werten von 130 - 140° liegen diese weit oberhalb von 60°, des kritischen Winkels für die Benetzung. Dies zeigt, daß die Oberflächenspannung zwischen eisenreichen Schmelzen und Körnern aus Mantelsilikaten unter den untersuchten Bedingungen durch die Beimischung von Si nicht reduziert wird. Perkolation als Separationsmechanismus für metallische Kernschmelzen im Innern von Planeten wurde deshalb unter reduzierenden Bedingungen durch die Anwesenheit von Si in der Legierung nicht ausgelöst oder begünstigt.

In der zweiten Studie wurden die Verteilungskoeffizienten zwischen Metall- und Silikatschmelze für die Elemente Ta, Nb, V, Cr, Si, Mn, Ga, In und Zn mit Hochdruck-Hochtemperaturexperimenten im Bereich von 2 - 24 GPa, 1750 - 2600°C und unter Sauerstoff fugazitäten von -1.3 bis -4.2  $\Delta$  IW bestimmt. Gleichungen für die Einflüsse von Druck, Temperatur und Sauerstoff fugazität auf das Verteilungsverhalten dieser Elemente wurden abgeleitet, um anschließend die Konsequenzen für ihre theoretische Verarmung unter verschiedenen Bedingungen zu testen, wie sie in Modellen zur Erdkernbildung vorgeschlagen werden. Die Ergebnisse zeigen, daß das Verhalten von Nb eine bedeutende Einschränkung für die Sauerstoff fugazität und den Druck während der Äquilibrierung von Metall- und Silikatschmelze liefert. Unter relativ reduzierenden Bedingungen, die notwendig sind, um V mit einer Kernschmelze teilweise aus dem Mantel zu entfernen, müßten Drücke von deutlich > 20 GPa vorherrschen, da andernfalls eine gleichzeitig starke Verarmung von Nb im Mantel die Folge wäre. Die Studie zeigt außerdem, daß bei Drücken < 60 GPa und Temperaturen am Peridotitliquidus die volatilen Elemente Mn und Ga während der Äquilibrierung zwischen Kern und Mantel eine starke Fraktionierung erfahren hätten, was nicht mit dem annähernd chondritischen Verhältnis der beiden Elemente im Erdmantel vereinbar ist. In noch stärkerem Maße trifft dies auch für die volatilen Elemente Zn und In zu, indem Drücke von deutlich > 80 GPa erforderlich wären, um ihr nahezu chondritisches Verhältnis im Mantel zu erklären. Diese Beobachtungen unterstützen das Konzept der Existenz eines tiefen Magmaozeans während der Abtrennung des Erdkerns vom silikatischen Mantel, welches Grundbestandteil

vieler moderner, polybarischer Kernbildungsmodelle ist. Obwohl es mit diesen Modellen gelingt, die Häufigkeiten vieler siderophiler und mäßig siderophiler Element im Erdmantel zu reproduzieren, ist dennoch vermutlich ein zusätzlicher Prozeß anzunehmen, mit dem das beobachtete Verhalten der volatilen Elemente Mn, Ga, In und Zn erklärt werden kann. Einen solchen Prozeß könnte die späte Hinzufügung volatiler Elemente darstellen, enthalten in Material, welches keine Differentiation aufgrund von Kern-Mantelbildung oder starke Fraktionierung durch Kondensationsprozesse im solaren Nebel erfahren hat.

In dieser Arbeit wurden außerdem erstmals unter hohen Drücken bis zu 18 GPa und Temperaturen bis zu 2500 °C die Verteilungskoeffizienten zwischen Metall- und Silikatschmelze für die extrem siderophilen Elemente (HSE) Ru, Rh, Pd, Re, Ir und Pt bestimmt. Vor allem aufgrund ihrer hohen Metall/Silikat-Verteilungskoeffizienten, ergeben sich für die Untersuchungen zu dieser Gruppe von Elementen einige experimentelle und analytische Schwierigkeiten. Neben einer Verbesserung der experimentellen Technik ist es in dieser Arbeit gelungen, geeignete Glasstandards herzustellen, die für die Analyse von Spuren dieser Elemente in Silikatmaterialien mittels LA-ICP-MS dienen können. Es konnte gezeigt werden, daß die Verteilungskoeffizienten aller dieser HSE sowohl mit zunehmendem Druck als auch zunehmender Temperatur verringert werden. Die Form dieser Abnahme ähnelt dem Verhalten, der siderophilen Elemente Ni und Co. Dabei können zwei Bereiche mit unterschiedlich starkem Druckeffekt unterschieden werden: bei geringen Drücken < 6 GPa kann eine rasche Abnahme der Verteilungskoeffizienten beobachtet werden, während bei hohen Drücken nur noch eine schwache Abnahme erfolgt. Dieser Effekt ist sehr wahrscheinlich auf Änderungen in der Silikatstruktur in diesem Druckbereich zurückzuführen. Um die Verteilungskoeffizienten, die mit dieser Studie bestimmt wurden, für quantitative Modellrechnungen verwenden zu können, müßten zunächst Korrekturen vorgenommen werden. Dies ist notwendig, um die Ergebnisse dieser Experimente, bei denen Konzentrationen einiger Gewichtsprozent für die HSE in der Metallegierung verwendet wurden, mit den Konzentrationen weniger ppm, wie sie für die Legierung des Erdkerns relevant sind, vergleichen zu können. Am Beispiel von Rh, für das die nötigen thermodynamischen Daten (konzentrationsabhängige Aktivitäten des Elements in der Legierung) verfügbar waren, wurde eine solche Korrektur durchgeführt. Dabei zeigte sich, daß für diesen Fall unbegrenzter Mischbarkeit keine wesentliche Änderung des beobachteten Druck- und Temperaturtrends zu erwarten ist. Es ist deshalb anzunehmen, daß der Einfluß von hohem Druck nicht ausreichen würde, um die HSE-Verteilungskoeffizienten genügend stark zu verringern, so daß die Konzentrationen der HSE im Erdmantel erklärt werden könnten. Ein zusätzlicher Prozeß, beispielsweise die späte Hinzufügung von undifferenziertem Material, scheint deshalb zur Erklärung notwendig zu sein.





# Chapter 1

## Introduction

The formation of the Earth's metallic Fe-rich core as it separated from the silicate mantle was one of the most important differentiation events in Earth's history. The partitioning of elements between the mantle and core determined the concentrations of many important elements in both reservoirs. In particular core formation dictated the concentration of Fe in the mantle and resulted in the presence of one or more light alloying elements in the Earth's core, which influence the density of the core and may drive the geodynamo through compositionally-driven convection.

Ratios of many elements in the Earth's mantle indicate that the Earth likely formed from material that was chemically similar to carbonaceous chondritic meteorites. However, in comparison to such meteorites, the Earth's mantle is depleted in many of the so-called siderophile elements that are known to favourably partition into metallic Fe. Depletions of siderophile elements in the mantle occurred as a result of core-mantle equilibration as the core separated. Studies of short-lived isotopes indicate that this process occurred at about 30 million years after the beginning of the solar system and over a time span of  $< 20$  million years (Kleine et al., 2002; Yin et al., 2002). For core formation to have been completed so quickly would have required particular conditions favourable to the rapid separation of the metal from the silicate, such as high temperatures and the formation of a significantly-molten mantle. The extent to which certain siderophile elements were depleted from the mantle would have depended on the conditions under which core formation occurred. An idea of these conditions can be obtained by experimentally reproducing the partitioning of elements between metal and silicate under controlled conditions and using these data to build models that simulate element depletions in the mantle. In addition further information as to the likely speed and efficiency of core formation and conditions of equilibration can be gained by examining the mechanism of metal-silicate separation both theoretically and experimentally.

Understanding accretion and core formation on the Earth is key to explaining the diversity between terrestrial planets and is crucial for determining the route by which Earth-like planets evolve. It also sheds light on the nature of material from which the Earth formed, the homogeneity of the solar nebula and the timing by which material was supplied to the Earth. Core formation models can be broadly divided into two types. Homogeneous models propose that the Earth formed from material which on average remained constant with time (Li and Agee, 1996; Wade and Wood, 2005), whereas heterogeneous models argue for a change in the composition of material as the Earth formed. Heterogeneous models therefore infer that changes in composition due to nebula condensation processes were at least as important as the

compositional implications derived from core-mantle partitioning. Whether the Earth formed homogeneously or heterogeneously has many important implications for mantle geochemistry and accretion conditions. If the Earth formed homogeneously, for example, it becomes much easier to estimate concentrations of volatile elements that are otherwise hard to estimate in the Earth as a whole. The conditions implied by core formation also provide a starting point for examining the early development of the Earth.

In this work metal-silicate element partitioning and mechanical separation mechanisms have been studied experimentally in order to evaluate and test core formation models. Rather than proposing a specific set of conditions under which the core and mantle fractionated, of which there may be a great range, the data collected in this thesis are employed to place constraints on conditions and processes that could have been important during the development of the core and the mantle. In turn, this helps to identify processes and related core formation models that are realistic.

## 1.1 The Geochemical Signature of the Earth

A number of studies have proposed an average bulk composition of the silicate part of the Earth derived from analyses of mantle xenoliths and mid ocean ridge basalts (Allegre et al, 1995; McDonough and Sun, 1995). Based on mantle concentrations of elements that do not partition into the core and were not lost from the Earth as a result of volatility, (i.e. lithophile, non-volatile or refractory elements), it appears that the silicate portion of the Earth is chemically similar to carbonaceous chondrites. Carbonaceous chondrites also display a range of volatile depletions and fractionations due to nebular processes. However, the least-fractionated meteorites are CI chondrites which have element ratios very similar to those of the solar photosphere. The ratios of refractory lithophile elements in the Earth are also considered to be similar to those of CI chondrites (Palme and O'Neil, 2003).

Fig. 1 shows the relative abundances of elements in the Earth's mantle normalized to CI chondrite and Ti, plotted against their condensation temperatures which were thermodynamically determined by Wasson (1985). Several groups of elements can be distinguished that show different degrees of depletion in the Earth's mantle. Elements such as Al, Ca, Ta and rare earth elements are lithophile, i.e. partition preferentially into silicates over metallic or sulphide phases, and are non-volatile or refractory. Consequently, these elements were not removed from the mantle by a core forming liquid or by volatility and their concentrations are very similar to those in the CI chondrites. Volatile elements on the other hand are depleted from the mantle in comparison to CI either by fractionation as a result of partial condensation from the solar nebula or due to volatility during high temperature accretion. The degree to which volatile elements have been lost from the mantle has been considered to be reflected by their 50 % condensation

temperatures (Wasson 1985; Lodders, 2003). Plotting the element concentrations, as in Fig. 1, a trend of increasing depletion is formed that is called the volatility trend (O'Neill and Palme, 1998; Palme, 2000;).

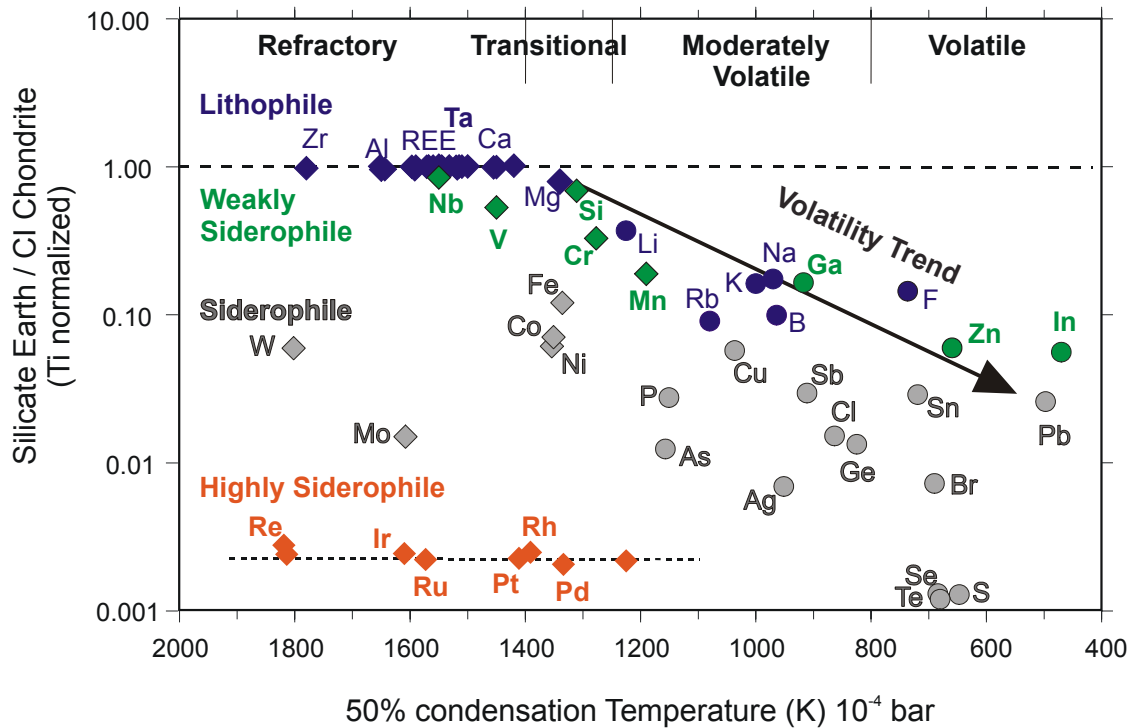


Fig. 1: Element abundances of the Earth's mantle normalized to CI chondrite and Ti (data from Palme and O'Neill, 2003). In general, siderophile elements have metal-silicate partition coefficients that are  $> 1$  and were therefore depleted from the mantle during core formation. They can be divided into three basic groups, weakly siderophile (green symbols), siderophile (grey symbols) and highly siderophile (orange squares). All blue symbols are lithophile elements. Transposed upon the effects of siderophile behavior is an additional depletion trend resulting from volatile behaviour (all circle symbols), which is considered to be a broad function of the 50 % condensation temperature (data from Wasson, 1985).

A large proportion of both refractory and volatile elements, however, are siderophile and have been depleted from the mantle as a result of core formation. Refractory siderophile elements such as W and Re are depleted from the mantle only as a result of core formation, while a large number of elements are depleted as a result of being both volatile and siderophile. Many elements are also indicated in Fig. 1 as transitional in character between refractory and volatile meaning that a minor degree of their depletion from the mantle may result from volatility. Siderophile elements are also divided into three groups based on their 1 bar metal/silicate partition coefficients: weakly siderophile (e.g. V, Cr and Mn), siderophile (e.g. Ni, Co, W) and highly siderophile (e.g. Pt, Ir). Weakly siderophile elements will partition into metallic Fe but only at very reducing conditions where the equilibrium silicate phase will be strongly depleted in Fe.

Siderophile elements, such as Ni and Co, are depleted from silicates even at redox conditions where the silicate retains a significant portion of Fe, such as that found in the present day mantle. Highly siderophile elements (HSE's) are strongly depleted from silicates under all redox conditions where Fe-rich metals are stable.

The depletions of siderophile elements in the mantle are not compatible with metal-silicate element partitioning at a single set of conditions at low pressure (Ringwood, 1979; Wänke 1981; O'Neill, 1991; Wade and Wood, 2005). The mantle depletions of weakly siderophile elements, such as V or Cr for example, would have required core-mantle equilibration at very reducing conditions where siderophile elements such as Fe, Ni and Co would have been much more depleted from the mantle than they actually are. In addition, Ni and Co 1 bar partition coefficients should have resulted in much more Ni being depleted from the mantle in comparison to Co, whereas they are present in the mantle in a nearly unfractionated chondritic ratio. Core-mantle equilibration should have also depleted highly siderophile elements from the mantle to a greater extent and by differing degrees when compared to each other. HSE's are not only overabundant in the mantle when compared to their 1 bar partition coefficients but are present in broadly chondritic relative proportions. The disagreement between 1 bar partition coefficients and siderophile element concentrations in the mantle is often referred to as the "excess siderophile element problem". Resolving this paradox is the main challenge of the models that have been developed to describe core formation.

## 1.2 Core Formation Models

A number of models have been proposed to explain the depletions of siderophile elements in the mantle. A successful model of core formation needs to also explain the presence of approximately 10 % of light alloying elements in the Earth's outer core that are known to exist from geophysical observations (Birch, 1964; Jeanloz, 1979, Mao et al. 1990). While many early models were developed only to address the geochemical aspects of core formation (Wänke, 1981), more recent models (Righter, et al., 1997; Wade and Wood, 2005) have also attempted to consider constraints from geophysical modelling of giant impacts, mantle melting and melt separation (Wetherill, 1985; Stevenson, 1990; Chambers, 2003; Rubie et al, 2003; Canup, 2004)

Core formation models can be categorised into two end member types. Heterogeneous models argue that the material from which the Earth formed changed with time from initially very reducing to more oxidised. Homogeneous models, on the other hand, argue that the Earth formed from material of constant composition and redox state but that equilibration at high pressures and temperatures at the base of a deep magma ocean rendered metal-silicate partition coefficients suitable for the attainment of the present day mantle abundances. Early heterogeneous models employed low pressure metal-silicate partitioning data as high pressure

data were not available. Many of these models therefore ignored the possibility that a deep magma ocean may have formed. The latter is an important component of homogeneous models, a number of which were proposed in the 90s (Li and Agee, 1996; Righter and Drake, 1997; Righter et al., 1997) as high pressure and temperature experiments started to be performed in this field.

Heterogeneous accretion models suggest a multi-stage equilibration process during which the composition of the accreting material changes in oxygen content, presumably as a result of different reservoirs within the accretion disk being tapped at different times. In the 2-stage core formation model of Wänke (1981) a period of early accretion occurs involving volatile-poor, reduced material (component A in Fig. 2) from which all elements more siderophile than Fe would have been completely extracted to the core. Moreover, even some slightly siderophile elements would have partitioned into the metal, thus explaining the depletions of V, Cr, Mn and also Si from the mantle. Si is then the major light element in the core. In the second stage, oxidised and volatile-bearing material (component B) that contained no metallic Fe was accreted to the mantle. As a result of the material being so oxidised that it contained no metal, no core formation takes place but the pre-existing reduced mantle and the accreting oxidised material mix efficiently to form the present day mantle. In the first stage of the model the siderophile elements are almost completely extracted from the mantle and even the weakly siderophile elements experience some depletion. The siderophile abundances of the mantle are then established by mixing in the oxidised CI-like material in the second stage that undergoes no core formation and thus retains chondritic relative proportions of the siderophile elements Ni, Co and also W.

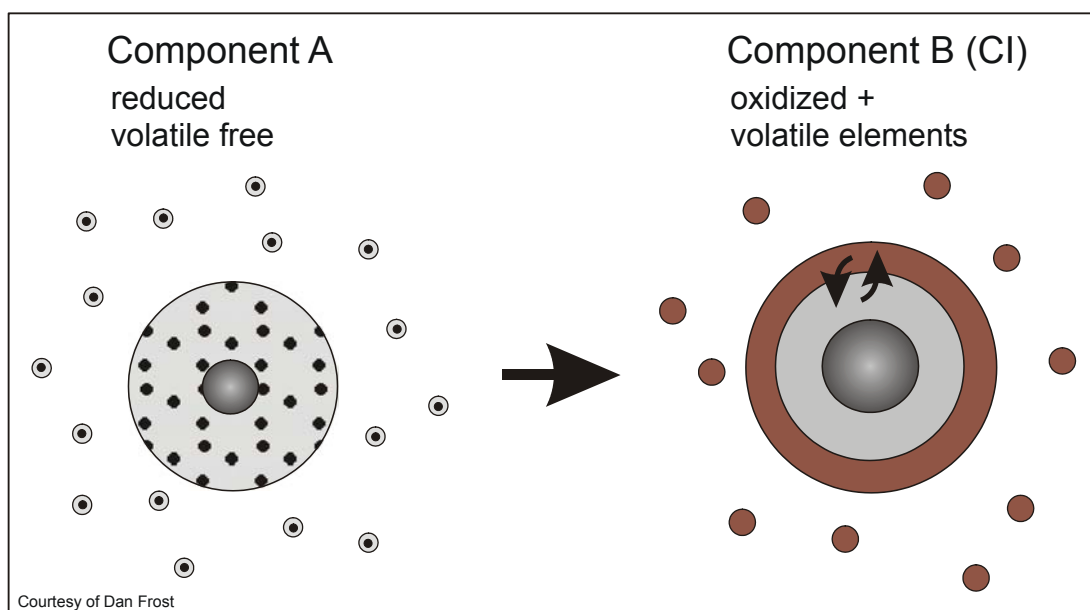


Fig. 2: Schematic diagram showing the two major steps of the low pressure accretion process as proposed with the heterogeneous core formation model of Wänke (1981). For details see text.

O'Neill (1991) recognised that the model of Wänke (1981) would have left HSE's overly abundant in the mantle and he therefore proposed a modified model in which two final steps in the heterogeneous process were added (Fig. 3). In the second oxidised stage (B) of the model, which O'Neill (1991) associated with the moon forming-impact, the accreting CI-type material contains no Fe metal but does contain sulphide which separates to the core (C). The proportion of the sulphide phase, which O'Neill (1991) termed the "Hadean Matte", is not sufficient to fractionate siderophile elements but does effectively extract HSE's from the mantle. In a final stage, a so-called "late veneer" of highly oxidised material that contained no core-forming metal nor sulphide accreted and mixed with the mantle providing HSE's in broadly chondritic relative proportions.

Heterogeneous models are quite robust as they have a number of steps that can be adjusted in terms of proportions of material and redox state until a satisfactory match to the mantle is achieved. These models are poorly constrained by the observations, however, and therefore their ability to predict conditions during core formation is limited.

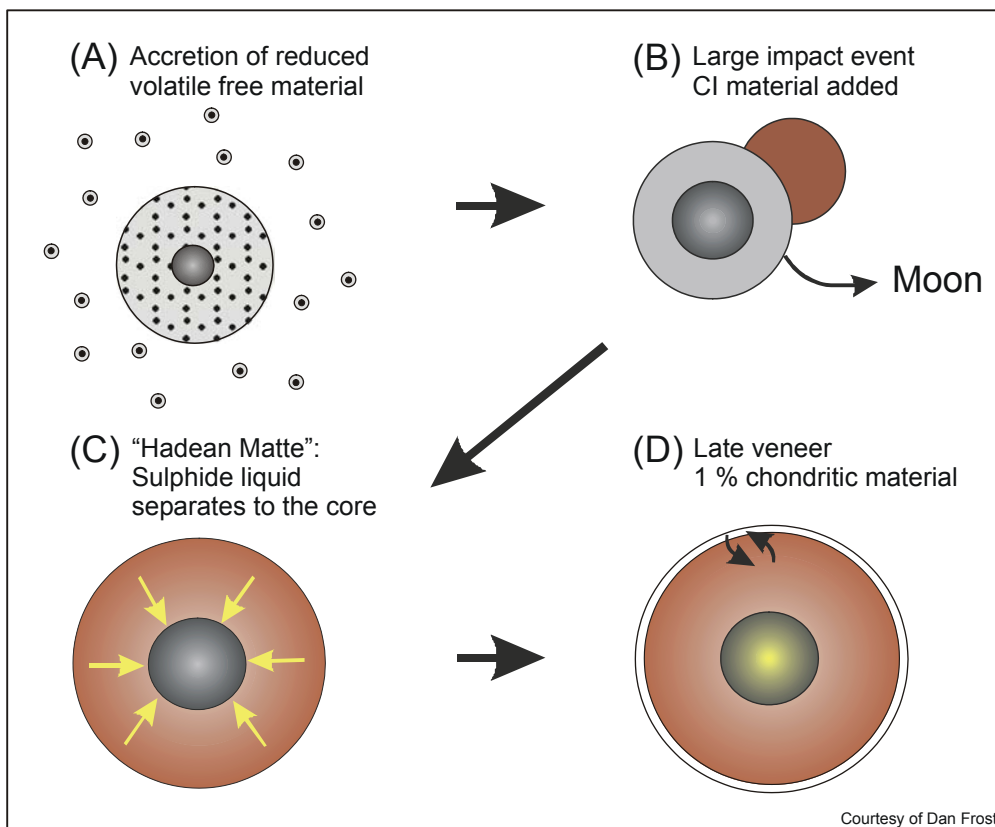


Fig. 3: Core formation model of O'Neill (1991). The first two stages are similar to the model of Wänke (1981) except that component (B) is associated with the accretion of material during the impact that formed the moon. In stage (C) sulphide liquid termed the Hadean Matte separates to the core removing HSEs from the mantle. In the final stage (D) approximately 1 % chondritic material is added to the mantle to provide the present day mantle HSE abundances.

Homogeneous models, on the other hand, propose that the Earth accreted from material with a broadly constant composition and redox state, but argue that core-mantle equilibration occurred at high pressures and temperatures where element metal-silicate partition coefficients can explain mantle abundances (Li and Agee, 1996; Righter and Drake, 1997). Such models draw support from a number of geochemical and geophysical arguments. Accretion is considered to occur from a well-mixed reservoir of material that therefore will have retained a constant composition over time (Righter et al., 1997). Some geophysical studies have predicted extreme temperatures at the Earth's surface during the sustained bombardment of accretion (Stevenson, 1990; Abe, 1993). High temperatures would have substantially melted the Earth's interior producing a deep magma ocean. Metal and silicate melts are assumed to have equilibrated at the base of the magma ocean at high pressures and temperatures (Fig. 4).

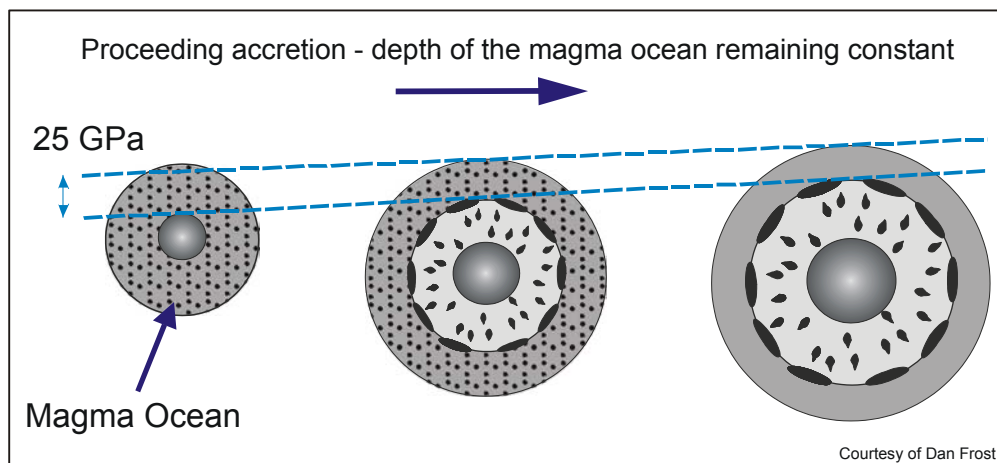


Fig. 4: Homogeneous core formation model of Righter et al. (1997) proposing the accretion of material of constant composition and the existence of a deep magma ocean. As the Earth grows, lower mantle minerals crystallize at the bottom of the magma ocean forming a solid lower part whereas continuing bombardment and related heat supply preserve the magma ocean. The metal portion of the accreted material rains out through the magma ocean and ponds at its base where it equilibrates with the silicate melt before sinking as large diapirs through the solidified lower mantle without further chemical re-equilibration.

The main geochemical evidence in support of homogeneous accretion comes from the effect of pressure on the partition coefficients of Ni and Co. At room-pressure metal-silicate equilibration would extract far more Ni from the mantle than Co, which is inconsistent with their unfractionated chondritic ratio in the mantle. However, high pressure experiments have shown that Ni becomes less siderophile with increasing pressure to a greater extent than Co and that the Ni and Co partition coefficients would converge at high pressure to a value consistent with the Ni/Co ratio in the mantle. Li and Agee (1996) proposed this would be at approximately 25 GPa, however other studies have argued for substantially higher pressures (Gessmann and Rubie, 2000; Chabot et al., 2005; Kegler et al., 2007) and all studies to date require extrapolation of data to

determine the convergence pressure of Ni and Co partitioning. The partitioning behaviour of Ni and Co lead to the proposal of the existence of a magma ocean with pressure and temperature at its base remaining relatively constant throughout accretion (Li and Agee 1996; Righter and Drake, 1997). The metal component of accreting material rained out through the magma ocean, and accumulated and equilibrated at its base, before descending as diapirs through the remaining solid silicate mantle underneath (Fig. 4). The diapirs were of sufficient size that further chemical re-equilibration with the solid mantle was minimal (Karato and Murthy, 1997; Walter et al., 2000).

Instead of basing their core formation model only on Ni, Co and Fe concentrations in the mantle, Wade and Wood (2005) tried to additionally match the concentrations of Si, V, Mn and W. They found that a single set of pressure, temperature and redox state could be identified for core-mantle equilibration that produced the required mantle element concentrations but the required temperature was far above the peridotite liquidus, meaning that these conditions could not correspond to the base of a magma ocean. They also argued that a magma ocean of constant depth was quite unlikely during core formation. They reasoned that as the Earth grew the bodies colliding with the Earth also increased in size. The more energetic collisions would have led to a magma ocean which increased in depth with time and resulted in an increase in the pressure and temperature of metal-silicate partitioning. They then modelled the effects of core-mantle equilibration at conditions of increasing pressure along the peridotite liquidus. The Earth was considered to form by 100 accretion steps where the accreted metals equilibrated at the base of a magma ocean that increased in depth with time. However, in this model it was impossible to match mantle concentrations of weakly siderophile elements such as V and Cr at the same redox conditions at which the mantle Ni and Co abundances were attained. A satisfactory match to the mantle concentrations of all elements could only be obtained if the oxygen fugacity of equilibration increased from initially reducing conditions to more oxidising conditions towards the end of core-mantle equilibration. In this respect, this concept is similar to the traditional heterogeneous models (Wänke, 1981; O'Neill 1991).

Existing models therefore seem to indicate that mantle depletions of weakly siderophile elements such as V and Cr could not have resulted from metal-silicate equilibration at the same redox conditions as siderophile element depletions. This seems to be a strong argument in favour of heterogeneous accretion. In addition, to date the existing experimental studies seem to indicate that HSE abundances in the mantle cannot be explained by high pressure and temperature equilibration in a magma ocean (Holzheid et al., 2000) and a late stage accretion of material that did not separate to the core, termed the 'late veneer', seems to be required.

### 1.3 Geochemical Constraints from Liquid Metal - Liquid Silicate Partitioning Behaviour

The compositional variables in heterogeneous core formation models are poorly constrained by the observed element depletions in the mantle. Testing the likelihood that the Earth formed from heterogeneous material rather than from a homogeneous composition at a specific set of as yet undetermined pressures and temperatures is difficult. However, a major implication of most heterogeneous models is that an initial reducing stage of core-mantle equilibration occurred where V, Cr and Si were extracted to the core. If some independent method can be found to test the most reducing conditions plausible for core-mantle equilibration then some constraints can be placed on the effectiveness of heterogeneous models in explaining Earth's composition. Placing such constraints is important for a number of other reasons. Several particularly significant elements, such as U or Hf, could have potentially entered the core at very reducing conditions. In addition, the nature of the light element in the core will have been influenced by the redox state of core formation with Si being favoured at reducing conditions and O at more oxidizing conditions. Some heterogeneous models also propose that metal-silicate partitioning occurred only in smaller planetisimals at lower pressure and they do not require the existence of a deep magma ocean. For this to have been the case, however, particularly reducing conditions would have been required.

The minimum  $f_{O_2}$  attained during core formation can be determined by examining the partitioning behaviour, principally as a function of  $f_{O_2}$ , of elements that have clearly not been depleted from the Earth's mantle as a result of core formation. Among the lithophile elements the element with the most siderophile tendency therefore places the tightest constraints on the redox state during core formation. Refractory elements are preferable in this respect because the bulk Earth concentration of volatile elements is more uncertain. Identifying such element behaviour can be enormously guided by examining thermodynamic data on metal-oxide reactions. The partitioning of Fe and an element M between metal and silicate melt can be described using the redox exchange reaction:



where  $n$  is the valence of the element M. The free energy change of the reaction which is zero at equilibrium is written:

$$\Delta G_{P,T} = \Delta G^0 + RT \ln \frac{[X_M^{metal}][X_{FeO}^{silicate}]^{\frac{n}{2}}}{[X_{MO_{\frac{n}{2}}}^{silicate}][X_{Fe}^{metal}]^{\frac{n}{2}}} + RT \ln \frac{[\gamma_M^{metal}][\gamma_{FeO}^{silicate}]^{\frac{n}{2}}}{[\gamma_{MO_{\frac{n}{2}}}^{silicate}][\gamma_{Fe}^{metal}]^{\frac{n}{2}}} \quad [2]$$

$\Delta G^0$  is the free energy change of the reaction involving the pure components at 1 bar and the temperature of interest and is calculated from the free energy of formation ( $\Delta_f G^0$ ) of each metal oxide from the elements by:

$$\Delta G^0 = \frac{n}{2} \Delta_f G^0(\text{FeO}) - \Delta_f G^0(\text{MO}_{\frac{n}{2}}) \quad [3]$$

Moreover, a distribution coefficient  $K_D$  (Righter and Drake, 2003) can be defined for the redox exchange reaction of equation [1] from the mole fractions  $X$  of the elements and the oxides in the metal and the silicate phase respectively:

$$K_D = \frac{[X_M^{\text{metal}}][X_{\text{FeO}}^{\text{silicate}}]^{\frac{n}{2}}}{[X_{\text{MO}_{\frac{n}{2}}}^{\text{silicate}}][X_{\text{Fe}}^{\text{metal}}]^{\frac{n}{2}}} \quad [4]$$

In this way  $K_D$  can be predicted using thermodynamic data for the pure oxides and data on the activity coefficients  $\gamma$  of the elements and the oxides in liquid alloys and silicate melts. The activity coefficients account for the difference in atomic environment in the liquid silicate or metal alloy compared to the pure components and will ultimately account for the differences between measured partition coefficients and those estimated with equation [4]. In Fig. 5  $K_D$  has been estimated for a range of metal oxides using thermodynamic data from the literature (Chase et al. 1998) and setting all activity coefficients to 1. When compared to available experimental data Fe-metal/silicate partitioning behavior is well predicted by equation [3] with known siderophile elements having  $K_D > 1$ , weakly siderophile elements having  $K_D < 0.1$  and lithophile elements  $< 10^{-5}$ .

In general, thermodynamic data for the oxides predicts that siderophile character increases across each transition metal row. The first weakly siderophile element appearing on the first row is V, which is in the same column as Nb and Ta. Nb is also known to be weakly siderophile and is also slightly depleted from the mantle and Ta and Si are predicted to be the next most siderophile elements. Figure 5 shows that elements to the left (Ti, Zr and Hf) and right (Cr, Mo, W) of this column are both more lithophile and more siderophile respectively. Lanthanide and actinide elements are all predicted to be strongly lithophile and metals in groups 3 and 4 are generally quite volatile except for Al which is shown in Fig. 1 to be more lithophile than Si or Ta. Therefore, based on 1 bar thermodynamic data, Ta is predicted to have the largest siderophile tendency of any element that is clearly not depleted as a result of core formation or volatility from the Earth's mantle. Ta is also of interest because it is predicted to have similar siderophile tendencies to Si, which is often proposed as a light alloying element in the core. Core formation models that propose conditions where Ta is depleted from the mantle while extracting slightly siderophile elements such as V and Cr can therefore be excluded. Similarly, as depletions of Nb in the mantle are relatively small ( $< 15\%$ ) any conditions that result in strong depletions of Nb can also be discounted.

The least depleted volatile elements might also be used to constrain core formation conditions. As shown in Fig. 1, Li, Ga, Na, F, Zn follow a broad trend of increasing depletion with 50 % condensation temperature which is often taken to indicate that these elements were also only depleted from the mantle as a result of volatility. Thus, conditions where any of these elements would be strongly depleted from the mantle during core formation can also be excluded. In heterogeneous models volatile elements are also considered to accrete in later, more oxidised stages. Examining likely fractionations of volatile elements as a result of core formation can place constraints on the timing of volatile element accretion and be used to evaluate the degree to which volatile elements accreted heterogeneously.

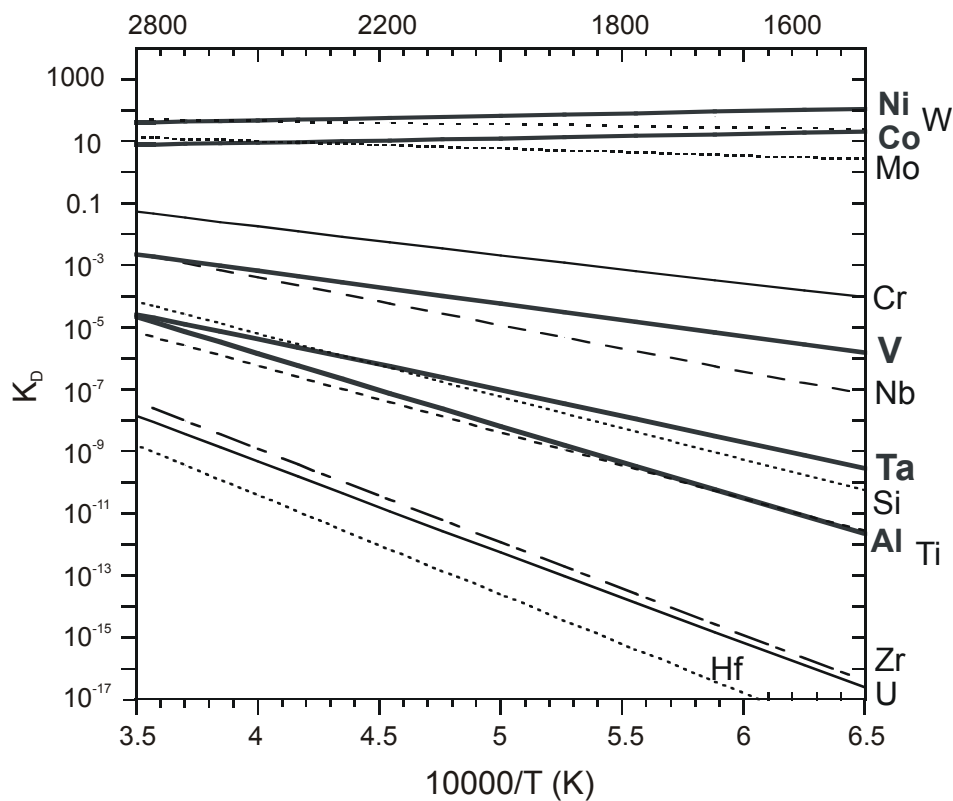


Fig. 5: Comparison of the liquid metal - liquid silicate distribution coefficient  $K_D$  of Fe relative to several elements considered to be lithophile ( $K_D < 10^{-5}$ ), weakly siderophile ( $K_D < 0.1$ ) and siderophile ( $K_D > 1$ ) at 1 bar plotted as a function of temperature. Exceptions like Pb and K are discussed in the text. All activity coefficients are set to 1.

## 1.4 Mechanical Separation Processes of Core Forming Liquids

A central issue in the context of planetary core formation is the mechanism by which core forming Fe-rich metal separated efficiently from the silicate mantle. The nature of this process is important because it will have influenced the time duration of core formation and the geochemical signatures of the two resulting reservoirs (Stevenson, 1990; Poirier, 1994).

A number of arguments support the idea that metal-silicate separation occurred through the formation of a terrestrial magma ocean that allowed metal to pond at its base and sink through the underlying solid mantle as diapirs (Stevenson, 1990; Li and Agee, 1996; Righter and Drake, 1997; Rubie et al., 2003). In such a model, metal-silicate equilibration would occur at the base of the magma ocean but re-equilibration during the passage of the liquid metal through the underlying solid mantle would be minimal (Karato and Murthy, 1997). A further mechanism that may have significantly aided the relatively rapid process of core formation on terrestrial planets is the percolation of liquid metal through solid silicate mantle (Stevenson, 1990). Percolation is an attractive mechanism to explain core formation on small bodies where temperatures during accretion may be below the silicate liquidus and for larger bodies, such as the Earth, in the later stages of accretion, when a significant portion of the mantle may have been crystallised. In both cases percolation could have drastically influenced the geochemistry of the core and mantle because in contrast to liquid metal separating as large diapirs, percolative flow would allow re-equilibration of core forming liquids during their entire transit through the solid mantle.

In texturally-equilibrated solid-liquid systems the occurrence of percolative flow is largely controlled by the melt fraction and the solid-solid ( $\gamma_{ss}$ ) and solid-liquid ( $\gamma_{sl}$ ) interfacial energies of the phases involved (von Bagen and Waff, 1986). The ratio of the interfacial energies determines the geometry of a melt pocket in a solid matrix by controlling the contact angle between the melt and the confining grains (Fig. 6), known as the dihedral angle  $\theta$  (Bulau et al., 1979; Laporte and Provost, 2000):

$$\frac{\gamma_{ss}}{\gamma_{sl}} = 2 \cos \frac{\theta}{2} \quad [5]$$

If the dihedral angle  $\theta$  is below the so-called wetting boundary of  $60^\circ$  an interconnected melt network can be formed and melt can migrate through the solid matrix independently of the melt fraction. If, on the other hand,  $\theta > 60^\circ$ , melt will be confined to disconnected pockets unless a critical melt fraction (approximately 6 %) is exceeded. In the latter case, percolation can occur; however, the melt will not be completely removed from the matrix because a pinch-off melt fraction will be reached where a certain quantity of melt, slightly below the critical melt fraction, is trapped at grain boundaries (von Bagen and Waff, 1986; Yoshino et al., 2003). Therefore, only in cases where  $\theta \leq 60^\circ$  can core separation by percolation through a solid silicate matrix be completed efficiently.

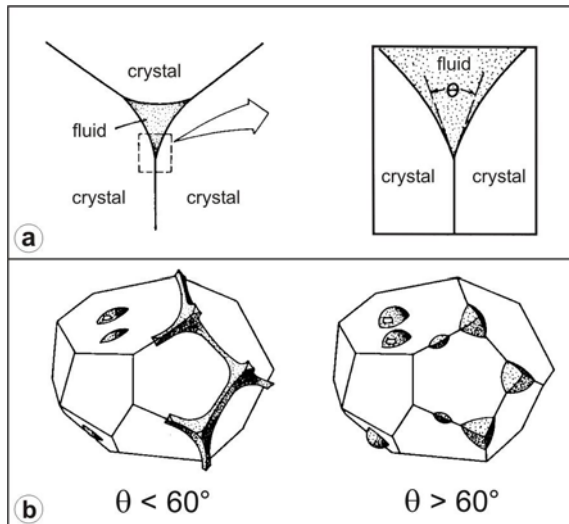


Fig. 6: Sketches illustrating the definition of the dihedral angle  $\theta$  and the wetting boundary (from Stevenson, 1990).

a) In a 2 D section across a melt pocket  $\theta$  is the contact angle between the melt and two confining grains.

b) 3 D view of single grains, the neighbouring grains removed: below the critical value of  $60^\circ$  for  $\theta$  the melt is distributed along grain edges forming an interconnected network, whereas above this wetting boundary the melt is trapped in pockets at three grain contacts.

## 1.5 High Pressure - High Temperature Experimental Techniques

The major method employed for high-pressure experiments for both the wetting behaviour and the metal-silicate partitioning studies is the multi-anvil technique. Details on this well-established high-pressure technique, pressure calibrations for different systems and temperature measurement can be found in Kawai and Endo (1970), Walker et al. (1990), Rubie (1999), Frost et al. (2004) and Keppler and Frost (2005). The apparatus works with a hydraulic press that generates a large uniaxial force which is transformed to a quasi-hydrostatic pressure by a system of 6 outer steel and 8 inner tungsten carbide anvils of cubic shape (Fig. 7). The cubic arrangement of the 8 inner anvils which are each truncated to form a triangular face at the corner pointing towards the centre of the cubic set, leaves an octahedron-shaped gap in which the pressure cell is placed. This octahedral pressure medium consists of MgO doped with 5 wt%  $\text{Cr}_2\text{O}_3$  which becomes mechanically weak at high temperatures thus producing a quasi-hydrostatic pressure on the sample at its centre. It also contains a  $\text{LaCrO}_3$  heating element and a thermocouple.

By applying different endloads with the hydraulic press and combining different edge truncations of the cubic anvils with various octahedral edge lengths, a broad pressure range up to 26 GPa can be covered. In this study, presses capable of producing maximum endloads of 500, 1000, 1200 and 5000 tonnes have been used. The typical configuration for the inner pressure cell and the cubic anvil truncation was a so called 18/11 assembly, meaning a 18 mm edge length for the octahedron and a 11 mm edge length for the triangular truncation, which was employed to attain pressures of 6 and 18 GPa in the 500 and the 5000 tonne presses respectively. For higher pressures of 20 and 24 GPa, 10/5 and 10/4 assemblies were used. For this study the routinely-used pressure calibrations for the different presses at BGI were employed. Such calibration curves are based on univariant phase transitions at known pressures and temperatures that are

observed in test runs and that can be related to the applied load of the press. In the temperature range of 1000-1900°C well defined phase transitions in  $\text{SiO}_2$ ,  $\text{Mg}_2\text{SiO}_4$ ,  $\text{CaGeO}_3$ , and  $\text{MgSiO}_3$  are typically employed for calibrations. In Frost et al. (2004), details of the pressure calibration of the 5000 tonne press can be found.

While the maximum pressure on the sample cannot be increased using the higher load of the 5000 tonne press (18 GPa with a 18/11 assembly), the advantage of this press is that it allows a larger assembly and thus a larger sample volume to be used at a given pressure when compared to the 1000 and 1200 tonne presses. In this way the same 18/11 assembly could be used for experiments at 6 and 18 GPa, providing the same sample environment and enhancing consistency between the experiments. The larger volume additionally provides the possibility to reduce thermal gradients within the sample and increases the accuracy of the temperature measurement (Frost et al., 2004). This can also be improved with the stepped  $\text{LaCrO}_3$  heaters (Rubie, 1999) of the 18/11 assemblies.

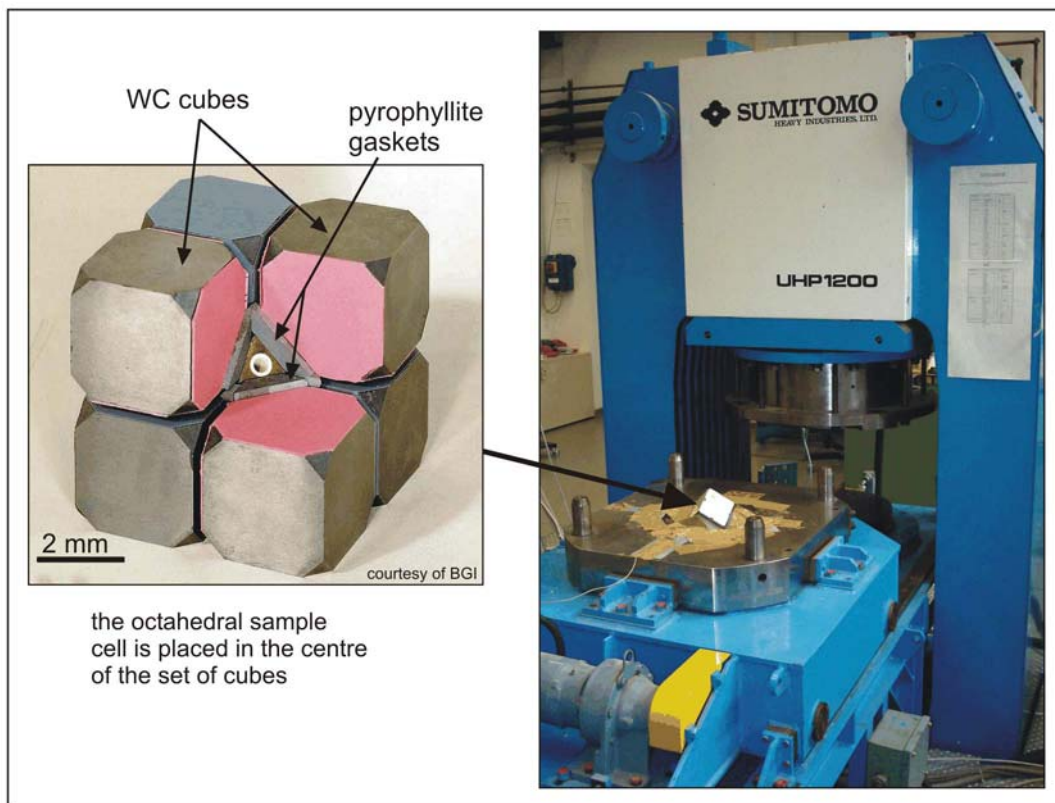


Fig. 7: The 1200 tonne multi-anvil press at BGI (right side). The image to the left displays a set of tungsten carbide cubes (corners are truncated), where one has been removed to show where the octahedral pressure cell is placed in the centre, sealed with the pyrophyllite gaskets that also work as spacers between the cubes.

The cross section of Fig. 8 gives details of the internal structure of the pressure cell. It consists of an array of cylindrical-shaped pieces made of different materials in order to fulfill different functions. In this study the samples were contained in graphite or MgO single crystal capsules (see below) of 2.3 - 2.5 mm length and with outer diameters of 1.6 - 2 mm. In some cases the graphite capsules were wrapped in Re foil for protection on recovering the run products and in all cases capsules were insulated from the electrically conducting parts by an MgO sleeve and MgO spacers at the top and the bottom. For heating, the sample is surrounded with a tubular resistance heater of  $\text{LaCrO}_3$  which is connected by Mo disks with the WC cubes. Electrical power is connected to the outer steel anvils but guided through the cubic anvils along the sample axis only. A  $\text{ZrO}_2$  sleeve around the  $\text{LaCrO}_3$  heater serves as thermal insulation. When placing the pressure cell within the cubic WC anvil set, it is sealed with pyrophyllite gaskets that help in confining the pressure medium under high pressures and temperatures (Fig. 7).

In a typical experiment, the assembly is slowly brought to the desired pressure at room temperature, then heated at a rate of about  $100^\circ\text{C}/\text{min}$ . Above  $2000^\circ\text{C}$  the heating rate was faster in order to avoid too much reaction of the sample with the capsule material (see below) before reaching the final temperature. An experiment is quenched rapidly by switching off the electrical power to the furnace. Decompression was performed gradually over a period of 15-17 hours.

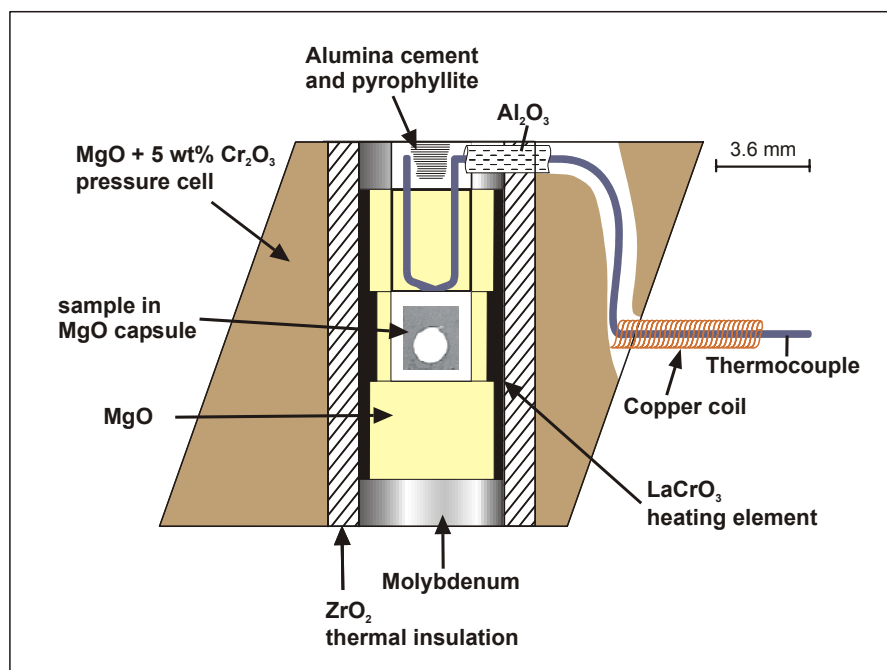
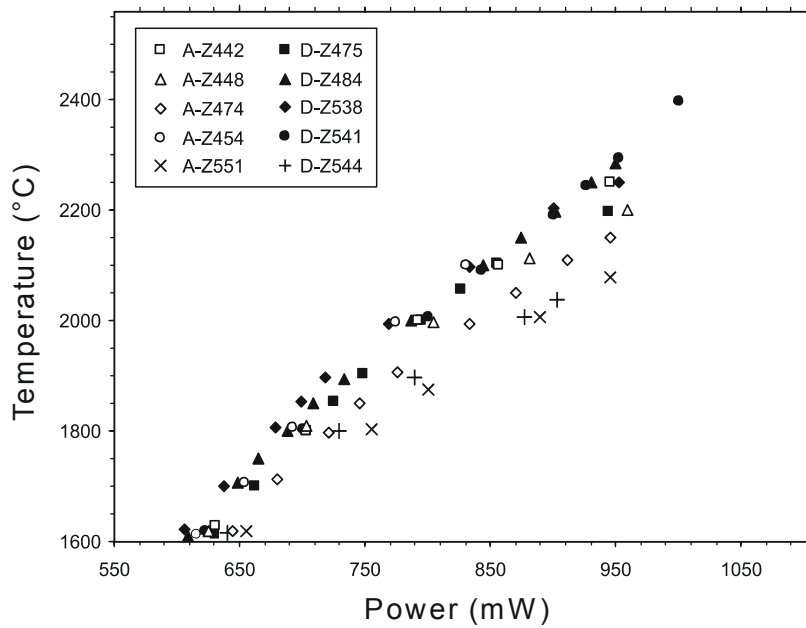


Fig. 8: Schematic cross-section of a typical pressure cell for multi-anvil experiments (18/11 assembly). See text for details. Modified image, courtesy of Dan Frost.

To monitor temperature during each experiment, a thermocouple is inserted axially at one end of the capsule (Fig. 8). For experiments where high temperatures of 2000 - 2600 °C are employed,  $W_{97}Re_3$  -  $W_{75}Re_{25}$  thermocouples (type D) with high melting points are most suitable. The effect of high pressures and temperatures on the electromotive force (emf), on which the calibration of the thermocouples is based, is not well known and temperature readings at such conditions could underestimate the real temperature. In this study no corrections of the thermocouple emf have been performed.

Employing run temperatures < 1850°C using 18/11 assemblies, as in the study of chapter 2, we found the precision of the thermocouple temperature reading within < 100 °C. At temperatures above 2000°C applied for the liquid metal - liquid silicate partitioning experiments (chapters 3 and 4) the thermocouple reading is usually less reliable. For isothermal experiments we therefore always employed the same power value. At maximum temperature the thermocouple reading usually starts dropping after the first 10 s whereas power and voltage stayed constant indicating stable conditions. One reason for this effect could be that Re starts to diffuse between the two thermocouple wires at these temperatures thus lowering the emf and consequently the indicated temperature. By extrapolation for temperatures  $\geq 2300^\circ\text{C}$  and in cases where thermocouples failed the temperature was estimated from the temperature versus power relationship derived from the most stable thermocouple readings. The temperature - power calibrations for the 18/11 assemblies from experiments at 18 GPa in the 5000 tonne press are shown in Fig. 9. According to the observed temperature ranges the uncertainty on the run temperature is about  $\pm 150^\circ\text{C}$ . The same value for the uncertainty was also observed applying this method on runs in 18/11 assemblies at 6 GPa, and on those using 10/4 and 10/5 assemblies. For the latter, two results from previous experiments performed at BGI using the same cells were included due to the small number of experiments of this study. One should note that in the smaller 10/5 and 10/4 assemblies with a straight  $LaCrO_3$  heater the thermocouple reading represents the temperature at a certain position along the thermal gradient rather than at where the sample is placed. Previous studies have shown that for the 10/4 assembly the thermal gradient is about 170 °C/mm at 1650°C. For the much higher temperatures involved in our experiments (> 2000°C) we therefore have to assume thermal gradients of at least 200 °C/mm.



High pressure and temperature experiments can be used to measure the partitioning of elements between silicate melt and liquid Fe-rich metal. In this way core formation conditions can be identified at which appropriate concentrations of siderophile elements in the Earth's mantle would have been obtained. In order to build and test models of core-mantle equilibration in a magma ocean, element partition coefficients need to be determined as a function temperature, pressure and oxygen fugacity; however, additional chemical variables such as S content and melt composition may also be important.

The metal-silicate partitioning experiments use synthetic starting powders of suitable composition to produce an ultramafic peridotitic melt with a composition similar to that of the bulk silicate Earth and an Fe-Ni rich metal. Minor amounts of siderophile elements are then added such that their partitioning between final metal and silicate can be measured. Due to detection limits of analytical techniques minor elements must be generally added in much greater quantities than their concentrations in the mantle. If very high concentrations of such elements are dissolved in Fe metal their activities may influence the partition coefficients and the "Henry's Law" region of compositionally-independent partitioning may no longer apply. For this reason it is appropriate to examine siderophile element partitioning in a series of experiments where only a few siderophile elements (4 - 5) are doped at the 1 % level in each composition. The oxygen fugacity of an experiment is varied by reducing the FeO content of the silicate melt to achieve very reducing conditions by adding Si as metal rather than SiO<sub>2</sub>. Oxygen fugacity can also be varied by employing variable amounts of the highly siderophile elements in the metal, as has been done in the study of chapter 4.

A major problem in metal-silicate partitioning is encapsulating the liquids. Metallic liquids react with metal capsules that are used in many other types of high-pressure experiments and silicate liquids react with ceramic capsules. Graphite has been frequently used as it has limited reaction with silicates and metals. However the solubility of C in Fe metal is still high and can influence partitioning of some siderophile elements by affecting their activities in Fe metal (Wade and Wood 2005). Ceramic capsules, such as Al<sub>2</sub>O<sub>3</sub> and MgO, result in increased levels of these oxides in the silicate melt. In addition, silicate melts can wet and percolate through polycrystalline ceramic capsules. One technique is to employ a single crystal MgO capsule which has no grain boundaries along which melts can percolate. Although MgO will still dissolve in the silicate melt, the effect on partitioning can potentially be quantified. The use of both MgO and graphite capsules at similar conditions can help to identify the contamination problems of both types of capsules.

## 1.6 Aims of this Study

By experimentally addressing several aspects and processes relevant to core formation the aim of this study was to test and evaluate different accretion scenarios for the Earth.

If the surface tension of Fe-rich melts in a matrix of solid silicate minerals was significantly lowered by the presence of an alloying component, this would give support to the idea that percolative metal separation could have played a role during differentiation of some planetary bodies without employing large-scale melting processes. Among the proposed light elements in the core which could possibly have concentrations in the metal high enough for percolation to become effective, the influence of S, O and C has been studied but data on Si are missing so far. As a significant amount of Si can enter the Fe-rich metal melts at low oxygen fugacities, the wetting characteristic of such alloys in a typical mantle mineral matrix has been studied for a range of Si concentrations and high pressures and temperatures in order to evaluate percolation as a relevant core formation process under reducing conditions (Chapter 2).

A plausible core formation model should be consistent with all element abundances observed in the mantle. According to many proposals, this signature is set by the metal-silicate partitioning behaviour of the elements while both phases were in the molten state thus assuming larger melting events and the existence of magma oceans during accretion and core formation on planetary bodies. While these models work with various pressures and temperatures, most of them have to employ quite reducing conditions at least for some period during metal-silicate equilibration to explain the depletions of weakly siderophile elements like V, Cr or Si. However, such conditions could also result in the preferred metal-partitioning of elements that are not or are only weakly-depleted in the mantle, like Ta and Nb. Moreover, this could lead to the additional extraction of several elements that are assumed to have experienced volatile depletion like Mn, Ga, In or Zn. Though the latter group is less well defined in their actual mantle concentrations, significant deviations from the required partition coefficients should be identified for all these elements and they can therefore be used to set constraints on the reducing stage of core formation models, because any conditions that would lead to their strong depletion can be excluded. The number of high-pressure, high-temperature experimental data for such indicator elements, especially for Ta, Nb and Ga, and their relative partitioning behaviour in comparison with weakly siderophile elements is very low and to date no data exist for Zn and In. The aim of this study was to extend the existing data base for the partition coefficients of these elements and to examine their behaviour relative to the weakly siderophile elements Cr, V, Si and Mn. Defining relationships for the dependence of the partitioning of each of these elements on pressure, temperature and oxygen fugacity allows us to simulate their behaviour under conditions suggested by the respective core formation model. Finally, this enables us to critically evaluate such models and place constraints on certain parameters that they involve. (Chapter 3).

The metal-silicate partition coefficients of the highly siderophile elements, experimentally determined at 1 bar, are extremely high which is inconsistent with their presence in the mantle. By determining their partitioning behaviour at high pressures and temperatures this study has tried to evaluate whether metal-silicate equilibration in a deep magma ocean is a plausible explanation for their apparent overabundance. This is one possible theory which has to date not been extensively tested due to the experimental and analytical difficulties involved (Chapter 4).

## Chapter 2

# The Wetting Ability of Si-bearing Liquid Fe-alloys in Solid Silicate Mantle Matrix

### 2.1 Previous Work

Pure liquid Fe has a high dihedral angle ( $> 100^\circ$ ) in silicate assemblages (Jurewicz and Jones, 1995). However, in addition to Ni it is known that the Earth's core also contains approximately 10 % of one or more light alloying elements with Si, S, O, C, and H being the most likely candidates (Poirier, 1994). Among them, S and O became of special interest, as the study of Idia and Guthrie (1988) had shown that both elements, in contrast to C for example, significantly lower the surface tension of liquid Fe (Fig. 10). Therefore, previous studies have systematically examined the effects of Ni, S and O on liquid metal-silicate matrix dihedral angles over a wide range of pressure, temperature and silicate mineralogy (Minarik et al., 1996; Ballhaus and Ellis, 1996; Shannon and Agee, 1998; Terasaki et al., 2005). These experiments have shown that S and especially O can strongly reduce the wetting angles so that values  $\leq 60^\circ$  can be reached at pressures  $< 3.5$  GPa (Minarik

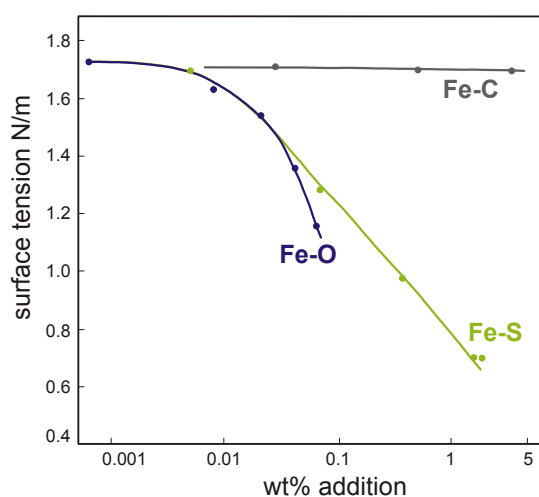


Fig. 10: The effect of C, O and S on the surface tension of the respective liquid Fe-alloy at 1 bar. From Iida and Guthrie (1988).

et al., 1996; Gaetani and Grove, 1999). At pressures representative of most of the Earth's upper mantle, transition zone and the upper part of the lower mantle, high O and S contents do not result in dihedral angles  $< 60^\circ$  (Shannon and Agee 1998; Terasaki et al., 2005; Terasaki et al., 2007) but there is some very preliminary evidence to suggest this situation may change in the deep lower mantle (Takafuji et al., 2004). The effects of Si on the wetting behaviour of liquid Fe-alloys in a silicate matrix have not been systematically examined at concentrations compatible with it possibly being the major light element in the Earth's core. Poirier (1994) recognized this deficiency and suggested that, based on the low surface energy of pure silicon (Iida and Guthrie, 1988), Fe-alloys containing Si may have lower surface tensions than pure liquid Fe as suggested by the studies of Ixanov et al. (1978) and Utigard (1994). Some heterogeneous accretion models propose an early reducing phase of core formation during which Si would have been extracted into the core (O'Neill, 1991; Javoy, 1995; Wade and Wood, 2005). Some models even propose

that such conditions prevailed over the entire core formation process (Wänke, 1981; Javoy, 1995; Allègre et al., 1995) with Si therefore accounting for the majority of the light element in the core (Allègre et al., 1995; McDonough and Sun, 1995). Such models are supported by the observation that the Earth's mantle is apparently depleted in Si relative to chondritic meteorites. If the presence of Si in core-forming Fe-rich liquids increased their ability to wet a silicate matrix and allowed porous flow to occur, this would be an important factor lending at least some support to such models. In this study we report wetting angles between Fe-rich melts with variable Si contents and typical silicate mantle minerals covering a wide P-T range relevant to core formation on terrestrial planets under reducing conditions. As such data would also help to clarify whether Si could have aided percolative core formation on some small reduced differentiated asteroids such as the parent body of the aubrite meteorites (Lodders et al., 1993) we performed a low pressure wetting experiment that contained S in addition to Si in the metal melt.

### 2.2 Experimental Setup and Analytical Techniques

Mixtures of Fe-Si alloys and synthetic silicate minerals were employed as starting materials. Forsterite was used in experiments performed up to 5 GPa and for experiments at 25 GPa enstatite was the precursor for Mg-Si perovskite. The Fe-Si alloys had Si contents of 9 and 17 wt% and 5 wt% of the respective alloy was added to the silicates. For the S-bearing run at 2.7 GPa, powdered Fe, Fe-Si-alloy (17 wt%) and FeS were mixed in proportions such that the resulting Fe-alloy contained 5 wt% Si and 5 wt% S. This mixture was placed in the centre of a capsule between two layers of synthetic forsterite.

High-pressure experiments were performed using a piston-cylinder press at 2 GPa and 1600°C and a multi-anvil apparatus at conditions of 2.7, 5 and 25 GPa and 1600-2000 °C. In the piston-cylinder experiment talc-pyrex was used as the pressure medium with a graphite furnace. For the 2.7 and 5 GPa experiments a 500-tonne Walker style multi-anvil press was used with a Cr-doped MgO octahedral pressure medium of 18 mm edge length and tungsten carbide cube truncations of 11 mm (18/11 assembly). At 25 GPa a 1200-tonne Kawai-type press with a 10/4 assembly was employed. To ensure reducing conditions graphite sample containers were wrapped in Re foil and a few runs at  $T > 1830^{\circ}\text{C}$  were performed with polycrystalline and single crystal MgO capsules. Stepped  $\text{LaCrO}_3$  heaters were employed in order to minimize thermal gradients across the sample. At 25 GPa a Re foil furnace was used. In all high-pressure experiments the temperatures were chosen such that they lay between the melting temperatures of the Fe-alloy and of the silicate phase and temperature was monitored with D-Type W-Re thermocouples. The run durations were varied between 0.75 and 71 hours. Experiments were quenched by turning off the electrical power to the furnace. Details of the experimental conditions are listed in Table 1.

The recovered samples were imbedded in epoxy resin and final polishing was performed with colloidal silica in order to produce a slight relief between differently oriented silicate grains for better imaging contrast. Imaging, phase identification and semi-quantitative chemical analyses were carried out with a SEM/EDX system (LEO 1530). Textures, especially silicate grain boundaries, could be best documented using low angles of incidence ( $70^\circ$ ) for the electron beam and thus combining orientational and Z-contrast back scattered electron (BSE) signals from the sample. From such BSE images with clearly visible liquid metal pocket-forsterite triple junctions the dihedral angles were measured with the angle tool of Corel Draw software. As a 2-D section of a sample cuts through melt-grain junctions in various orientations a single measurement will give an apparent angle value, which may be an over- or underestimation of the true angle measured perpendicular to the solid-solid-liquid contact. To account for this effect, the median value of an observed angle population in a sample was taken as this has been shown to be a good approximation of the true wetting angle (Jurewicz and Jurewicz, 1986). Accordingly, the measurement error for a population was determined from the 95% confidence interval around the median. To achieve a statistically adequate result a large number of angles, if possible  $> 100$ , should be analysed (Stickels and Hucke, 1964). In our study the number of angles measured on each sample containing a forsterite matrix ranges from 100 - 211, with the exception of three samples where only 76, 78 and 90 angles could be obtained from the respective sections. However, in these cases we also think that the numbers of analyses should be sufficient and that a representative median value is approached for the following reasons. In the case of the sample with 211 measurements, we used two sections oriented at  $90^\circ$  to each other and the medians of the obtained populations, consisting of 91 and 120 analyses, differ from the bulk median by only  $-3^\circ$  and  $+1^\circ$  respectively. In another sample, with a total of 150 measurements, we tested the median after every 10 analyses from 50 onwards and the deviation from the final median value ranges from  $0^\circ$  to  $+2.5^\circ$ . In the samples with the Mg-Si perovskite matrix, polishing with colloidal silica solution produced a strong relief between the metal and silicate phases, while the silicate grain boundaries are still not clearly visible. This hampered the identification of melt-grain junctions and the small number of measurable angles (9) gives only a very qualitative result. In the S-bearing run angles could only be determined for a S-rich Fe-melt that had separated and the number of 61 is also quite low so that we treat it as qualitative result only.

## 2.3 Results

### S-free Samples

Initial experiments of the 5 GPa series were performed with Fe-bearing olivine, but as a consequence of the low redox conditions, 3-4 log units below the iron-wüstite oxygen buffer, tiny metallic Fe droplets formed and pinned the grain boundaries thus inhibiting grain growth and the attainment of textural equilibration. For subsequent experiments, pure forsterite was employed. In these cases dry three-grain contacts of forsterite with angles close to  $120^\circ$  as well as the smoothly-curved forsterite grain boundaries provided a good indication that the matrix phase had reached textural equilibrium (Fig. 11 a, b). In a previous high-pressure study on the wetting behavior of Fe-S alloys in an olivine matrix (Terasaki et al., 2005) a time series of experiments performed over run durations of up to 24 hours indicated that textural equilibrium was approached after 12 hours at  $1600^\circ\text{C}$ . In our study experiments were performed for various time durations between 0.75 and 71 hours but measured dihedral angles remained unchanged over these durations. Given that significant grain growth occurred, even in the shortest runs, textural equilibrium was evidently reached quite rapidly.

Typical textures from recovered samples, including both forsterite and Mg-Si perovskite experiments, are shown in Fig. 11. In the 5 GPa forsterite samples, the majority of the quenched metal is present in pockets with convex-shaped contacts towards the silicate grains (Fig. 11a and 11b). Additionally, smaller melt pockets occur as nearly spherical inclusions within the recrystallized forsterite grains. In one sample, crystal growth was so rapid that metal was only observed as such inclusions. In the Mg-Si perovskite sample shown in Fig. 11c most of the metallic melt has been overgrown by perovskites and a relatively small amount of melt remained at grain junctions. Both features - round inclusions and convex pockets that are seen in all samples - are general indicators for high liquid-solid surface tensions (Bulau et al., 1979; Laporte and Provost, 2000; Walte et al., 2007), as are other characteristics such as an uneven melt distribution and abnormal grain growth, that result from the low melt mobility of high dihedral angle systems (Walte et al. 2007). Such behaviour causes the equilibrium texture to deviate from those observed in low dihedral angle systems.

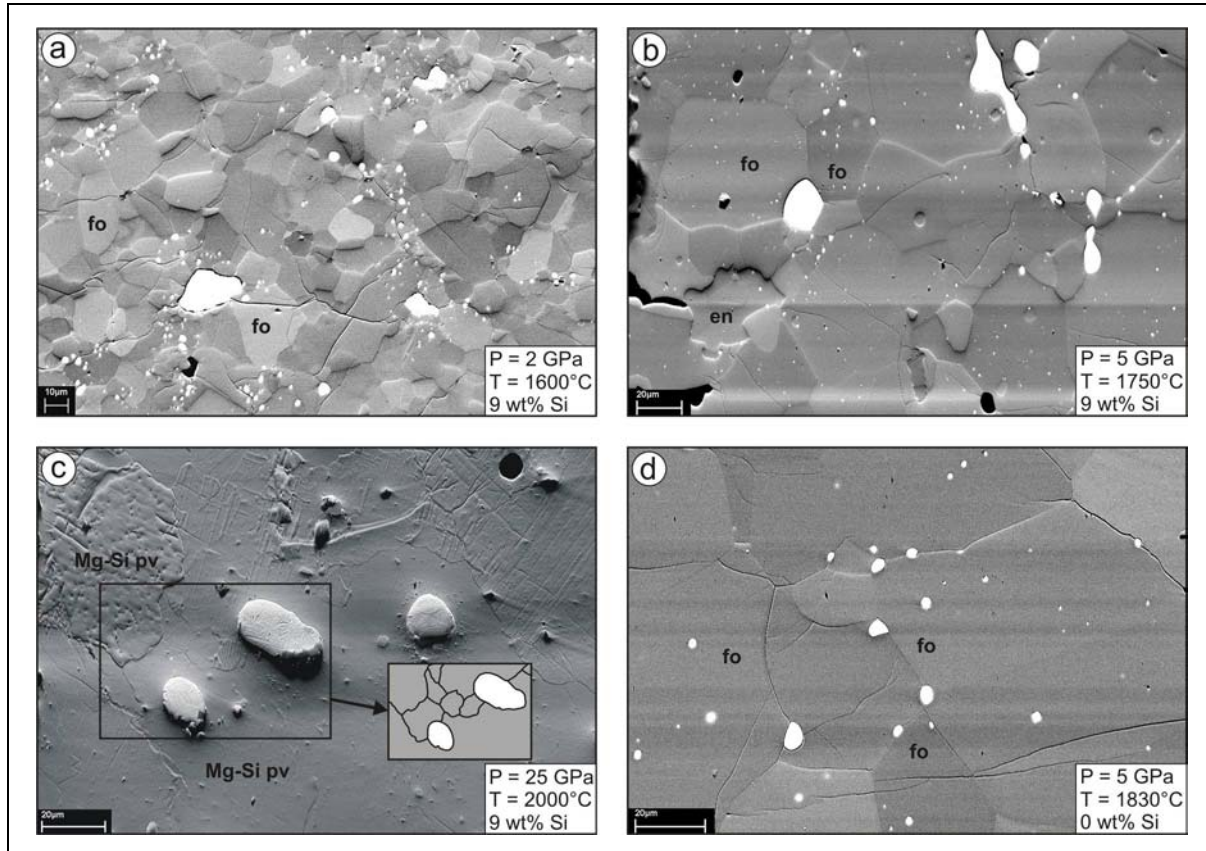


Fig. 11: BSE images of typical run products with quenched Fe-alloy melt pockets (white, bright grey in (c)) contained in a polycrystalline matrix of silicate grains (various grey colours). fo: forsterite, Mg-Si pv: Mg-Si perovskite, en: enstatite. All S-free metal compositions; the wt% values give the Si content in the metal phase of recovered samples. (a) Run product of the piston cylinder experiment at 2 GPa (Dh-1-P1). (b) The silicate phase of an experiment run at 5 GPa additionally shows enstatite, occurring in irregular shaped patches (negative relief) between the fo grains (V298) (c) At 25 GPa most of the metal melt occurs as inclusions within the Mg-Si pv. The black areas around the metal blebs are shadows resulting from the strong relief between metal and Mg-Si pv after polishing combined with a low angle of incident of the electron beam (S3533). In the inserted sketch the grain boundaries in the area around the two metal blebs are indicated (d) At 5 GPa the highest temperature resulted in complete Si loss from the metal phase (V302).

In some of the samples Si metal was observed to oxidize. Using MgO capsules, oxidation phenomena were observed in all cases, whereas in graphite capsules this effect was minimized. In the 5 GPa series, Si loss from the metal phase occurred to different degrees (Table 1 a) and was generally accompanied by the formation of enstatite occurring either as irregular patches in the forsterite matrix (Fig. 11 b) or completely enclosing some of the metal pockets. Such metal-silicate contacts including at least one enstatite grain were excluded from the dihedral angle measurements. At 1830 °C, Si loss from the alloy was most extreme and resulted in a pure Fe melt (Fig. 11 d). For comparison with the wetting behaviour of the Fe-Si alloys we also measured the pure Fe-liquid/forsterite wetting angles in this sample.

In test runs at 25 GPa using a  $\text{LaCrO}_3$  furnace we observed strong oxidation of the metal phase that was then Si-free after the experiment. In some cases excess  $\text{SiO}_2$  (stishovite) was formed either in direct contact with the metal phase or within the perovskite matrix. Moreover, even Fe was oxidized and partly incorporated in the perovskite that shows reaction zones around metal pockets while tiny Fe-metal droplets pin the perovskite grain boundaries. With such intensive chemical reaction, textural equilibrium was clearly not achieved. By replacing the  $\text{LaCrO}_3$  furnace with a Re foil heater, redox conditions in the experiment were drastically lowered and no Si loss from the metal phase or FeO-rich reaction rims in perovskite were observed.

In some samples the metal phase shows an internal texture with patches of variable Si content that most likely result from phase separation during quenching. In order to obtain the bulk metal composition, such metal pockets were analysed using a scanning mode over a rectangular area.

The median values of the wetting angles are listed in Table 1. Up to 5 GPa within a forsterite matrix all values lie within an interval of  $130^\circ - 140^\circ$  and are thus far above the wetting boundary of  $60^\circ$ . No dependency of the wetting characteristics on P, T or Si content of the Fe-alloy was observed, within error. Moreover, at  $1830^\circ\text{C}$  the contact angle of pure Fe ( $119^\circ\text{C}$ ) is actually lower than for all the Si-bearing Fe-alloys studied in this work. For the Mg-Si perovskite matrix at 25 GPa, even though a statistically-adequate evaluation was not possible, from the few measurements and the texture displaying mainly round metal inclusions it is obvious that liquid-solid interfacial energies are high and wetting angles are likewise  $\geq 140^\circ$ .

### Si- and S-bearing Run at Low Pressure

In the experiment where S was added to the Fe-Si-alloy the run product contained a S-rich metallic liquid in addition to a Si-rich liquid. A third liquid which was a 55:45 mixture of Re and Fe, resulting from contamination by the foil capsule, was also present in some areas. Interestingly this Re-rich liquid appeared to fully wet the forsterite grain boundaries.

From the starting Fe-S-Si mixture two melts formed which is in qualitative agreement with the phase diagram (Raghavan, 1988) except that the S content of the Si-rich melt was only 0.1 % (Table 1 b) whereas the phase diagram would predict at least 1-2 wt %. This melt formed small round droplets between the forsterite grains and showed no sign of wetting the silicate matrix. We qualitatively estimate wetting angles in excess of  $120^\circ$ . The S-rich melt on the other hand was nearly Si-free and formed angular melt pockets at forsterite grain contacts with an approximate wetting angle of  $94^\circ$  (Table 1b). Angles in the range of  $85 - 100^\circ$  have also been reported for reduced Fe-rich metal melts with S-concentrations of 24-35 wt% at similar conditions of 2 GPa and  $1350^\circ\text{C}$  by Ballhaus and Ellis (1996).

## 2. The Wetting Ability of Si-bearing Liquid Fe-alloys in Solid Silicate Mantle Matrix

**Table 1:** Experimental conditions, starting compositions<sup>1</sup> and results.

a) Experiments with Fe-Si alloys

run no.	P (GPa)	T (°C)	Duration (h)	Initial Si content of the alloy (wt%)	Si content in recovered alloy (wt%) <sup>2</sup>	Silicate phase <sup>3</sup>	Wetting angle (median)	95% C.I. <sup>4</sup> -	95% C.I. <sup>4</sup> +	Number of angles measured
Dh-1-P1	2	1600	0.75	9.0	9.0	fo	137°	4°	4°	150
Dh-2-P1	2	1600	0.75	17.0	18.0	fo	132°	2°	5°	150
V297	5	1600	19.5	9.0	6.0	fo	140°	6°	3°	90
V298	5	1750	18.8	9.0	9.0	fo	134°	3°	1°	211
V299	5	1750	71.0	9.0	8.0	fo	134°	4°	3°	100
V300	5	1750	31.7	17.0	16.0	fo	138°	5°	5°	78
V313	5	1750	1.5	17.0	17.0	fo	136°	4°	4°	76
V302	5	1830	7.0	9.0	0.0	fo	119°	4°	4°	103
S3533 <sup>5</sup>	25	2000	2.3	9.0	9.0	Mg-Si pv	≥ 140° <sup>6</sup>			9

b) Experiment with two liquids: (1) FeS melt and (2) Fe-Si alloy

run no.	P (GPa)	T (°C)	Duration (h)	Initial comp. of metal mix (wt%)	recovered Fe-alloys (wt%) <sup>2</sup>	Silicate phase <sup>3</sup>	Wetting angle (median)	95% C.I. <sup>4</sup> -	95% C.I. <sup>4</sup> +	Number of angles measured
V360	2.7	1650	7.0	5 Si, 5 S	1) 0.1 Si, 36.5 S 2) 5.9 Si, 0.1 S	fo	94°	10°	7°	61
							> 120° <sup>6</sup>			-

<sup>1</sup> Melt fraction of Fe-alloy: 5wt%

<sup>2</sup> semiquantitative analysis with EDX device of SEM. Uncertainties of approximately 1 %

<sup>3</sup> fo: forsterite, Mg-Si pv: Mg-Si perovskite; phases identified with SEM

<sup>4</sup> Error for the median of the angle population based on the 95% confidence interval

<sup>5</sup> Re heater used

<sup>6</sup> semiquantitative value

## 2.4 Discussion and Conclusions

Over the studied range of pressure (2 - 25 GPa), temperature (1600 - 2000°C) and liquid Fe compositions (Si contents of 9 - 17 wt%), Si does not lower the dihedral angle between liquid Fe-rich alloy and silicate minerals. Up to the highest Si content in the metal, dihedral angles remain high (132-140°) and lie far above the wetting boundary of 60°, as shown in Fig. 12. Therefore, in contrast to the suggestion of Poirier (1994), Si actually seems to raise the interfacial energy of liquid iron alloys. This is most likely because, in contrast to S and O (Iida and Guthrie, 1988; Terasaki et al., 2005), Si apparently does not behave as a surface-active element that reduces the surface tension of liquid Fe. As shown in Fig 12, anions such as S and O have significant effects on the liquid Fe surface tension, while metallic alloying components such as Si do not. This is consistent with the observation that Ni, also, has little effect on the surface tension of liquid Fe (Gaetani and Grove, 1999). As Si does not favourably influence the liquid wetting behaviour, it is likely that interfacial energies between Si-bearing Fe liquids and other silicate minerals are also high.

Under reducing core formation conditions, where significant amounts of Si would partition into the metal phase, efficient liquid metal separation cannot occur by percolation alone. Aubrite achondrites are a family of meteorites that seem to come from a reduced parent body where metal segregation has occurred (Lodders et al., 1993). Under strongly reducing conditions, which resulted in very low FeO contents of silicate minerals, the separated metal must have contained significant Si. Our results indicate that the presence of Si did not aid percolation of the Fe-rich liquid and segregation must therefore have occurred through large degree melting of the silicate matrix. Although the aubrite parent body also contained significant S, Si-Fe liquids have a large immiscibility gap with S-Fe liquids at these low-pressure conditions (Raghavan, 1988). This is supported by our results from 2.7 GPa that show immiscible Si-Fe liquids to have low S contents that had no influence on the liquid interfacial energy. Perhaps more importantly, even though the coexisting S-Fe liquid has a lower surface tension, it still has a dihedral angle of  $\sim 94^\circ$  that is still far above the wetting boundary. Although Fe-S melts have been observed to wet a silicate matrix at more oxidizing conditions (Gaetani and Grove, 1999) this clearly results from a higher solubility of O in the melt. Under reducing conditions even if the Si contents of the Fe-S melts are low, O contents are likely to be also low, thus ensuring a high metal-silicate dihedral angle even for high S contents.

The results, moreover, imply that Si would not have aided liquid metal percolation through the Earth's solid silicate perovskite bearing lower mantle as our preliminary qualitative data indicate that dihedral angles remain very high under these conditions. Although lower interfacial energies have been claimed (Takafuji, 2004) for some O and Si bearing metallic Fe-liquids at very high pressures ( $> 70$  GPa), this effect, if correct, most likely arises from the influence of dissolved O rather than Si.

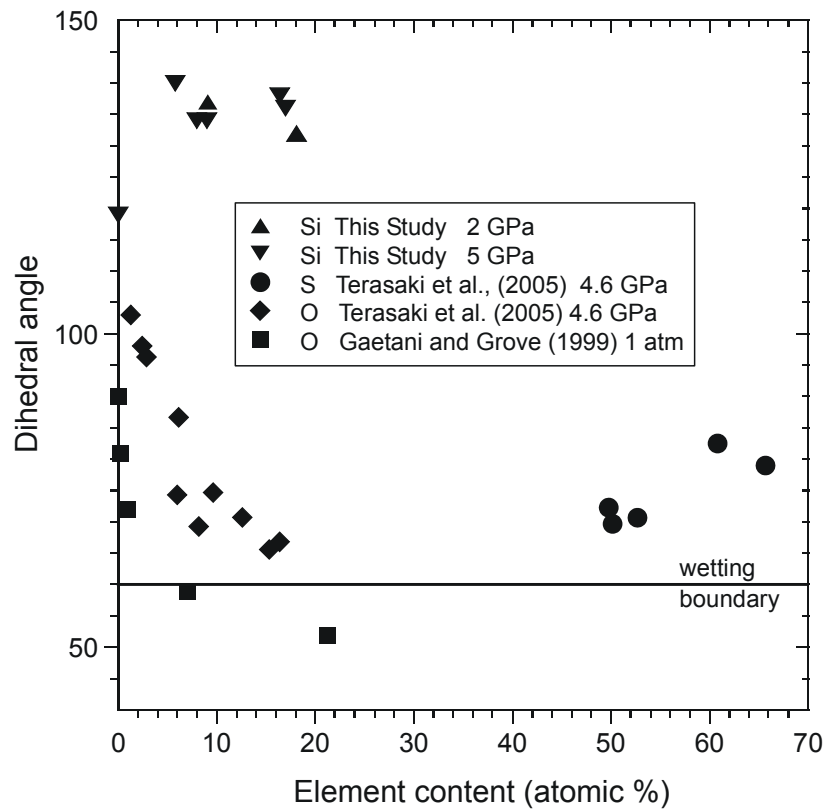


Fig. 12: Dihedral angles between silicate melt and metal or metal sulphide melt as a function of the light alloying elements Si, S and O in the metal. All data are for olivine matrix. Data for oxygen are from melts that also contained S. O and S experiments were performed in the range 1623-1850 K, while those for Si were performed between 1873-2096 K.



## Chapter 3

# Liquid Metal - Liquid Silicate Partitioning of Nominally Lithophile and Weakly Siderophile Elements

### 3.1 Introduction

The partitioning behaviour of several siderophile elements (Ni, Co) have been relatively well investigated and form the basis for a number of core formation models (O'Neill, 1991; Righter et al., 1997; Li and Agee, 2001; Gessmann and Rubie, 2000; Chabot et al., 2005; Wade and Wood, 2005). However, for a core formation model to be entirely plausible, it has to be able to reproduce the entire pattern of observed element abundances in the Earth's mantle (Fig. 1). Therefore, any model involving liquid metal - liquid silicate partitioning can be tested by determining whether the partition coefficients for certain elements under conditions suggested by the model are consistent with their mantle concentrations. Some elements that are categorized by their mantle abundance as refractory and lithophile can play a key role in this context because any model that requires conditions where these elements are strongly depleted as a result of core-mantle equilibration can be excluded. As their free energies of formation at 1 bar relative to Fe indicate (Fig. 5), the elements Ta and Nb might become siderophile during core formation under strongly reducing conditions (see chapter 1) but these elements are not significantly depleted from the mantle. On the other hand, the depletion of V, Cr and Si relative to an assumed CI chondritic bulk composition for the Earth is often assigned to their extraction to the core. The extraction of V, Cr and Si, which are only weakly siderophile, however, would have required strongly reducing conditions. By examining the partitioning behaviour of Ta and Nb relative to that of V, it should be possible to set constraints on the level of such a reducing phase of core formation and to evaluate the possible range of pressure, temperature and oxygen fugacity conditions with respect to that suggested by core formation models.

Similar constraints on the conditions of core formation can be obtained by examining the high-pressure, high-temperature partitioning behaviour of elements that are mainly considered to be depleted from the mantle as a result of volatility such as Mn, Ga, In or Zn (Fig. 1). The mantle depletions of these elements plot on a trend of increasing depletion from the mantle as a function of their 50 % condensation temperature, which is often referred to as the volatility trend. This implies that they are depleted from the mantle mainly as a result of volatility. However, these elements may also become siderophile under certain conditions proposed by core formation models. If models for core formation result in conditions that significantly upset the volatility trend then important constraints can be placed on either the conditions of core formation or the processes of volatile fractionation during condensation and accretion.

Partitioning studies that examine the siderophile behaviour of Ga relative to Mn and In relative to Zn may be particularly useful as the mantle Ga/Mn and In/Zn ratios are near-chondritic and appear not to have been significantly fractionated by core-mantle differentiation.

## 3.2 Experimental Conditions

Liquid metal-liquid silicate partitioning experiments at high pressures of 2 - 24 GPa and high temperatures of 1750 to 2600°C were carried out in multi-anvil and piston cylinder devices.

The experiments were performed in two separate series both doped with Ta in addition to fixed proportions of (A) Ga, In, Zn and (B) V, Cr, Mn, Nb, Ti (see Table 2). In all cases these elements were added as oxides in bulk concentrations of (A) 4 wt% and (B) 10 wt% to powdered starting mixtures of 55-56 wt% synthetic peridotite and 35-40 wt% of an Fe-rich metal mix.

The silicate component was a composition mixed from major element oxides (primitive mantle, ~ 8 wt% FeO, as reported by Palme and O'Neill 2003), additionally containing small traces of Ti, Cr and Mn which allowed partitioning data to be collected for these elements from all samples. A mixture of pure, dried powders of MgO, SiO<sub>2</sub>, Al<sub>2</sub>O<sub>3</sub>, TiO<sub>2</sub>, MnO, Cr<sub>2</sub>O<sub>3</sub>, CaCO<sub>3</sub> and Fe<sub>2</sub>O<sub>3</sub> was pressed into pellets, slowly decarbonated in air by heating from 600 to 1000°C and afterwards reduced in a gas-mixing furnace in a CO-CO<sub>2</sub> atmosphere at 1200°C and 2 log units below the fayalite-magnetite-quartz buffer for 24 h. The Fe-rich metal mixture always contained 2 wt% Ni and 1 wt% Co and variable proportions of Si (0.1 - 16.5 wt%) which was added in the form of Fe<sub>84</sub>Si<sub>16</sub> or Fe<sub>71</sub>Si<sub>29</sub> alloys. The addition of metallic Si allowed the oxygen fugacity to be varied in a range of -1.3 to -4.2 log units below the iron wüstite buffer ( $\Delta$  IW). In one experiment the metal phase additionally contained 7 wt% S (added as FeS) whereas all other experiments were S-free (see Table 2).

Graphite and MgO single crystal capsules were employed as sample containers. As will be discussed below, neither material is ideal. At high temperatures, the tendency of the capsules to react with the sample charge limits the run duration which ranged between 20 s and 25 min depending on T. Run durations were in accordance with suitable time scales for equilibrium partitioning of Ni and Co reported by Thibault and Walter (1995) and Li and Agee (2001). According to Thibault and Walter (1995), durations up to 300 s should be sufficient for homogenization of the liquids.

Details of the experimental conditions are listed in Table 3. Two experiments were performed in a piston cylinder press at 2 GPa and 1740-1750°C. In both cases a graphite furnace, a talc-pyrex pressure assembly and an alumina sleeve were employed. In run P1 (Table 3) three graphite capsules were each wrapped in Re foil and placed on top of each other, separated by thin alumina disks. In experiment C15 two MgO capsules were run together in a MgO tube contained within an outer Pt tube. All other experiments were carried out in various multi-anvil devices. In all

### 3. Liquid Metal - Liquid Silicate Partitioning of Lithophile and Weakly Siderophile Elements

cases  $\text{Cr}_2\text{O}_3$  doped MgO octahedra as pressure medium and tungsten carbide cubic inner anvils were employed. For the experiments at 6 GPa and 18 GPa, 18/11 assemblies (see chapter 1) were used in a 500-tonne Walker style press and the 5000-tonne large volume press respectively. 20 GPa experiments were performed in 10/5 assemblies in a 1000-tonne Kawai-type press and a 1200-tonne Kawai-type press in combination with a 10/4 assembly was used to reach 24 GPa. For 18/11 assemblies involving stepped  $\text{LaCrO}_3$  heaters the temperature gradient across the sample length was reduced. At each pressure between 2 - 20 GPa the effect of  $f_{\text{O}_2}$  on the partitioning behaviour was studied at constant T. Moreover, we have varied the temperature in isobaric runs at 6 and 18 GPa.

For the piston cylinder run P1 the temperature was controlled using a type B Pt-Pt<sub>87</sub>Rh<sub>13</sub> thermocouple. In all other experiments type D W<sub>97</sub>Re<sub>3</sub>-W<sub>75</sub>Re<sub>25</sub> thermocouples were employed. The temperature calibration for experiments above 2000°C was performed as described in chapter 1 (see also Fig. 9).

**Table 2:** Compositions of the starting materials (wt%)

doped with:	(A) Ta, Ga, In, Zn					(B) Ta, V, Mn, Cr, Nb, Ti		
	A-1	A-5	A-2	A-3	A-4	A-R5	A-R2	A-R-S1
SiO <sub>2</sub>	25.65	25.65	25.65	25.65	25.65	25.37	25.37	25.37
MgO	20.77	20.77	20.77	20.77	20.77	20.55	20.55	20.55
Al <sub>2</sub> O <sub>3</sub>	2.54	2.54	2.54	2.54	2.54	2.51	2.51	2.51
CaO	2.06	2.06	2.06	2.06	2.06	2.04	2.04	2.04
FeO	4.58	4.58	4.58	4.58	4.58	4.53	4.53	4.53
TiO <sub>2</sub>	0.12	0.12	0.12	0.12	0.12	2.00	2.00	2.00
Cr <sub>2</sub> O <sub>3</sub>	0.21	0.21	0.21	0.21	0.21	1.50	1.50	1.50
MnO	0.08	0.08	0.08	0.08	0.08	1.50	1.50	1.50
Ta <sub>2</sub> O <sub>5</sub>	2.00	2.00	2.00	2.00	2.00	1.50	1.50	1.50
Nb <sub>2</sub> O <sub>5</sub>	-	-	-	-	-	1.50	1.50	1.50
V <sub>2</sub> O <sub>5</sub>	-	-	-	-	-	2.00	2.00	2.00
Ga <sub>2</sub> O <sub>3</sub>	1.00	1.00	1.00	1.00	1.00	-	-	-
In <sub>2</sub> O <sub>3</sub>	0.50	0.50	0.50	0.50	0.50	-	-	-
ZnO	0.50	0.50	0.50	0.50	0.50	-	-	-
Fe	32.20	35.60	37.00	38.40	38.76	31.15	32.38	29.05
Si	6.60	3.20	1.80	0.40	0.04	2.80	1.58	2.45
S	-	-	-	-	-	-	-	2.45
Ni	0.80	0.80	0.80	0.80	0.80	0.70	0.70	0.70
Co	0.40	0.40	0.40	0.40	0.40	0.35	0.35	0.35

### 3. Liquid Metal - Liquid Silicate Partitioning of Lithophile and Weakly Siderophile Elements

**Table 3:** Details of the experimental conditions;  
Si, C and S contents of the quenched metal melt and Mg/Si ratio of the quenched silicate melt

run	starting comp.	capsule material	t (s)	P (GPa)	T (°C)	log $f_{O_2}$ ( $\Delta IW$ )	quenched metal melt			quenched silicate melt
							$X_C$	$X_S$	$X_{Si}$	Mg/Si (mol%)
P1-19	A-5	graphite	70	2	1740	-4.04	0.16	-	0.06	0.97
P1-21	A-2	graphite	70	2	1740	-3.19	0.28	-	0.00	0.97
P1-20	A-3	graphite	70	2	1740	-1.78	0.22	-	0.00	1.31
C15-9	A-R5	MgO	150	2	1750	-3.02	-	-	0.04	1.23
C15-10	A-R2	MgO	150	2	1750	-2.29	-	-	0.00	1.28
V307	A-1	graphite	300	6	2100	-4.20	0.04	-	0.20	0.97
V312	A-5	graphite	1500	6	2100	-3.24	0.15	-	0.04	1.23
V334	A-R5	graphite	600	6	2100	-2.65	0.24	-	0.00	1.03
V310	A-2	graphite	1500	6	2100	-2.27	0.23	-	0.00	1.05
V337	A-R2	graphite	600	6	2100	-1.89	0.23	-	0.00	1.20
V309	A-3	graphite	900	6	2100	-1.40	0.25	-	0.00	1.16
V311	A-4	graphite	1500	6	2100	-1.37	0.22	-	0.00	1.30
V346	A-R5	MgO	300	6	2100	-3.57	-	-	0.03	1.88
V366	A-R5	MgO	130	6	2100	-3.41	-	-	0.03	2.02
V365	A-R2	MgO	120	6	2100	-2.84	-	-	0.00	2.09
V367	A-R5	MgO	120	6	2300	-3.39	-	-	0.03	2.20
Z457	A-3	MgO	90	18	2200	-1.59	-	-	0.00	1.27
Z442	A-5	MgO	90	18	2300	-2.78	-	-	0.08	1.39
Z469	A-R5	MgO	90	18	2300	-2.50	-	-	0.06	1.54
Z447	A-2	MgO	90	18	2300	(-2.44)	-	-	0.04	1.41
Z474	A-R2	MgO	95	18	2300	-2.04	-	-	0.03	1.45
Z448	A-5	MgO	20	18	2550	-2.71	-	-	0.09	1.40
Z551	A-RS1	MgO	120	18	2300	-2.47	-	0.13	0.02	1.49
H2333	A-1	graphite	330	20	2100	-3.39	0.22	-	0.07	1.08
H2340	A-5	graphite	480	20	2100	-2.25	0.31	-	0.00	1.13
H2347	A-3	graphite	320	20	2100	-1.64	0.28	-	0.00	1.16
H2350	A-4	graphite	285	20	2100	-1.31	0.25	-	0.00	1.17
S3658	A-5	MgO	90	24	2600	-2.56	-	-	0.09	1.15

P = pressure, T = temperature, t = run duration,  $f_{O_2}$  calculated relative to the IW buffer (see text)

MgO = MgO single crystal capsule

### 3.3 Run Products

Typical run products contained a metal blob that separated from the silicate while both phases were in the molten state under run conditions. The back scattered electron (BSE) images of Fig. 13 show sections through samples from both capsule materials recovered from a) 18 GPa, 2300 °C run in a MgO single crystal capsule and from b) 6 GPa, 2100 °C contained in a graphite capsule. In the latter case the metal usually quenches to a more irregular shaped blob containing laths of graphite. A brighter rim around the sample charge indicates melt infiltration into the capsule wall. At 20 GPa the transformation of the capsule into diamond enhances this effect and complicates sample preparation. Moreover, C diffusion into the iron liquid can be observed, an extreme example of which is displayed in Fig. 13 d. When using MgO single crystal capsules, the MgO reacts with the silicate melt resulting in patches of ferropericlasite (Fig. 13 c) that sometimes form a discontinuous rim around the metal blobs.

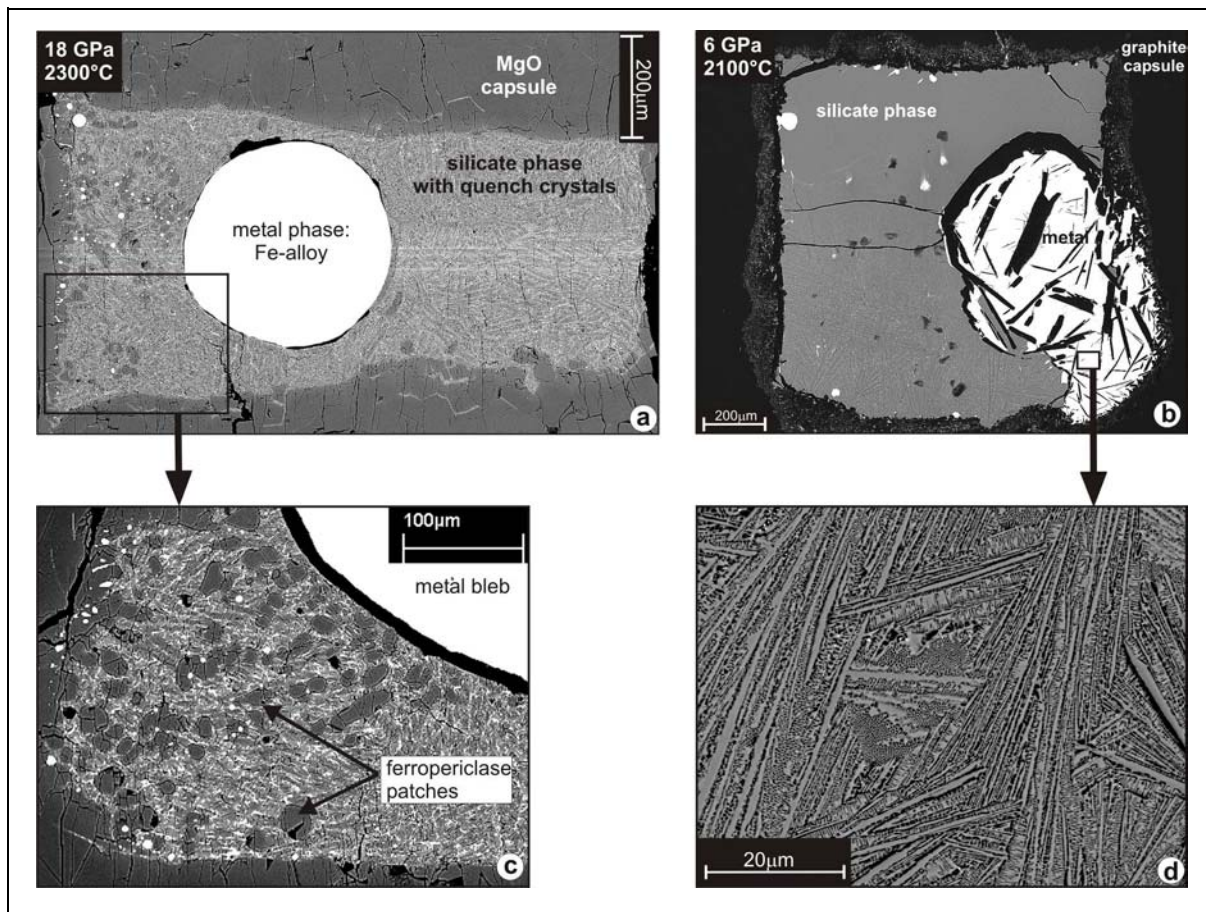


Fig. 13: Back scattered electron images of samples run in (a) a MgO single crystal capsule (Z442) and (b) a graphite capsule (V312). (a) and (b) show sections through the full sample, the respective run conditions are indicated in the image; typical feature is a metal blob that separated from the silicate liquid. In (b) large graphite pieces (black laths) are included in the blob. Details of the effects of the respective capsule material are shown in (c) where MgO forms ferropericlasite patches in the silicate and (d) displaying an extreme example for the reaction of carbon (black) with the iron liquid.

Both metal and silicate phases have developed heterogeneous textures during the quench process. The BSE-image of Fig. 14 a) shows an example of a relatively coarse quench texture in the metal phase from sample V307 run at 6 GPa, 2100 °C. Under very reducing conditions Ta-rich flower shaped quench crystals can be found in a heterogeneous matrix. Depending on the starting composition such quench crystals are additionally composed of Ga and In or Nb and V. In samples starting from composition (B), in addition to these crystals the typical quench phenomenon are rounded blebs with diameters up to 2.5 µm enriched in variable concentrations of Si, Mn, Cr, V, Ti, Ta and Nb compared to the surrounding metal matrix. Additionally these blobs contain O and Fe. A texture like this was also observed in the experiments of Gessmann and Rubie (1998), O'Neill et al. (1998) and Chabot and Agee (2003) who interpreted them as silicates and oxides that exsolved from the metal liquid during the quench process.

An example of a silicate quench texture is shown in Fig. 14 b. Large elongated skeletal olivine crystals are the characteristic feature in samples run at pressures up to 6 GPa. The interstitial matrix is enriched in Fe, Ca and Al and exsolves phases that are enriched in the respective trace elements. At pressures of 18-24 GPa the textures are usually less coarse which makes the analysis of the silicate phase much easier. Only in sample V307, run under most reducing conditions, did the silicate melt quench to a glass.

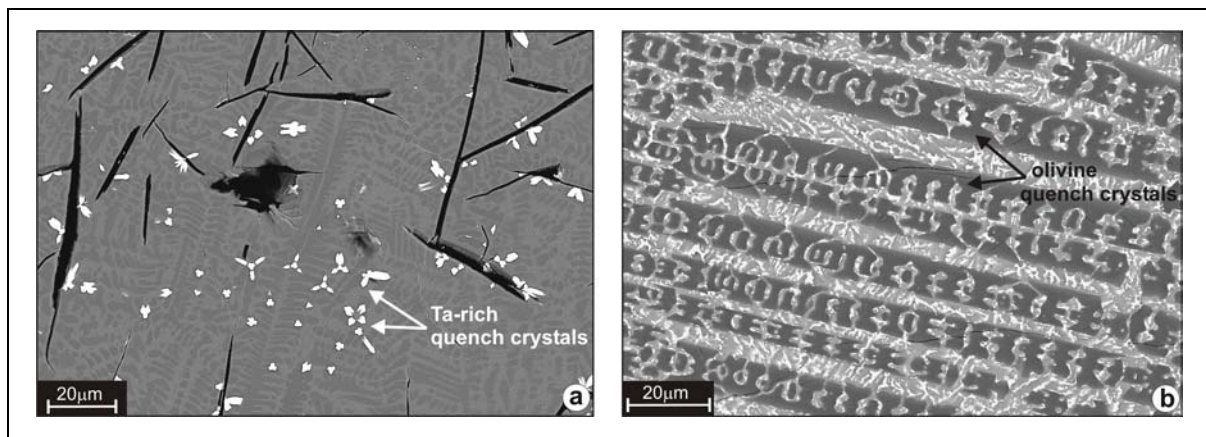


Fig. 14: Typical quench textures of (a) the metal (sample V307) and (b) the silicate phase (sample V311), both from samples run at 6 GPa, 2100°C (BSE images). (a) Under very reducing conditions up to 3.4 wt% Ta can be found in the metal phase resulting in the formation of flower shaped crystals upon quenching; the darker grey areas of the matrix are richer in Si, Ni and Co compared to the brighter grey ones; black features are cracks. (b) The quenched silicate melt has formed elongated skeletal olivine crystals. The brighter grey matrix is enriched in Fe, Ca and Al and in this example, under more oxidized conditions, exsolved Ta-,Ga- and In-rich phases (white flakes).

### 3.4 Analytical Techniques

For both metal and silicate phases quantitative analyses were carried out with the JEOL JXA-8200 electron probe micro-analyzer (EMPA) at the Bayerisches Geoinstitut (BGI). The results are listed in Table I of the appendix. Uncertainties are given in terms of 2 standard deviations. In all cases an accelerating voltage of 20 kV and a probe current of 50 nA were applied. Peak counting times were always 20 s for the major elements Mg, Al, Ca, Fe and Si in the silicate phase and for Fe in the quenched metals. For the minor and trace elements (Ta, Nb, Ti, V, Cr, Mn and Ga, In, Zn) 120-180s were used in both silicate and metal phases as well as for Si in the metal. Ni and Co were analyzed for 120 and 60 s in silicate and metal respectively. In most samples we additionally analysed for W (60s) in order to detect any contamination from the thermocouple which occurred in case of sample Z447 resulting in 35.8 wt% W in the metal. For the S-bearing sample we used 40 s (metal) and 180 s (silicate) for S. Background counting times on each side of the peaks were half as long as the peak counting times. Pure Fe, Co, Ni, V, Cr, Nb, Ta and W metals were employed as standards together with andradite, spinel, MgO, entstatite, MnTiO<sub>3</sub> and AsGa, InAs, ZnS and FeS<sub>2</sub>. Ta, Nb, In and W were analyzed on their L<sub>α</sub> lines and for Ga the K<sub>β1</sub> line had to be used as the Ga K<sub>α</sub> line is overlapped by Ta L<sub>β</sub> and the Ga L<sub>α</sub> line by a higher order In L<sub>α</sub>. All microprobe data were corrected using the phi-rho-z routine. The oxygen content of the silicate phase was calculated by stoichiometry.

In all samples contained in graphite capsules some carbon was dissolved in the metals at run conditions. As carbon was not measured by microprobe, the analyses of these quenched metals have totals less than 100 % (see appendix Table I). We used the difference between the obtained totals and 100 % as an estimate for the carbon concentration in these metals from which we calculated the mole fractions of carbon in the metal ( $X_c$ ) as listed in Table 3. The determined carbon concentrations will therefore depend on the accuracy of the totals and could represent a minimum if some of the graphite laths avoided for analysis formed on quench.

In order to account for the heterogeneous quench textures (Fig. 14) both phases were analyzed with a defocused electron beam ranging in diameter from 20-30 μm for the silicate and from 10-20 μm for the metal. For samples where the metal phase bears irregularly distributed quench crystals several microns in size the bulk metal composition was calculated from the volume fractions, the densities and the compositions of the occurring phases (quench crystals were analysed with a focused electron beam). The volumetric proportions within the metal blobs were derived from the area proportions of matrix and quench crystals determined from BSE images showing the full blobs assuming that the analyzed sections are representative for the whole blob. This image analysis was carried out with the public domain software ImageJ 1.34s from the National Institute of Health, USA. We preferred this technique to scanning areas with the electron beam as the quality of the analysis decreases rapidly for fields greater than 20 x 20 μm which are required to ensure a homogeneous analysis.

In some samples, depending on the capsule material, a carbon or a MgO rim formed at the metal-silicate interface. To ensure that this did not inhibit equilibration between silicate and metal liquids we additionally analyzed smaller metal blobs that were in direct contact with the silicate and found compositions identical to those of the large blobs. In most samples we analyzed the metals along profiles across the blobs revealing the absence of compositional zoning. Additionally, we found no systematic variation of the silicate phases over the respective capsule sections and we take both as an indication that chemical equilibration had been achieved.

At the extreme ends of the studied redox range some trace element concentrations are very low in one of the respective phases. For some of our samples we have counterchecked the EPMA data with laser ablation inductively coupled plasma mass spectrometry (LA-ICP-MS) at BGI (coherent COMPexPRO 102 excimer laser, Perkin Elmer ELAN DRC-e mass spectrometer, 80 mJ energy density, 40 s signal counting times, 5-10 Hz ablation rate, 40-80  $\mu\text{m}$  pit) and with secondary ion mass spectrometry (SIMS) at the Institute of Meteoritics, University of New Mexico, Albuquerque (Cameca ims 4f ion microprobe, O<sup>-</sup> primary beam, 10 kV accelerating voltage, 25 nA primary beam current, 30  $\mu\text{m}$  spot size, 105 V voltage offset and  $\pm 25\text{V}$  energy window for the secondary beam, glass standards). Because of a lack of better standards, we employed the NIST 610 glass for both silicate and metal phases for the LA-ICP-MS analyses. For Cr and Mn, results from EPMA and LA-ICP-MS are in good agreement for both phases (concentrations obtained with LA-ICP-MS differ from EMPA results by: 5% (Cr) and 11% (Mn) in metal; 4-15% (Cr) and 4% (Mn) in silicate). Vanadium was only analyzed in the metal phase and agrees within 10-14%, Ti agrees within 4% in the silicate but as in most cases for EPMA is close to or below the detection limit for the metal phase as were Co and Ni in the silicate. Silicon, in some metal samples, is close to or below the detection limit with EPMA, but cannot easily be analyzed at low concentrations with our LA-ICP-MS device as there is an overlap for all its three isotopes with CO in different isotopic combinations resulting in a relatively high background and a bad signal to background ratio. Both Ta and Nb show a very unsteady ablation characteristic in the metal phase and concentrations differ by more than 50% from the EPMA results (usually lower with LA-ICP-MS). The Ga and In concentrations differ greatly from microprobe results in both metal and silicate phases. With SIMS we have tested only the silicate phase of sample V307 which was run under the most reducing conditions. The results for Ta, Ga, In and Zn from all three analytical techniques are compared in Table 4 below. The EPMA results for Ga and In are in relatively good agreement with the obtained range from SIMS, however the results for Ta and Zn do not match. With LA-ICP-MS the opposite is the case. We found that under the given conditions including standards and settings of the machines both LA-ICP-MS and SIMS techniques could not deliver more accurate results for all the trace elements under question and we have not included their results in this study. However, for some elements EPMA results display the upper limit in some samples and we have marked the respective values in Table I of the appendix.

Except for samples Z469 and Z474 we also determined the ferropericlase composition in samples contained in MgO single crystal capsules (peak counting times: Mg 20s; Fe, Ca, Si, Ni and Co, 30-60s; Al 120s; all other trace elements 180s). For the analyses we chose small patches of ferropericlase that were in direct contact with either the big metal blob or small metal spheres. In some cases we additionally analysed the MgO capsule close to the interface with the sample charge where a brighter grey tone in the BSE image due to a higher Fe content indicates a diffusive reaction rim. The results are reported in Table II in the appendix.

**Table 4:**

Comparison of some trace element concentrations (ppm) in the silicate phase of sample V307 obtained from various techniques.

	EPMA	LA-ICP-MS	SIMS
Ta	1048	1006-1142	532-747
Ga	391	155-167	347-477
In	703	436-460	400-599
Zn	1177	1306-1339	470-636

## 3.5 Results

### 3.5.1 Calculation of the Oxygen Fugacity

The distribution of any element M with a valence n between a liquid metal and a liquid silicate is controlled by the redox equilibrium



and it therefore strongly depends on the oxygen fugacity of the system. In our experiments the oxygen fugacity can be estimated relative to the pure iron (Fe) - wüstite (FeO) equilibrium, the IW-buffer, from the respective Fe and FeO contents of either metal and silicate melt (Thibault and Walter, 1995; Li and Agee, 2001) or of the metal liquid and a silicate or oxide phase that was in equilibrium with the system under run conditions (Kilburn and Wood, 1997; Gessmann et al., 1999).

For this study we use the presence of ferropericlase (Fp) in many of the samples including those from partitioning experiments on highly siderophile elements (chapter 4) to derive a general equation for the calculation of the relative oxygen fugacity of such experiments. For the Fe-FeO redox reaction between metal in equilibrium with Fp under the conditions of any experiment (exp.) in the form of equation [6] but normalized to one mol O<sub>2</sub> the free energy change is zero and can be expressed by the following equation:

$$0 = \Delta G^0 + 2 RT \ln (a_{FeO}^{Fp}) - 2 RT \ln (a_{Fe}^{metal}) - RT \ln f_{O_2} \quad [7]$$

where  $\Delta G^0$  describes the free energy change for the reaction at the respective experimental P and T conditions in the pure system, that is at the IW buffer.

For the iron-rich alloys in our experiments "Raoult's Law" should be valid such that we can assume that  $a_{\text{Fe}}^{\text{metal}} = X_{\text{Fe}}^{\text{metal}}$  (mole fraction of Fe in the metal). However, for Fp which in all our experiments has a very low iron content (see appendix Table II) we have to account for the activity coefficient of FeO ( $\gamma_{\text{FeO}}^{\text{Fp}}$ ) when calculating the activity of FeO in Fp from the mole fraction of FeO ( $a_{\text{FeO}}^{\text{Fp}} = X_{\text{FeO}}^{\text{Fp}} * \gamma_{\text{FeO}}^{\text{Fp}}$ ). The activity coefficient as well depends on the Fp composition and the mixing behaviour of FeO in Fp in the following way:

$$RT \ln (\gamma_{\text{FeO}}^{\text{Fp}}) = W_{\text{FeO-MgO}}^{\text{Fp}} (1 - X_{\text{FeO}}^{\text{Fp}})^2 \quad [8]$$

where the Margules interaction parameter  $W_{\text{FeO-MgO}}^{\text{Fp}}$  increases with the degree of non-ideality of mixing. Recent studies on the Fe-Mg partitioning between mantle silicates and Fp have shown that such a symmetric model describes the Fe-Mg mixing in Fp very well (Frost et al. 2001; Frost, 2003). Moreover, the pressure variation of this interaction parameter at 1400°C has been experimentally determined by Frost (2003) which we apply here, neglecting the effect of T which is comparably small, especially at higher temperatures (Srećec et al, 1987):

$$W_{\text{FeMg}}^{\text{Fp}} = 11000 + 0.011 * P \text{ (bar)} \quad [9]$$

By combining equations [7] and [8] we can then derive a relationship for calculating  $f_{\text{O}_2}$  relative to the iron-wüstite buffer:

$$\log f_{\text{O}_2}^{\text{exp.}} - \log f_{\text{O}_2}^{\text{IW}} = \Delta IW = 2 \log \left[ \frac{X_{\text{FeO}}^{\text{Fp}}}{X_{\text{Fe}}^{\text{metal}}} \right] + \frac{2 W_{\text{FeMg}}^{\text{Fp}} (1 - X_{\text{FeO}}^{\text{Fp}})^2}{RT \ln 10} \quad [10]$$

However, in our experiments the mole fraction of FeO in Fp is not only related to Fe in the metal phase but additionally depends on the Fe-Mg exchange with the silicate melt. We have used data on this exchange reaction from our experiments as well as from the literature (Trønnes and Frost, 2002) covering a pressure range up to 24.5 GPa, to determine a general relationship between the mole fractions of FeO in Fp and in the silicate liquid. We found that the silicate-Fp  $K_D$  (analogue to equation [4]) for this exchange reaction shows no strong pressure dependence and is constant for  $P > 6$  GPa such that we can define a constant relationship as :

$$X_{\text{FeO}}^{\text{Fp}} = 0.72 * X_{\text{FeO}}^{\text{sil. liquid}} \quad [11]$$

This enables us to use equation [10] to determine the relative  $\log f_{\text{O}_2}$  even in samples that lack Fp, that is all our experiments from graphite capsules, avoiding the FeO activity composition relation for the silicate melt which is less well studied at high pressures than for Fp. The results we obtained for  $\Delta IW$  are listed in Table 3 together with the run conditions.

### 3.5.2 Metal-Silicate Partition Coefficients - Dependence on Oxygen Fugacity

In this study we use the partition coefficient  $D$  (M) based on the molar concentration ratio of an element M and its oxide in the metal and the silicate phases respectively:

$$D_{\text{silicate}}^{\text{metal}}(\text{M}) = \left[ \frac{X_{\text{M}}^{\text{metal}}}{X_{\text{MO}_{\frac{n}{2}}}^{\text{silicate}}} \right] \quad [12]$$

The  $D$  values for all studied elements are presented in Table III (appendix). The uncertainties ( $\Delta D$ ) were derived from the standard deviation of each concentration and the respective error propagation on calculating  $D$ . The errors for logarithmic values of  $D$  were estimated as maximum deviations through  $\pm \Delta \log D = \log(D + \Delta D) - \log(D)$ . In Fig. 15 the  $\log D$  values are plotted against the relative  $\log f_{\text{O}_2}$  values. We include the results for Ni, Co and Ti although, as can be seen from Table I (appendix) the concentrations of these elements in most samples are close to or below the detection limit in either the silicate or the metal phase, resulting in large errors for the  $D$  values (Table III, appendix). Ni and Co results are therefore only reliable above  $\Delta IW$  -3 and Ti results below  $\Delta IW$  -2. For several samples this is additionally observed for the concentrations of Ta and at most oxidising conditions for Si in the metal and on the other hand of Ga and In in the quenched silicate liquids as well as for Cr and Mn in samples where they were added at a low concentration level (see Tables 2 and 3). However, as can be seen in Fig. 15, we include most of these results in our plots as they fall well within the trends defined by the other samples with higher concentrations. The S-bearing sample and sample Z447 that experienced a high W contamination (appendix Table I) were excluded from these plots. On the logarithmic scale of such diagrams positive values for  $\log D$  indicate siderophile and negative values lithophile behaviour. For all elements there is a good linear correlation and a general increase of  $\log D$  with decreasing oxygen fugacity. As a consequence, V, Nb, Zn and Cr have partition coefficients of  $D > 1$  under reducing conditions below  $\Delta IW$  -2.8, -2.8, -2.5 and -1.7, respectively. Besides the siderophile elements Ni and Co, the elements Ga and In which are additionally volatile, show siderophile behaviour over the whole studied range of  $f_{\text{O}_2}$ .

Applying an equation of the form of [7] for the redox exchange of an element M according to [6] and using the definition of  $D$  (equation [12]) one obtains the following relationship between partition coefficient and oxygen fugacity :

$$\log D_{\text{silicate}}^{\text{metal}}(\text{M}) = -\frac{n}{4} \log f_{\text{O}_2}^{\text{exp}} - \log \left[ \frac{\gamma_{\text{M}}^{\text{metal}}}{\gamma_{\text{MO}_{\frac{n}{2}}}^{\text{silicate}}} \right] + \frac{\Delta G^0}{RT \ln 10} \quad [13-1]$$

For experiments at constant pressure and temperature, the  $\Delta G^0$  term is fixed. Moreover, according to Henry's law the ratio of the activity coefficients should stay constant at constant T as long as each component shows an infinite dilution behaviour in the respective phase, which is assumed here but will be further discussed below. Thus, at constant P and T, D shows a linear dependence on the oxygen fugacity of an experiment which is, using the  $\Delta IW$  term as in the diagrams of Fig. 15 (the oxygen fugacity at the IW buffer,  $\log f_{O_2}^{IW}$  also has a constant value for a fixed pressure and temperature), expressed as:

$$\log D_{\text{silicate}}^{\text{metal}}(M) = -\frac{n}{4} \Delta IW + \text{const.} \quad [13-2]$$

Such plots can therefore be used to estimate the valence state  $n$  of an element in the silicate liquid. The linear trends shown in Figs. 15a and 15b indicate the theoretical valence state that is most likely for each respective element taking into account the experimental data. Their slopes yield valences of  $5^+$  for Ta and Nb,  $4^+$  for Si,  $3^+$  for V and  $2^+$  for Cr, Mn, Co, Ni, Zn and also for Ga which was found to be trivalent in 1 bar partitioning experiments (e.g. Schmitt et al., 1989; Capobianco et al. 1999). For In a  $1^+$  trend fits best and Ti, regarding the uncertainties of the data, might occur as both  $3^+$  and  $2^+$ . The trends fit the data sets of the various P series and no valence changes are observed as a function of  $f_{O_2}$ . A steeper slope for some experiments run in graphite capsules like Nb (6 GPa), Ta, Si, Ga and In (20 GPa) is caused by the presence of carbon in the metal liquid and a resulting change in the activity coefficient  $\gamma_M^{\text{metal}}$  which will be discussed in the next section.

### 3. Liquid Metal - Liquid Silicate Partitioning of Lithophile and Weakly Siderophile Elements

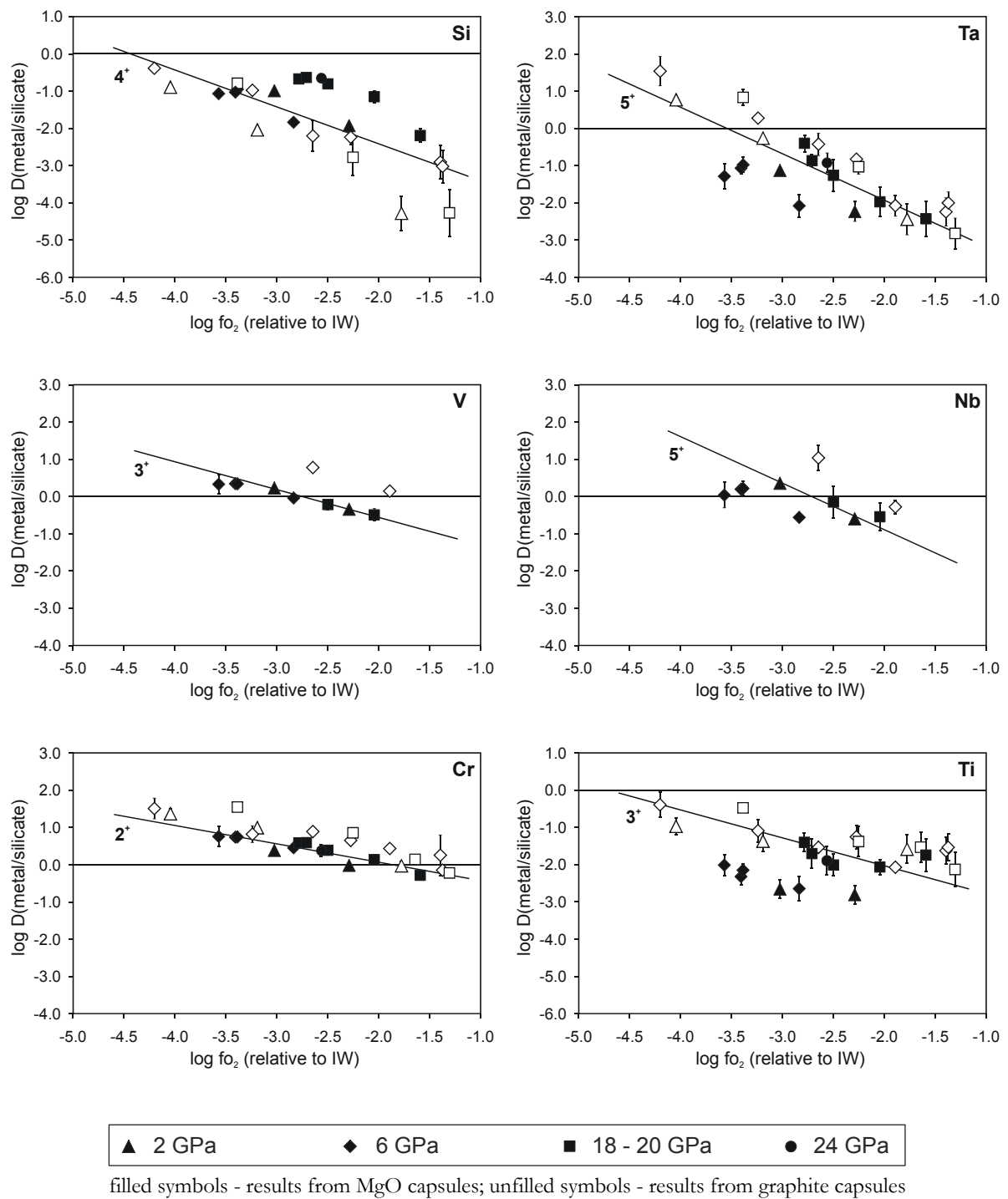


Fig. 15a: Metal-silicate partition coefficients ( $D$ , mol% basis) of S-free samples for Si, Ta, V, Nb, Cr and Ti plotted as a function of oxygen fugacity relative to the iron-wüstite buffer ( $\Delta\text{IW}$ ), as logarithmic values. Where no error bars are shown the uncertainties do not exceed the symbol size. Isobaric results from different temperatures are not distinguished. The lines indicate the valence ( $n^+$ ) trend most likely for the respective element that is consistent with the data (see equation [13-2] and text).

### 3. Liquid Metal - Liquid Silicate Partitioning of Lithophile and Weakly Siderophile Elements

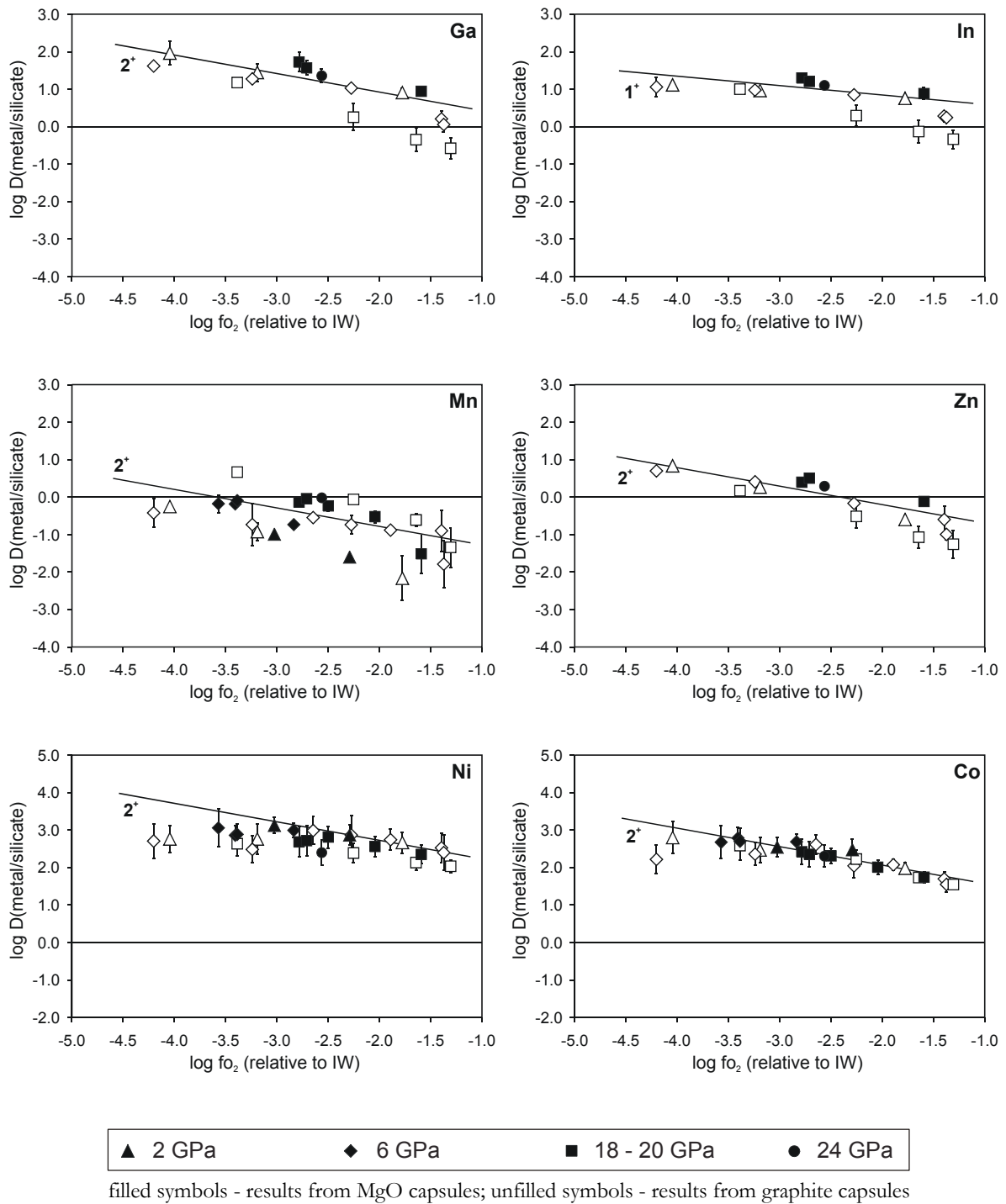


Fig. 15b: Metal-silicate partition coefficients ( $D$ , mol% basis) of S-free samples for Ga, In, Mn, Zn, Ni and Co plotted as a function of oxygen fugacity relative to the iron-wüstite buffer ( $\Delta\text{IW}$ ), as logarithmic values. Where no error bars are shown the uncertainties do not exceed the symbol size. Isobaric results from different temperatures are not distinguished. The lines indicate the valence ( $n^+$ ) trend most likely for the respective element that is consistent with the data (see equation [13-2] and text).

### 3.5.3 Compositional Effects and Influence of the Capsule Material

As described in chapter 1.3 we can regard the metal-silicate partitioning of an element relative to the Fe exchange by dividing its partition coefficient  $D$  (M) by  $D$  (Fe) (equation [12]) which defines the distribution coefficient  $K_D$  of equation [4]. This has the advantage that the partitioning of the elements can be compared independently of  $f_{O_2}$  (Righter and Drake, 2003) once the valence states of the elements have been derived. Rearranging equation [2]  $K_D$  at any pressure and temperature can be expressed as:

$$\log K_D^{\text{Fe-M}}(P,T) = \frac{-\Delta G_{P,T}^0}{RT \ln 10} - \log \left[ \frac{\gamma_M^{\text{metal}}}{(\gamma_{\text{Fe}}^{\text{metal}})^{\frac{n}{2}}} \right] - \log \left[ \frac{(\gamma_{\text{FeO}}^{\text{silicate}})^{\frac{n}{2}}}{\gamma_{\text{MO}_{\frac{n}{2}}}^{\text{silicate}}} \right] \quad [14]$$

As mentioned above, the distribution coefficient is, next to  $P$  and  $T$ , a function of the activity coefficients of the individual components in the metal and silicate liquids which themselves can vary with  $T$ . For most of the individual oxide components the activity coefficients in the silicate liquid are not well known. Studies at 1 bar have shown that activity coefficients of NiO and CoO relative to FeO at 1400°C do not vary over a wide range of silicate melt compositions (O'Neill and Eggins, 2002) and that all three are independent of temperature in the range 1300-1600 °C (Holzheid et al., 1997). Wade and Wood (2005) suggest that this should also apply to other divalent trace cations but might change for highly charged ( $> 4^+$ ) cations like the high field strength elements (e.g. Ta, Nb), as has been observed for W (Jana and Walker, 1997<sup>b</sup>) or Mo (O'Neill and Eggins, 2002). However, the latter study considered CaO (8-47 wt%) and Al<sub>2</sub>O<sub>3</sub> (5-23 wt%) rich melts only whereas in our study MgO-rich and quite depolymerized melts relevant for the Earth's mantle were involved. For a simplification we therefore neglect the influence of silicate melt composition and assume that the activity coefficient ratio for FeO and the respective element oxide component is constant.

If element concentrations in the Fe-rich metal liquid reach several wt%, this can influence the partitioning behaviour of the trace elements of interest by changing their activity coefficient in the metal. This is the case for samples run in graphite capsules where some C dissolved in the metal liquid, as well as for sample Z551 due to the presence of S. Experimental studies have shown that both C and S increase the partition coefficients of some transition metals like V, Cr and Mn (Chabot and Agee, 2003), whereas Ni and Co partition coefficients are slightly decreased by both elements (e.g. Jana and Walker, 1997<sup>a</sup>, 1997<sup>c</sup>). For many elements the activity coefficients  $\gamma$  in Fe-rich metal liquids are defined in the metallurgical literature. The influence on the thermochemical behaviour of an element can be expressed using so-called interaction parameters  $\epsilon$  that are compiled in the Steelmaking Data Sourcebook (1988). At high dilution, the  $\gamma$  values can be corrected by applying a simplified thermodynamic approach developed by Wagner (1962). According to this, and considering two elements M and N in an iron alloy, the activity coefficient of  $\gamma_M$  depends on the mole fractions  $X$  of both elements and is expressed as:

$$\log \gamma_M = (\ln \gamma_M^0(T) + \varepsilon_M^M(T) * X_M + \varepsilon_M^N(T) * X_N) / \ln(10) \quad [15]$$

where  $\gamma_M^0$  is the activity coefficient of M at infinite dilution and  $\varepsilon_M^M$ ,  $\varepsilon_M^N$  are first-order interaction parameters on the element M by itself and by N. All three parameters are additionally a function of temperature and a respective correction to higher temperatures is relevant for our study as the Steelmaking Data Sourcebook (1988) usually lists values that refer to a temperature  $T^0 = 1873\text{K}$  though suggesting an extrapolation to higher temperatures in the form of:

$$\ln \gamma_M^0(T) = \frac{T^0}{T} * \ln \gamma_M^0(T^0) \quad [16]$$

$$\varepsilon_M^0(T) = \frac{T^0}{T} * \varepsilon_M^0(T^0) \quad [17]$$

For the elements of interest in this study the  $\gamma^0$  ( $T^0$ ) values are for Si = 0.0013, Ta = 0.04, Nb = 0.2, Mn = 1.44, V = 0.08, Cr = 1. No data are reported for Ga, Zn and In.

### Influence of the Capsule Material

Using graphite capsules, carbon diffusion results in 1 - 9 wt% C in the metal liquid in our experiments which effects the partitioning behaviour of the individual elements to varying extents. In Fig. 16 this is illustrated for Si and Ta where the log D values are plotted as in Fig. 15a but comparing the results from MgO and from graphite capsules at different pressures. In the presence of carbon in the metal the Si partition coefficient is much lower at both 2 GPa and 18 - 20 GPa. However, this effect not only results in a linear shift of the data as equation [15] would imply for a constant temperature, but gets stronger at higher oxygen fugacity. This is because the solubility of C shows a negative correlation with the Si content of the iron liquid (Bouchard and Bale, 1995) that is itself decreasing with increasing oxygen fugacity. Such an apparently steeper trend for results from graphite capsules can be observed for most elements especially for the 20 GPa series or for Nb at 6 GPa (see Fig. 15a). In these cases, a simple correction of the activity coefficient using equation [15] would not be sufficient or only applicable to results at low oxygen fugacities. However, having results from both capsule materials the data from MgO capsules serve as a good reference for where graphite capsule results should be expected. For Si, below  $\Delta IW -2.5$  the corrected values calculated from thermochemical data are in good agreement with the MgO capsule results. This is not the case for Ta, which additionally shows the opposite behaviour of becoming more siderophile in the presence of carbon (see Fig. 16). In addition, a positive C effect is observed for Cr, Nb and V, whereas, as with Si, the D-values for Ga, In and Zn are decreased by C as can be seen in Fig. 15b. Mn shows no obvious variation with C although a slight positive effect seems possible in the case of the 20 and 18 GPa samples, as was observed in the experiments of Chabot and Agee, 2003.

For correcting the graphite capsule results we used equation [15] for Si and in case of Ta and Cr the difference in the log D value compared to results from MgO capsules at 2 GPa as a reference for all data. For Ga, In and Zn, where we had no 2 GPa MgO data, we used the difference at 20 GPa (graphite) compared to the 18 GPa (MgO) values to get an estimate for the shift caused by C. This will result in greater uncertainties for the  $K_D$  pressure and temperature trends as these experiments were additionally run at different temperatures. For V and Nb no correction was possible for the only two experiments run in graphite capsules at 6 GPa. This is because we observe in general some inconsistencies for the experiments at 6 GPa using MgO capsules which is illustrated in Fig. 17 with examples for Si and Ta. In both cases the  $K_D$  values from MgO capsules differ by one log unit from the graphite capsule results which were corrected as described above. For some reason these samples have unusually high MgO concentrations in the silicate melt with an average Mg/Si (mol) ratio of 2.0 whereas in all other samples this ratio is  $< 1.6$  independent of the capsule material (see Table 3). In addition to Si and Ta, the elevated MgO concentration in these silicate melts decreased the partition coefficients of Nb and Ti and to a lesser extent of V and we therefore excluded these results for data regression. For Cr and Mn on the other hand we observe no great deviation which is consistent with the activity coefficients of divalent cations being more or less independent of silicate melt composition as discussed above. In general we conclude that both capsule materials are not ideal.

#### **Influence of S in the Metal Phase**

One S-bearing experiment has been performed at 18 GPa, 2300°C within the series using starting composition B. The quenched metal of this sample has 7.6 wt% S which corresponds to a mole fraction of 0.13 (see Table 3). In Fig. 18 the  $K_D$  values for Ta, V, Mn, Cr, Nb, Si, Ti, Ni and Co from this sample are compared with the results from a S-free experiment run at the same P-T conditions (Z469). Here we assume that at this relatively low S concentration  $\gamma_{Fe}$  is still constant and not changed by the interaction with S. Having only one S-bearing sample and considering the uncertainties we can only estimate the tendency for the S-effect. We observe that in the presence of S in the metal the  $K_D$  coefficient decreases for Si and Ti by a factor of about  $\leq 3$ , and increases for Ta, V and Nb by factors of 1.5-2 and maybe slightly for Cr. The changes for Ni, Co and Mn are smaller than the uncertainties.

The contamination of the metal with  $> 35\%$  W in sample Z447 exhibits another compositional effect on the partitioning behaviour of several elements which is most effective for Ta (decrease of D) and Zn and Ga (increase of D). Moreover,  $\gamma_{Fe}$  would have to be corrected when calculating oxygen fugacity which is why the respective value in Table 3 is put into brackets. As it displays a metal composition not relevant for core formation we exclude this sample from further considerations.

### 3. Liquid Metal - Liquid Silicate Partitioning of Lithophile and Weakly Siderophile Elements

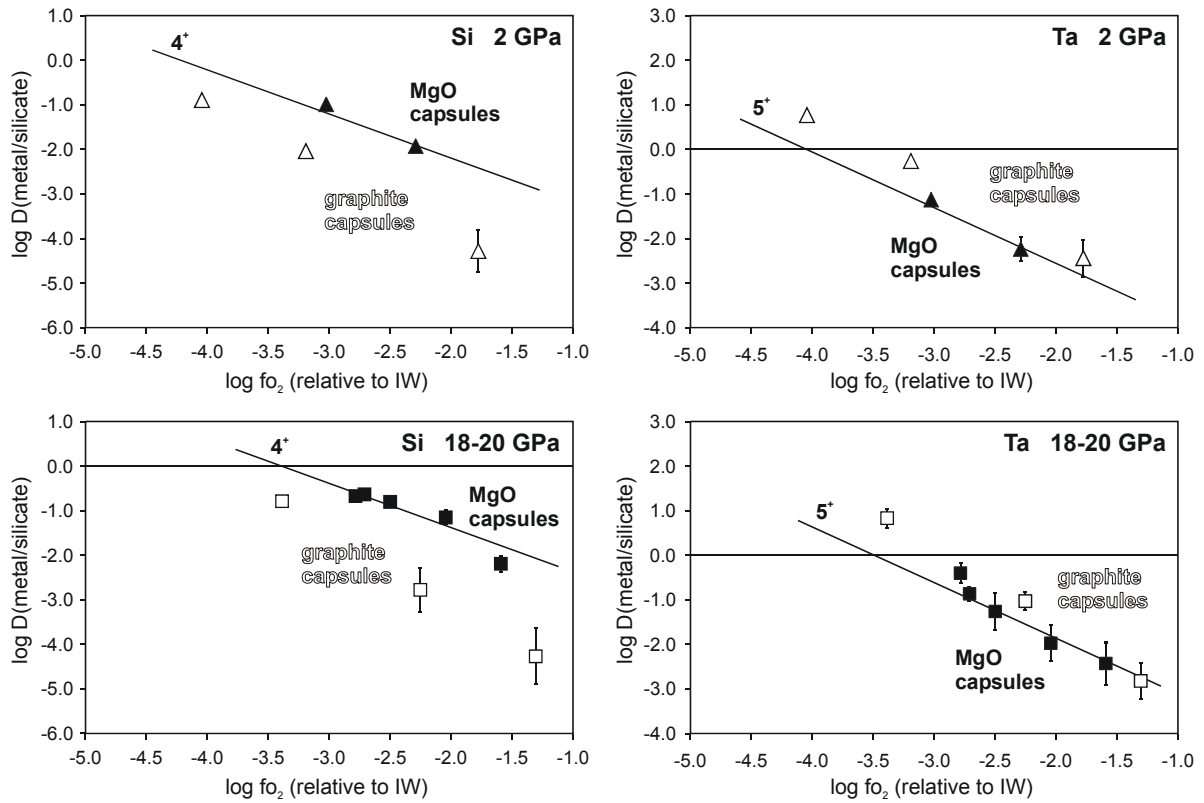


Fig. 16: Influence of the capsule material on the partition coefficients ( $D$ ) of Si and Ta displayed as a function of oxygen fugacity at 2 GPa, 1740-1750°C and 18-20 GPa, 2100-2300°C. In graphite capsules (unfilled symbols) the presence of C in the iron liquid lowers the Si partition coefficient whereas it increases that for Ta. Results from MgO single crystal capsules (black symbols) serve as reference for correcting graphite capsule results.

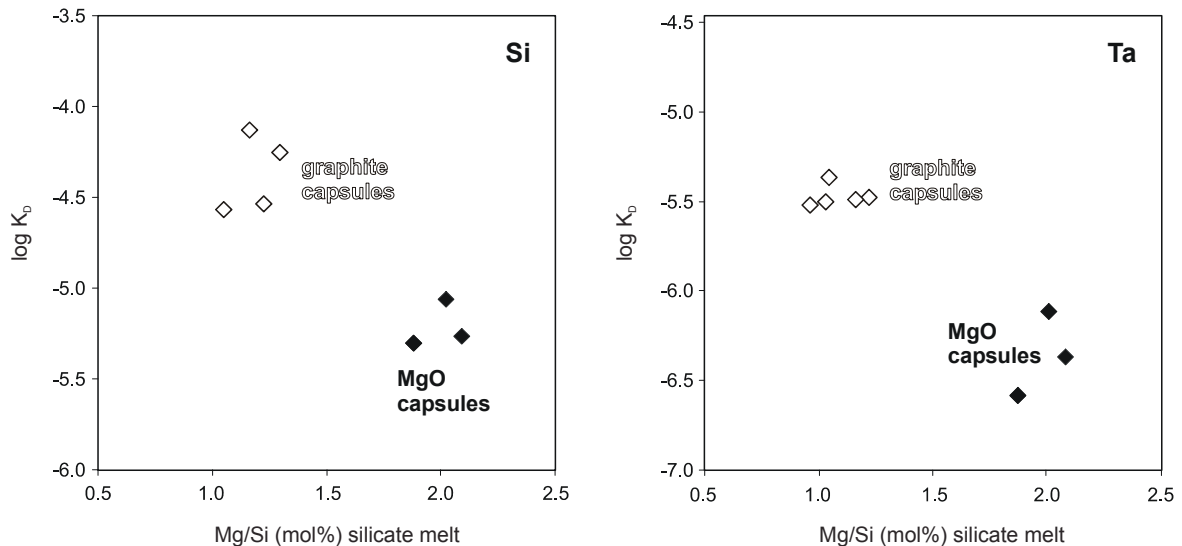


Fig. 17: Influence of the capsule material on the distribution coefficients ( $K_D$ ) of Si and Ta at 6 GPa, 2100°C plotted against the Mg/Si ratio of the silicate melt which is unusually high for these MgO capsule experiments (black symbols). The  $K_D$  values from graphite capsules have been corrected for the effect of C in the metal (see text).

### 3. Liquid Metal - Liquid Silicate Partitioning of Lithophile and Weakly Siderophile Elements

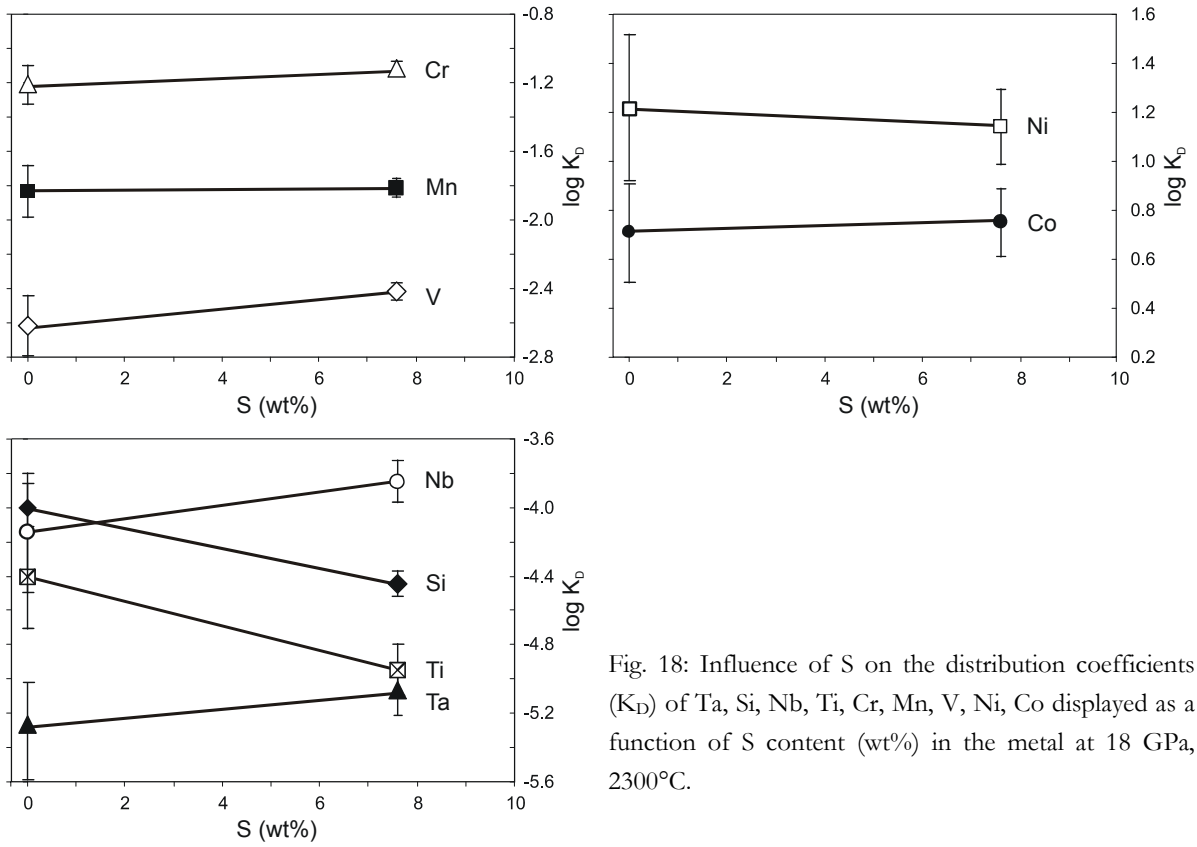


Fig. 18: Influence of S on the distribution coefficients ( $K_D$ ) of Ta, Si, Nb, Ti, Cr, Mn, V, Ni, Co displayed as a function of S content (wt%) in the metal at 18 GPa, 2300°C.

### 3.5.4 Change of the Partitioning Behaviour with Pressure and Temperature

Having sorted out the compositional interaction effects, the distribution coefficient  $K_D$  is mainly a function of pressure and temperature which is expressed in the temperature dependence of  $\gamma_M^0$  (equation [16]) and the  $-\Delta G_{p,T}^0/RT$  term of equation [14] and thus with the thermodynamic parameters of the exchange reaction. With a simplified approach the pressure and temperature dependence of  $K_D$  can then be determined using an equation of the form (Righter et al, 1997, Righter and Drake, 2003):

$$\log K_D^{\text{Fe-M}}(P,T) = a + \frac{b}{T} + \frac{c * P}{T} \quad [18]$$

where  $a$ ,  $b$  and  $c$  are constants,  $T$  is temperature in K and  $P$  is pressure in GPa. Constant  $a$  is related to the entropy change and activity coefficients of the oxides, constant  $b$  to the enthalpy change and the activity coefficients in the metal at infinite dilution and  $c$  is related to the volume change which we assume to be constant. Wade and Wood (2005) suggest that the 1 bar free energy data of the endmember reactions combined with equation [16] for the  $\gamma_M^0$  correction give a first estimate of the temperature dependence factor  $b$ . Plotting the experimental data for  $K_D$  as a function of inverse temperature should then allow the intercept  $a$  and the pressure constant  $c$  to be determined by data regression. Such fits for our results on Si, Ta, Nb, V, Cr, Mn, Ga, In and Zn are shown in Fig. 19, Fig. 21 - 24 and Fig. 26 - 29, in some cases including data from the literature as indicated. With the exception of In and Zn, the partition coefficients of all these elements show a distinct dependence on temperature such that they increase towards higher temperatures. As the slope for these trends results mainly from enthalpy change of the exchange reaction it will also reflect the valence of the particular oxide and higher-charged cations will display steeper trends. To some extent the use of the free energy data for estimating the slopes is limited as data for CrO, GaO and In<sub>2</sub>O are not available in the literature (Chase et al. 1998; Barin, 1989).

#### Silicon

As Fig. 19 shows, our experimental data indicate a negative pressure trend for the partition coefficient of Si. Several previous studies have observed an increase of Si solubility in liquid Fe up to upper mantle pressures of about 25 GPa when the metal is in equilibrium with silicate phases of the Mg<sub>2</sub>SiO<sub>4</sub> system (Ito et al., 1995; Gessmann et al., 2001; Malavergne et al. 2004). However, as soon as MgSiO<sub>3</sub> is the equilibrium silicate phase the liquid-metal solubility of Si goes down due to the coordination change from 4 to 6 for Si in the solid silicates (O'Neill et al., 1998) which results in a volume change that is not constant. Such a P-induced coordination change could also be relevant regarding silicate melts and a simple approach for determining the effect of pressure on  $K_D$  in the form of equation [18] might not be sufficient.

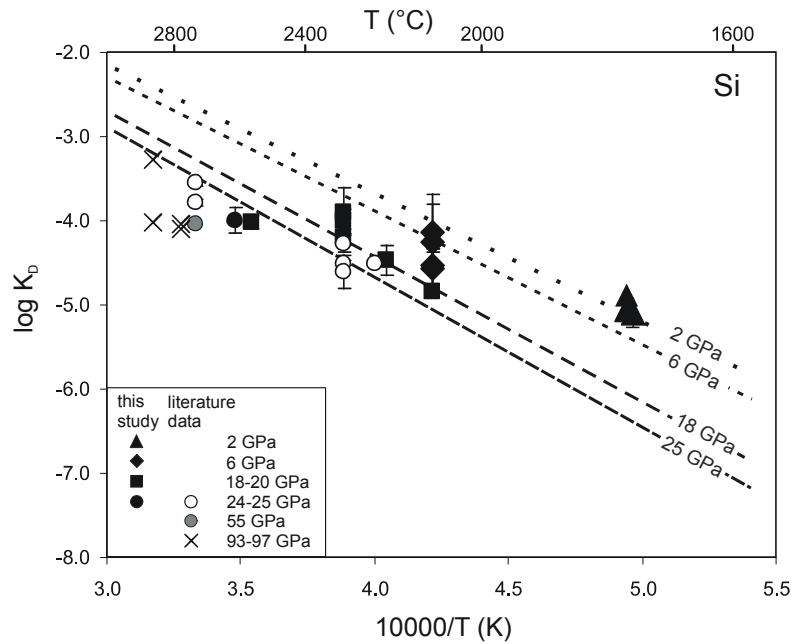


Fig. 19: The logarithmic value of the Si distribution coefficient ( $K_D$ ) plotted as a function of inverse  $T$  ( $10000/T$ ). Black symbols are data from this study. Data from the literature include: 25 GPa - Wade and Wood (2001, 2005); 25-97 GPa - metal-MgSi-Pv partitioning experiments of Takafuji et al. (2005). Where no error bars are shown the uncertainties do not exceed the symbol size. The lines show the pressure-temperature trends obtained from data regression for the pressures as indicated (see text).

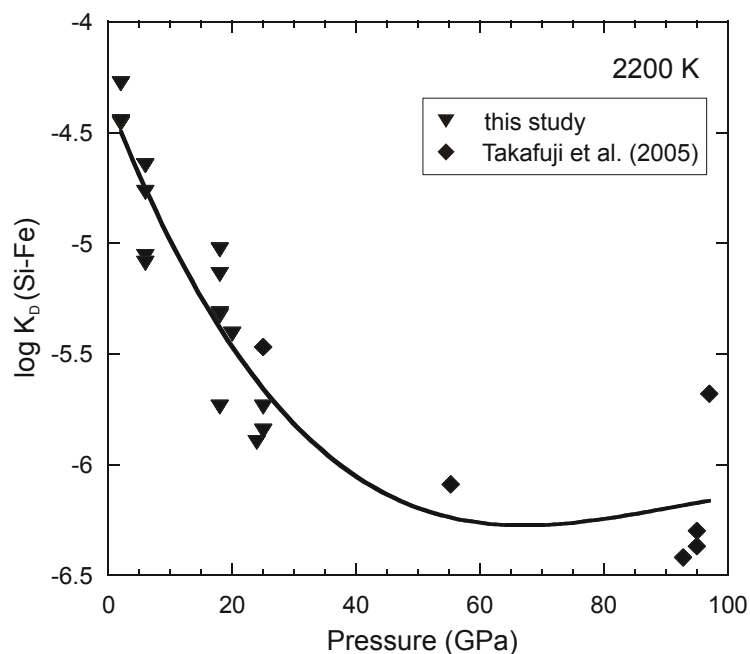


Fig. 20: The logarithmic value of the Si distribution coefficient ( $K_D$ ) for results from this study and for metal-MgSi-Pv partitioning experiments of Takafuji et al. (2005). In both cases the  $K_D$  values were corrected to a common temperature of 2200K. The solid line indicates the P-trend derived by fitting the data with a third order polynomial as discussed in the text.

In order to have data from a broader P-range for regression we included experimental results from Takafuji et al. (2005), who performed metal-Mg-Si-perovskite (MgSi-Pv) partition experiments in a diamond anvil cell up to 97 GPa and 3150 K. Applying a T dependence as derived from the free energy trend (see above) we corrected all data to the same temperature of 2200K and subsequently determined the pressure effect. The resulting  $K_D$  values are plotted in Fig. 20 as a function of P together with the derived P-trend. We used a third order polynomial to fit the data because the influence of P not only gets weaker with increasing P but might also cause  $K_D$  to increase again at very high pressures (> 60 GPa). Moreover, the derived term represents the lower limit for the observed trend as the employed  $K_D$  values from Takafuji, et al. 2005 are data for perovskite. A qualitative correction of their data using silicate-perovskite partitioning data from the literature (Trønnes and Frost, 2002; Ito et al, 2004) indicates that the corresponding metal-silicate  $K_D$  values could be even higher. However, the experiments of these studies were performed over a different pressure range (24 -35 GPa) and with Al-bearing samples in contrast to the Al-free perovskites of Takafuji et al. (2005), which is why we use the original data here. The combined trends of pressure and temperature result in the following relationship for the Si- $K_D$ :

$$\log K_D^{\text{Si-Fe}}(T, P) = 2.4703 - \frac{15000}{T} + \frac{-0.0069 * P^3 + 1.8651 * P^2 - 156.87 * P}{T} \quad [19]$$

### Tantalum and Niobium

For both Ta and Nb, a positive temperature and a negative pressure trend are observed (Fig. 21, Fig. 22), with the latter being much stronger for Nb. The temperature trend for both elements is based on the free energy data of the 5<sup>+</sup> oxides but corrected for the temperature dependence of the respective  $\gamma_M^0$  values. For fitting the pressure trends in both cases we used the linear relationship of equation [18] including data of Wade and Wood (2001) and additionally of Wade and Wood (2005) for Nb, leading to equations [20] and [21]:

$$\log K_D^{\text{Ta-Fe}}(T, P) = 0.6045 - \frac{13382}{T} - 94.1 * \frac{P}{T} \quad [20]$$

$$\log K_D^{\text{Nb-Fe}}(T, P) = 2.4453 - \frac{13707}{T} - 180.8 * \frac{P}{T} \quad [21]$$

In Fig. 21 we have plotted the result of a Ta-partitioning experiment of Rammensee et al. (1983), performed in an alumina capsule at 1 bar. In general this is consistent with the trend defined by the high pressure data, though it might indicate a higher pressure dependence at P < 2 GPa. For fitting the Nb trend only the experimental results from 2 and 18 GPa could be used. However, all 6 GPa data were left in the diagram of Fig. 22 to illustrate the effects of the respective capsule materials. Compared to the calculated trend at 6 GPa, the shift towards higher  $K_D$ -values in the presence of C is not as great as Fig. 15a might imply. Results from MgO capsules on the other

hand, i.e. in the Mg enriched silicate melts, are much lower, although they show the same slope for the T-dependence.

### Vanadium and Chromium

For both V and Cr we found the partitioning behaviour to be independent of pressure resulting in simplified  $K_D$  terms of:

$$\log K_D^{\text{Cr-Fe}}(T) = - \frac{3100}{T} \quad [22]$$

$$\log K_D^{\text{V-Fe}}(T) = - 0.2126 - \frac{5678}{T} \quad [23]$$

Fitting the temperature trend for Cr, the much steeper slope derived from the free energy data of  $\text{Cr}_2\text{O}_3$  does not satisfy the observed experimental trend (Fig. 23) reflecting divalent Cr in the case of our experiments. The final trend was obtained by extending the data set of this study with experimental results at 2.5-3 and 25 GPa from the literature (Chabot and Agee, 2003; Wade and Wood, 2001 and 2005). Regarding the  $K_D$  plot of Fig. 23 there might be a slight negative pressure effect within the uncertainty range of the data, but this was neglected for data regression.

For determining the  $K_D$ -trend for V we included data on metal-ferropericlasite partitioning. Besides the incorporation of some Fe the ferropericlasite in our experiments (small patches; diffusion rim along the capsule-sample contact) is characterized by the inclusion of some Al, Mn, Cr and, depending on the starting material, Zn or V (see appendix Table II). Our data for the metal-ferropericlasite partitioning of V show a weak positive P-dependence which is in good agreement with the results of Gessmann and Rubie (2000). The corresponding equation for the metal-ferropericlasite  $K_D$  can be formulated as:

$$\log K_{D_{\text{metal-Fp}}}^{\text{V-Fe}}(T,P) = - 0.0002 + \frac{3}{T} + \frac{0.29 * P}{T} \quad [23-1]$$

On the other hand we can also determine a silicate-ferropericlasite  $K_D$  from our results which also shows a slight positive, linear dependence on P. This relationship allows us to calculate the theoretical, corresponding metal-silicate  $K_D$  values from the 9 GPa data set of Gessmann et al. (2000) which were then used together with our results to define equation [23]. It shows that the two pressure effects cancel out in the case of metal-silicate partitioning in the range 6-25 GPa. In Fig. 24, for comparison we have also plotted data at 3 GPa of Chabot and Agee (2003), at 25 GPa from Wade and Wood (2005) and the corrected values at 9 and 23 GPa of Gessmann and Rubie (2000). However, the 2 GPa data from our study show a slight deviation towards higher  $K_D$  values that, together with the result of Rammensee et al. (1983) from 1 bar, could indicate a slight negative P-effect at low P (< 6 GPa) but there are not enough experimental data to support this. As for Nb, the 6 GPa data from graphite capsules are plotted in Fig. 24 and illustrate the large effect of C on V partitioning.

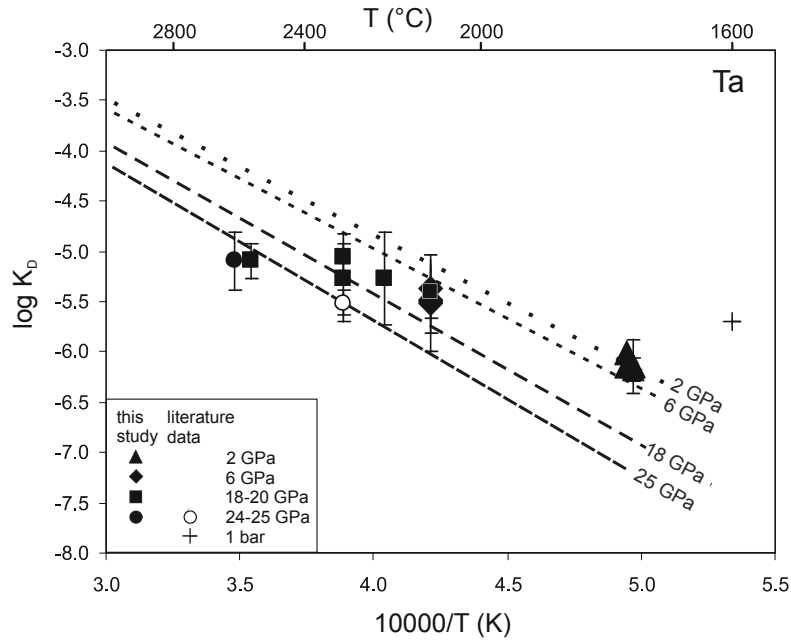


Fig. 21: The logarithmic value of the Ta distribution coefficient ( $K_D$ ) plotted as a function of inverse T ( $10000/T$ ). Black symbols are data from this study. Data from the literature include: 1 bar experiment run in alumina capsule - Rammensee et al. (1983); 25 GPa from Wade and Wood (2001). Where no error bars are shown the uncertainties do not exceed the symbol size. The lines show the pressure-temperature trends obtained from data regression for the pressures as indicated (see text).

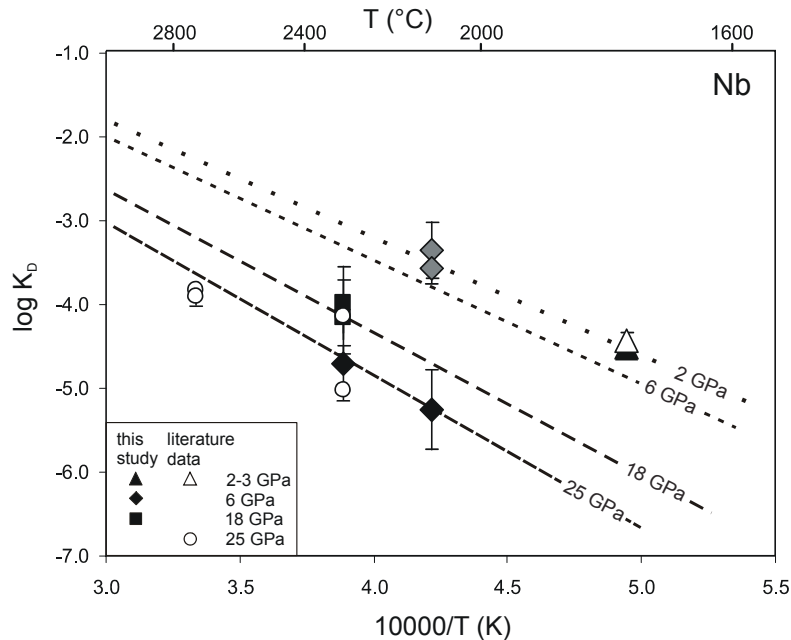


Fig. 22: The logarithmic value of the Nb distribution coefficient ( $K_D$ ) plotted as a function of inverse T ( $10000/T$ ). Black symbols are data from this study. For discussion of the deviation of all 6 GPa data (grey symbols - data obtained from graphite capsules) see text. Unfilled symbols are data from the literature: 2.5 GPa and 25 GPa from Wade and Wood (2001, 2005). Where no error bars are shown the uncertainties do not exceed the symbol size. The lines show the pressure-temperature trends obtained from data regression for the pressures as indicated (see text).

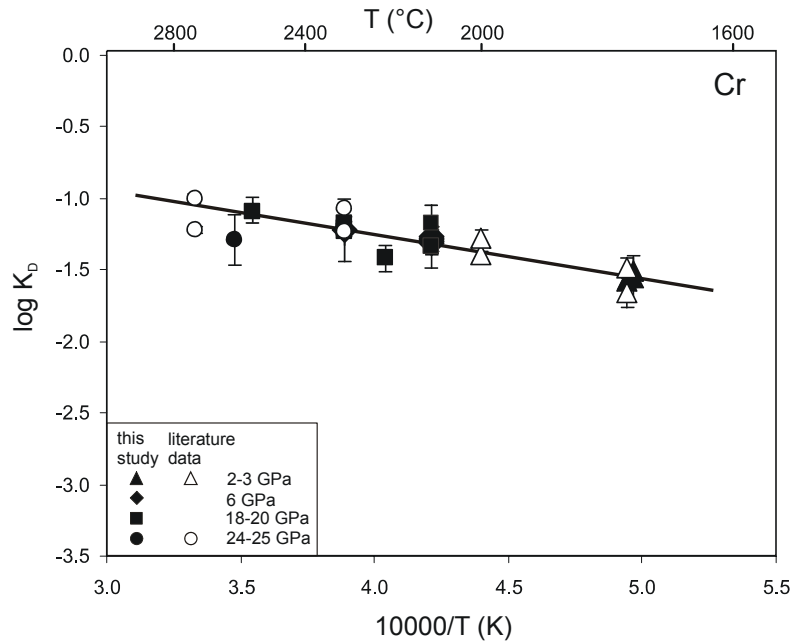


Fig. 23: The logarithmic value of the Cr distribution coefficient ( $K_D$ ) plotted as a function of inverse T ( $10000/T$ ). Black symbols are data from this study. Data from the literature include: 2.5 GPa - Wade & Wood (2001); 3 GPa - Chabot & Agee (2003); 25 GPa - Wade & Wood (2001, 2005). Where no error bars are shown the uncertainties do not exceed the symbol size. The line corresponds to the pressure-independent best-fit equation as explained in the text.

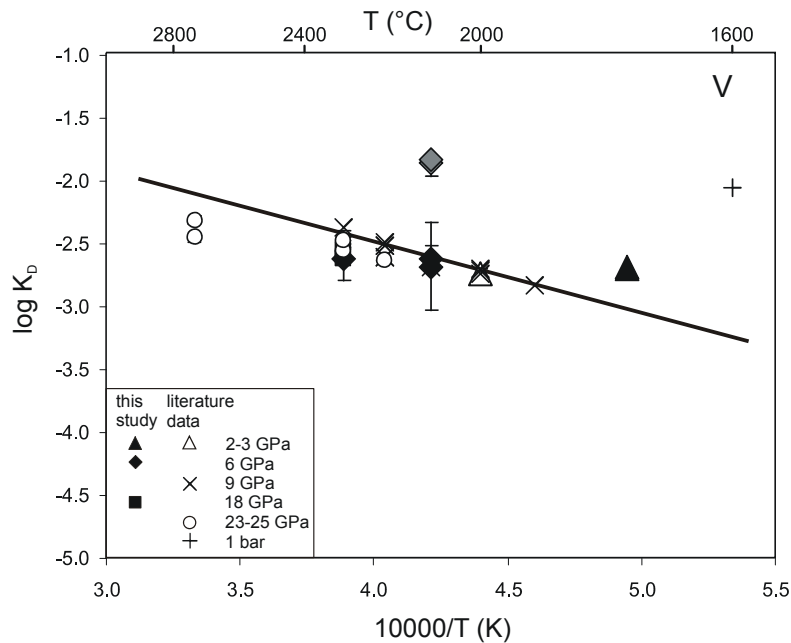


Fig. 24: The logarithmic value of the V distribution coefficient ( $K_D$ ) plotted as a function of inverse T ( $10000/T$ ). Black symbols are data from this study. For discussion of the 6 GPa data (grey diamonds - data obtained from graphite capsules) see text. Data from the literature include: 1 bar experiment (alumina capsule) - Rammensee et al. (1983); 3 GPa - Chabot & Agee (2003); 9 & 23 GPa corrected data from metal-MgO partitioning experiments (see text) - Gessmann and Rubie (2000); 25 GPa - Wade & Wood (2001, 2005). Where no error bars are shown the uncertainties do not exceed the symbol size. The line corresponds to the pressure-independent best-fit equation as explained in the text.

### Manganese

Some of the Mn partitioning data show relatively large uncertainties (see Fig. 26), especially in samples to which Mn was added at a low concentration level (starting composition A). On the other hand we found graphite capsule data at both 2 and 6 GPa to lie within the range of uncertainty of the MgO capsule results so that we also plotted literature data obtained at 2 GPa in graphite capsules (Wade and Wood, 2005), as well as other literature data from MgO capsules at 2-3 and 25 GPa (Kilburn and Wood, 1997; Chabot and Agee, 2003; Wade and Wood, 2001). The graphite capsule data at 20 GPa show a strong shift towards higher  $K_D$  values (Fig. 26) and were therefore not included for data regression. For fitting the temperature trend we started from the free energy data for MnO and corrected them for the effect of temperature on  $\gamma^0$ . The slope for the derived trend is in good agreement with the temperature dependence of the metal-ferropericlase  $K_D$  of our samples and of Gessmann and Rubie (2000). Consequently, the silicate-ferropericlase  $K_D$  for Mn is considered to be constant. Based on this, all data were corrected to a common temperature of 2000 °C and plotted against pressure in Fig. 25. This indicates a positive pressure trend, though very weak, with  $K_D$  increasing by a factor of 1.2 from 2 to about 20 GPa. Moreover, the P-effect gets weaker towards higher pressures as has been observed for Si in this study and as is known from recent data for Ni and Co (Kegler et al., 2007), although all these elements become less siderophile with increasing P. For defining the  $K_D$  trend we applied a linear P-relationship only:

$$\log K_D^{\text{Mn-Fe}}(T, P) = 0.6896 - \frac{7300}{T} + 36.5 * \frac{P}{T} \quad [24]$$

A weak positive P-trend has also been derived by Ohtani et al. (1997) though from graphite capsule results, whereas Chabot and Agee (2003) could not detect a clear P-dependence between 3 and 14 GPa.

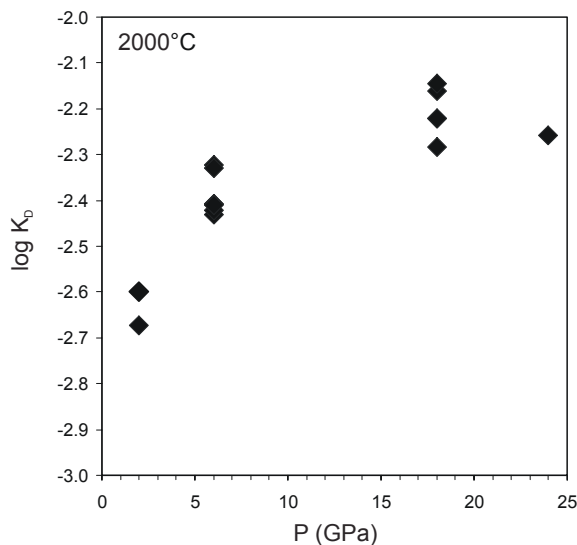


Fig. 25: The logarithmic values of the Mn distribution coefficient ( $K_D$ ) of this study corrected to a common temperature of 2000°C and plotted as a function of pressure.

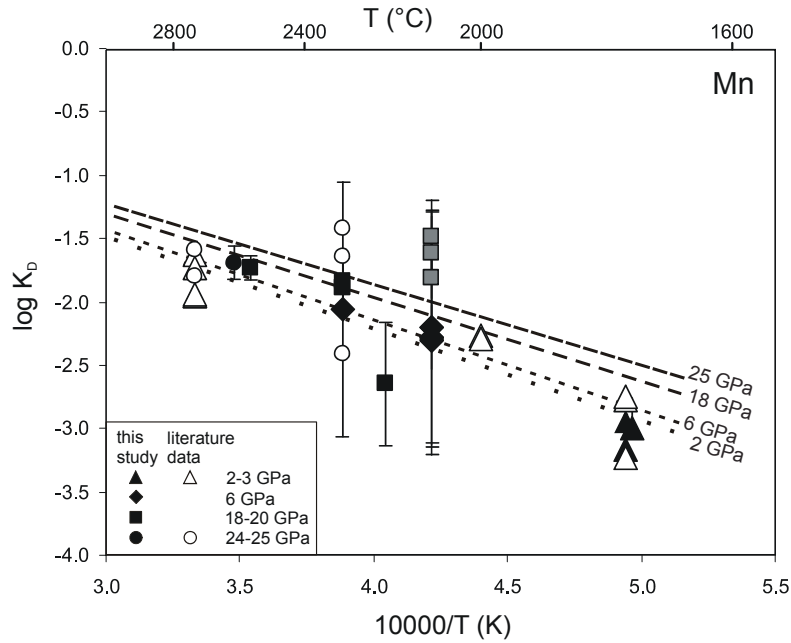


Fig. 26: The logarithmic value of the Mn distribution coefficient ( $K_D$ ) plotted as a function of inverse T ( $10000/T$ ). Black symbols are data from this study. For discussion of the 20 GPa data (grey squares) obtained from graphite capsules see text. Data from the literature include: 2.5 GPa - Kilburn & Wood (1997); 3 GPa - Chabot & Agee (2003); 2-2.5 and 25 GPa - Wade & Wood (2001, 2005). Where no error bars are shown the uncertainties do not exceed the symbol size. The lines show the pressure-temperature trends obtained from data regression for the pressures as indicated (see text).

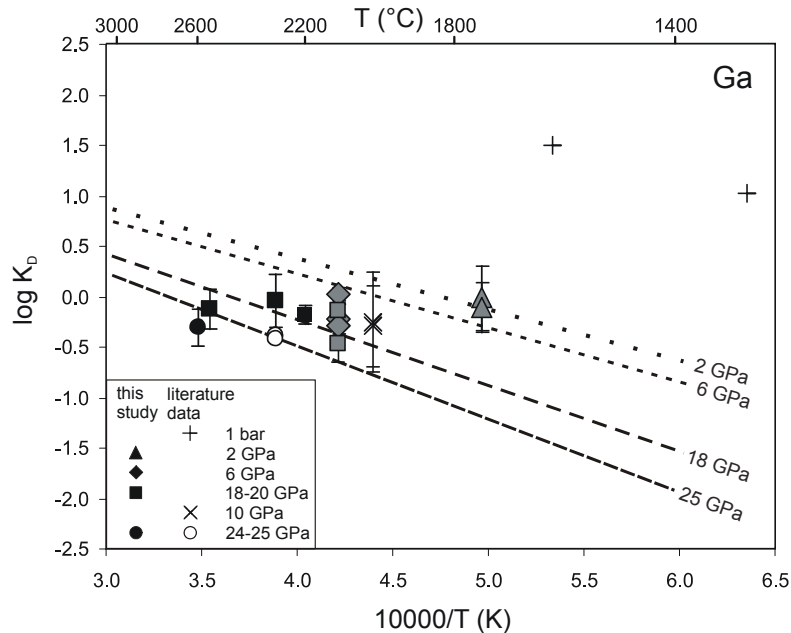


Fig. 27: The logarithmic value of the Ga distribution coefficient ( $K_D$ ) plotted as a function of inverse T ( $10000/T$ ). Black and grey (corrected data from graphite capsules) symbols are data from this study. Data from the literature include: 1 bar experiment run in alumina capsule - Schmitt et al. (1989); 10 GPa - Hillgren et al. (1996); 25 GPa - Wade & Wood (2001). Where no error bars are shown the uncertainties do not exceed the symbol size. The lines show the pressure-temperature trends obtained from data regression for the pressures as indicated (see text).

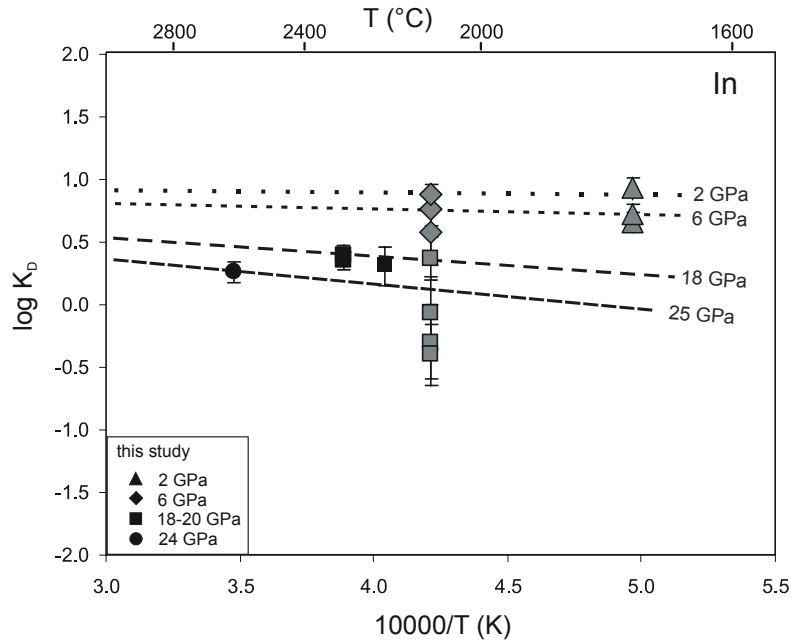


Fig. 28: The logarithmic value of the In distribution coefficient ( $K_D$ ) plotted as a function of inverse T ( $10000/T$ ). All data from this study. Grey symbols are corrected data from experiments in graphite capsules (see text). Where no error bars are shown the uncertainties do not exceed the symbol size. The lines show the pressure-temperature trends obtained from data regression for the pressures as indicated (see text).

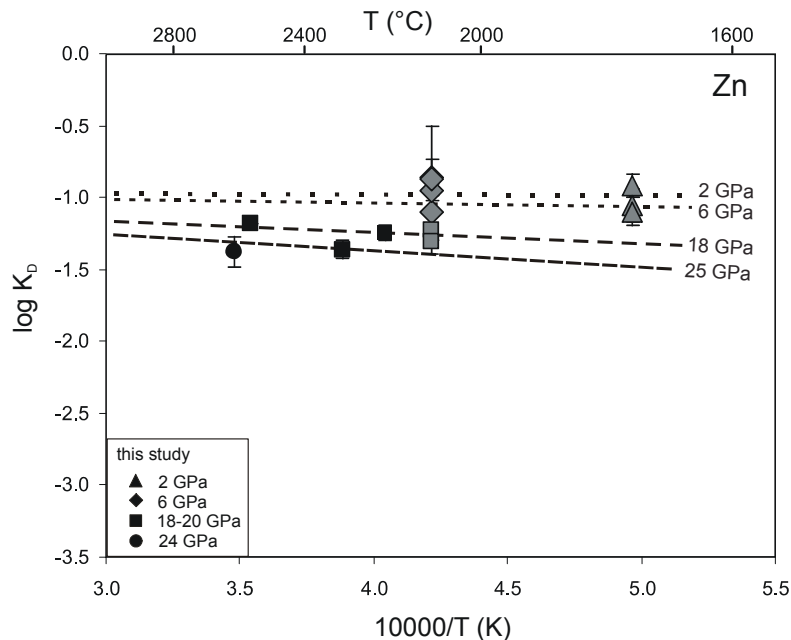


Fig. 29: The logarithmic value of the Zn distribution coefficient ( $K_D$ ) plotted as a function of inverse T ( $10000/T$ ). All data from this study. Grey symbols are corrected data from experiments in graphite capsules (see text). Where no error bars are shown the uncertainties do not exceed the symbol size. The lines show the pressure-temperature trends obtained from data regression for the pressures as indicated (see text).

### Gallium, Indium and Zinc

For all three elements Ga, In and Zn our data indicate that they become less siderophile with increasing pressure. For defining the Ga- $K_D$  trend, free energy and  $\gamma^0$  data were not available for GaO. However, an estimate of the temperature dependence can be derived from the 1 bar partitioning data of Schmitt et al. (1989) that were corrected to  $Ga^{2+}$  (Fig. 27). Equation [25] was then fitted including literature data at 10 and 25 GPa (Hillgren et al., 1996; Wade and Wood, 2001). Most experiments on Ga partitioning from the literature could not be used for refining our trend as they employ Ni-rich (> 25 wt%) metals or MgO-poor silicates (< 13 wt%) not comparable to our compositions. A comparison of results from Hillgren et al. (1996) and Righter and Drake (2000) shows that at about 9-10 GPa and 2000 °C the  $K_D$  for Ga is increased by a factor of 3 in the presence of 30 wt% Ni in the metal, which has a similar effect as W in our contaminated sample Z447.

For In (Fig. 28) and Zn (Fig. 29) there is no or only a very weak temperature dependence and therefore the respective temperature dependence factor b was set to 0 in both regression equations [26] and [27]. Moreover, for both elements there are no published data available and for fitting the P dependence, data from graphite capsules were included based on the correction of 20 GPa data (graphite) relative to 18 GPa (MgO) results. At these conditions  $K_D$  is at least 4 - 5 times lower in the presence of C in the metal liquid which is also the case for Ga. Regression on the data for the three elements yields the following equations:

$$\log K_D^{Ga-Fe}(T, P) = 2.3858 - \frac{4810}{T} - 95.9 * \frac{P}{T} \quad [25]$$

$$\log K_D^{In-Fe}(P) = 0.9682 - 81.0 * \frac{P}{T} \quad [26]$$

$$\log K_D^{Zn-Fe}(P) = -0.9317 - 44.0 * \frac{P}{T} \quad [27]$$

### Uncertainty Range for the $K_D$ Pressure and Temperature Dependencies

So far we have not discussed uncertainties on the above derived equations [19]-[27] for the pressure and temperature dependency of  $K_D$ . In many studies the errors are presented separately for each of the constant parameters (a, b and c in our case) as calculated while fitting the trend (Chabot et al., 2005; Wade and Wood, 2005). However, we find it more useful to consider the uncertainty for the calculated bulk  $K_D$  value. As an estimate for this, we derive the average deviation (mean value) of the experimentally determined  $\log K_D$  values from the theoretical  $\log K_D$  value given with the fitted curve. These uncertainties are listed in the following table.

**Table 5:** Uncertainties for the P-T-trends of  $\log K_D$

	Si	Ta	Nb	Cr	V	Mn	Ga	In	Zn
$\pm \log K_D$	0.48	0.21	0.10	0.06	0.10	0.14	0.13	0.09	0.08

### 3.6 Discussion and Implications for Existing Core Formation Models

Having defined the pressure, temperature and oxygen fugacity dependence for the partition coefficients of the studied elements, they can be used to test and constrain existing core formation models. The partition coefficients will set the chemical signature of a planetary body differentiating into a silicate mantle and metallic core. In the simplest case, full equilibration between the two reservoirs takes place and their composition reflects the D value for the conditions under which equilibration took place. In more complex core formation scenarios the final D value for any element that underwent partitioning in a differentiated body is a result of the whole accretion history and can be determined from the core to mantle concentration ratio of this element. Because the core composition is not directly accessible, such core/mantle partition coefficients can be obtained by mass balance considerations if the mass fractions X of the silicate (= mantle) and the metal (=core) reservoirs are known:

$$C_0 = C_{\text{silicate}} * X_{\text{silicate}} + C_{\text{metal}} * X_{\text{metal}} \quad [28-1]$$

With a knowledge of the mantle concentration of an element and the assumptions that the bulk composition  $C_0$  for the Earth is chondritic (normally CI) and the metal proportion is 0.32, this can be rearranged to:

$$D_{\frac{\text{core}}{\text{mantle}}} = \frac{C_{\text{CI}} - C_{\text{mantle}}}{C_{\text{mantle}} * X_{\text{core}}} + 1 \quad [28-2]$$

Estimates for the D values that match the present day mantle, calculated with the data from McDonough and Sun (1995) and compiled by Wood et al. (2006) are listed in Table 6. The uncertainties for elements like In, Zn, Ga and Mn are high due to the proportion that could have been lost before accretion as a result of volatility. The upper limit represents D if the depletion of the element from the mantle occurred by core formation only, 0 is the value for full volatile loss.

The aim of a core formation model is to obtain final values of D that are consistent with the observed mantle concentrations. Moreover, using equation [28-2], D can be defined at any point in a multi-stage core formation model to describe the partitioning between core and mantle at that stage of accretion and to display equilibration paths.

$D_V$	1.5 - 2.2
$D_{Cr}$	0.5 - 3.5
$D_{Co}$	23 - 26
$D_{Ni}$	24 - 27
$D_{Nb}$	< 0.8
$D_{Ta}$	< 0.5
$D_{Mn}$	0 - 5
$D_{Ga}$	0 - 5
$D_{Zn}$	0 - 20
$D_{In}$	0 - 20

**Table 6:**

Partition coefficients necessary to match the element concentrations of the present day mantle assuming a CI chondrite as starting material according to equation [28-2]. Estimates from McDonough and Sun, 1995 and compiled by Wade and Wood 2005.

### 3.6.1 Testing Heterogeneous Low Pressure Core Formation Scenarios

First, we have tested a classical heterogeneous core formation scenario which proposes accretion in two episodes and which was formulated by Wänke (1981) as one of the first viable core formation models. It attempts to explain the mantle's siderophile element abundance, such as the chondritic Ni/Co ratio and the depletion of weakly siderophile elements like V, Cr and Si. A similar model that also accounts for the highly siderophile element abundances was proposed by O'Neill (1991). The only parameter that influences partitioning in this type of model is oxygen fugacity; high pressures and temperatures are not required in these models for core-mantle equilibration which is assumed to have occurred only in small bodies at low pressures. Placing constraints on such low-pressure models is also important for testing high-pressure scenarios involving equilibration in a deep magma ocean. By examining how successful they are at explaining the mantle's siderophile element budget, the main features of high pressure equilibration can then be distinguished.

The initial stage of the model of Wänke (1981) is characterized by the accretion of very reduced and volatile depleted material forming about 80% of the later Earth. Equilibration with the core-forming metal left a mantle strongly depleted in siderophile elements and even depleted in some weakly siderophile elements such as V, Cr and Si. In the second stage, undifferentiated, oxidized material containing only very small amounts of metallic iron, accreted and mixed with the pre-existing reduced mantle without any further core formation. Thus siderophile elements that were completely or strongly depleted before were replenished in the mantle and the chondritic signature of elements such as Co and Ni, although still depleted relative to chondritic proportions, was produced.

An important aspect of heterogeneous models, in general, is that they require a very reducing stage to allow for the depletion of weakly siderophile elements like V and Cr from the mantle. Therefore, an important constraint is to examine whether at low pressure such a reducing stage would remove other elements which are not depleted from the mantle or which are not significantly depleted.

One simulation of such a low pressure heterogeneous accretion scenario has been performed by Dave Rubie employing the partition coefficients determined in this study and the equations of Kegler et al. (2007) for Ni and Co. This numerical model considers mass-balanced partitioning between mantle and core at fixed conditions of 1 GPa and 1500-1700 K. Accretion occurs by the stepwise addition of 24 impactors which all entirely equilibrate with the pre-existing body, but two episodes with different oxygen fugacities are distinguished. The development, with progressive accretion, of the partition coefficients of Ni, Co and V and of the FeO content of the mantle (wt%) is shown in Fig. 30. Initially-reducing conditions of approximately  $-4.8 \Delta IW$  result in very high values of  $D$  (Ni) and  $D$  (Co) which extract both elements almost completely to the core. But also V is depleted with a core/mantle  $D$  (V) of 1-5 and the FeO content of the mantle is  $< 1$  wt%. After approximately 80% accretion the material becomes oxidized and contains virtually no metallic Fe ( $f_{O_2} > -0.5 \Delta IW$ ). As a result, approximately chondritic ratios of Ni and Co are established, the FeO content of the mantle becomes 8 wt % and the final  $D$  (V) is about 1.5.

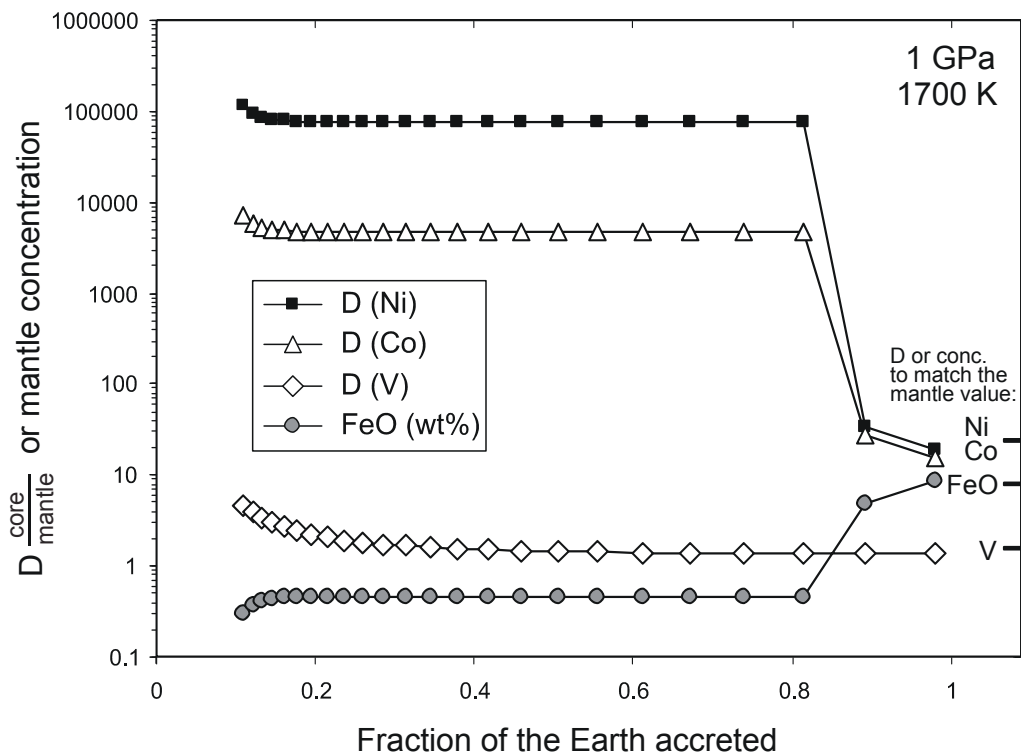


Fig. 30: Development of the core/mantle partition coefficients for Ni, Co (both based on the equations of Kegler et al., 2007) and V (equation of this study) and of the FeO (wt%) content of the mantle with progressing accretion simulating a low pressure two stage scenario at fixed conditions of 1 GPa and 1700 K. The initial 80 % of the accretion occur under very reducing conditions, resulting in strong depletions for the siderophile elements Ni and Co. But also V has a partition coefficient of 1-5. Only the last two impactors provide highly oxidized material allowing the observed mantle concentrations for these siderophile elements to be reached as indicated with the bars at the right side. Calculation was performed with a numerical mass balance model by Dave Rubie.

We have also simulated such a low pressure core formation scenario employing a mass balance equation for the two steps of accretion and testing several temperatures from 1700-2200 K. For this we assumed that core-mantle equilibration took place at 1 GPa, at low oxygen fugacities in the range of about -4 to -5  $\Delta$  IW and in the first accretion stage only. The final mantle concentration was obtained by adding a variable amount of CI chondritic composition to the reduced mantle resulting from the first step. For each temperature the oxygen fugacity for the first stage was constrained by the level required to produce a final D (V) of 1.5, which is the least reducing end of the possible range, when combined with an adjusted proportion of the oxidised phase. The latter was additionally constrained by the level required to attain the mantle FeO content of 8 wt%. At temperatures higher than 2200 K more than 20 wt% Si would enter the core, while 10 wt%, the plausible light element content of the core, is reached at approximately 2000 K. In Fig. 31 the obtained results for the final core/mantle partition coefficients after complete accretion are shown as a function of temperature.

Over the whole temperature range the final partition coefficients of Ni and Co are the same, i.e. their ratio in the mantle would be chondritic. However, the absolute values of approximately 10 are significantly below those for the Earth (see Table 6) if it formed from CI material. As we fixed the amount of chondritic material added to match the concentrations for Fe and V, the resulting concentrations for Ni and Co are too high. A slightly better fit can be obtained for these elements if we allow a small amount of metal fractionation in the second oxidised step as is done in the above model of Dave Rubie. The D values for all other elements from the latter model are identical to ours found at 1700 K and will be discussed in the following sections.

The necessary core/mantle D value for Cr is well reproduced at all temperatures. Although D (Ta) increases with temperature it is barely depleted from the mantle at the conditions required to obtain the correct D (V). Even though D (Ta) increases with temperature it does not reach a value higher than 0.5. This is the probable level where its depletion in the mantle would be detected when compared to a refractory highly lithophile element like La. Based on the data of Rudnick et al. (2000), the La/Ta ratio determined for the depleted mantle lies within the range of values observed for chondrites. The concentrations of both elements normalized to CI are relatively constant over the whole range of chondrites and show no fractionation (Fig. 32). In contrast, the depletion of Nb from the Earth's mantle with a value of 0.8 for D (Nb) can be detected by mantle ratios of Nb/La and Nb/Ta (Rudnick et al., 2000) that deviate by about 10% from the respective average ratios of the range of chondrites (Wasson and Kallemeyn, 1988).

However, if the P-T- $f_{O_2}$  dependence of D (Ta) would have been derived from experiments employing graphite capsules alone and without suitable corrections for the presence of C in the Fe-rich metal, a much higher degree of depletion would be reached for Ta in these simulations. The fact that in this case Ta would appear much more siderophile than V would result in incorrect conclusions for the lower limit of oxygen fugacity and in general the viability of such a low pressure core formation model.

Nb on the other hand is predicted to be strongly depleted from the mantle over the range of all temperatures used to simulate a low-pressure scenario as proposed by Wänke (1981). With  $D(\text{Nb})$  increasing with temperature from 2.8 to 6, even its lowest value is much greater than the value corresponding to that observed for the mantle (0.8). Under such reducing conditions, necessary to match the correct  $D(\text{V})$ , Nb would be much more strongly depleted than V which indicates that the extraction of V from the mantle cannot be explained with a scenario involving such low oxygen fugacities at low pressure.

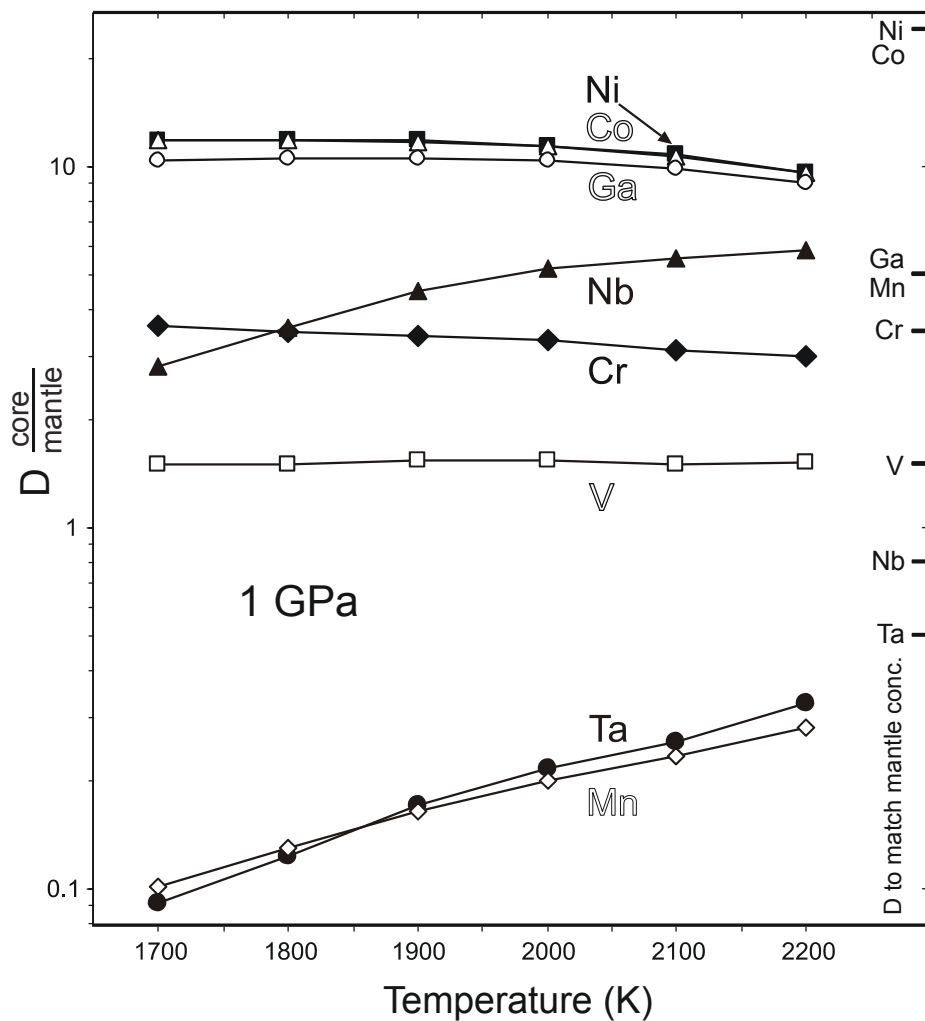


Fig. 31: The final core/mantle partition coefficients for V, Cr, Mn, Ga, Nb, Ta, Ni and Co after complete accretion calculated for a two stage low pressure core formation scenario at 1 GPa at various temperatures. In each case the  $f_{\text{O}_2}$  of the first reducing stage of accretion was constrained by the level required to produce a final  $D(\text{V})$  of 1.5. The proportion of material added in the second, oxidised phase was adjusted by the level required to attain the final mantle FeO content. The bars at the right side indicate the core/mantle partition coefficients necessary to match the observed mantle concentrations as listed in Table 6. Data for Ni and Co are based on the equations of Kegler et al. (2007).

In addition, Ga is also predicted to be strongly depleted from the mantle in this model which gives a  $D(\text{Ga})$  of about 10 which is far from the maximum value of 5 obtained for the Earth if no Ga was removed from the mantle relative to CI as a result of volatility. Therefore, in the oxidised stage of core formation the supply for Ga is insufficient to explain the mantle's abundance even without any loss of Ga due to volatility. An even better constraint however is provided by the comparative depletion of Ga and Mn. Both elements have a similar degree of depletion in the mantle (Fig. 1) thus showing an almost chondritic ratio. As Ga is more volatile than Mn, the excess depletion of Mn relative to the volatility trend must be a result of core formation. However, our results show that at low pressures Ga is much more siderophile than Mn and its degree of depletion by core formation would have been higher by two orders of magnitude compared to Mn. It would therefore seem to be impossible to reconcile the depletions of Mn relative to Ga as a result of either volatility or core formation at these conditions as both processes would have removed Ga to a much greater extent than Mn.

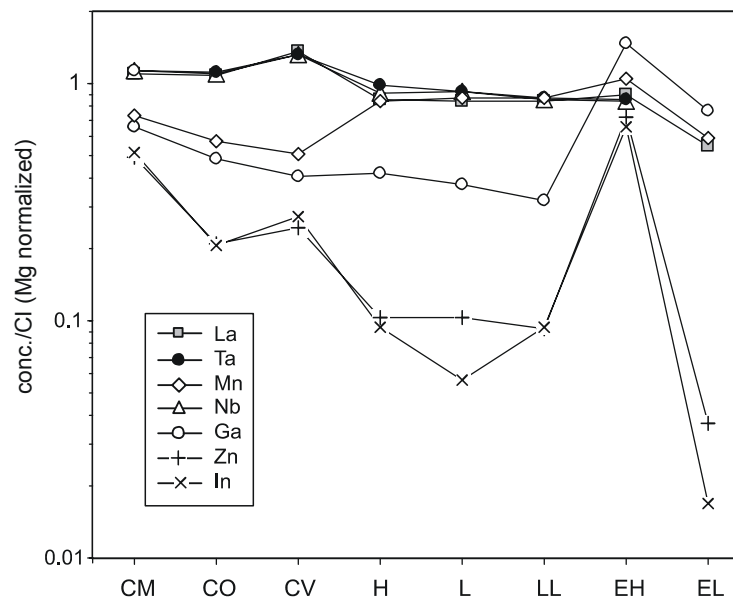


Fig. 32: The concentrations of selected refractory and moderately volatile elements in carbonaceous, ordinary and enstatite chondrites normalized to CI carbonaceous chondrite and to Mg (data from Wasson and Kallemeyn, 1988).

### 3.6.2 Constraints on High Pressure Core Formation Models

As an alternative to heterogeneous core formation at low pressure with adjustable proportions of material of changing composition, Li and Agee (1996) and Righter et al. (1997) have suggested core-mantle equilibration at high pressures and temperatures in order to explain the observed mantle depletions of the siderophile elements. Such conditions were supposed to be provided at the base of a deep magma ocean that would have persisted in the early Earth during continuous accretion of material supplied by impactors. While the conditions in such a magma ocean were initially derived only from the observed metal-silicate partitioning behaviour of Ni and Co, the increasing number of experimental data allows for refinements. Based on the combined behaviour of siderophile elements like Ni and Co and weakly siderophile elements like V, Mn and W on the other hand, Wade and Wood (2005) had excluded homogeneous core formation in the strict sense, i.e. core-mantle equilibration being explained by a single, fixed set of oxygen fugacity, pressure and temperature conditions. The latter could only be matched at temperatures way above the peridotite liquidus which is unlikely to be realistic. Instead, they modelled accretion paths involving increasing pressures and temperatures fixed along the peridotite liquidus and found that a change in redox conditions was vital to match the depletions of both the siderophile and the weakly siderophile elements.

A model of this kind involves a number of adjustable parameters and it is the aim of the current research on core formation to define further constraints and refinements for them. Employing the dataset of this study and the observed inconsistencies for the relative behaviour of certain element pairs at reducing conditions and low pressure, we can test core formation models that work at higher pressures and temperatures.

The partitioning behaviour of Nb compared to V seems to exclude core-mantle equilibration at low pressure at any redox condition. However, as the equations [23] and [21] imply, there is no or maybe only a weak P dependence for the partition coefficient of V whereas the experimental data so far available indicate a relatively strong decrease of the Nb partition coefficient with increasing pressure. We have therefore calculated the variation of  $D(\text{Nb})$  as a function of pressure, along the peridotite liquidus and at 200 K above the liquidus, at oxygen fugacities compatible with  $D(\text{V})$  of 1.5, the required value for the Earth's mantle. The results are plotted in Fig. 33. This shows that, with the V concentration of the mantle as the defining factor for the redox conditions, we have to assume high pressures of  $> 20$  GPa for metal-silicate equilibration. At lower pressures, Nb would be strongly depleted from the mantle leaving a much higher value for the core/mantle ratio than the observed  $D(\text{Nb})$  of 0.8 which is shown for reference with the horizontal line in Fig. 33.

Towards higher temperatures the necessary pressure would have to be even higher to fulfill the criteria for both elements. This provides an important constraint for the lower pressure limit of such core formation scenarios and gives strong support for metal-silicate equilibration in a deep magma ocean. At conditions constrained by the peridotite liquidus, temperature becomes an important parameter in such a scenario as  $D$  shows a positive temperature dependence for both elements. Even though this is stronger for Nb, the combined effect of high pressures and temperatures allows for much less reducing conditions than had to be employed in the low pressure models. In our example, for conditions 200 K above the peridotite liquidus the required value for  $f_{O_2}$  at 30 GPa would be about  $-3 \Delta IW$  and at 60 GPa only  $-2.5 \Delta IW$ .

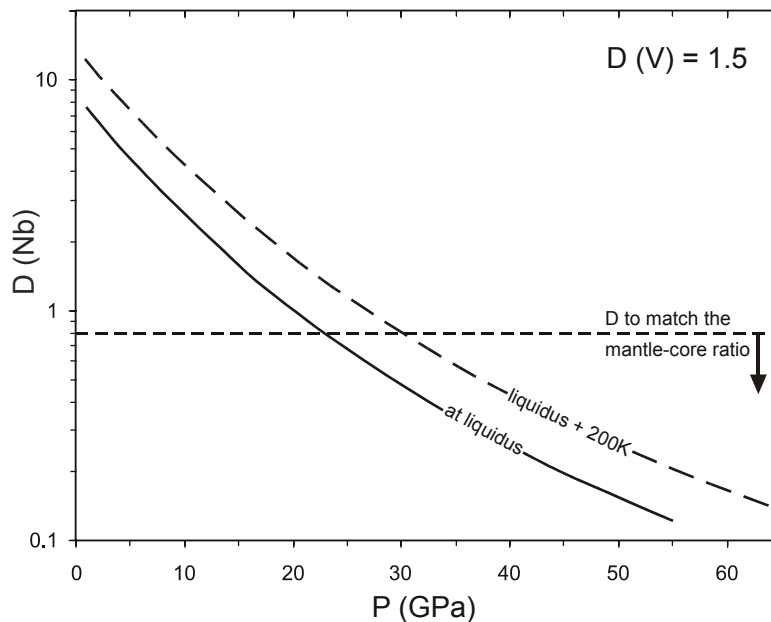


Fig. 33: The partition coefficient  $D$  of Nb as a function of pressure calculated for an oxygen fugacity where the partition coefficient for V ( $= 1.5$ ) matches the observed present day mantle abundance. The temperature is fixed along the peridotite liquidus (solid line) and 200 K above it (dashed curve), as derived from Wade and Wood (2005). The required  $D$  (Nb) for the core/mantle ratio ( $= 0.8$ ) is indicated with the horizontal line.

### 3. Liquid Metal - Liquid Silicate Partitioning of Lithophile and Weakly Siderophile Elements

We can then use our dataset of partition coefficients in order to test more complex models of core formation. A polybaric multi-stage accretion model has been developed by Dave Rubie. The framework for the parameters is set to explain the Ni, Co and V concentrations in addition to the FeO content of the Earth's mantle. This numerical model assumes accretion from differentiated impactors that grow progressively in size. These bodies re-equilibrate to a large degree at the base of a magma ocean, i.e. with the molten silicate mantle of the proto-Earth. As the Earth grows the pressure at the base of the magma ocean increases from 13 to 85 GPa at the final impact. While the initial bodies are reduced, with < 1 % FeO in their mantles, the final 25 % of the accreted material is delivered by more oxidized impactors that additionally grow in size. In the final stages, only part of their cores re-equilibrate with the magma ocean of the Earth. The results for the core/mantle partition coefficients after each equilibration step along with progressing accretion for the elements examined in this study are shown in Fig. 34. The data for Ni and Co were obtained with the equations of Kegler et al. (2007).

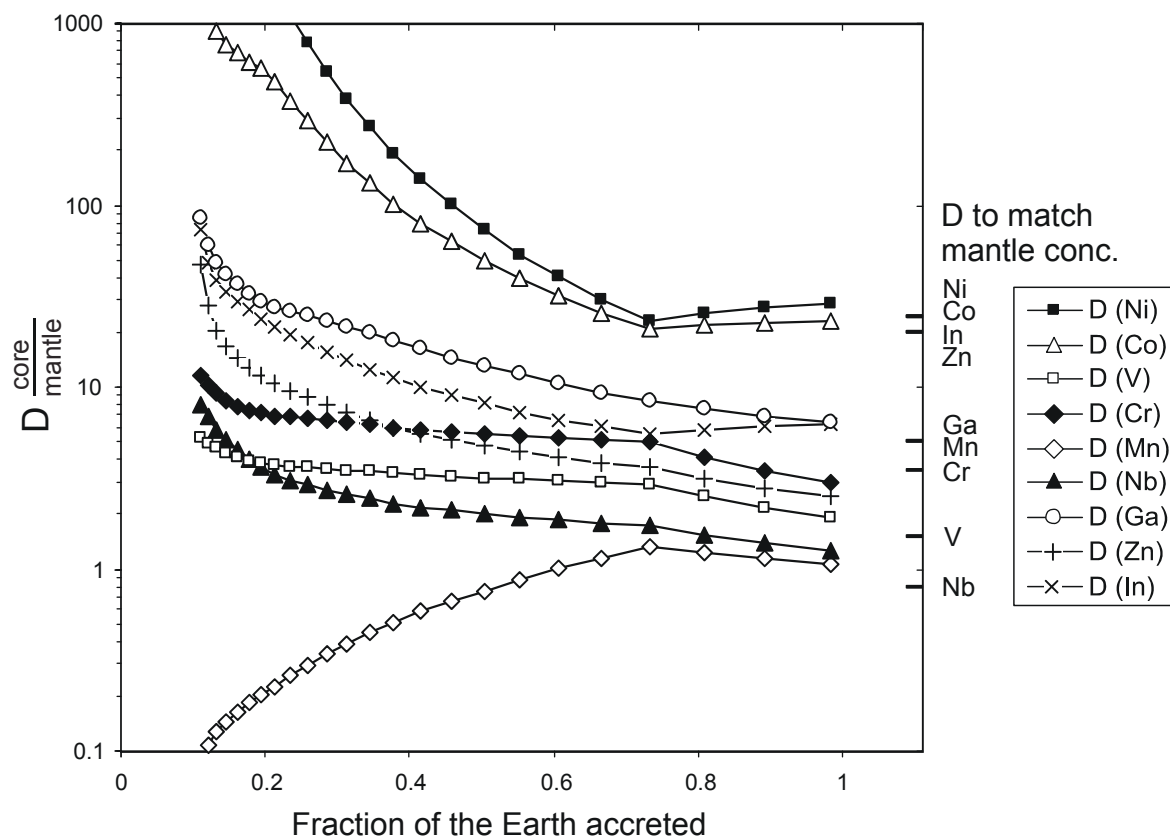


Fig. 34: Evolution of the core/mantle partition coefficients for elements examined in this study and for Ni and Co with data from Kegler et al. (2007) with progressing accretion simulating a polybaric multi-stage scenario. This numerical mass balance model was designed by Dave Rubie to match the observed concentrations of Ni, Co, V and the FeO content of the Earth's mantle. Details of the parameters of the model are given in the text. Final D values required to match the mantle concentrations of all elements displayed are indicated with the bars to the right.

As Fig. 34 shows, the model succeeds well in reproducing the final core/mantle  $D$  values for Ni and Co as well as for V and Cr given their range of uncertainties for the mantle. The value for Nb is still too high in this high pressure scenario. However, this could be due to the uncertainty resulting from our experimentally determined relationship for  $D$  which has to be extrapolated to 85 GPa in this model. This is a large extrapolation considering the relatively small number of experimental data available for Nb with pressures not exceeding 25 GPa (Fig. 22).

While Ga reaches its mantle  $D$  value in this model by metal-silicate partitioning starting from a CI composition undepleted in volatiles, the value for  $D$  (Mn) which should be at least as high as  $D$  (Ga), even ignoring volatility, is almost one order of magnitude too low. So the relative behaviour of the two elements observed at low pressures and very reducing conditions is maintained in such a polybaric model at high pressures, even though  $D$  (Ga) shows a negative and  $D$  (Mn) a positive pressure dependence (compare equations [25] and [24]). This can further be demonstrated with the relative Ga to Mn distribution coefficient  $K_D$  (Ga-Mn) (dividing  $D$  (Ga) through  $D$  (Mn), analogous to equation [4]) plotted as a function of temperature. As both elements have the same valence  $K_D$  is independent of oxygen fugacity. In Fig. 35 we regard various pressures in the range of 1 - 80 GPa and temperatures of values on the peridotite liquidus and up to 300 K above the liquidus. It shows that at any pressure below 60 GPa the required  $K_D$  for the mantle which has to be  $\leq 1.4$ , would not be attained. Only at extremely high pressures, of about 80 GPa, does  $K_D$  reach reasonable values, if one assumes that both elements have experienced depletion to some degree by volatility. In the presented model such conditions are only provided in the last few accretion steps which are not sufficient to reset the whole mantle chemistry.

One possible explanation for how this inconsistency could be resolved would be the presence of an element in the metal that strongly influences the partitioning behaviour of both elements in opposite ways, making Ga less and Mn more siderophile. Such effects have been observed for S in experiments at low pressures  $< 3$  GPa (Righter and Drake, 2000; Chabot and Agee, 2003). However, according to the result of sample Z551 for Mn (Fig. 18) and our current data from samples containing S, Mn and Ga, S seems to have little effect at higher pressures and the necessary amount of S for causing any significant effect would have to be unrealistically high.

Another explanation could be that the starting material from which the Earth mainly accreted had a composition different from CI chondrite. If nebular fractionation processes could produce a material with an initial Ga concentration that was much higher than that of Mn (i.e. a high Ga/Mn ratio), this would then allow much stronger depletions of Ga compared to Mn during core formation, which would then return the Ga/Mn ratio to the near chondritic ratio observed in the Earth's mantle. As Fig. 32 shows, almost all meteorite groups have  $Ga < Mn$  compared to CI, only the enstatite chondrites exhibit concentrations of  $Ga > Mn$ , but even then the difference is actually quite small.

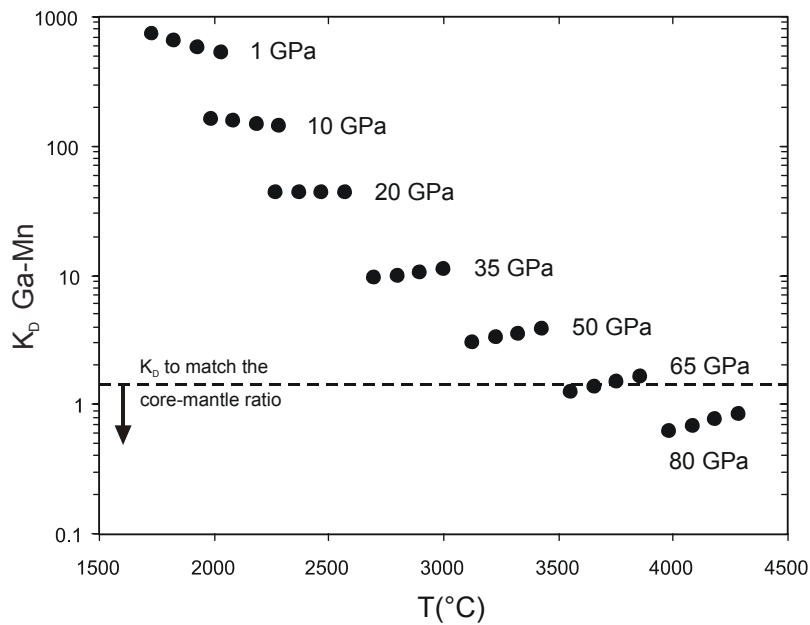


Fig. 35: The partition coefficient of Ga relative to Mn as a function of temperature. Data are plotted at various pressures and temperatures corresponding to the peridotite liquidus and 100 K, 200 K and 300 K above. The required  $K_D$  (Ga-Mn) for the mantle (= 1.4) is indicated by the horizontal line.

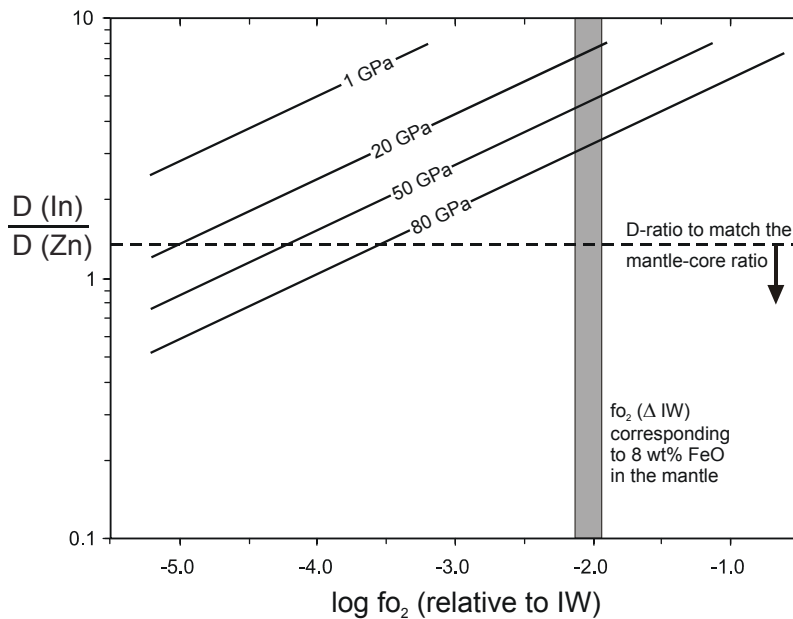


Fig. 36: The partition coefficients  $D$  of In ( $1^+$ ) relative to that of Zn ( $2^+$ ) as a function of oxygen fugacity, expressed relative to the iron wüstite buffer, testing different pressures. At each pressure the temperature is fixed at 100 K above the peridotite liquidus. The maximum  $D$  ratio for the two elements in the Earth must not exceed a value of 1.3 (indicated with the dashed line) which is the upper limit if both elements were depleted from the mantle by core formation only. Involving volatility the value must always fall below. The grey bar indicates the range of oxygen fugacity consistent with the FeO content of the mantle.

Another geochemical inconsistency is revealed for the relative behaviour of In and Zn. In the above model (Fig. 34) we observe that over the whole range of conditions involved, In has a partition coefficient consistently higher than that of Zn. This can be illustrated by considering the ratio of the two partition coefficients  $D(\text{In}) / D(\text{Zn})$ . As the elements have different valences ( $\text{In}^{1+}$ ,  $\text{Zn}^{2+}$ ), this ratio changes with oxygen fugacity (Fig. 36). Calculating over a pressure range of 1-80 GPa combined with temperatures 100 K above the peridotite liquidus, shows that under none of these conditions would it be possible to match a plausible D ratio for the two elements in the mantle in a range of oxygen fugacity that is consistent with the observed FeO content of the mantle. Consequently, in any core formation scenario In would be more depleted from the mantle. Additionally, volatility should have depleted In to a higher degree than Zn. However, In and Zn are not fractionated from each other in the mantle. Therefore it is difficult to explain their relative abundances by any core-mantle fractionation process. Moreover, none of the nebular fractionation processes reflected by the different chondrite compositions has produced material that has a much higher In concentration relative to that of Zn (Fig. 32). Their close to chondritic ratio in the mantle actually seems to be more consistent with their addition as an oxidised late veneer. However, the extent of such a veneer would have to be much larger than that required to explain the highly siderophile elements.

### 3.7 Conclusions

The final partition coefficients of Nb, Ga and Mn of the mantle can not be reproduced in a heterogeneous core formation scenario at low pressure based on the classical model of Wänke (1981), as this requires initially very reducing conditions in order to explain the depletions of weakly siderophile elements like V. Regarding more complex heterogeneous models, Nb can serve as the main constraint on the reducing phase of core formation as it requires high pressures for it not to be depleted compared to V. However, in the future the present data will need stronger experimental support for our extrapolations to pressures above 30 GPa.

Even in high pressure scenarios the siderophile character of Ga and In is maintained so that they would be depleted from the mantle by core formation, in addition to their volatile behaviour. This causes major inconsistencies when comparing these elements to less volatile elements that display very similar mantle abundances, e.g. Ga to Mn and In to Zn. The classical mantle abundance diagrams categorize the elements by their volatility and a volatility trend is defined from elements that are supposed to be depleted by volatility alone as has previously been done for Ga (Palme and O'Neill, 2003). In this way the depletions of elements such as Mn relative to the volatility trend had been assigned to core formation. However, our data suggest that the chondritic ratio of Mn and Ga cannot be explained by any core-mantle fractionation process as Ga is always more siderophile than Mn, in addition to its higher volatility. The same observation has been made for In compared to Zn and we therefore conclude that the volatility trend is unreliable. The most likely explanation for the nearly chondritic ratios of these element pairs is that CI material did not deliver the Earth's volatile elements.



## Chapter 4

# Liquid Metal - Liquid Silicate Partitioning of Highly Siderophile Elements at High Pressures and High Temperatures

### 4.1 Introduction

The term 'highly siderophile' for the platinum group elements (PGE: Ru, Rh, Pd, Os, Ir, Pt) and Re categorizes their geochemical character observed in 1 bar partitioning experiments, which is extremely metal loving. As a consequence, these elements have metal-silicate partition coefficients of  $\geq 10^4$  which would result in their almost complete removal from a molten silicate mantle equilibrating with molten metal during planetary core formation. However, in Earth's mantle, concentrations of these highly siderophile elements (HSE's) are unexpectedly high. The most widely accepted explanation for this overabundance is that these elements were added to the mantle, in chondritic ratios, following the main stage of core formation as a 'late veneer' of chondritic material for which no reequilibration occurred (O'Neill, 1991 & 1995). However, the late-veneer hypothesis may require reevaluation because improved analytical techniques have revealed that some of the HSE ratios of the primitive upper mantle are non-chondritic (Becker et al., 2006). An alternative possibility, that metal-silicate equilibration at high pressure and high temperature (e.g. 30 - 40 GPa, > 3000 K) has contributed to the current abundances of HSE's, has not been tested due to lack of experimental data. While the solubilities of some HSE's in silicate liquid at 1 bar and moderate temperatures are quite well known (Ru - Borisov and Nachtweyh, 1998; Rh - Ertel et al., 1999; Fortenfant et al., 2003<sup>a</sup>; Pd - Borisov et al., 1994; O'Neill, 1995; Ir - Borisov and Palme, 1995; O'Neill, 1995; Pt - Borisov and Palme, 1997; Ertel et al., 1999; Fortenfant et al., 2003<sup>a</sup>; Re - O'Neill, 1995; Ertel et al., 2001) the number of high-pressure and/or high-temperature studies is limited. Existing studies cover a maximum pressure range of  $\leq 16$  GPa at  $\leq 2000^\circ\text{C}$  and high-temperature experiments ( $\leq 2500^\circ\text{C}$ ) were performed at relatively low pressures ( $\sim 2$  GPa). Moreover, these studies have often concentrated on individual elements, mainly Pt (Holzheid et al., 2000; Cottrell and Walker, 2006; Ertel et al., 2006) or Pd (Holzheid et al., 2000; Richter et al., 2006), whereas the relative behaviour is important for explaining HSE mantle abundances. From the partitioning of other siderophile elements like Ni and Co it is known that their partition coefficients decrease drastically with increasing P and T (Li and Agee, 1996 & 2001; Chabot et al., 2005; Kegler et al., 2007). The aim of the present study is to evaluate metal – silicate equilibration in a magma ocean as a possible explanation for the HSE

inventory of the Earth's mantle by investigating the behavior of a range of HSE's in a system consisting of liquid Fe-alloy and molten peridotite at 3 - 18 GPa and temperatures > 2000°C.

##### **The Nugget Effect**

A problem involved in HSE research is the so-called nugget effect which has been reported in many previous studies, e.g. by Borisov and Palme (1997), Ertel et al. (1999 & 2006), Cottrell and Walker (2006). A review of possible explanations for this effect is given by Righter (2005). Due to their high reduction potentials (O'Neill et al., 1995) the oxides of the HSE are easily reduced to the respective metals and their solubility in silicate melts decreases with decreasing oxygen fugacity. However, below a certain level of oxygen fugacity, correlation between HSE concentration and  $f_{O_2}$  is not maintained, but the HSE concentrations scatter around a certain value on a level still detectable with laser-ablation ICP-MS or neutron activation analysis. In the reported solubility experiments, this results from the occurrence of the metals in form of tiny particles up to  $\sim 1 \mu\text{m}$  in the quenched silicate glass. In most cases this is assigned to a physical or mechanical process and consequently, trace element analyses of the silicate will be contaminated leading to an overestimation of the HSE concentration the degree of which will increase at low oxygen fugacity.

In order to address the nugget effect both the design of such experiments as well as the analytical detectability should be regarded. To increase oxygen fugacity, high concentrations of the HSE in the metal phase should be chosen. For this reason previous studies have often equilibrated a silicate melt using 'loop' or 'stirred crucible' techniques (Borisov et al., 1994; O'Neill et al., 1995) at 1 bar or capsules of HSE-alloys of either low Fe concentration or without Fe for piston cylinder and multi-anvil experiments at higher pressures (Holzheid et al., 2000; Ertl et al. 2006). Another advantage of such experimental setups is that the nugget effect cannot be ascribed to tiny metal clusters or droplets that were mechanically not completely separated from the silicate melt if the starting silicate phase was entirely HSE free. However, such experiments can only provide a maximum solubility for the respective element, often employing Fe-free melts, which is far from a realistic scenario.

Additionally, microanalytical results should be treated with care and the analytical technique should enable nuggets to be detected in the silicate phase. A method like laser-ablation ICP-MS acquires data in time-resolved mode and provides 3-dimensional information about the trace element distribution in the sample. If nuggets are present in the ablated sample volume this will result in a distinct increase of intensity in the spectrum. Recently, Ertel et al. (2006) have presented nanonugget corrected Pt LA-ICP-MS analyses in quenched silicate glasses where they only take minimum intensities from highly variable signals for further integration. However, this leaves extremely short effective signal counting times and can be only applied to glasses. In case of coarse silicate quench textures (see below), the concentration might even be underestimated if

the HSE's had been dissolved in the silicate liquid but crystallized as separate phases on quench which can give similar ablation signals as nuggets. Therefore, as an indicator for genuine concentrations in the silicate phase we will use the existence of a correlation between HSE partition coefficient and oxygen fugacity as derived from the redox equilibrium [6] with equation [13-2].

An alternative explanation for the occurrence of nuggets has been given by Cottrell and Walker (2006), who propose that the nuggets form during quench. They performed experiments on Pt solubility, that were set up in a way such that mechanical contamination of the silicate melt can most likely be excluded. Identical Pt concentrations from zones within the silicate sample that displayed Pt nuggets visible on  $\mu\text{m}$  scale (included in the analyses) and from areas at the graphite capsule - sample contact, virtually micro-nugget free, were taken as evidence that the Pt occurring as nuggets had been dissolved in the silicate under run conditions. Depending on the quench rate, nuggets were supposed to have formed in the centre of the sample while the more rapidly cooled rim stayed nugget free. The experiments had been performed at 2 GPa and at much higher temperatures and lower oxygen fugacities (0 to 2 log units below the IW buffer) than previous studies (Borisov and Palme, 1997; Ertl et al., 1999; Holzheid et al., 2000) and the observed concentrations are much higher by at least one order of magnitude. The fact that measured concentrations in these samples, in contrast to previous 1 bar studies, at these reducing conditions show no linear correlation with oxygen fugacity had been assigned to Pt being dissolved in the silicate melt as neutral metal atoms (see section on oxygen fugacity).

#### **Analytical Difficulties Involved in Highly Siderophile Element Studies**

Another difficulty in such studies arises for the analysis of highly siderophile elements in the silicate phase. Microanalytical techniques like LA-ICP-MS or SIMS have to be employed because of the extremely low concentrations (ppm to ppb level). However, at present there is a lack of appropriate standards for HSE measurements in silicate phases using such techniques. Previous studies have used Fe-Ni metals or sulfides but the disadvantage of such standards is that they are often not homogeneous. This is the case with some meteorite metal standards due to exsolution textures and in addition they contain either only some of the HSE's of interest for our study or in an inappropriate concentration range. Moreover, their major element compositions are totally different from that of silicates, introducing potential analytical errors due to matrix effects. Commercial glass standards, such as the NIST series, include no certified HSE values. The compilation of Pearce et al. (1997) for the NIST 610 glass only lists analyses for Re, suggesting an average value of 103.7 ppm gained from 3 analyses with a standard deviation of 90 ppm. The study of Sylvester and Eggins (1997) on the NIST 610 glass shows that only Re, Rh, Pt and Pd have concentrations above the detection limit for LA-ICP-MS, with the latter three only having concentrations  $< 4$  ppm. For this reason, previous studies have often employed their own 'in-

house' synthetic glass standards doped with the elements relevant for the respective study (Capobianco et al., 1994; Holzheid et al., 2000; Fortenfant et al., 2003<sup>b</sup>). We therefore have synthesized silicate glass standards doped with the HSE's Ru, Rh, Pd, Re, Ir and Pt at two different concentration levels ranging between 1 - 4 ppm and 10 - 40 ppm. The procedure of the synthesis and quality control of the glass standards are described below.

## 4.2 HSE Glass Standards for Trace Element Microanalysis and Analytical Techniques

### 4.2.1 Synthesis of the Glass Standards

For the trace analysis of HSE's in quenched silicate melts with various microanalytical techniques, silicate glasses of eutectic diopside-anorthite bulk composition doped with Ru, Rh, Pd, Re, Ir and Pt at two different concentration levels have been produced. This additionally allows us to analyse most of the major elements in our quenched sample silicates of primitive mantle composition.

In order to optimize the homogeneity of the resulting glasses, gels were employed as starting materials. In Table 7 the proportions of the individual components in the starting mixtures for the gels are listed. For each composition, a batch of 5 g of gel was prepared. The gel synthesis is based on the method of Edgar (1979). First, separate nitrate solutions of Mg, Ca and Al were produced in teflon beakers starting from powders of MgO, CaCO<sub>3</sub> and metallic Al. The HSE's were added to these mixed solutions employing purchased ICP-standard solutions (chloride solutions for Ru, Rh, Ir, Pd, Pt and nitrate solution for Re) with concentrations of 1000 µg/ml. SiO<sub>2</sub> was added to the mixture in form of standardized TEOS solution together with about the same volume of ethanol. Gelling of the constantly stirred bulk mix was induced by adding ammonia solution. After complete precipitation, the gels were first dried on a hot plate at 70 °C for one day then transferred to Pt crucibles and dried at 110 °C in an oven for 2.5 days. Afterwards they were stepwise heated to 500 °C over 1 day and finally slowly heated to 800°C where they were fired for 45 min until constant weight was achieved ensuring that all nitrates were transformed to oxides.

Glasses were produced in two melt runs, in each case using Pt crucibles in a 1 atm furnace. In the first run only a relatively small amount of each gel was melted at 1350°C for 5 minutes. Short run times were chosen in order to minimize the loss of the HSE's to the Pt crucible. Of each quenched melt composition one chip (3 - 7 mm across) was mounted in epoxy. As we detected some metallic 'nuggets' on a first check with SEM (Fig. 37), a second batch of each composition was produced, pressing the gels into pellets prior to melting and consuming the rest of them. This time the melts were held for 25 minutes at 1450 °C. The quenched glasses were crushed,

#### 4. Liquid Metal - Liquid Silicate Partitioning of HSE at High Pressures and High Temperatures

homogenized in an agate mortar for 30 minutes and then again melted at 1650 °C for 5 minutes. The aim of employing longer run times and higher temperatures was to increase the solubility of the HSE's in the silicate melt. On the other hand this also increases diffusion rates, resulting in some loss of the HSE's to the Pt crucible, for which the larger melt volume to Pt-contact surface area ratio should partly compensate. Another possible cause for losing some of the HSE content might be their relatively high volatility. Glass chips from these batches were carefully selected, preferably from the center of the sample and with fresh fractured surfaces. Where pieces had been in contact with the Pt crucible, surfaces were ground down on SiC disks to remove the outer  $\geq 0.5$  mm thick layer.

	1	2
wt%		
SiO <sub>2</sub>	49.56	49.56
Al <sub>2</sub> O <sub>3</sub>	17.66	17.66
CaO	23.13	23.13
MgO	9.64	9.64
ppm (wt)		
Ru	3	30
Rh	1	10
Pd	2	20
Re	1	10
Ir	2	20
Pt	4	40

**Table 7:**

Composition of the two starting mixtures for the gel syntheses, the aim of which was to produce synthetic HSE glass standards. The basis is a stoichiometric eutectic anorthite-diopside glass composition containing ppm concentrations of Ru, Rh, Pd, Re, Ir and Pt.

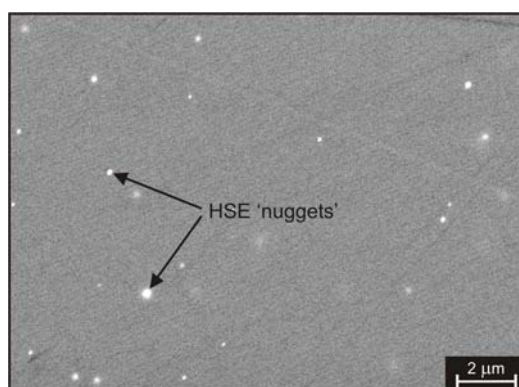


Fig 37: Back scattered electron images of HSE glass I-2. Tiny metallic nuggets have formed, predominantly consisting of Pt.

In total, four different glasses have been produced. They have been labelled with Roman numbers to indicate melt runs I and II and arabic numbers for the starting compositions 1 and 2. From run I, one glass piece of each composition was separately imbedded in epoxy and two pieces of each were mounted together in an epoxy block from melt run II. Imaging of these chips with a scanning electron microscope (LEO 1530-SEM) revealed, that in all four glass types, tiny metallic 'nugget-like' spheres are present. They are more frequent in both glasses from starting material 2 and the higher melting temperature of run II did not result in their complete dissolution. The back scattered electron (BSE) image of Fig. 37 displays a section from the glass I-2 chip. The largest nuggets have diameters up to 200 nm, thus approaching the resolution limit of the SEM. A semiquantitative EDX analysis of some of the nuggets indicated an accumulation of Pt and for some larger ones Rh and Ir. However, the glasses can still be regarded as homogeneous as long as such element concentrations are homogeneously spread over a volume relevant for microanalytical techniques, which was tested with LA-ICP-MS.

#### **4.2.2 Quantitative Analysis of the Glasses and Evaluation of their Suitability as Standards for HSE Microanalysis**

##### **Electron Microprobe Analysis**

The major element compositions (Si, Mg, Al, Ca) of the four glasses were determined with electron probe microanalysis (EPMA) using the JEOL JXA-8200 machine at BGI. The analytical conditions were 20 kV for the accelerating voltage, 50 nA for the probe current and 20 s for the peak counting times on each element. Mineral standards were andradite for Si and Ca, enstatite for Mg and spinel for Al. For each composition, the imbedded chips were analyzed with randomly set points and along two line profiles (30-60  $\mu\text{m}$  point spacing) from rim to rim across each chip. The bulk compositions were determined from the mean value of all analyses per glass type and are listed in Table 9. In general, the glass chips from melt run I are a bit less homogeneous than from run II, although relative standard deviations for all elements are below 3.5 %. For the run I chips, a small variation towards the rim occurs where the concentration of  $\text{SiO}_2$  increases (1.5 - 3 wt%) and that of  $\text{Al}_2\text{O}_3$  (1 - 2 wt%) decreases. This heterogeneity can be correlated with a curved rim which indicates the contact with the crucible wall during melting, which had evidently not been removed. However, central regions of both run I glass chips are homogeneous with respect to the major element composition. For run II glasses, analyses were taken from both imbedded pieces and the relative standard deviation for all elements is below 0.6 %. The major element compositions of glasses I-1 and II-1 correspond to the starting concentrations within analytical uncertainty whereas glasses I-2 and II-2 have a lower  $\text{SiO}_2$  and accordingly slightly higher  $\text{Al}_2\text{O}_3$ , MgO and CaO contents. This is probably due to a loss of  $\text{SiO}_2$  during the gel synthesis, involving the very volatile TEOS solution, before gelling occurred.

##### **Isotope Dilution ICP-MS Analysis**

The concentrations of the HSE's in the glass standards were determined with isotope dilution technique in cooperation with H. Becker at the Freie Universität in Berlin. A mixed spike with roughly chondritic proportions of  $^{191}\text{Ir}$ ,  $^{99}\text{Ru}$ ,  $^{194}\text{Pt}$  and  $^{105}\text{Pd}$  and a separate pure  $^{185}\text{Re}$ -spike from the laboratory in Berlin were employed. For the monoisotopic Rh, Iridium served as an internal standard.

Two samples from glass I-1, three samples from each of the glasses I-2 and II-2, and 4 samples from glass II-1 were chosen for analysis. Surfaces that had probably been in contact with the Pt crucible during melting were ground off from the pieces before they were crushed and finely ground in an agate mortar. The amounts of the sample powders ranged from 10 to 46 mg (see Table 8). The applied technique for digestion of the material is routinely used for HSE samples in the laboratory in Berlin and a description is given by Becker et al. (2006). It is a modified closed-system method where samples, sealed into borosilicate glass Carius tubes, are treated with reverse aqua regia (2:1 mixture of both concentrated  $\text{HNO}_3$  and  $\text{HCl}$ ) at about  $300^\circ\text{C}$ . It is employed to enhance the dissolution of PGE- and especially Os- and Ir-bearing oxides and silicates. In a first step the samples were weighed into the glass tubes together with the appropriate spike amount and a total volume of 8 ml acid and were predigested in the sealed capsules at  $220^\circ\text{C}$  overnight. This additionally served as a stability test before taking the mixtures to higher temperatures where high internal pressures develop in the glass tubes. For this reason they were enclosed in steel vessels together with 20g dry ice providing a  $\text{CO}_2$  counter pressure while heating them at  $295^\circ\text{C}$  for 12h. Yet, one tube broke during this process and we lost one sample of glass II-2. The applied maximum temperature should be sufficient for digesting even the nm sized nuggets as they are surrounded by silicate glass matrix and the sample powders were finely ground. Additionally, the liquids had been agitated in an ultrasonic bath between the two heating steps.

After centrifugating and evaporating the samples to remove the remaining aqua regia, the residues were redissolved in 7.5 ml of 0.2N  $\text{HCl}$ . The chemical separation of the HSE's from the silicate matrix was performed by cation exchange chromatography using a 200 mesh DOWEX resin. The columns were prewashed with 20 ml of 0.2 N  $\text{HCl}$  and the HSE's were stepwise collected in a total volume of 8 ml 0.2 N  $\text{HCl}$ . After evaporating the liquids to near-dryness they were redissolved in 3-4 ml of 2%  $\text{HNO}_3$ .

The determination of the HSE abundances was carried out with the Thermo Electron Element XR inductively coupled plasma mass spectrometer (ICP-MS) in Berlin which provides a high mass-resolution double focussing sector field system. The ion signals were detected with an electron multiplier in pulse counting mode. The solutions were transferred into the Ar-plasma using an Aridus Membrane desolvating nebulizer device to increase sensitivity and to reduce oxide formation (flow rate  $100\ \mu\text{l}/\text{min}$ ). The analysed masses comprised 98, 99, 101, 102 and 104 for Ru, 103 for Rh, 105, 106, 108 and 110 for Pd, 185 and 187 for Re, 191 and 193 for Ir and

194, 195, 196 and 198 for Pt. The mass sequence was scanned 400 times with dwell times of 45 ms on each peak. At the beginning and after the analysis of the samples an in-house HSE-standard solution and the 2% nitric acid were analyzed to monitor mass discrimination and instrumental drift and to monitor memory effects and allow for blank corrections respectively. Total chemistry blanks were subtracted and were small for Re, Ir (10 pg) and Ru (30 pg) but relatively high for Pd (300 pg) and Pt (700 pg). The mass fractionations for the sample isotopes were corrected based on an exponential mass fractionation law and the isotopic ratios of the standard.

The results for the single samples are compiled in Table 8. Due to technical problems the HSE concentrations could be obtained only for two of the four samples from glass II-1. The reproducibility for the elements in each of the glass types is very good and the respective mean values, listed in Table 9, were taken to represent the concentrations in the standard glasses. Even though only 2 - 3 aliquots were analyzed per glass type, we use the relative standard deviation (RSD in %) in Table 9 as a means to express reproducibility. The RSD is maximal with 32% for Pt in glass I-2, can reach values between 11 - 19 % for Pd, Rh or Re and is < 8 % in all other cases. Compared to the starting compositions the concentrations of the HSE strongly deviate in all four glass types, though to different extents. Except for Pt and in one case Rh, all elements have much lower concentrations in the final glasses, with Ru and Pd being affected most and Rh least. Two processes could be responsible for these depletions. While melting at 1 bar and high temperatures in air, several elements might be lost due to volatility though the degree of depletion does not correspond to the succession for reduction potentials at 1350 - 1650°C as presented by O'Neill et al. (1995). Another possibility for the loss of HSE from the silicate melt is the use of a Pt crucible. At the same time this provides a source for Pt getting massively enriched with about 50 - 60 ppm instead of 4 ppm and 90 - 119 ppm instead of 40 ppm for the respective starting compositions. However, applying the relationship reported by Fortenfant et al. (2003)<sup>a</sup>, the solubility of Pt in an anorthite-diopside melt at 1 bar, 1650°C and in air should not exceed 40 ppm after several hours of equilibration. Due to the higher temperatures and longer run times the depletion effect is much greater in the glasses of melt run II such that the concentrations of all elements except for Pt are < 0.7 ppm in glass II-1 with at least Ru getting close to the detection limit for some analytical methods. For this reason we have not further tested or used glass II-1 for any analysis. The evaluation of the other three glass types I-1, I-2 and II-2 will follow in the next section.

**Table 8:** Concentrations of the HSE's (ppb) determined with ICP-MS in aliquots of the four standard glasses and respective sample amounts.

	Sample weight (g)	Re	Ir	Ru	Pt	Pd	Rh*
<b>glass I-1</b>							
UM1	0.02223	872.9	1308	442.7	62083	1294	1351
UM2	0.03699	914.6	1331	446.2	57649	1416	1395
<b>glass II-1</b>							
UM3	0.03972	430.4	630.0	60.89	51019	130.8	397.6
UM5	0.03522	435.7	639.5	67.41	50172	168.4	500.5
<b>glass I-2</b>							
UM7	0.0158	8353	13608	4427	102922	13901	14109
UM8	0.04455	8051*	13301	4101	91559	11664	13133
UM9	0.0101	8515	13856	4476	162348	14268	18698
<b>glass II-2</b>							
UM10	0.03453	4563	8140	1068	90399	2265	5456
UM12	0.04566	3527*	8034	1002	88696	2124	5557

\* standardization via Ir and external HSE standard

### Laser Ablation Inductively Coupled Mass Spectrometry

Homogeneity with respect to the HSE distribution had been tested in the mounted chips of both run I glass compositions before the run II glasses were produced and before all glass types were analyzed with ICP-MS in Berlin. This was performed with the laser-ablation inductively coupled plasma mass-spectrometer (LA-ICP-MS) device at BGI which consists of a Coherent COMPexPRO 102 excimer laser (ArF, wavelength 193 nm) combined with a Perkin Elmer ELAN DRC-e inductively coupled plasma and a quadrupole mass-spectrometer device. A technique like LA-ICP-MS delivers relative element abundancies only, which need to be transferred into absolute values by means of an internal standard. As an internal standard, any other element in the sample (usually a major element) can be employed, of which the concentration is known from another analytical technique. Moreover, this element has to be present also in an external standard which is analyzed along with the sample (e.g. NIST 610 glass). Element concentration ratios are then calculated by comparing their intensity ratios (absolute counts) in the sample to their intensity ratios in the external standard. In the absence of certified HSE concentrations in an external standard, LA-ICP-MS can still be used to monitor the distribution of the HSE's within our glass standard, by normalizing all intensities of the HSE's to the intensity of a major element, such as Mg, which has been shown to be very homogeneous in both glasses (see RSD, Table 9). Moreover we found  $^{25}\text{Mg}$  to provide the best signal to background ratio among the major element isotopes in our glasses. Other isotopes analyzed were  $^{29}\text{Si}$ ,  $^{27}\text{Al}$ ,  $^{42}\text{Ca}$ ,  $^{101}\text{Ru}$ ,  $^{103}\text{Rh}$ ,  $^{105}\text{Pd}$ ,  $^{185}\text{Re}$ ,  $^{193}\text{Ir}$ ,  $^{195}\text{Pt}$ . For all these analyses we used a

laser energy density of 80 mJ and counting times of 30 s for the background and about 50 s for the signal. The best signals were achieved with ablation rates of 10 Hz and a pit size of 70  $\mu\text{m}$  for the low concentration glass I-1 and of 50  $\mu\text{m}$  for glass I-2. To provide a control for possible instrumental drift we used a NIST 610 glass which was ablated with a 50  $\mu\text{m}$  diameter. Both glasses were analyzed with two profiles on each chip with similar positions as for the EPMA analyses.

##### **Test of Glass I-1**

No systematic variation of the respective  $^{25}\text{Mg}$  to HSE intensity ratios has been observed along the profiles for glass I-1, but RSD's of 20-50% are in general relatively high. The signal intensities for Ru, showing the highest RSD up to 60%, are very low, corresponding to the low concentration determined for Ru with ICP-MS (Table 9). Due to this fact and to the observation that in some places the imbedded glass chip displayed larger nuggets, we decided that this glass was not suitable as a standard material for this study and have not employed it for further analyses.

##### **Test of Glass I-2**

In glass I-2 the signals for all HSE's are smooth, indicating no distinct variation that could be assigned to the ablation of nuggets, and intensities are in a well-detectable range of  $> 100$  counts per second, even for Ru. Along the profiles the absolute counts for the HSE's relative to Mg decrease towards the curved quench rims of the glass chip that had been in contact with the Pt crucible, supporting our assumption that there has been a HSE-loss during the melting process by diffusion into the crucible. In these areas the average deviation of the relative HSE-intensities from the mean value of the analysis in the centre of the chip is 120 % for Ru and ranges between 30 - 90 % for all other elements. Among the 12 analyses from the interior parts, the precision is within 8 - 17 % for all HSE. The loss of HSE seems to be limited to the contact rims with the crucible whereas at a sufficient distance of about 600 - 700  $\mu\text{m}$  from these rims, the glass shows satisfactory homogeneity to serve as a standard. As only a small amount of material had been melted and some of it was additionally consumed for the ICP-MS analyses, not many additional pieces remained. So far we have therefore used the imbedded piece of glass I-2 described here as a standard, with analyses being only taken from the central region. It has initially been employed for the LA-ICP-MS analyses of the silicate phase in five samples from the metal-silicate partitioning experiments of this study (V347, V348, Z475, Z484, Z505) before the run II glasses had been produced. Evaluating all of the 32 ( $^{25}\text{Mg}/\text{HSE}$ )-ratios then available, the maximal

relative uncertainty of the HSE in this standard ranges between 25 - 30 % for Ru, Rh, Pd, Re and 35 - 40% for Ir and Pt.

When analysing the silicates from experimental samples we had as well always included the NIST 610 glass in order to provide a standard for other elements not contained in the HSE glass standard. This involved the analysis of  $^{49}\text{Ti}$ ,  $^{53}\text{Cr}$ ,  $^{55}\text{Mn}$ ,  $^{57}\text{Fe}$  and  $^{60}\text{Ni}$ . Using NIST 610 and  $^{42}\text{Ca}$  as internal standard allowed us to test and quantify possible contaminations with these elements in glass I-2 that could have occurred during the preparation process. No Cr, Mn, Fe or Ni were detected but about 8.6 ppm Ti were determined as an average value from 18 analyses.

In addition, we have used the NIST 610 abundancies reported by Sylvester and Eggins (1997) to quantify the concentrations of Rh, Pd, Re and Pt in glass I-2. For comparison with the ICP-MS results we have listed these values in Table 9. The precision for these analyses was within 5-11%. The accuracy with respect to the ICP-MS results is within 16 - 31% for Pt, Re and Rh and 54% for Pd. We found no certified value for Ir and Ru in NIST 610 glass, but our LA-ICP-MS signals indicate that Ru is at the detection limit and based on our standard glasses the Ir concentration should be  $< 0.2$  ppm.

#### **Test of Glass II-2**

We have exclusively used one of the imbedded chips of glass II-2 for the LA-ICP-MS analysis of five of our partitioning experiment samples (V363, V364, Z538, Z541, Z544). During these analyses the entire glass chip was sampled. Again based on the  $^{25}\text{Mg}/\text{HSE}$  ratios, the precision for these 20 analyses is within 11 - 24 %. This is consistent with the precision, if concentrations of Rh, Pd, Re and Pt are quantified in this glass based on NIST 610 as described above.

The respective concentrations are listed in Table 9 and we find the accuracy to be within 4 to 27 % based on the ICP-MS analyses. The laser-ablation signals for the HSE's are quite smooth, only Pt in some cases indicates the ablation of a nugget. However, using long counting times of 50 s this levels off and does not affect the reproducibility of the Pt concentration. This glass was therefore also chosen as a standard.

Employing NIST 610 and  $^{42}\text{Ca}$  as external and internal standards, we have additionally detected low concentrations of about 3 - 17 ppm for Ni, Ti and Mn and 1083 ppm Fe, all with a high precision within 4 - 6% (see Table 9). Cr is close to the detection limit. We assume that this contamination originates from crushing and grinding the glass between the two melting steps with a steel tool which has not been performed on the run I glasses.

#### 4. Liquid Metal - Liquid Silicate Partitioning of HSE at High Pressures and High Temperatures

**Table 9:** Composition of the HSE glass standards determined by EPMA, ICP-MS and LA-ICP-MS

	glass I-1		glass II-1		glass I-2		glass II-2	
EPMA	No.= 250*		No.= 219		No.= 250		No.= 222	
wt%		RSD %		RSD %		RSD %		RSD %
SiO <sub>2</sub>	49.4	1.5	47.9	0.22	45.1	1.9	45.6	0.21
Al <sub>2</sub> O <sub>3</sub>	16.6	3.3	17.8	0.53	18.5	2.1	18.7	0.39
CaO	23.5	0.63	23.8	0.25	25.0	1.5	24.7	0.24
MgO	9.49	1.2	9.67	0.54	10.3	1.5	10.2	0.46
Total	99.0	0.38	99.2	0.16	99.0	0.32	99.3	0.12
ICP-MS	No.= 2		No.= 2		No.= 3		No.= 2	
ppm		RSD %		RSD %		RSD %		RSD %
Ru	0.444	0.55	0.064	7.2	4.33	4.7	1.03	4.5
Rh	1.37	2.3	0.449	16	15.3	19	5.51	1.3
Pd	1.35	6.4	0.150	18	13.3	11	2.19	4.6
Re	0.894	3.3	0.417	6.8	8.31	2.8	4.04	18
Ir	1.32	1.2	0.635	1.1	13.6	2.0	8.09	0.93
Pt	59.9	5.2	50.6	1.2	119	32	89.5	1.3
LA-ICPMS <sup>a</sup>					No.= 18		No.= 20	
ppm						RSD %		RSD %
Ti					8.58	9.2	9.90	6.4
Cr					l.o.d		< 3.06#	119
Mn					l.o.d		16.6	4.3
Fe					l.o.d		1083	3.7
Ni					l.o.d		2.71	4.5
Rh					10.6	8.0	3.99	16
Pd					20.4	11	2.52	11
Re					9.84	4.9	3.82	24
Pt					100.2	11	93.0	4.9

RSD relative standard deviation      No.= 250\* number of analyses

l.o.d. limit of detection      # close to detection limit

<sup>a</sup> LA-ICP-MS: concentrations determined with NIST 610 glass and <sup>42</sup>Ca as internal standard; as reference for the Rh, Pd, Re and Pt concentrations in NIST 610 the values reported by Sylvester and Eggins (1997) were used.

### Secondary Ion Mass Spectrometry

For the determination of the HSE concentrations in the quenched silicates of our experimental samples we have tested secondary ion mass spectrometry (SIMS) as an additional technique. These measurements were carried out using the Cameca ims 4f ion microprobe in the Institute of Meteoritics at the University of New Mexico in cooperation with C. Shearer and C. Agee. Employing our own glass standards gave the possibility to evaluate both the suitability of the standards combined with this technique for HSE analyses in silicate materials at low concentration levels.

Using SIMS, we observed the ionic yields for the HSE's in general to be very low as has also been reported by Righter (2005). Using an O<sup>-</sup> primary beam, the signal for all Pt isotopes is below the detection limit. To increase the sensitivity we used a relatively high accelerating voltage of 12.5 kV for the primary beam, which could be maintained for three sessions only. For the analysis of samples V347, V348, V364, Z505, Z541, Z544 in the fourth session we had to switch to 10 kV due to instrumental instability. Moreover, a primary beam current of 30 nA was employed resulting in a spot size of ~35 - 40  $\mu\text{m}$  on the sample. In order to minimize isobaric interferences, the secondary positive ions produced from the sample were filtered with an energy window of  $\pm 25$  eV before entering the mass spectrometer and measurements were performed on an offset position of 75 eV from the peaks. With these conditions the ionic yield for Ir was still extremely low so that only the relatively abundant <sup>193</sup>Ir isotope could be detected. For the other HSE's we analysed the isotopes <sup>101</sup>Ru, <sup>103</sup>Rh, <sup>108</sup>Pd and <sup>187</sup>Re. Each analysis was carried out by sampling for 2 s on two background positions and 4 s for <sup>30</sup>Si which served as internal standard. Then the single masses were scanned in 10 cycles, collecting for 30 s on each mass such that count rates could be averaged over 300 s.

Using the SIMS technique, the absolute concentrations of the elements in the unknowns are determined from calibration curves. These are defined from the count rates of the respective isotope in a standard material normalized to the count rate of the internal standard element (here <sup>30</sup>Si) multiplied by the known concentration of the internal standard (here wt% SiO<sub>2</sub>). This value is plotted against the known concentration of the element in the standard material and linear regression yields the calibration curve. In order to span a broader concentration range for data regression we have employed both glass I-2 and glass II-2. The concentrations for all elements are very low in our standards and a material with higher concentrations would have been helpful for determining more robust calibration curves. Analysing our HSE glasses, we observed some inconsistencies such that we decided to sample each of them three times per session together with the unknowns. We found that in most cases one of the analyses shows a significant deviation from the other two. One reason for this uncertainty will be the very low ionic yields, that combined with the low concentrations in the glasses, result in counting rates of  $\leq 15$  counts per second (cps) in glass I-2 and  $\leq 7$  cps in glass II-2, with only Rh exceeding 5 cps among all elements. On the other hand, the variations could also reflect a lower level of homogeneity of the

glasses when applying the SIMS technique. Compared to LA-ICP-MS the material is analyzed on a much smaller scale regarding both the excited surface area and the sampled volume such that the presence of nuggets could cause variation in the results. However, by excluding the count rates which deviate most, relatively good correlation curves could be defined that all went through the origin and had correlation coefficients  $\geq 0.95$  for Re, Ru, Pd and  $\geq 0.89$  for Rh and  $\geq 0.78$  Ir. Using these correlation curves to calculate the HSE concentrations in our glasses the deviations of single analyses can be quantified. Among the SIMS analyses we find the precision to be within 3-17% for glass I-2. In glass II-2 the precision is within 16 - 20 % for Re, Pd, Ru but 77% and 86% for Ir and Rh respectively, which could reflect their higher concentration in nuggets. The accuracy with respect to the ICP-MS values is within 3-15 % in glass I-2, and within 12-40 % in glass II-2, except for Rh (65%).

Employing an  $O^-$  beam, successful SIMS analyses for Rh and Ru in silicate materials even in the concentration range of 1 - 10 ppm, as in our HSE glasses, have been performed by Capobianco et al. (1994) and Richter et al. (2004). However, they had 'in-house' glasses from Capobianco et al. (1994) available with concentrations of up to 160 ppm Ru and 250 ppm Rh which makes the definition of the calibration curve much more precise. Employing another primary source, such as  $Cs^+$ , as used by Hervig et al. (2004) for the analysis of Au in silicates, would probably also not improve the analyses in our case as only ionic yields of Ir and Pt would increase whereas those for Pd, Ru, Rh and Re would decrease by about two orders of magnitude.

We have analysed all quenched silicates from the experiments of this study with SIMS, however, given the much longer durations (30 min per analysis), the much smaller volume sampled and the higher uncertainty for the available standards we regard SIMS as the less appropriate technique for our purpose.

## 4.3 Metal-Silicate Partitioning Experiments

### 4.3.1 Starting Materials and Experimental Setup

High pressure and high temperature experiments to study the liquid metal-liquid silicate partitioning of the highly siderophile elements Ru, Rh, Pd, Re, Ir and Pt were carried out in multi-anvil apparatus (500- and 5000-tonne presses at BGI, see chapter 1). Two isothermal series were run at 6 GPa, 2150°C and 18 GPa, 2300°C to study the effect of  $f_{O_2}$  on the partitioning behaviour of the HSE. Moreover, at 18 GPa experiments were performed covering a temperature range of 2200 - 2400°C. To provide a link to low pressure studies, one experiment was run at 3.5 GPa and 2500°C. Details of the run conditions are listed in Table 10. In all cases, samples were contained in MgO single crystal capsules of 1.6 mm outer diameter and 2.3 mm length. With the 5000-tonne press, 18/11 assemblies could be used for all experiments, providing a relatively large and constant sample volume. Combined with a stepped LaCrO<sub>3</sub> heater, the thermal gradient across the sample is then minimized. The temperature was monitored with type D W<sub>97</sub>Re<sub>3</sub>-W<sub>75</sub>Re<sub>25</sub> thermocouples. Based on these temperature readings and those of the chapter 3 study (same assemblies at 6 and 18 GPa) the temperature versus power relationship was calibrated for the employed pressures such that we could estimate the temperature in cases where it exceeded 2300 °C or thermocouples failed (for details of the temperature calibration see chapter 1 and Fig. 9). The experiments were kept for 70 - 180 s at run temperature and were quenched by turning off the electrical power to the furnace.

Starting materials consisted of 60 - 66 wt% synthetic peridotite containing about 8 wt% FeO (oxides of the major elements, Ti, Mn and Cr mixed in the proportions after Palme and O'Neill (2003) and produced as described in chapter 3) plus 34 - 40 wt% metal. The combined concentration of the HSE's (equal proportions of Ru, Rh, Pd, Re, Ir, Pt) in this Fe-alloy metal phase was varied from 47 to 90 wt%. This provided oxygen fugacities in the range of -1.3 to +2.5 log units relative to the iron wüstite buffer ( $\Delta IW$ ). Initially, we had mixed the peridotite, Fe and the single HSE metals all together as powders that were filled into the capsules (see Table 11, starting compositions D-2 and D-3). However, using mixed powders might result in incomplete metal-silicate separation and the formation of metallic micro-nuggets which could lead to an overestimation of the HSE concentrations in the silicate phase. Therefore, in subsequent experiments the HSE's were added as weighed chips of a previously alloyed metal. This HSE-alloy was also produced using multi-anvil apparatus (500-tonne press). Metallic powders of the HSE's were mixed and prepressed into a pellet (3.1 mm diameter, 2 mm length) which was directly placed in the polycrystalline MgO sleeve of a 25/17 assembly. At 4 GPa and 2100°C the metal was melted for 6 minutes. The quenched alloy was cut into tiny slices of (150 - 250  $\mu\text{m}$ ) x 500  $\mu\text{m}$  x 240  $\mu\text{m}$  size with a diamond wire saw. These chips were loaded into the centre of the MgO capsules between two layers of powdered peridotite-iron mixtures. The compositions of the respective starting mixtures are listed in Table 11.

#### 4. Liquid Metal - Liquid Silicate Partitioning of HSE at High Pressures and High Temperatures

**Table 10:** Details of the conditions of multi-anvil experiments and the Mg/Si ratio of the quenched silicate melt

run	starting comp.	capsule material	t (s)	P (GPa)	T (°C)	log $f_{O_2}$ ( $\Delta IW$ )	Mg/Si (mol%) quenched silicate melt
V364	D-2b	MgO	120	3.5	2500	-0.62	2.10
V363	D-4a	MgO	90	6	2150	-1.28	1.85
V347	D-2	MgO	90	6	2150	-0.11	1.73
V348	D-3	MgO	90	6	2150	1.44	1.78
Z544	D-2a	MgO	180	18	2200	0.02	1.28
Z538	D-4b	MgO	120	18	2300	-1.32	1.34
Z475	D-2	MgO	70	18	2300	-0.14	1.43
Z484	D-3	MgO	90	18	2300	1.45	1.36
Z541	D-2b	MgO	180	18	2400	-0.45	1.41
Z505	PM	Pt <sub>70</sub> Rh <sub>30</sub> alloy	3600	18	2200	2.48	1.25

P = pressure, T = temperature, t = run duration;  $f_{O_2}$  calculated relative to the IW buffer (see text);

MgO = MgO single crystal capsule

PM synthetic peridotite (proportions after Palme and O'Neill, 2003):

wt%: 45.80 SiO<sub>2</sub>, 37.09 MgO, 4.53 Al<sub>2</sub>O<sub>3</sub>, 3.68 CaO, 8.17 FeO, 0.22 TiO<sub>2</sub>, 0.37 Cr<sub>2</sub>O<sub>3</sub>, 0.14 MnO

**Table 11:** Starting compositions of the metal-silicate partitioning experiments

HSE added as:	mixed powders		alloyed chips			
	D-2	D-3	D-2a	D-2b	D-4a	D-4b
metal contains						
wt% HSE	75	90	76	71	57	47
<b>wt%</b>						
SiO <sub>2</sub>	27.48	27.48	27.25	29.40	28.37	30.42
MgO	22.26	22.26	22.07	23.81	22.98	24.64
Al <sub>2</sub> O <sub>3</sub>	2.72	2.72	2.70	2.91	2.81	3.01
CaO	2.21	2.21	2.19	2.36	2.28	2.45
FeO	4.90	4.90	4.86	5.25	5.06	5.43
TiO <sub>2</sub>	0.13	0.13	0.13	0.14	0.13	0.14
Cr <sub>2</sub> O <sub>3</sub>	0.22	0.22	0.22	0.24	0.23	0.25
MnO	0.08	0.08	0.08	0.09	0.08	0.09
Fe	10.00	4.00	9.69	10.45	16.52	17.71
Ru	5.00	6.00	5.13	4.22	3.59	2.65
Rh	5.00	6.00	5.13	4.22	3.59	2.65
Pd	5.00	6.00	5.13	4.22	3.59	2.65
Re	5.00	6.00	5.13	4.22	3.59	2.65
Ir	5.00	6.00	5.13	4.22	3.59	2.65
Pt	5.00	6.00	5.13	4.22	3.59	2.65

Additionally, we performed one experiment to study the solubility of Pt and Rh in silicate melt at 18 GPa and 2200°C. The same synthetic peridotite as for the other experiments was equilibrated in a Pt<sub>70</sub>Rh<sub>30</sub> sample container. This was fabricated from a commercially available thermocouple alloy that was welded to beads, equilibrated for 3 h at 1200°C and hammered into a capsule dia of 1.2 mm diameter. The little rod of 1.4 mm length was spark eroded to drill a 500 µm diameter inner hole and lids were cut from the same material with a diamond wire saw. The experiment was run with the same 18/11 mm multi-anvil setup as the 18 GPa experiments described above. At 2200°C, the conditions were above the peridotite liquidus and below the Pt<sub>70</sub>Rh<sub>30</sub>-alloy melting temperature. As the Pt-solubility study of Ertel et al. (2006) has shown, the chosen run time of 60 minutes should be sufficient to attain equilibrium at such high temperatures when employing a relatively small sample volume.

### 4.3.2 Run Products and Analytical Techniques

During the HSE-partitioning experiments between silicate and metal melts, the latter phase separates and forms several spheres that vary in abundance and size. Typical examples of run products where a single metal blob has formed are displayed in the BSE images of Figs. 38 a - b. Both metal and silicate show heterogeneous textures that developed during the quench process. The silicates recovered from experiments at ≤ 6 GPa are dominated by elongated, skeletal olivine crystals with a low FeO content. As the example of Fig. 39 shows, the interstitial regions between the olivines consist of a brighter silicate phase in the centre, enriched in Ca and Al and a metallic phase that is concentrated along the boundaries of the olivine crystals. We interpret this as a quench phenomenon and assume that this metal had been dissolved in the silicate melt prior to the quench. In the 18 GPa experiments the texture of the silicate is finer and the interstitial spaces between the MgO- and SiO<sub>2</sub>-rich quench crystals (Fig. 38b) cannot be properly resolved with SEM imaging. In all cases the MgO capsule has reacted with the silicate melt releasing small patches of ferropericlasite especially in experiments run at high temperature (Fig. 38a). In some cases these patches accumulate in form of a rim around the big metal blobs.

The quenched metal melts display various textures (2 - 50 µm scale) including coarse zoned grains (Fig. 40a), dendritic crystals and lamellae (Fig. 40b). In the metal blob of sample Z484 an unusual internal structure is preserved comprising many single cells that might be interpreted as isolated convection cells (Fig. 40c). In several metal blobs an accumulation of spherical holes with diameters up to 1 µm can be observed that are reminiscent of the metal texture described in chapter 3. However, in this HSE study we could not identify any filling except for sample Z484 where we detected a composition typical of the silicate melt using the EDX device of the SEM. In several experiments some metal is trapped between the silicate quench crystals. These areas were avoided in the analyses with large laser-ablation pits.

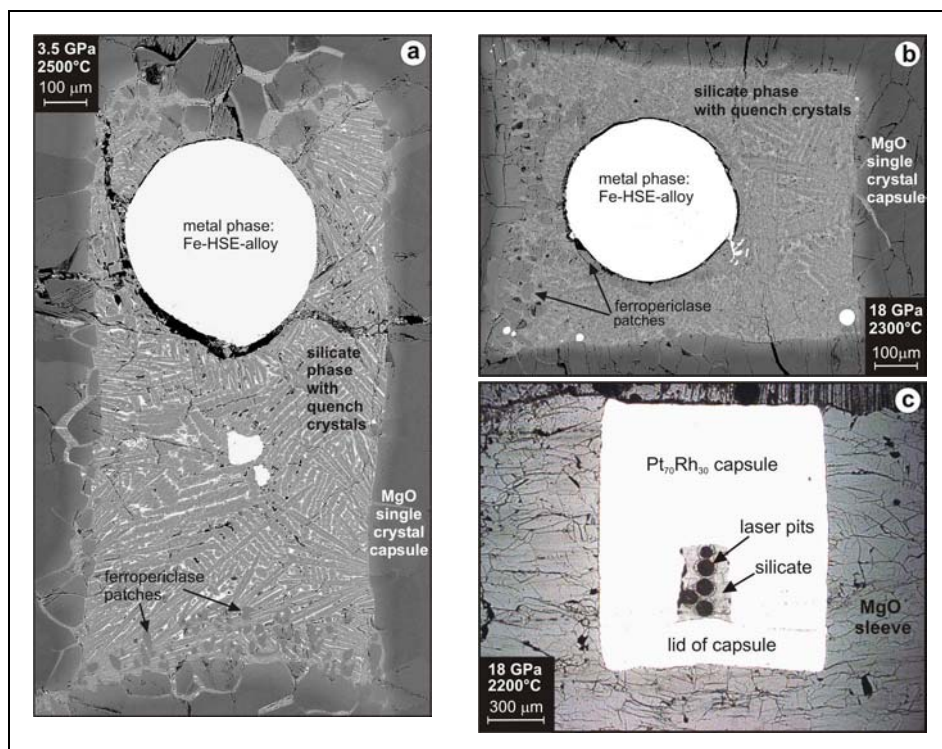


Fig 38: Sections through recovered capsules from various experiments. The run conditions are indicated in the respective images. BSE images of run products from the liquid metal-liquid silicate partitioning experiments: (a) sample V364 and (b) sample Z475. At run conditions the metal melt forms a sphere shaped blob. On quenching, large crystals have developed in the silicate phase. In experiments at  $\leq 6$  GPa, these are olivine laths that have a length up to  $100 \mu\text{m}$  (a). The MgO capsules in (a) and (b) have reacted with the silicate melt. (c) Reflected light image of the run product from the Pt-Rh-solubility study (sample Z505). The metal capsule stayed intact and only the silicate phase was molten in this experiment. Silicate quench crystals are not visible at this magnification scale. Black circles mark the position of the LA-ICP-MS analyses.

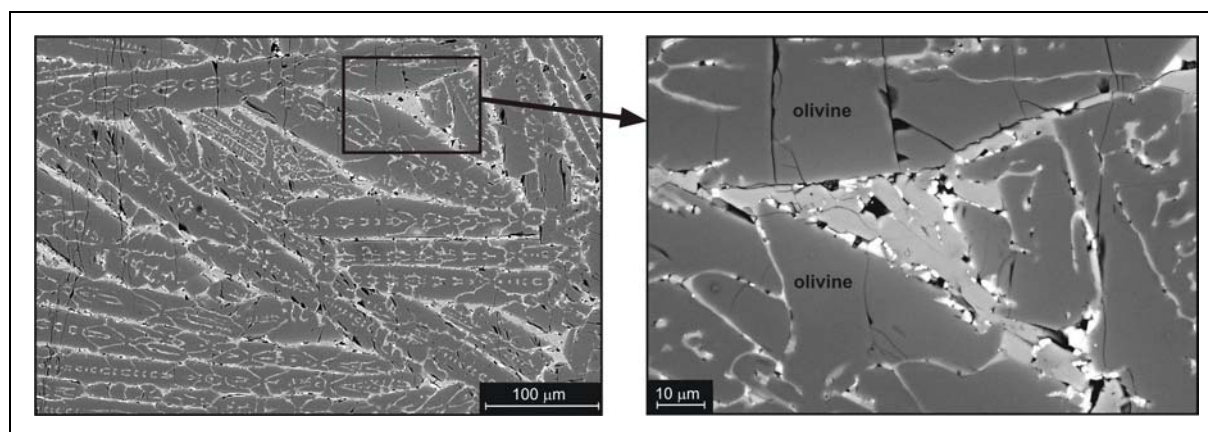


Fig. 39: Detail of the quenched silicate phase in sample V348, run at 6 GPa, 2150°C, in which large skeletal olivine crystals have formed. The magnified section on the right side shows an interstitial pocket between the olivines where the bright grey phase is enriched in Ca and Al. The white phase is metal that is considered to have been dissolved in the silicate liquid at high pressure and temperature.

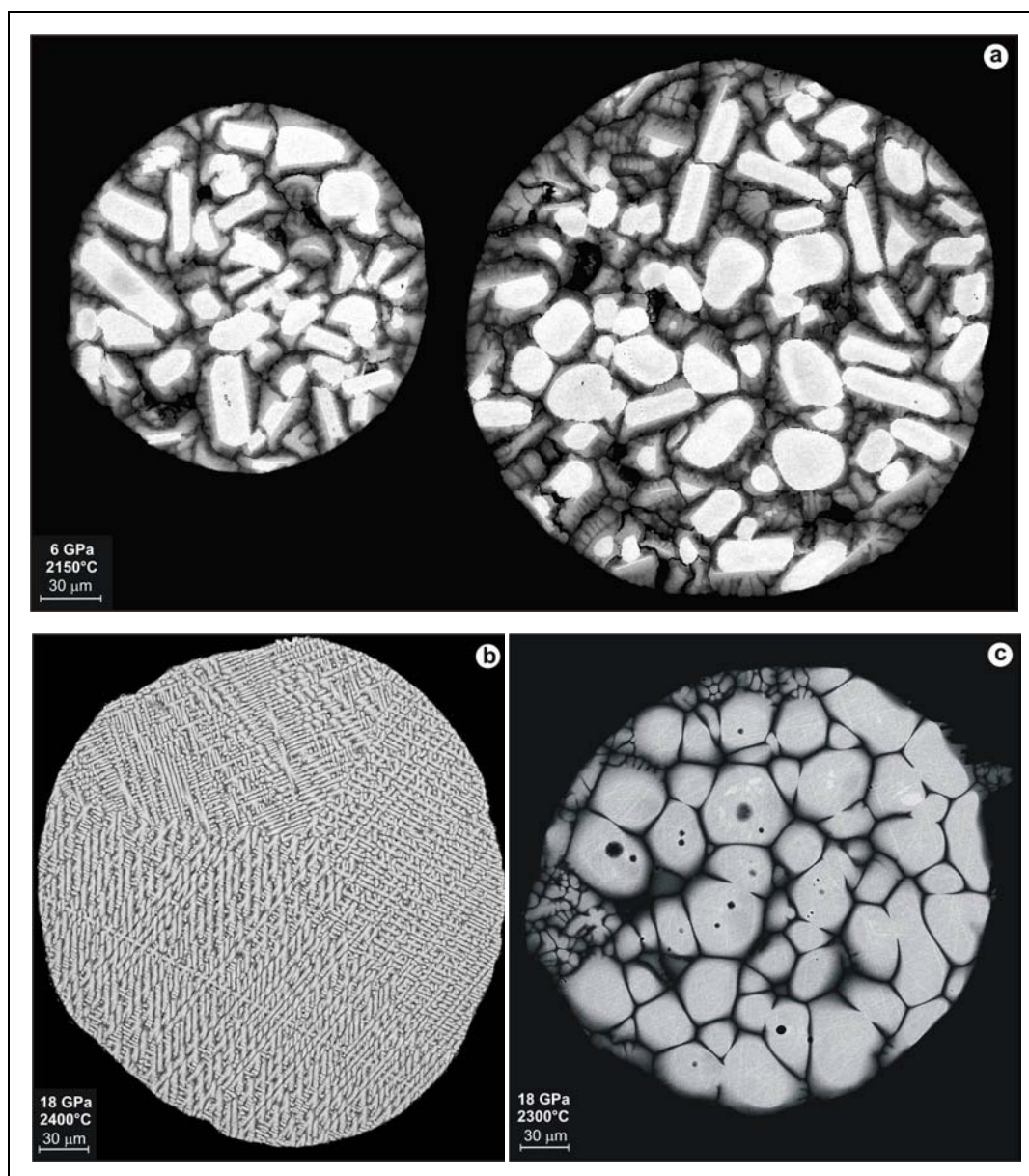


Fig. 40: Various quench textures in the metal blobs. The respective run conditions are indicated in the images. (a) Two big metal spheres have formed next to each other in sample V348, both displaying a very coarse texture with zoned grains. (b) The single big blob in sample Z541 shows a finer and more regular quench pattern. (c) This exceptional texture, reminiscent of convection cells, has only developed in the big blob of sample Z484.

A reflected light image of the run product of the Pt-Rh-solubility experiment is shown in Fig. 38c. The metal capsule is intact and shows no sign of melting whereas the filling displays a quenched silicate melt containing some dendritic crystals. The black circles in the silicate part mark pits from the laser beam which had a diameter of 50-70  $\mu\text{m}$ .

### Electron Microprobe Analysis

In the quenched samples the metal compositions as well as the major element compositions of the silicates were determined with EPMA (facility at BGI, see above). For both phases the accelerating voltage was 20 kV and the probe current was 20 nA for all analyses.

For the metals, we employed the respective pure metals as standards and peak counting times of 20 s for Fe, 40 s for Ru, Rh, Re, Ir, Pt and 60 s for Pd. Additionally, we analyzed for Si, Mn and Cr counting for 150 s on the peak position and using andradite,  $\text{MnTiO}_3$ , and pure Cr standards. For samples V347, V348 and Z475, O was included in the measurement (40 s,  $\text{MgO}$  standard).

Analyzing materials with EPMA that contain almost all of the HSE's is complicated: as some of the HSE's have quite similar atomic masses, several peak interferences occur. The elements Ru, Rh and Pd are restricted to analysis of the L-series signals on the PET crystal where  $L\alpha$  and  $L\beta$  peaks of several orders overlap with each other. The flank and positive background of the Rh  $L\alpha$  peak is slightly overlapped by the first order Ru- $L\beta$  peak but a very large overlap of first order Rh  $L\beta$  and Pd- $L\alpha$  peaks excludes both of them for analysis (Fig. 41). Measuring with the Rh  $L\alpha$  peak a value of 2.3 wt% Rh was calculated, repeatedly analyzing the pure Ru standard. However, from the degree of overlap this seems to be rather high as an interference of the Rh  $L\alpha$  peak in the negative flank part with a second-order Cr  $K\alpha$  peak produced only about 0.2 wt% Rh in the pure Cr standard (Fig. 41). We therefore assume that our Ru standard might be not 100% pure but contains some Rh. However, considering the coarse quench textures of our samples the possibly resulting error will be within the analytical uncertainties.

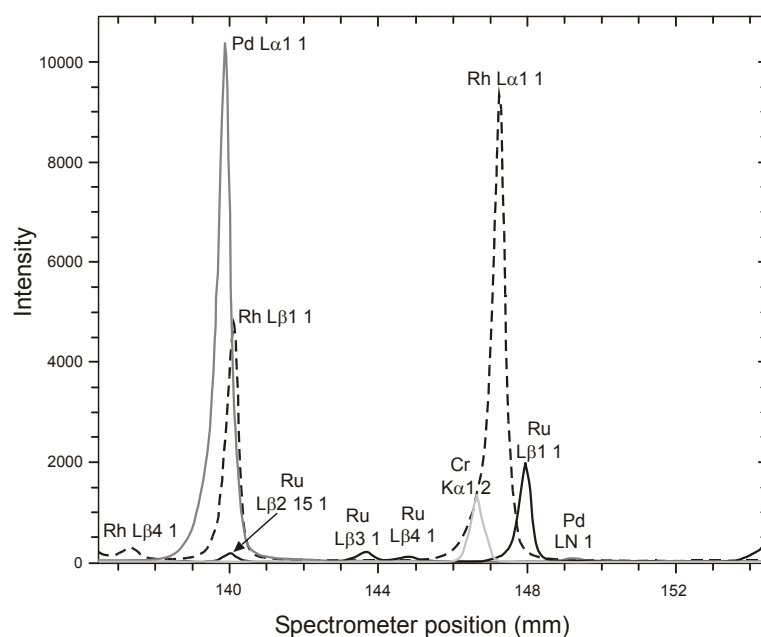


Fig. 41: Wavelength dispersive X-ray spectra for Ru, Rh and Pd on PET crystal with EPMA

For Pd we had to use the  $L\beta$  peak. This is still not an optimal solution as it is interfered by a higher order Rh  $L\beta_2$  peak resulting in about 0.4 wt% Pd analyzed in the pure Rh standard. As this comprises a rather small error we ignored it for the present analysis. However, as the intensity of the Pd  $L\beta$  peak is only about half that of the Pd- $L\alpha$  peak we increased counting times to 60 s compared to 40 s for the other HSE's (all  $L\alpha$  peaks). For the pure Rh standard repeated analyses always detected about 2.8 wt% Fe. As there is absolutely no interference of any Rh peak on the Fe- $K\alpha$  position we conclude that the Rh standard is not pure. This was confirmed with a high resolution peak-scan on the standard. For the following measurements we corrected for this Fe content. For Re and especially Ir and Pt analyzed on a LIF crystal the positions of the  $L\alpha$  peaks are also quite close to each other but are still distinct enough to be properly resolved.

For each sample all of the larger metal blobs present in a section were analyzed as slight compositional variations had been detected with EDX scan analyses. Because of the coarse quench textures in the metals (Fig. 40), a defocused electron beam (20-30  $\mu\text{m}$  diameter) was used and single analysis points were set along rectangular grids with an average edge length of 100 - 200  $\mu\text{m}$  such that some overlap of the excited areas occurred. The average of such grid analyses should then reflect the bulk composition of the metal blob. However, the compositional variation among single analyses from samples with extremely-coarse quench patterns e.g. the grain structure in Fig. 40a, can be extremely high. Taking the standard deviation of such a population would certainly not reflect the analytical and compositional uncertainty for the metal. In order to estimate the errors in such cases we have therefore divided the analyses in groups of 4-6 and determined the standard deviation among the mean values for the individual groups, which by representing a larger area, should deliver a more integrated value for the bulk metal composition. The Pt-Rh-capsule of sample Z505 was analyzed with a focused electron beam along the rim in contact with the sample charge. Details of all analyzed metal compositions are listed in Table IV of the appendix.

For analyses of the silicate phase we have employed peak counting times of 20 s (Si, Mg, Al, Ca, Fe) and 100 s (Mn, Cr, Ti) and MgO, spinel, andradite,  $\text{MnTiO}_3$  and pure Fe and Cr as standards. In all cases the electron beam was defocused (30  $\mu\text{m}$ ) and coarse textured samples from experiments at  $\leq 6$  GPa were covered with several grids (150  $\mu\text{m}$  average length), in the same manner as described for the metals, in order to equally include large olivines and interstitial phases. The results are presented in Table V of the appendix together with the LA-ICP-MS and the SIMS trace analyses. Errors for the EPMA values are given as two standard deviations which in the case of analyses along grids were determined as explained above.

Additionally, we determined ferropericlase (Fp) compositions with EPMA (peak counting times: Mg, Ca 20 s; Si, Al, Fe 60s; Mn, Cr, Ti 60-180s; standards as for the silicates) results of which are listed in the appendix Table VI. The analyses were taken from Fp patches in contact

with the metal blobs and from the diffusion zones along the capsule rims in contact with the sample charge.

#### **Laser Ablation Inductively Coupled Mass Spectrometry**

The concentrations of the HSE's in the quenched silicates were determined with LA-ICP-MS. Details of the operating parameters and the instrumental setting are given in section 4.2.2 where the LA-ICP-MS analysis of the glass standards is described. The samples of this study were analysed in two sessions for the isotopes  $^{29}\text{Si}$ ,  $^{27}\text{Al}$ ,  $^{25}\text{Mg}$ ,  $^{42}\text{Ca}$ ,  $^{57}\text{Fe}$ ,  $^{49}\text{Ti}$ ,  $^{53}\text{Cr}$ ,  $^{55}\text{Mn}$  and for the HSE's  $^{101}\text{Ru}$ ,  $^{103}\text{Rh}$ ,  $^{105}\text{Pd}$ ,  $^{185}\text{Re}$ ,  $^{193}\text{Ir}$ ,  $^{195}\text{Pt}$ . For the first session we used our glass I-2 as HSE-standard for the samples V347, V348, Z475, Z484, Z505, in the second we employed glass II-2 for the samples V363, V364, Z538, Z541, Z544. In all cases  $^{25}\text{Mg}$  served as an internal standard to correct for ablation yields and instrument sensitivity over the course of a single analysis. Additionally, a NIST 610 glass standard was included for all measurements. Samples were analysed in separate blocks each consisting of 4-5 analyses of the quenched silicate and starting and ending with two analyses of the NIST 610 glass and of one of our HSE-doped glasses. In the first session, the pit diameter and the ablation rate were 50  $\mu\text{m}$  and 10 Hz for both the NIST 610 glass and glass I-2 and 70  $\mu\text{m}$  and 5 Hz for the samples. For the second session we used 70  $\mu\text{m}$  and 10 Hz for the NIST 610 glass, 80  $\mu\text{m}$  and 10 Hz for glass II-2, and 80  $\mu\text{m}$  and 15-20 Hz for the samples.

Signals were collected over 40 - 50 s, following 30 s of background measurement. In several samples the count rates for Ru and Ir are quite low, ranging between 100-300 cps, corresponding to low concentrations of < 0.1 ppm. In samples V364 and Z538, Ir is below the detection limit which is set as three times the standard deviation for the background. Ru is also close to the detection limit in Z538 and for one or both elements the uncertainties are higher in samples V363, V347, Z544 such that their concentrations might be overestimated in these silicates. In general, signals from the first session, in which the samples where the HSE's had been added as powders in the starting material (see Tables 10 and 11), are less steady, sometimes displaying tiny spikes for all elements which become more emphasized in the signals of Pt, Ru and Ir at low concentrations. This variation is strongest for sample Z484. Whether this can be assigned to metallic relics not fully separated from the silicate is difficult to judge in samples displaying coarse multi-phase quench textures. One should also note that the laser repetition rates of 5 Hz might have been too low for those samples. Tests on samples in the second session had shown that, especially for the elements with low concentrations, even 10 Hz might not be enough and that the signals were much more constant when increasing the rates from 10 to 20 Hz.

The results we obtained for the HSE concentrations in the silicates are listed in Table V of the appendix. Uncertainties on the values are given as one standard deviation. As a quality check for the results obtained by using our HSE-doped glasses as standards, we also determined the concentrations of Re, Pd, Pt and Rh of the NIST 610 glass for each sample block. The values reported by Sylvester and Eggins (1997) are reproduced within 15% for the higher concentrated Re (~ 50 ppm) and within 20 - 40% for Pt (3.15 ppm), Pd (1.05 ppm) and Rh (1.31 ppm). Employing glass II-2 in the second session, more accurate results for the NIST 610 glass were achieved than with glass I-2. This could also be related to the larger pit diameter used in the second session for the NIST 610 glass which is more appropriate for low concentrations.

Additionally, we have determined the concentrations of Rh, Pd, Re and Pt in our sample silicates based on these NIST 610 abundancies of Sylvester and Eggins (1997) using  $^{42}\text{Ca}$  as internal standard. In general they are in good agreement with the other results (employing our standard glasses), attaining better results when using the larger pit diameter in the second session. For comparison we have listed these values in Table V (appendix) together with the concentrations for Ti, Cr and Mn which were as well standardized with NIST 610 and  $^{42}\text{Ca}$ .

#### **Secondary Ion Mass Spectrometry**

Except for Pt, the quenched sample silicates were additionally analysed for the HSE's with SIMS using the device and operating conditions as described in chapter 4.2.2 for the glass standards. Because of the long counting times we could collect three analyses per sample only. In most cases one analysis deviates strongly from the other two, resulting in high relative standard deviations. On the one hand this can be assigned to the low number of analyses, insufficiently representing the bulk silicate composition as the 40  $\mu\text{m}$  spot size does not cover the coarse quench textures especially in the case of the  $\leq 6$  GPa samples. Additionally, as discussed above, in samples where the concentrations for most of the HSE's are even lower than in our standard glasses, the SIMS technique is not sensitive enough and will deliver erroneous data. This is especially the case for very low abundances of Ru and Ir. For the latter, the standard calibration curve is also less well defined, resulting in constant values of 5-7 ppm for all samples which is much higher than values from LA-ICP-MS measurements. Only for samples with higher HSE concentrations of  $\geq 5$  ppm (V348, Z475, Z484) do the SIMS results become more comparable with the LA-ICP-MS data. To illustrate this, we have included the SIMS results for our samples in Table V (appendix).

### 4.3.3 Results

#### Calculation of the oxygen fugacity

The oxygen fugacity in our experiments was derived using the relationships of equations 7-9 as explained in chapter 3. However, the experiments of this study were performed at much higher oxygen fugacities than those of chapter 3 and as Fe is not the dominating constituent of the alloy ( $X_{\text{Fe}} = 0.14-0.67$  in the partitioning experiments, 0.03 in the Pt-Rh solubility study) the activity of Fe cannot be regarded within the scope of "Raoult's Law". Thus, the term of equation [10] has to be modified to include the activity coefficient for Fe in the metal  $\gamma_{\text{Fe}}$ :

$$\Delta IW = 2 \log \left[ \frac{X_{\text{FeO}}^{\text{Fp}}}{X_{\text{Fe}}^{\text{metal}} * \gamma_{\text{Fe}}^{\text{metal}}} \right] + \frac{2 W_{\text{FeMg}}^{\text{Fp}} (1 - X_{\text{FeO}}^{\text{Fp}})^2}{RT \ln 10} \quad [10-1]$$

From the literature there is not much data available on the thermodynamic parameters for Fe in HSE-bearing alloys, especially not for multi-component systems, although several of the binary Fe-HSE systems have been studied. To obtain an estimate for  $\gamma_{\text{Fe}}$  in our experiments we have tested some values from such binaries. Applying the equation of Heald (1967) from his study of the thermodynamics of solid Fe-Pt alloys yields quite low values of 0.003 - 0.49 for  $\gamma_{\text{Fe}}$  in the metals of our partitioning experiments and is most extreme with 0.0005 in the Pt-Rh metal capsule. The  $\gamma_{\text{Fe}}$  values, calculated from the excess free energy terms for mixing in liquid metals on the Fe-Ir and the Fe-Rh binaries (Schwartzendruber, 1984<sup>a,b</sup>), are very similar to each other: 0.05 - 0.64 in the Ir-system and 0.06 - 0.67 in the Rh-system over the  $X_{\text{Fe}}$  range of the partitioning experiments and in both cases 0.03 for sample Z505. Therefore, we decided to use the data from the liquid Ir-binary system to be representative for calculating  $\gamma_{\text{Fe}}$  in our mixed HSE-Fe melts. Moreover, we have extrapolated the relationship determined from Schwartzendruber, 1984<sup>a</sup> to our experimental run temperatures as the iron activity coefficient should increase with temperature. Inserting the respective values in equation [10-1] yields a range of -1.3 to +2.5 log units relative to the iron wüstite buffer ( $\Delta IW$ ) for the oxygen fugacities in our experiments. For comparison, without any activity correction for Fe we would obtain values of -1.8 to 0.1  $\Delta IW$  whereas using temperature corrected data from the solid Pt-system would give a range of -1.2 to +4.3  $\Delta IW$ .

### Metal-silicate Partition Coefficients - Dependence on Oxygen Fugacity

The partitioning of the HSE's between the liquid metal and the silicate melt can be regarded on the basis of the redox equilibrium given by equation [6], if the HSE's are present as ions in the silicate melt. Applying equation [12], the HSE partition coefficients  $D$  for our experiments can be determined from the respective molar metal to silicate concentration ratios. As equation [13-1] shows, at a fixed pressure and temperature these partition coefficients are not only a function of oxygen fugacity but also depend on the activity coefficients  $\gamma$  of each element and its oxide in the respective melts. For very low HSE concentrations (ppm) in the silicate melt, infinite dilution and constant activity coefficients can be assumed. For the HSE-rich metal melts however, "Henry's Law" is not valid and the  $\gamma_M^{\text{metal}}$  values depend on the concentrations of the elements. On the other hand, regarding conditions relevant for the accretion of the Earth, core-forming alloys will have contained HSE's on the ppm-level only. Thus, in order to regard realistic values of  $D^0$  on the basis of such an infinite dilution behaviour of the HSE's in the metal with a constant activity coefficient  $\gamma_M^{0, \text{metal}}$ , our experimentally determined  $D^{\text{exp.}}$  values would have to be corrected for the respective activity coefficient ratio using the following equation:

$$\log D^0 \frac{\text{metal}}{\text{silicate}} = \log D^{\text{exp.}} \frac{\text{metal}}{\text{silicate}} + \log \left[ \frac{\gamma_M^{\text{metal}}(X_M)}{\gamma_M^{0, \text{metal}}} \right] \quad [29]$$

At high concentrations of  $M$ ,  $\gamma_M^{\text{metal}}$  depends on the mole fraction  $X_M$  of the element in the metal and both activity coefficients are a function of temperature. As mentioned above, there is not much thermodynamic data available for HSE-rich alloys and such corrections cannot easily be performed. In general,  $X_M$  is, in addition, a function of oxygen fugacity and both  $X_M$  and  $\gamma_M^{\text{metal}}$  would increase with increasing  $f_{O_2}$  such that the necessary correction for  $D^{\text{exp.}}$  is not constant but increases with  $f_{O_2}$ . However, over the relatively small  $f_{O_2}$  range of our partitioning experiments, the variation of  $X_M$  for each of the HSE's is not large (0.02 - 0.12 for Re, Ir, Pt and 0.06 - 0.20 for Ru, Rh, Pd) and consequently  $\gamma_M^{\text{metal}}$  will not change very much either. Therefore, even though our experimental partition coefficients are significantly shifted from the values of  $D^0$ , we regard this deviation to be constant over the studied  $f_{O_2}$  range and  $D^{\text{exp.}}$  should display the same dependence on oxygen fugacity as  $D^0$ , expressed with equation [13-2], but with a different value for the intercept on the  $\log D$  axis.

The  $D$  values for our experimental metal compositions are compiled in Table VII of the appendix, the uncertainties are derived from the standard deviations of the respective concentrations and the propagation of the error on calculating  $D$ . In the diagrams of Fig. 42 the  $\log D$  values are plotted against the relative  $\log f_{O_2}$  and results are distinguished by pressure, regardless of temperature. Based on equation [13-2], the  $\log$  values of the partition coefficients should show a linear correlation with oxygen fugacity, if the measured HSE concentrations in the

quenched silicates result from material that has been dissolved in the silicate melt at run conditions. In this case the valence of the HSE cation can be derived from the slope of the correlation trend. However, the valence of an element might change over a studied  $f_{O_2}$  range and decrease towards more reducing conditions, resulting in flatter slopes. Therefore, partition coefficients might be overestimated when extrapolating from experimental conditions towards a redox range more realistic for core formation ( $\leq -2 \Delta IW$ ). Moreover, a valence change within a studied range of oxygen fugacities might be hidden, if it results from the simultaneous presence of cations with different valences as discussed by Borisov et al. (1994). It might also be possible that some HSE's become stable as neutral metal atoms at low oxygen fugacities. The independency of D and  $f_{O_2}$  in this case might not be distinguishable from a saturation value caused by the presence of metallic nuggets in the silicate melt at low redox conditions.

Previous studies performed at 1 bar and employing solid pure metals usually determine the solubility of the HSE in the silicate melt, rather than the partition coefficient, as a function of oxygen fugacity. This is defined as the logarithmic value of the mole fraction of a HSE in the silicate phase, and can be derived from equations [12] and [13-1] as:

$$\log X_M^{\text{silicate}} = \frac{n}{4} \Delta IW + \log \left[ X_M^{\text{metal}} * \gamma_M^{\text{metal}}(X) \right] + \text{const.} \quad [30]$$

In most cases, the mole fraction is transformed into weight fraction or into concentration in ppm by weight which only changes the constant term at the end of equation [30] (Borisov et al., 1994). Although, strictly speaking, the activity of the element in the metal  $a_M^{\text{metal}} = X_M^{\text{metal}} * \gamma_M^{\text{metal}}(X)$  is not constant, we can regard it as being approximately constant over the  $f_{O_2}$  range in our experiments as discussed above. For comparison, we have also plotted the HSE solubilities, using ppm (weight) concentrations on a logarithmic scale as a function of  $f_{O_2}$  relative to the IW buffer (Fig. 43) and we discuss the observed trends together with those of the partition coefficients.

#### 4. Liquid Metal - Liquid Silicate Partitioning of HSE at High Pressures and High Temperatures

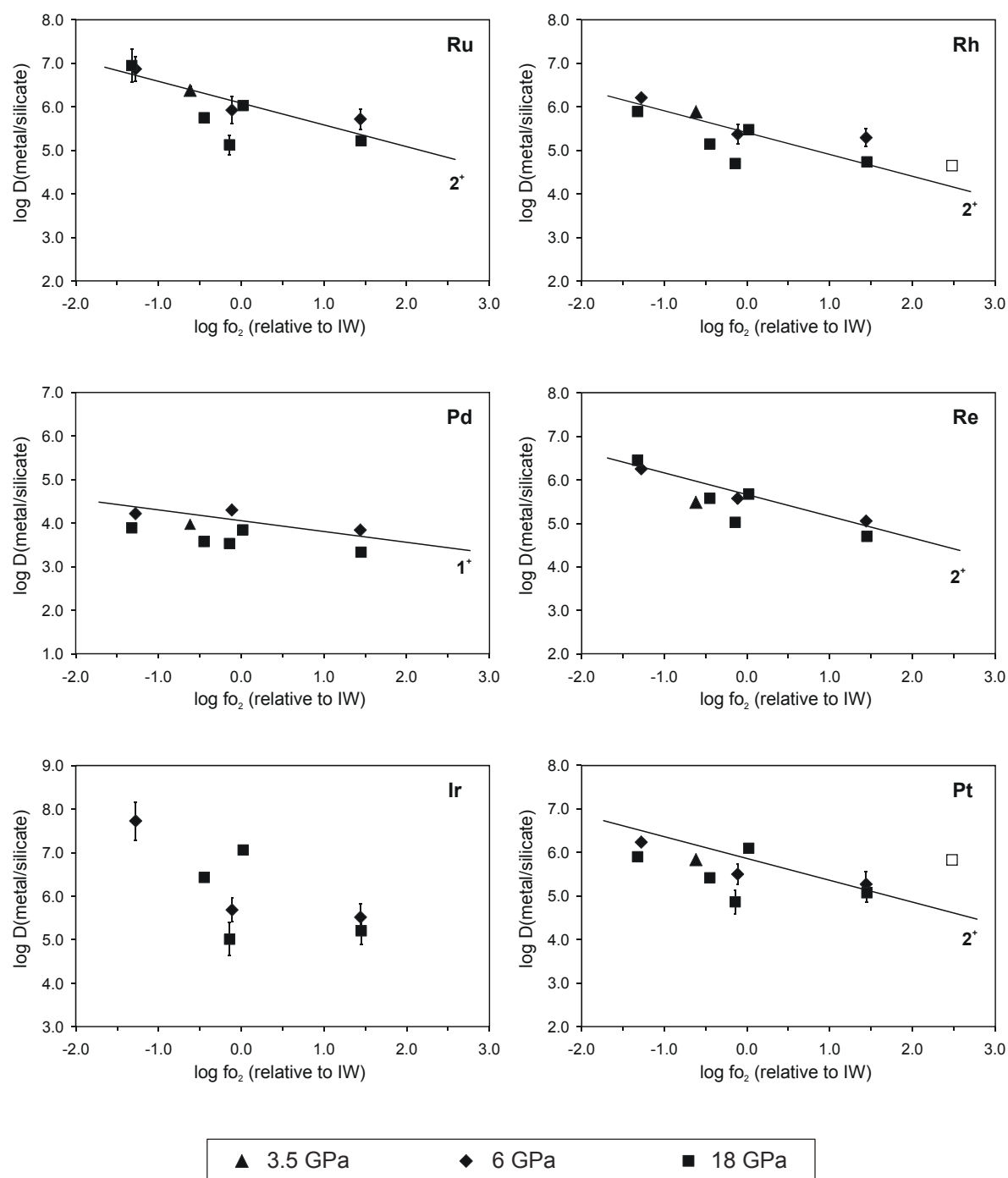


Fig. 42: Liquid metal-liquid silicate partition coefficients ( $D$ , mol% basis) for Ru, Rh, Pd, Re, Ir and Pt plotted as a function of relative oxygen fugacity ( $\Delta IW$ ), as logarithmic values. The oxygen fugacity has been corrected for  $\gamma_{\text{Fe}}$  in the metal but no corrections have been applied for the activity coefficients of the HSE's in the metal on calculating  $D$  (compare equation [29]). The unfilled squares for Rh and Pt are the results from the solubility experiment Z505 at 18 GPa. Where no error bars are shown the uncertainties do not exceed the symbol size. Results are not distinguished by temperature which ranges from 2150 to 2500 °C. Indicated lines show the valence ( $n^+$ ) trend most likely for the respective element (see equation [13-2] and text).

#### 4. Liquid Metal - Liquid Silicate Partitioning of HSE at High Pressures and High Temperatures

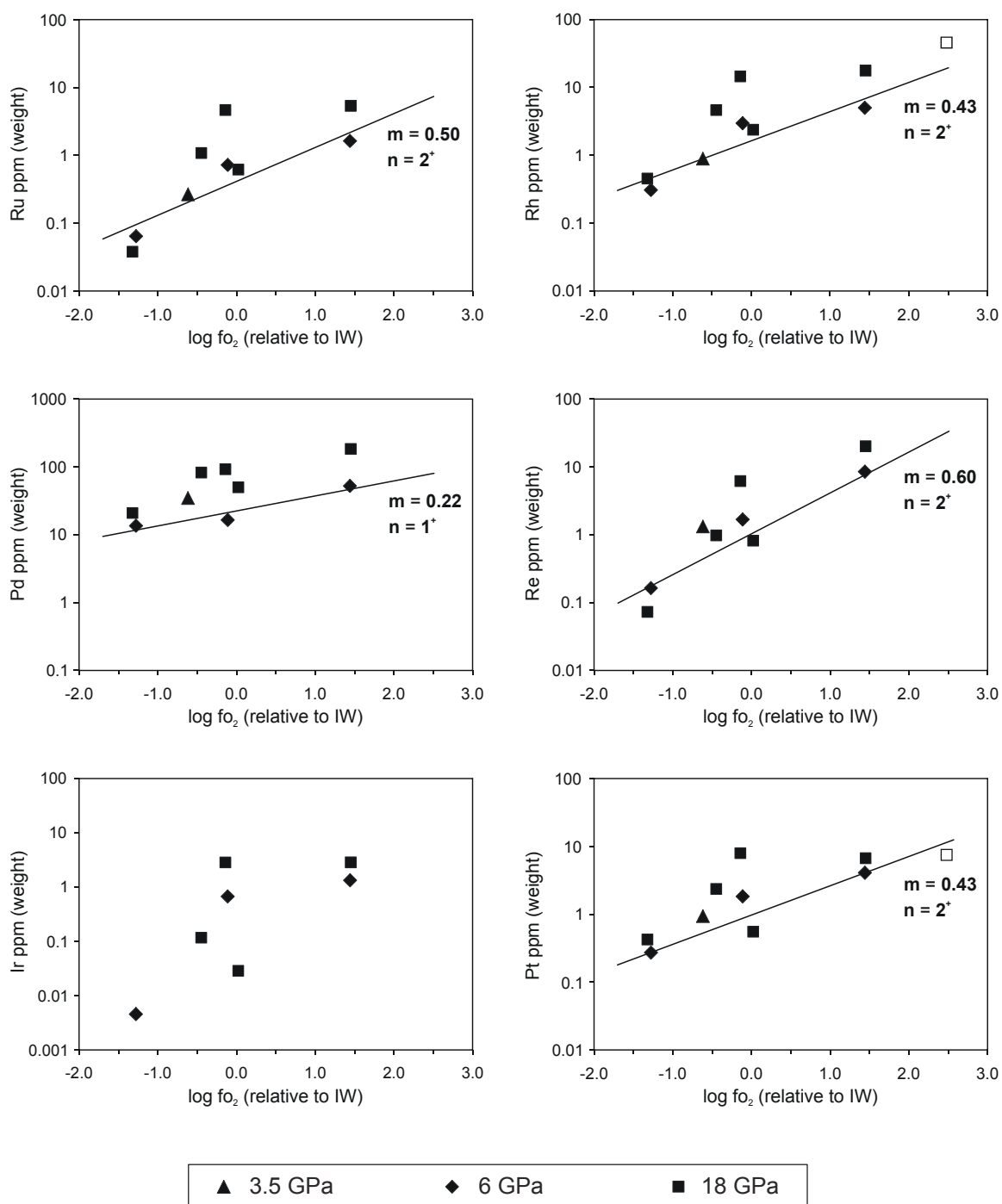


Fig. 43: Solubilities of Ru, Rh, Pd, Re, Ir and Pt (in wt ppm) in peridotitic silicate melt as a function of relative oxygen fugacity ( $\Delta IW$ ), as logarithmic values. The oxygen fugacity has been corrected for  $\gamma_{Fe}$  in the metal but no corrections have been applied for the activity coefficients of the HSE's in the metal on calculating the solubility (compare equation [30]). The unfilled squares for Rh and Pt are the results from the solubility experiment Z505 at 18 GPa. Where no error bars are shown the uncertainties do not exceed the symbol size. Results are not distinguished by temperature which ranges from 2150 to 2500 °C. The lines are fitted trends for the experiments at 6 GPa and 2150°C. The valence of the respective element is defined by  $n = 4*m$  (slope) and is discussed in the text.

In both cases a linear correlation with oxygen fugacity is observed for all elements except for Ir. From separate regressions of the 6 GPa, 2150°C and the 18 GPa, 2300°C data, the valence for each element was derived. In the diagrams showing the partition coefficients (Fig. 42) the lines indicate the ideal slope for the assumed valence  $n$ , whereas in the solubility diagrams (Fig. 43) the fitted trends for the results at 6 GPa and the obtained slopes ( $m$ ) are shown. As an average from both fitted parameters ( $D$  and  $X$ ) and each pressure, we obtain  $2^+$  for Ru, Rh, Re and Pt and  $1^+$  for Pd. Minor uncertainties for fitting these data include the exact activity correction for  $f_{O_2}$  and the possible shift of the trends towards higher  $f_{O_2}$  as discussed above. Another uncertainty arises from the fact that from the data we use for regression, two of three results at each pressure are from experiments where the HSE had been added as metal powders (see Tables 10 and 11). Sample Z475 (18 GPa), at an oxygen fugacity of -0.14, deviates most strongly from the likely trends for all HSE's and we assume that their concentration in the silicate is overestimated due to the presence of some metallic material that was not fully separated from the silicate. As a result, the determined partition coefficient is too low. We regard this uncertainty, especially for the 18 GPa series, to be responsible for less clear results for the valence as in case of Re (average 2.4), Rh (average 1.7), Pt (average 1.5) and Ru (2.3 - 2.9 at 18GPa), rather than the presence of a mixed valence species. For all HSE's we have rounded to the nearest integer number and the results are generally in good agreement with the 1 bar literature data, although Borisov and Nachtweyh (1998) reported  $3^+$  for Ru at higher oxygen fugacities and lower temperatures. For Re a valence of  $1^+$  to  $2^+$  is derived by O'Neill et al. (1995) and Richter and Drake (1997) while Ertel et al. (2001) observed  $4^+$ . Like Ertel et al. (1999) and Fortenfant et al. (2003)<sup>a</sup> we assume  $2^+$  for Rh and Pt for further calculations, although  $1^+$  and even 0 have been discussed for Pt in context with the nugget issue by Cottrell and Walker (2006). For Pd our trend is very flat and data regression yields  $1^+$  though the slope might level off to 0 at oxygen fugacities lower than the IW buffer. As such a flattening of the trend does not show for the other elements it is unlikely that is caused by nuggets. Neutral Pd atoms in the silicate melt have also been discussed by Borisov et al (1994), but in accordance with these authors and given the uncertainty of the data we regard  $Pd^{1+}$  as the likely dominating species. The data for Ir show a large scatter that results from very low concentrations of Ir in the silicate melt that are close to the detection limit in several samples (Fig. 43 and appendix Table V). Additionally, the highest concentrations occur in the four samples using powdered HSE starting material, and seem to be independent of  $f_{O_2}$  thus supporting the assumption of an incomplete separation of the metal in these samples. A valence value could therefore not be derived for Ir. At oxygen fugacities  $< +2 \Delta IW$ , previous studies at 1 bar found  $1^+$  (Borisov and Palme, 1995).

### Effect of Pressure and Temperature on the HSE Partitioning Behaviour

As in the study of chapter 3, we derived the influence of pressure and temperature on the metal-silicate partitioning behaviour of the highly siderophile elements relative to iron, by using the distribution coefficient  $K_D$  as defined by equation [4]. In general, this avoids extrapolation to oxygen fugacities relevant for core formation as our experiments have been performed at much higher redox conditions, provided the valence does not change to a lower value. Additionally, regarding equation [14] for the relationship of  $\log K_D$ , even if we assume  $\gamma_M^{\text{metal}}$  to show only a small variation over the studied redox range,  $\gamma_{\text{Fe}}^{\text{metal}}$  is not constant and can cause a scatter of the data at fixed P and T conditions. Moreover, to obtain distribution coefficients  $K_D^0$  valid for infinite dilution of the HSE's in the liquid metal and representative for a core-forming alloy, the experimentally determined values  $K_D^{\text{exp.}}$  would have to be corrected for the metal activity coefficients in a way analogous to the partition coefficient correction with the following relationship:

$$\log K_D^0 = \log K_D^{\text{exp.}} + \log \left[ \frac{\gamma_M^{\text{metal}}(\mathbf{X}_M, T)}{\gamma_M^{0, \text{metal}}(T)} \right] - \log \left[ \gamma_{\text{Fe}}^{\text{metal}}(\mathbf{X}_{\text{Fe}}, T) \right]^{\frac{n}{2}} \quad [31]$$

However, in order to test whether pressure and temperature have a significant effect on the partitioning of the HSE's, it is sufficient to regard the uncorrected  $K_D^{\text{exp.}}$  values only. This should also be the case for comparing the relative behaviour of the HSE's, as we assume that the ratio of the HSE activity coefficients between experimental compositions and at infinite dilution does not change significantly among the individual elements. We have tested this for Ir and Rh with the respective Fe-binary data for each  $\gamma_M^{\text{metal}}$  from Schwartzendruber (1984)<sup>a,b</sup> and for  $\gamma_{\text{Rh}}^{0, \text{metal}}$  and  $\gamma_{\text{Ir}}^{0, \text{metal}}$  from Fortenfant et al. (2003)<sup>a</sup> and O'Neill et al. (1995) respectively and found negligible differences of  $\leq 0.15$  log units over the temperature and compositional range of our experiments.

Our  $\log K_D^{\text{exp.}}$  values are displayed as a function of inverse temperature in the diagrams on the left side of Figs. 44-a and 44-b. As not many data on HSE's are available from the thermodynamic data base in the literature, employing 1 bar free energy data of the endmember exchange reactions for an estimation of the  $K_D$  temperature dependence as performed in the study of chapter 3 is more difficult in this case. Some data on the HSE oxides can only be found in Barin (1989), though most of them are for higher valence states that are not relevant for the redox range of this study ( $\text{RuO}_2$ ,  $\text{Rh}_2\text{O}_3$ ,  $\text{ReO}_2$ ,  $\text{IrO}_2$ ). As we found most of the HSE's to be present as  $2^+$  in our study, we have used the free energy data for PdO as a reference for fitting the  $K_D$  temperature trend. In the  $\log K_D$  vs.  $10000/T$  diagrams of Fig. 44, the  $K_D$  value at 3.5 GPa deviates significantly from the group of 6-18 GPa data, indicating a weak pressure effect in the latter range but a larger pressure effect at low P. We have therefore used all data from the

6 - 18 GPa pressure range for data regression, applying the thermodynamic relationship of equation [18], but fitting the effect of temperature only:

$$\log K_D^{\text{Fe-M}}(T) = a + \frac{b}{T} \quad [18-1]$$

The values we obtained for the parameters  $a$  and  $b$  are listed in Table 12. One should note that these are parameters for fitting our experimental  $K_D^{\text{exp}}$  values, not for  $K_D$  at infinite dilution. The slopes  $b$  for the temperature dependence are very close to the 1 bar free energy trend of PdO (listed in Table 12 for comparison) for all elements. The fitted trends are indicated with the lines in Figs. 44a and 44b. As discussed above, these trends should in principle be comparable with the trends for each  $K_D^0$ . We observe a decrease of  $K_D$  with increasing  $T$  for all elements.

	<b>a</b>	<b>b</b>
Ru (2+)	0.71	9841
Rh (2+)	0.13	9791
Pd (1+)	-0.77	9791
Re (2+)	0.25	10035
Pt (2+)	0.40	9791
Pd (2+) 1 bar free energy fit	2.08	9791

**Table 12:**

Fitted parameters for the thermodynamic relationship of equation [18-1] describing the T-dependence of  $K_D$  for the HSE under conditions of this study and for Pd<sup>2+</sup> at 1 bar (based on data from Barin, 1989)

As mentioned above, the Ir concentration in the silicate is most likely overestimated in the samples using metal powders as starting material, which results in much lower values for  $K_D$  compared to the other samples. With this high uncertainty for the dataset we did not determine a temperature trend for Ir. However, in order to be able to compare the Ir  $K_D$  relative to the other elements we have also plotted the Ir data in Fig. 44b as a function of inverse  $T$ . The three highest values should be representative for the  $K_D^{\text{exp}}$  and, as a reference for the possible T-slope, the free energy curve for PdO is shown and is consistent with the two points at 18 GPa. We therefore assume a negative temperature trend for Ir, quite similar to the other elements.

Based on the above derived temperature relationships we have corrected our experimental  $K_D$  values for all elements, except for Ir, to a common temperature of 2200 K. The results are displayed as a function of pressure in the diagrams on the right side of Figs. 44a and 44b. In the temperature plots described above, the  $K_D$  values from the two isothermal series at 6 and 18 GPa show a relatively large variation for most elements. This can be related to the above described shift resulting from  $\gamma_{\text{Fe}}^{\text{metal}}$  being not constant over the  $f_{\text{O}_2}$  range and might be accentuated for the samples where powdered metals were employed in the starting materials. In order to avoid any uncertainty that could arise from comparing data from different oxygen fugacities, only data from a restricted  $f_{\text{O}_2}$  range close to that of the 3.5 GPa sample have been included in the diagrams showing pressure dependence.

#### 4. Liquid Metal - Liquid Silicate Partitioning of HSE at High Pressures and High Temperatures

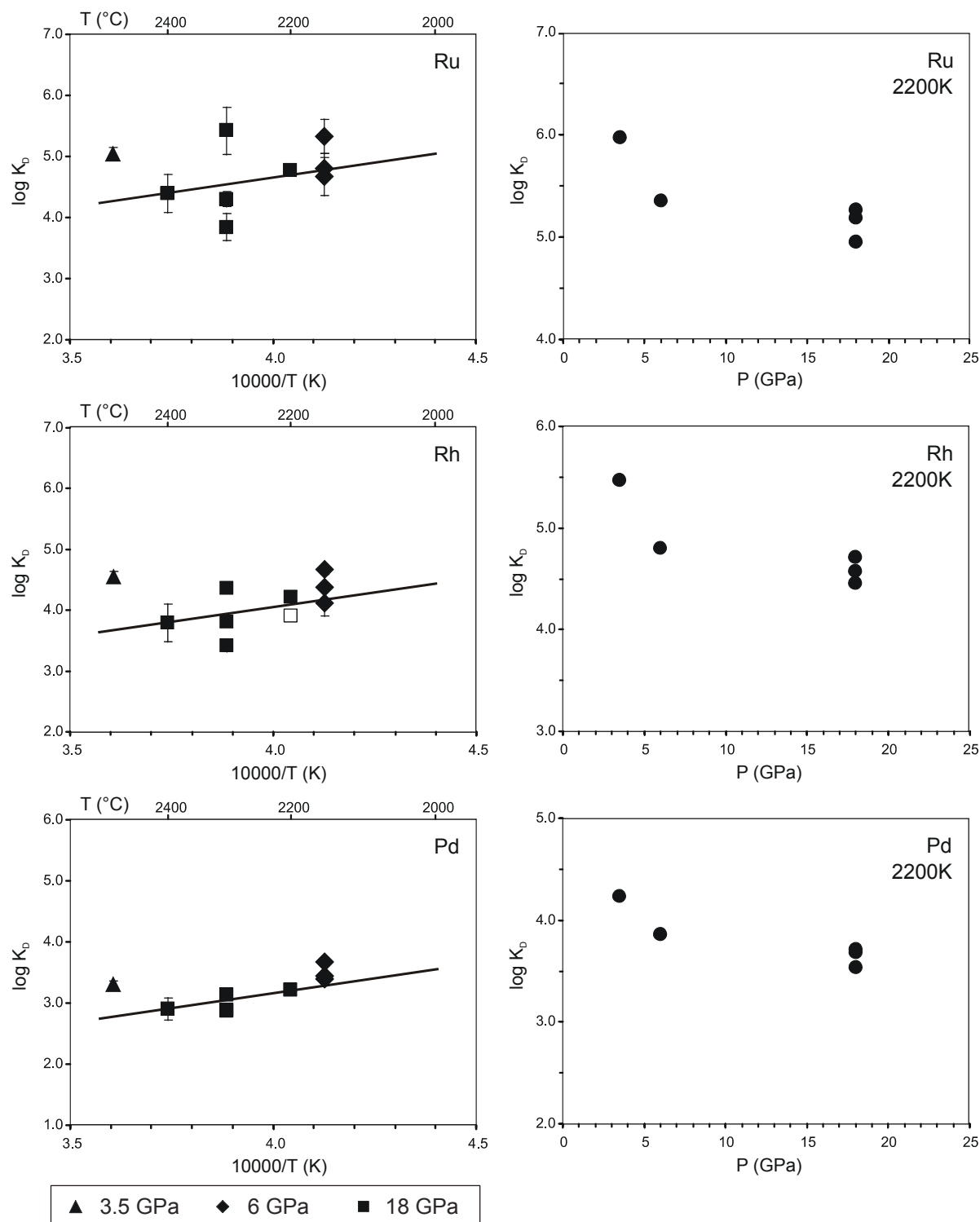


Fig. 44a: The logarithmic values of the distribution coefficients ( $K_D$ ) of Ru, Rh and Pd plotted in diagrams on the left side as a function of inverse  $T$  ( $10000/T$ ). Where no error bars are shown the uncertainties do not exceed the symbol size. The unfilled square for Rh is from sample Z505 (18 GPa). The lines indicate the temperature trends as derived from data regression in the range of 6 - 18 GPa (see text). In diagrams on the right side the  $K_D$  values from experiments in the range of  $-0.62$  to  $+0.02$   $\Delta IW$  were corrected to 2200 K and are plotted as a function of  $P$ .

#### 4. Liquid Metal - Liquid Silicate Partitioning of HSE at High Pressures and High Temperatures

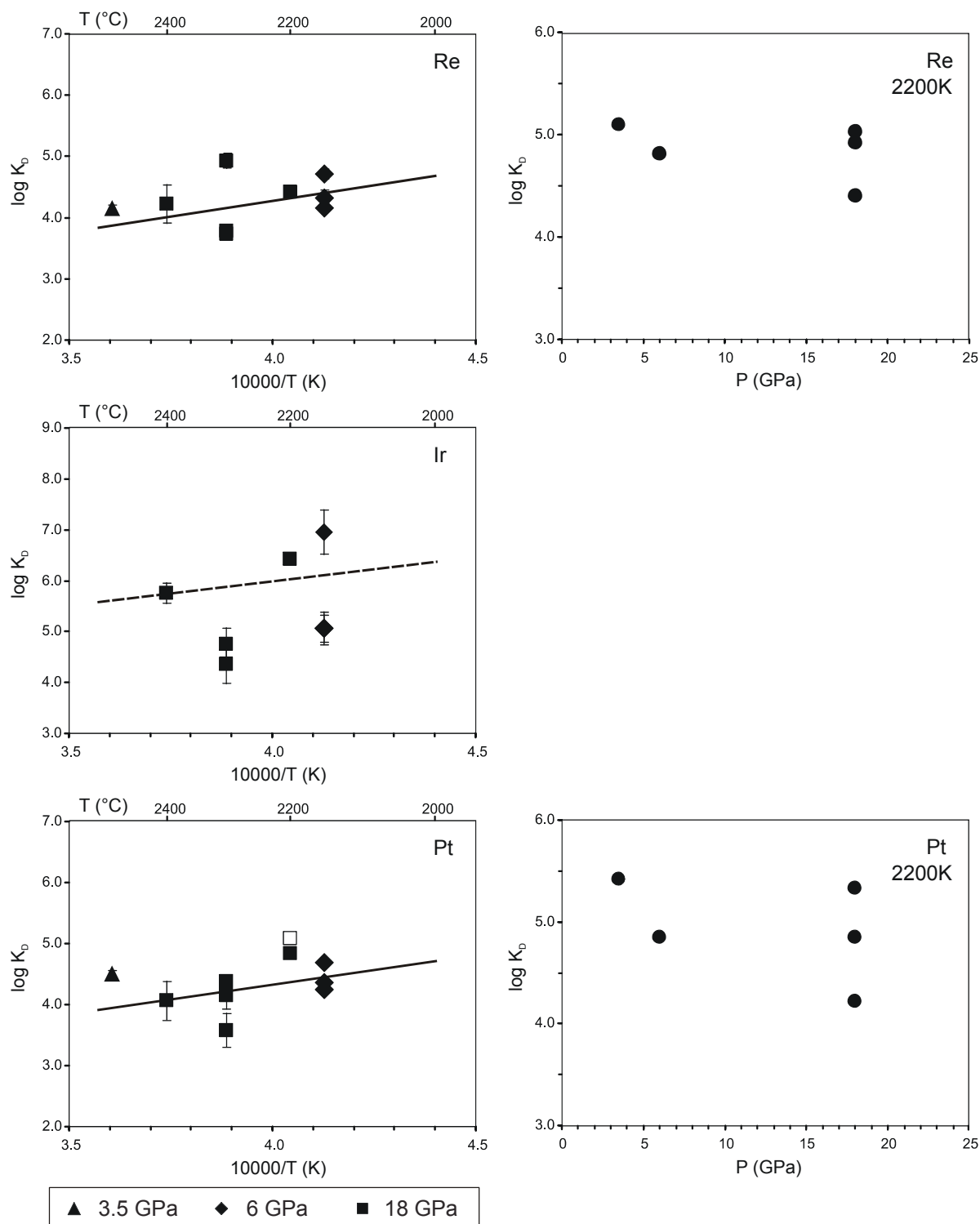


Fig. 44b: The logarithmic values of the distribution coefficients ( $K_D$ ) of Re, Ir and Pt plotted in diagrams on the left side as a function of inverse  $T$  ( $10000/T$ ). Where no error bars are shown the uncertainties do not exceed the symbol size. The unfilled square for Pt is from sample Z505 (18G Pa). For Re and Pt the lines indicate the temperature trends as derived from data regression in the range of 6 - 18 GPa (see text). For Ir no data regression was possible, but the line shows the 1 bar free energy trend for PdO for comparison. In diagrams on the right side the  $K_D$  values from experiments in the range of  $-0.62$  to  $+0.02 \Delta IW$  were corrected to 2200 K and are plotted as a function of  $P$ . As a lack of data, this was not possible for Ir.

The same general pressure trend can be observed for all elements, with  $K_D$  decreasing towards higher pressures and displaying different slopes above and below  $\sim 6$  GPa, such that the effect is much stronger at low pressures. In the range of 6 - 18 GPa,  $K_D$  decreases only weakly. Such a pressure dependence of the partitioning behaviour with a distinct change at about 5 GPa strongly resembles that observed for the siderophile elements Ni and Co, as reported recently by Kegler et al. (2007). Their partitioning data of Ni and Co seem to indicate that the molar volume for the respective redox exchange reaction with Fe (equation [1]) is not constant but changes with pressure. According to Keppler and Rubie (1993), this can be related to a coordination change for Ni and Co in the silicate melt that occurs with increasing pressure.

With only few data available so far, we have not quantified the P-effect. Moreover, it would be helpful to include the 1 bar data from the literature as the major change seems to occur at pressures  $< 6$  GPa. However, this is not possible without correcting our data for the Fe and HSE metal activity changes. As previous studies at 1 bar have involved maximum solubility experiments employing pure HSE metals ( $\gamma_M^{\text{metal}} = 1$ ) only, partition coefficients can easily be transferred into  $D^0$  values if the HSE activity coefficients for infinite dilution are known (compare equation [29]). Moreover, in the 1 bar experiments, the silicate composition is often Fe-free or even alkali-rich and silicate melt composition might also influence partitioning in these experiments, which makes the results difficult to compare with those of the present study in which a more realistic peridotitic melt composition has been employed. However, the effect of silicate melt composition will be small compared to the effects of the liquid metal composition, especially as the former mainly affects elements with high valence states  $\geq 4^+$  (Thibault and Walter, 1995).

As the necessary thermodynamic parameters for Rh are available, we use this element to demonstrate the effect of activity corrections and for comparing our data with 1 bar data from the literature. For the latter we use the T-dependent relationships for solubility and  $\gamma_{\text{Rh}}^{0, \text{metal}}$  as reported by Fortenfant et al. (2003)<sup>a</sup>. The values for  $\gamma_{\text{Rh}}^{\text{metal}}$  and  $\gamma_{\text{Fe}}^{\text{metal}}$  were calculated for the liquid metal from the parameters of the Fe-Rh binary determined by Schwartzenruber (1984)<sup>b</sup> and extrapolated to our experimental temperatures. In Fig 45a our corrected  $\log K_D$  values (calculation based on equation [31]) are shown as a function of inverse temperature together with the trend at 1 bar. The latter is much higher than our highest value at 3.5 GPa and we have used its slope to determine the temperature dependence for our corrected data. The parameters for the fitted trend are  $a = -3.37$  and  $b = 20637$  (equation [18-1]) with the slope being much steeper than the one obtained from the PdO free energy trend (compare Table 12). Using the new temperature relationship we have again corrected all data to 2200 K and the results are presented in Fig. 45b as a function of pressure (black symbols). For comparison the  $K_D^{\text{exp.}}$  values, uncorrected for activities and using the mean value for data at 18 GPa, are additionally shown in this diagram (unfilled symbols). This confirms that the principal pressure trend is present even in

the uncorrected data. Including the 1 bar result of Fortenfant et al. (2003)<sup>a</sup> (grey symbol) gives strong support for the steep pressure effect that we observe with our corrected dataset at  $P \leq 6$  GPa.

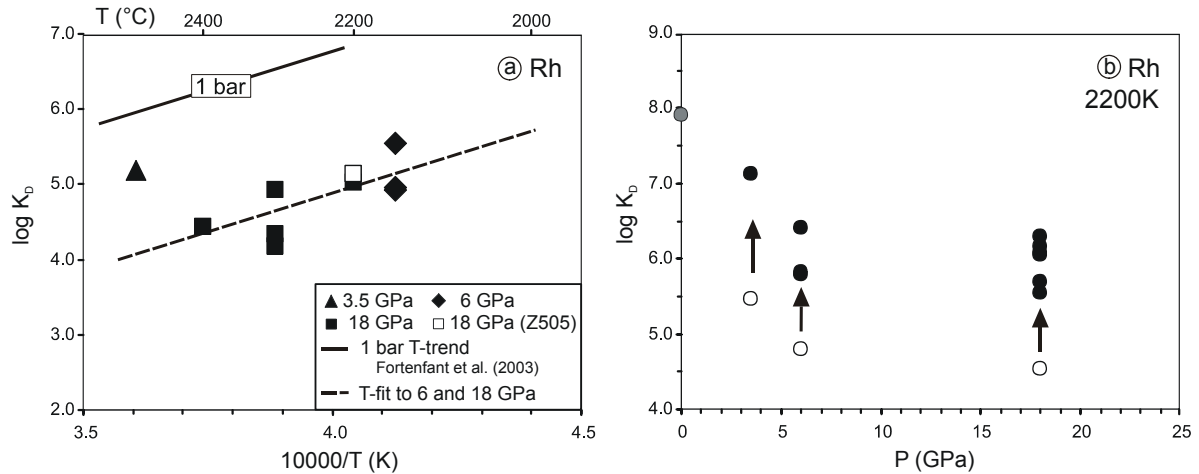


Fig. 45: The logarithmic values of  $K_D$  for Rh (corrected for activities of Rh and Fe in the metal melt) as a function of (a) inverse T ( $10000/T$ ) and (b) pressure after correcting to 2200K (black symbols). In both diagrams 1 bar data from Fortenfant et al. (2003)<sup>a</sup> are included (grey symbol in (b)). For comparison, our experimental  $K_D$  values, uncorrected for metal activities are shown in (b) with the unfilled symbols; the arrows indicate the effect of correction.

As mentioned above, for comparing the partitioning behaviour of the HSE relative to each other it is not necessary to correct to the  $K_D^0$  values. In Fig. 46 we show the pressure dependence of our experimental  $K_D$  values corrected to 2200 K together in one diagram. In all cases we use the mean value for the three results at 18 GPa in this diagram. As reported in the literature (Borisov and Nachtweyh, 1998) Ru has an extremely low solubility in the silicate melt and consequently displays the highest  $K_D$  values among the HSE presented here. Only Ir, not shown in Fig. 46 because of the uncertainties discussed above, would have a distinctly higher  $K_D$  by about 1 - 2 orders of magnitude. Pd on the contrary shows the highest solubility and over the whole pressure range the  $K_D$  values are about 1 order of magnitude lower than for the other elements. The  $K_D$  values of Pt, Re and Rh are relatively similar and differ by less than 0.5 log units which is within the range of uncertainty regarding the relatively large scatter for Pt and Re in Fig. 44b. All elements display a steeper pressure trend for  $P \leq 6$  GPa which is most extreme for Ru and Rh.

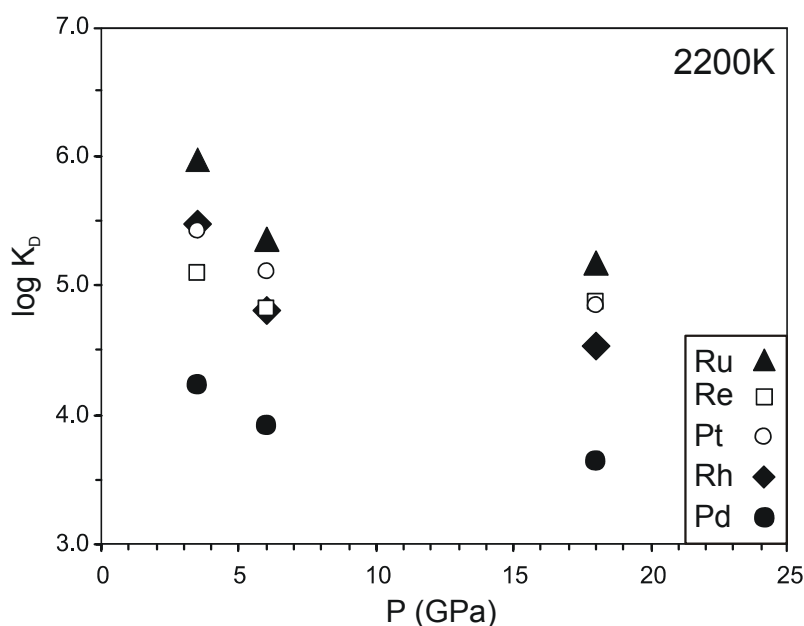


Fig. 46: Comparison of the pressure dependence of the  $K_D$  values of Ru, Rh, Pd, Re, Pt corrected to 2200K. Compositional effects on the metal activity coefficients were not corrected for.

#### 4.4 Summary and Conclusions

Studying the metal-silicate partitioning behaviour of highly siderophile elements at high pressure and high temperature yields several experimental and analytical difficulties compared to lithophile and weakly siderophile elements. The number of previous studies in this field is limited and microbeam techniques have not yet been routinely used for multi-HSE bearing silicate materials at concentration levels of a few ppm. An additional problem has been the availability of suitable standards. Our study has shown that LA-ICP-MS technique, unlike SIMS, delivers reproducible results for all elements of interest including Pt, although for the elements Ir and Ru, with the lowest solubilities in silicate melts, the detection limit is reached at concentrations of  $\sim 50$  ppb. Employing large pits of 80  $\mu\text{m}$  diameter and relatively high ablation rates of 15-20 Hz improves the signal quality and sensitivity for all elements. When producing silicate glass standards, it is probably not possible to fully avoid the formation of tiny, nm-sized metallic nuggets, though we could show that on the scale of the volume sampled with LA-ICP-MS homogeneity is reasonable.

In order to overcome the nugget problem, we have shown that using pre-alloyed chips as starting material for the HSE's helps in avoiding the incomplete separation of metal from silicate in comparison to samples in which metal powders had been employed. In the latter case, HSE concentrations in the quenched silicate melt can be overestimated and results show a relatively

large deviation from the linear trends in plots of solubility or partition coefficient versus oxygen fugacity. The observation of linear trends in these plots, even at oxygen fugacities as low as  $-1 \Delta IW$ , provides strong evidence for a lack of nuggets in the silicate melt. In the quenched silicates of our samples, we observe various metallic phases in the interstitial fields between large skeletal olivine crystals which we interpret to have formed on quench. With the EDX device of our SEM we could detect the presence of all HSE's in such grains. However, the resolution of this method is not high enough to quantify their composition and thus determine if they are different from the large metal blobs. In order to confirm the results we have obtained so far, especially before deriving P-T-trends for the partitioning behaviour of the HSE's, the experiments in the  $f_{O_2}$  range where we have only data from samples starting with powdered material should be repeated using pre-alloyed chips.

Partition coefficients that are determined from experiments as performed in this study, generally involve concentration levels that are higher than concentrations that are realistic for core formation. In order to obtain the absolute D values for infinite dilution, results would first have to be corrected for the difference in the activity coefficients for all metals involved. Knowledge of the correct  $\gamma_{Fe}^{metal}$  value is essential for the correct calculation of oxygen fugacity and thus deriving the correct valence state of the HSE's which will, in turn, influence  $K_D$ . Testing the values obtained from the Fe-Ir and Fe-Rh binary systems has shown that they are very similar and probably representative enough considering the other uncertainties. For comparison with the partition coefficients at 1 bar, determined from previous solubility studies, as well as for deriving actual trends for the pressure and temperature dependence that could be extrapolated to  $P > 25$  GPa and  $T > 2000$  °C, relevant for metal-silicate equilibration in a deep magma ocean, the activity coefficients of the HSE's at both infinite dilution and for metal concentrations as employed in our experiments need to be known. Using the temperature trends derived from 1 bar studies would then reduce the uncertainties for our temperature trends that arise from a lack of appropriate data in the thermodynamic data base. Currently we do not have the thermodynamic parameters for all the elements. However, the corrections performed with values from the Fe-binary system for Rh have shown, that the principal T- and P-trends are already defined by the uncorrected data and that correction results in a more or less constant shift of the data.

As the aim of this study was to test whether high temperatures and especially high pressures drastically change the partitioning behaviour of the HSE observed at 1 bar, it is sufficient to consider only the uncorrected data. The overall trend we observe in the range 3.5 - 18 GPa and 2150 - 2500 °C is that the partition coefficients for the HSE's decrease with increasing temperature and increasing pressure. At a fixed pressure the decrease of  $K_D$  over a temperature range of 200 °C is  $\leq 1$  log unit. Regarding the pressure effect on  $K_D$  at a constant temperature of 2200 K, two pressure regimes can be distinguished. At low pressures  $K_D$  decreases strongly, whereas above 6 GPa the trend becomes much weaker. Regarding the corrected data, the

example of Rh has shown that although its  $K_D$  decreases by about 2 orders of magnitude from 1 bar to 18 GPa, it still has a value at 18 GPa that corresponds to a partition coefficient on the order of  $10^5 - 10^6$ . Given the weak pressure dependence between 6 and 18 GPa, one can assume that the partition coefficients will not decrease strongly when extrapolating to  $P > 25$  GPa. This shows that it is important to have detailed information over a large pressure and temperature range, even at low pressures that might not seem to be directly relevant for core formation. In the case of Ni and Co, which show  $K_D$ -pressure trends that are similar to those of the HSE's, Kegler et al. (2007) have shown that extrapolation of low-P results to high pressures results in an overestimation of the P-effect in the high pressure range and misinterpretations with respect to possible core-mantle equilibration scenarios.

Even though we have not quantified partition coefficients for infinite dilution, we can conclude that the negative pressure and temperature effects are not high enough to effectively decrease the partition coefficients of the HSE's to explain their relatively high mantle abundances by a single stage equilibration in a deep magma ocean. Additionally, even though the partition coefficients of some of the HSE's are converging at 18 GPa, Pd and Ir still deviate strongly from the other elements, to much lower and higher values respectively, and given the weak pressure dependence, this relative behaviour will most likely be preserved at  $P > 20$  GPa. We therefore conclude that a mechanism other than high-pressure, high-temperature core-mantle equilibration is required to explain the observed near-chondritic HSE signature of the mantle. Our results therefore provide further support for the 'late veneer' scenario (O'Neill, 1991) as discussed in chapter 1.2.

## Chapter 5

### Constraints on Planetary Core Formation Models - Conclusions and Outlook

Recent isotopic studies give strong support to the proposal that core - mantle differentiation occurred even in relatively small planetary bodies (Greenwood et al. 2005) and must have been a rather rapid process that occurred in many bodies within a few million years (Kleine et al., 2002; Schersten, et al. 2006) of the formation of CAI's, which are considered to be the first condensates in the solar system. Considering the melting points for silicate materials and Fe/Fe - S alloys it seems plausible that both phases could have been in the molten state at temperatures that could have been achieved by radioactive decay of unstable nuclides in small bodies ( $< 5$  GPa) (Rushmer et al., 2000). In larger bodies at higher pressures the metal liquidus is below the silicate solidus such that melting of the whole body is only possible with heat sources such as those provided by large impacts. If core - mantle differentiation occurred on a large number of planetary objects of varying sizes several mechanisms for the metal - silicate separation might have played a role, including metal droplets raining out from a silicate magma ocean, metal diapirs sinking through solidified silicate or percolation of metal melts through a solid silicate matrix. Additionally, even if large scale melting will have dominated the major phase of core formation on many planetary bodies, percolative separation of metal liquid through solid silicate matrix might have played a role in the later stages when large portions of the planetary mantles may have been solid.

A number of models propose very reducing conditions during early core - mantle differentiation (Wänke, 1981; O'Neill, 1990; Wade and Wood, 2005) and a number of meteorite parent bodies, such as those of the aubrite meteorites, show evidence for such a scenario. Such reducing conditions would have allowed for a large portion of Si to partition into the separating metal phase. However, our study performed over a wide range of high pressures of 2 - 25 GPa has shown that the presence of Si in the metal does not aid percolative flow, and consequently another process must be assumed to have caused core separation on such planetary bodies. Previous studies have shown that among possible light elements discussed to be present in the core, it is mainly O which behaves as a surface active element that contributes in lowering the surface tension of Fe - rich alloys (Terasaki et al., 2005). Though the behaviour is similar for S its effect is much weaker and for both elements it is not strong enough to have allowed percolative flow to occur at pressures  $> 3.5$  GPa. We therefore have to assume that metal separation by large scale melting will be the dominating process and that magma oceans quite likely existed on many bodies in the solar system.

The liquid metal - liquid silicate partitioning behaviour of lithophile and weakly siderophile elements can be used as a tool to investigate and constrain the likely conditions in such magma oceans, especially on the Earth where the geochemical signature of the silicate mantle is quite well defined. The partitioning behaviour of the weakly siderophile element V compared to the very weakly siderophile element Nb has allowed us to place constraints on the lower limit of oxygen fugacity and pressure during metal - silicate equilibration in a magma ocean. The strong siderophile character that we observe for Nb at reducing conditions, where it displays an even higher partition coefficient than V, excludes a significant record of low pressure core formation < 20 GPa on the Earth. The observation that very high pressures are necessary to explain the observed mantle depletions of V and Nb gives strong support for the existence of a deep magma ocean. For a more accurate quantification of the likely mean pressure during core - mantle equilibration in a magma ocean the dependence of  $D$  (Nb) will have to be refined with experiments at higher  $P > 30$  GPa in the future.

Based on the dataset for  $D$  (Ni) and  $D$  (Co) from the literature (Kegler et al., 2007) and including our and literature data for  $D$  (V), current accretion models that assume repeated impact events and subsequent re-equilibration in an increasingly deeper magma ocean, succeed in explaining the abundances of the siderophile elements Ni, Co, Fe, V and Cr of the mantle. However, some problems remain unresolved with such models. This is the case for the highly siderophile element inventory of the mantle. Our new experiments at high pressures up to 18 GPa and temperatures up to 2500 °C have shown that the HSE partition coefficients decrease with increasing  $P$  and  $T$ . However, even though more data at both lower and higher pressure will be necessary to quantify this pressure dependency, the pressure trend we have obtained strongly indicates that the mantle abundances as well as the chondritic ratios of the HSE's cannot have been set by high - pressure metal - silicate equilibration in a magma ocean. Even at pressures of 20 GPa the partition coefficients of these elements, although smaller than at 1 bar, are still  $> 10^4$  and the weak positive pressure effect we derive for pressures  $> 20$  GPa would not be sufficient to drastically decrease them even at pressures as high as 80 GPa. This gives strong support that in any metal - silicate fractionation scenario the HSE's would have always been completely extracted from the silicate mantle into the metallic core, even if the final stages of core - mantle equilibration took place under relatively oxidising conditions ( $> -2 \Delta IW$ ).

A 'late veneer' event in which chondritic material is added to the Earth's mantle in the late stages of accretion from which no metal separates to the core, is therefore necessary to explain the HSE abundances in the mantle. Adding new, undifferentiated and highly oxidised material after the major accretion process and after core formation is completed, also provides the supply of HSE's in the required chondritic ratios. If added to a mantle that has previously been completely depleted in certain element groups and does not experience any further extraction or depletion processes, this will leave a chondritic signature for the added elements in the finally accreted Earth.

Our measurements of the partitioning behaviour of Mn, Ga, In and Zn indicate that an unfractionated 'veneer' of volatile material might also be necessary to explain the mantle abundances of these elements. From the pressure and temperature trends of the partition coefficients that we have determined for Zn and In, it would appear that their nearly chondritic ratio in the mantle, would be difficult to be explained by metal - silicate fractionation except at extremely high pressures ( $> 80$  GPa), because at lower pressures the more volatile element In is significantly more siderophile than Zn. One explanation would be for the volatile inventory of the Earth to have been mainly delivered by a late supply of volatile enriched material, similar to a late veneer, that never experienced core - mantle equilibration and thus preserved the near chondritic In/Zn ratio. For the elements Mn and Ga our data indicate a similar situation. The strong siderophile character of Ga, particularly at low pressures, and the very weak siderophile behaviour of Mn over a wide range of high pressures and temperatures excludes core - mantle equilibration at conditions  $< 60$  GPa to be consistent with the observed near chondritic ratio of the elements in the mantle. Alternatively the chondritic Ga/Mn ratio of the mantle could reflect accretion of volatile material that did not undergo significant core - mantle equilibration.

On the other hand, the influence of the light alloying component S in the core forming metal on the partitioning behaviour of Mn, Ga, Zn and In as well as on other volatile elements should be considered, as several of them are also considered to be chalcophile. In order to determine whether such an effect could be achieved with a reasonable amount of S, further experiments need to be performed in the future. In addition further experiments at pressures significantly greater than 20 GPa would help to solidify these conclusions.



## Acknowledgements

First of all, I want to say my very warm thanks to Dan Frost, who introduced me into the multi-anvil world and who always knew how to quench when pressures would get too high, especially during the last three months while writing this thesis.

Thanks for Your infinite supply of motivation and enthusiasm!!!

I also want to thank Dave Rubie for his support as supervisor of this thesis, his contribution with the core formation models and his loyalty when things were getting close.

Mein Dank gilt außerdem dem 'Elitenetzwerk Bayern' für die finanzielle Unterstützung meiner Doktorarbeit im Rahmen des internationalen Doktorandenkollegs 'Structure, Reactivity and Properties of Oxide Materials' am Bayerischen Forschungsinstitut für experimentelle Geochemie und Geophysik der Universität Bayreuth.

Mein besonderer Dank auch an alle, die die Arbeit am BGI wesentlich erleichtert haben, insbesondere an:

Hubert Schulze, der meinen Proben den letzten Schliff verpaßte, um den uns andere Labore beneiden. - Detlef Krauß für die Hilfe, moralische Unterstützung und Versorgung mit Gummibärchen bei endlosen Mikrosondensitzungen und die rasche Beseitigung jeglicher Computerprobleme.

Andreas Audetat für seine Mitwirkung bei allen LA-ICP-MS Analysen und der Bewertung der HSE - Standards. - Nico Walte für seine Hilfe bei der Interpretation der Texturen für die Benetzungswinkelstudie.

Heinz Fischer und Stefan Übelhack, die das Leben der Multi-Anvil-Wissenschaftler am BGI wesentlich vereinfachen. - Petra Buchert, Lydia Kison-Herzing und Stefan Keyssner für das Erleichtern so mancher organisatorischer Dinge.

Mein Dank außerdem an:

Harry Becker für die Erlaubnis zur Benutzung seiner Labore an der Freien Universität Berlin und für die ICP-Analysen der HSE-Glasstandards.

Thanks to Carl Agee to let me use the facilities at the Institute of Meteoritics, University of New Mexico and especially to Paul Burger and Chip Shearer for their support and help with the SIMS analyses.

Und natürlich:

Thanks Ashima, for sharing the highs and lows while struggling through the jungle of all sorts of *Extreme Conditions*.

Vielen lieben Dank, Gertrud und Dieter, für Eure Freundschaft und Eure guten Gedanken!!!



## References

- Abe, Y. (1993). Physical state of the very early Earth. *Lithos*, 30: 223 - 235.
- Allègre, C.J., Poirier, J.-P., Humler, E. and Hofmann, A.W. (1995). The chemical composition of the Earth. *Earth and Planetary Science Letters*, 134: 515 - 526.
- Ballhaus, C. and Ellis, D.J. (1996). Mobility of core melts during Earth's accretion. *Earth and Planetary Science Letters*, 143: 137-145.
- Bargen, v.N. and Waff, H.S. (1986). Permeabilities, interfacial areas and curvatures of partially molten systems: results of numerical computations of equilibrium microstructures. *Journal of Geophysical Research*, 91: 9261-76.
- Barin, I., Sauert, F., Schultze-Rhonhof, E. and Sheng, W.S. (1989). Thermochemical data of pure substances, Part I and Part II. Verlagsgesellschaft Weinheim, Germany, 1739 pp.
- Becker, H., Horan, M.F., Walker, R.J., Gao, S., Lorand, J.-P., Rudnick, R.L. (2006). Highly siderophile element composition of the Earth's primitive upper mantle: Constraints from new data on peridotite massifs and xenoliths. *Geochimica et Cosmochimica Acta*, 70: 4528 - 4550.
- Birch, F. (1964). Density and composition of mantle and core. *Journal of Geophysical Research*, 69: 4377 - 4388.
- Borisov, A. and Nachtweyh, K. (1998). Ru solubility in silicate melts: experimental results in oxidizing region. *XXIX Lunar and Planetary Science Conference*, Abstract, 1320.
- Borisov, A. and Palme, H. (1995). The solubility of iridium in silicate melts: New data from experiments with Ir<sub>10</sub>Pt<sub>90</sub> alloys. *Geochimica et Cosmochimica Acta*, 59: 481 - 485.
- Borisov, A. and Palme, H. (1997). Experimental determination of the solubility of platinum in silicate melts. *Geochimica et Cosmochimica Acta*, 61: 4349-4357.
- Borisov, A., Palme, H. and Spettel, B. (1994). Solubility of palladium in silicate melts: Implications for core formation in the Earth. *Geochimica et Cosmochimica Acta*, 58: 705 - 716.
- Bouchard, D. and Bale, C.W. (1995). Simultaneous - optimization of thermochemical data for liquid-iron alloys containing C, N, Ti, Si, Mn, S, and P. *Metallurgical and Materials Transactions B - Process Metallurgy and Materials Processing Science*, 26: 467 - 484.
- Bulau, J.R., Waff, H.S. and Tyburczy, J.A. (1979). Mechanical and thermodynamic constraints on fluid distribution in partial melts. *Journal of Geophysical Research*, B 84: 6102 - 6108.
- Canup, R.M. (2004). Simulations of a late lunar - forming impact. *Icarus*, 168: 433 - 456.
- Capobianco, C.J., Hervig, R. L. and Drake, M. J. (1994). Experiments on crystal/liquid partitioning of Ru, Rh and Pd for magnetite and hematite solid solutions crystallized from silicate melt. *Chemical Geology*, 113: 23 - 43.

- Chabot, N.L. and Agee, C.B. (2003). Core formation in the Earth and Moon: new experimental constraints from V, Cr, and Mn. *Geochimica et Cosmochimica Acta*, 67: 2077 - 2091.
- Chabot, N.L., Draper, D.S. and Agee, C.B. (2005). Conditions of core formation in the earth: Constraints from Nickel and Cobalt partitioning. *Geochimica et Cosmochimica Acta*, 69: 2141 - 2151.
- Chambers, J. E. (2003). Planet Formation. In: A.M. Davis (Editor), *Treatise on geochemistry*. Volume 1: *Meteorites, Planets and Comets*. Elsevier Pergamon, Oxford, pp. 461 - 475.
- Chase, M. W., Davies, C. A., Downey, J. R., Frurip, D. J., McDonald, R. A., Syverud, A. N. (1998). NIST - JANAF Thermochemical tables, 4th Edition, Part 1 and Part 2, vol. 14 Monograph. National Institute of Standards Technology.
- Cottrell, E. and Walker, D. (2006). Constraints on core formation from Pt partitioning in mafic silicate liquids at high temperatures. *Geochimica et Cosmochimica Acta*, 70: 1565 - 1580.
- Edgar, A.D. (1973). *Experimental petrology: basic principles and techniques*. Clarendon Press, Oxford.
- Ertel, W., Drake, M. J., Walter, M. J. and Sylvester, P. J. (2006). Experimental study of platinum solubility in silicate melt to 14 GPa and 2273 K: Implications for accretion and core formation in Earth. *Geochimica et Cosmochimica Acta*, 70: 2591 - 2602.
- Ertel, W., O'Neill, H. St. C., Sylvester, P. J. and Dingwell, D. B. (1999). Solubilities of Pt and Rh in a haplobasaltic silicate melt at 1300°C. *Geochimica et Cosmochimica Acta*, 63: 2439 - 2449.
- Ertel, W., O'Neill, H. St. C., Sylvester, P. J., Dingwell, D. B. and Spettel, B. (2001). The solubility of rhenium in silicate melts: Implications for the geochemical properties of rhenium at high temperatures. *Geochimica et Cosmochimica Acta*, 65: 2161 - 2170.
- Fortenfant, S.S., Günther, D., Dingwell, D. B., Rubie, D. C. (2003)<sup>a</sup>. Temperature dependence of Pt and Rh solubilities in a haplobasaltic melt. *Geochimica et Cosmochimica Acta*, 67: 123 - 131.
- Fortenfant, S.S., Rubie, D.C., Reid, J., Dalpé, C., Capmas, F., Gessmann, C.K. (2003)<sup>b</sup>. Partitioning of Re and Os between liquid metal and magnesiowüstite at high pressure. *Physics of the Earth and Planetary Interiors*, 139: 77 - 91.
- Frost, D.J. (2003). Fe<sup>2+</sup> - Mg partitioning between garnet, magnesiowüstite, and (Mg,Fe)<sub>2</sub>SiO<sub>4</sub> phases of the transition zone. *American Mineralogist*, 88: 387 - 397.
- Frost, D.J., Langenhorst, F. and van Aken, P.A. (2001). Fe-Mg partitioning between ringwoodite and magnesiowüstite and the effect of pressure, temperature and oxygen fugacity. *Physics and Chemistry of Minerals*, 28: 455 - 470.
- Frost, D.J., Poe, B. T., Tronnes, R. G., Liebske, C., Duba, A., Rubie, D. C. (2004). A new large-volume multianvil system. *Physics of the Earth and Planetary Interiors*, 143 - 144: 507 - 514.

- Gaetani, G.A. and Grove, T.L. (1999). Wetting of mantle olivine by sulfide melt: implications for Re/Os ratios in mantle peridotite and late-stage core formation. *Earth and Planetary Science Letters*, 169: 147-163.
- Gessmann, C.K. and Rubie, D.C. (1998). The Effect of Temperature on the partitioning of Nickel, Cobalt, Manganese, Chromium, and Vanadium at 9 GPa and constraints on formation of the Earth's core. *Geochimica et Cosmochimica Acta*, 62: 867 - 882.
- Gessmann, C.K. and Rubie, D.C. (2000). The origin of the depletions of V, Cr and Mn in the mantles of the Earth and Moon. *Earth and Planetary Science Letters*, 184: 95 - 107.
- Gessmann, C.K., Rubie, D.C. and McCammon, C.A. (1999). Oxygen fugacity dependence of Ni, Co, Mn, Cr, V, and Si partitioning between liquid metal and magnesiowustite at 9 - 18 GPa and 2200°C. *Geochimica Et Cosmochimica Acta*, 63: 1853 - 1863.
- Gessmann, C.K., Wood, B.J., Rubie, D.C. and Kilburn, M.R. (2001). Solubility of silicon in liquid metal at high pressure: implications for the composition of the Earth's core. *Earth and Planetary Science Letters*, 184: 367 - 376.
- Greenwood, R.C., Franchi, I.A., Jambon, A. and Buchanan, P.C. (2005). Widespread magma oceans on asteroidal bodies in the early Solar System. *Nature*, 435: 916 - 918.
- Heald, E.F. (1967). Thermodynamics of Iron-Platinum Alloys. *Transactions of the Metallurgical Society of Aime*, 239: 1337 - 1340.
- Hervig, R., Mazdab, F.K., Danielson, L., Sharp, T.G., Hamed, A., Williams, P. (2004). SIMS microanalyses for Au in silicates. *American Mineralogist*, 89: 498 - 504.
- Hillgren, V.J., Drake, M.J. and Rubie, D.C. (1996). High pressure and high temperature metal-silicate partitioning of siderophile elements: The importance of silicate liquid composition. *Geochimica Et Cosmochimica Acta*, 60: 2257 - 2263.
- Holzheid, A., Palme, H. and Chakraborty, S. (1997). The activities of NiO, CoO and FeO in silicate melts. *Chemical Geology*, 139: 21 - 38.
- Holzheid, A., Sylvester, P., O'Neill, H.S.C., Rubie, D.C. and Palme, H. (2000). Evidence for a late chondritic veneer in the Earth's mantle from high-pressure partitioning of palladium and platinum. *Nature*, 406: 396 - 399.
- Iida, T. and Guthrie, R.I.L. (1988). *The Physical Properties of the Liquid Metals*. Clarendon Press, Oxford, 287 pp.
- Ito, E., Kubo, A., Katsura, T. and Walter, M.J. (2004). Melting experiments of mantle materials under lower mantle conditions with implications for magma ocean differentiation. *Physics of The Earth and Planetary Interiors*, 143-144: 397 - 406.
- Ito, E., Morooka, K., Ujike, O. and Katsura, T. (1995). Reactions between molten iron and silicate melts at high-pressure - Implications for the chemical evolution of Earth's core. *Journal of Geophysical Research - Solid Earth*, 100: 5901 - 5910.

- Ixanov, B., Laty, P., Joud, J.C. and Desre, P. (1978). Surface - tension of Fe - Si liquid alloys. *Journal De Chimie Physique Et De Physico-Chimie Biologique*, 75: 550-552.
- Jana, D. and Walker, D. (1997)<sup>a</sup>. The impact of carbon on element distribution during core formation. *Geochimica Et Cosmochimica Acta*, 61: 2759 - 2763.
- Jana, D. and Walker, D. (1997)<sup>b</sup>. The influence of silicate melt composition on distribution of siderophile elements among metal and silicate liquids. *Earth and Planetary Science Letters*, 150: 463 - 472.
- Jana, D. and Walker, D. (1997)<sup>c</sup>. The influence of sulfur on partitioning of siderophile elements. *Geochimica Et Cosmochimica Acta*, 61: 5255 - 5277.
- Javoy, M. (1995). The integral enstatite chondrite model of the earth. *Geophysical Research Letters*, 22: 2219 - 2222.
- Jeanloz, R. (1979). Properties of Iron at High-Pressures and the State of the Core. *Journal of Geophysical Research*, 84: 6059 - 6069.
- Jurewicz, S.R. and Jones, J.H (1995). Preliminary results of olivine/metal wetting experiments and the direct measurement of metal phase interconnectivity. XXVI *Lunar and Planetary Science Conference*, Abstract, 709 - 710.
- Jurewicz, S.R. and Jurewicz, A.J.G. (1986). Distribution of Apparent Angles on Random Sections with Emphasis on Dihedral Angle Measurements. *Journal of Geophysical Research - Solid Earth and Planets*, 91: 9277 - 9282.
- Karato, S. and Murthy, V.R. (1997). Core formation and chemical equilibrium in the Earth .1. Physical considerations. *Physics of the Earth and Planetary Interiors*, 100: 61 - 79.
- Kawai, N. and Endo, S. (1970). The generation of ultrahigh hydrostatic pressures by a split sphere apparatus. *Reviews in Scientific Instruments*, 41: 1178 - 1181.
- Kegler, P., Holzheid, A., Frost, D.J., Rubie, D.C., Palme, H. (2007). New Ni and Co partition data call an early Earth single stage magma ocean into question. submitted to *Earth and Planetary Science Letters*.
- Keppler, H. and Frost, D.J. (2005). Introduction to minerals under extreme conditions. In: R. Miletich (Editor), *Mineral Behaviour at Extreme Conditions. EMU Notes in Mineralogy*, Budapest, pp. 1-30.
- Keppler, H. and Rubie, D.C. (1993). Pressure - Induced Coordination Changes of Transition - Metal Ions in Silicate Melts. *Nature*, 364: 54 - 56.
- Kilburn, M.R. and Wood, B.J. (1997). Metal-silicate partitioning and the incompatibility of S and Si during core formation. *Earth and Planetary Science Letters*, 152: 139 - 148.
- Kleine, T., Münker, C., Mezger, K. and Palme, H. (2002). Rapid accretion and early core formation on asteroids and the terrestrial planets from Hf - W chronometry. *Nature*, 418: 952 - 955.

- Laporte, D. and Provost, A. (2000). The grain - scale distribution of silicate, carbonate and metallosulfide partial melts : a review of theory and experiments. In: N.S. Bagdassarov, D. Laporte, A.B. Thomas (Editors). *Physics and Chemistry of Partially Molten Rocks. Petrology and Structural Geology*, 11, Kluwer Academic Press, Dordrecht: 93 - 140.
- Li, J. and Agee, C.B. (1996). Geochemistry of mantle - core differentiation at high pressure. *Nature*, 381: 686 - 689.
- Li, J. and Agee, C.B. (2001). The effect of pressure, temperature, oxygen fugacity and composition on partitioning of nickel and cobalt between liquid Fe-Ni-S alloy and liquid silicate: implications for the earth's core formation. *Geochimica et Cosmochimica Acta*, 65: 1821 - 1832.
- Lodders, K. (2003). Solar system abundances and condensation temperatures of the elements. *Astrophysical Journal*, 591: 1220 - 1247.
- Lodders, K., Palme, H. and Wlotzka, F. (1993). Trace - Elements in Mineral Separates of the Pena - Blanca Spring Aubrite - Implications for the Evolution of the Aubrite Parent Body. *Meteoritics*, 28: 538 - 551.
- Malavergne, V., Siebert, J., Guyot, F., Gautron, L., Combes, R., Hammouda, T., Borensztajn, S., Frost, D., Martinez, I. (2004). Si in the core? New high-pressure and high-temperature experimental data. *Geochimica et Cosmochimica Acta*, 68: 4201 - 4211.
- Mao, H.K., Wu, Y., Chen, L.C., Shu, J.F. and Jephcoat, A.P. (1990). Static compression of iron to 300 GPa and Fe<sub>0.8</sub>Ni<sub>0.2</sub> alloy to 260 GPa - Implications for composition of the core. *Journal of Geophysical Research - Solid Earth and Planets*, 95: 21737 - 21742.
- McDonough, W.F. and Sun, S.s. (1995). The composition of the Earth. *Chemical Geology*, 120: 223 - 253.
- Minarik, W.G., Ryerson, F.J. and Watson, E.B. (1996). Textural entrapment of core - forming melts. *Science*, 272: 530 - 533.
- O'Neill, H.S.C. (1991). The origin of the moon and the early history of the Earth - a chemical model. Part 2: The Earth. *Geochimica et Cosmochimica Acta*, 55: 1159 - 1172.
- O'Neill, H.S.C., Canil, D. and Rubie, D.C. (1998). Oxide - metal equilibria to 2500°C and 25GPa: Implications for core formation and the light component in the Earth's core. *Journal of Geophysical Research*, 103: 12239 - 12260.
- O'Neill, H.S.C., Dingwell, D.B., Borisov, A., Spettel, B. and Palme, H. (1995). Experimental petrochemistry of some highly siderophile elements at high temperatures, and some implications for core formation and the mantle's early history. *Chemical Geology*, 120: 255-273.
- O'Neill, H.S.C. and Eggins, S.M. (2002). The effect of melt composition on trace element partitioning: an experimental investigation of the activity coefficients of FeO, NiO, CoO, MoO<sub>2</sub> and MoO<sub>3</sub> in silicate melts. *Chemical Geology*, 186: 151 - 181.

- O'Neill, H.S.C. and Palme, H. (1998). Composition of the silicate Earth; implications for accretion and core formation. In: I. Jackson (Editor), *The Earth's mantle; composition, structure, and evolution*. Cambridge University Press, Cambridge, United Kingdom, pp. 3 - 126.
- Palme, H. (2000). Are there chemical gradients in the inner solar system? *Space Science Reviews*, 92: 237 - 262.
- Palme, H. and O'Neill, H.S.C. (2003). Cosmochemical Estimates of Mantle Composition. In: H.D. Holland (Editor), *Treatise on geochemistry*. Volume 2: *The mantle and core*. Elsevier Pergamon, Oxford, pp. 1 - 38.
- Pearce, N.J.G., Perkins W.T., Westgate J.A., Gorton M.P., Jackson S.E., Neal C.R. and Chenery S.P. (1997). A compilation of new and published major and trace element data for NIST SRM 610 and NIST SRM 612 glass reference materials. *Geostandards Newsletter: The Journal of Geostandards and Geoanalysis*, 21: 115 - 144.
- Poirier, J.-P. (1994). Light elements in the Earth's outer core: A critical review. *Physics of the earth and planetary interiors*, 85: 319 - 337.
- Raghavan, V. (1988). Phase diagrams of ternary iron alloys. Part 2: Tertiary systems containing iron and sulphur. Indian Institute of Metals, Calcutta.
- Rammensee, W., Palme, H. and Wänke, H. (1983). Experimental Investigation of Metal-Silicate Partitioning of Some Lithophile Elements (Ta, Mn, V, Cr). XIV, *Lunar and Planetary Science Conference*, Abstract, 628 - 629.
- Righter, K. (2005). Highly Siderophile elements: Constraints on Earth accretion and early differentiation. In: v.d.H. et al. (Editor), *The Earth's deep mantle*. Geophysical Monograph Series, AGU.
- Righter, K., Campbell, A.J., Humayun, M. and Hervig, R.L. (2004). Partitioning of Ru, Rh, Pd, Re, Ir, and Au between Cr-bearing spinel, olivine, pyroxene and silicate melts. *Geochimica et Cosmochimica Acta*, 68: 867-880.
- Righter, K. and Drake, M.J. (1997). Metal - silicate equilibrium in a homogeneously accreting earth: new results for Re. *Earth and Planetary Science Letters*, 146: 541 - 553.
- Righter, K. and Drake, M.J. (2000). Metal/silicate equilibrium in the early Earth - New constraints from the volatile moderately siderophile elements Ga, Cu, P, and Sn. *Geochimica Et Cosmochimica Acta*, 64: 3581 - 3597.
- Righter, K. and Drake, M.J. (2003). Partition coefficients at high pressure and temperature. In: H.D. Holland (Editor), *Treatise on geochemistry*. Volume 2: *The mantle and core*. Elsevier Pergamon, Oxford, pp. 425 - 449.
- Righter, K., Drake, M. J. and Yaxley, G. (1997). Prediction of siderophile element metal-silicate partition coefficients to 20 GPa and 2800°C: the effects of pressure, temperature, oxygen fugacity, and silicate and metallic melt compositions. *Physics of The Earth and Planetary Interiors*, 100: 115 - 134.

- Righter, K., Humayun, M. and Danielson, L. (2006). Highly Siderophile Elements in the Terrestrial Upper Mantle Require a Late Veneer? New Results for Palladium. Workshop on Early Planetary Differentiation: A Multi-Planetary and Multi-Disciplinary Perspective, Abstract, 4040.
- Ringwood, A.E. (1979). Origin of the Earth and Moon. Springer Verlag, Berlin.
- Rubie, D.C. (1999). Characterising the sample environment in multianvil high - pressure experiments. *Phase Transitions*, 68: 431 - 451.
- Rubie, D.C., Melosh, H.J., Reid, J.E., Liebske, C. and Righter, K. (2003). Mechanisms of metal - silicate equilibration in the terrestrial magma ocean. *Earth and Planetary Science Letters*, 205: 239 - 255.
- Rudnick, R.L., Barth, M., Horn, I. and McDonough, W.F. (2000). Rutile - bearing refractory eclogites: Missing link between continents and depleted mantle. *Science*, 287: 278 - 281.
- Rushmer, T., Minarik, W.G. and Taylor, G. J. (2000). Physical Processes of Core Formation. In: R.M. Canup, Righter, K. (Editor), *Origin of the Earth and Moon*. The University of Arizona space science series, pp. 227-244.
- Scherstén, A., Elliott, T., Hawkesworth, C., Russell, S. and Masarik, J. (2006). Hf - W evidence for rapid differentiation of iron meteorite parent bodies. *Earth and Planetary Science Letters*, 241: 530 - 542.
- Schmitt, W., Palme, H. and Wänke, H. (1989). Experimental determination of metal/silicate partition coefficients for P, Co, Ni, Cu, Ga, Ge, Mo and W and some implications for the early evolution of the Earth. *Geochimica et Cosmochimica Acta*, 53: 173 - 185.
- Schwartzendruber, L.J. (1984)<sup>a</sup>. The Fe - Ir (iron - iridium) system. *Bulletin of alloy phase diagrams*, 5: 48 - 52.
- Schwartzendruber, L.J. (1984)<sup>b</sup>. The Fe - Rh (iron - rhodium) system. *Bulletin of alloy phase diagrams*, 5: 456 - 462.
- Shannon, M.C. and Agee, C.B. (1998). Percolation of core melts at lower mantle conditions. *Science*, 280: 1059 - 1061.
- Srećec, I., Ender, A., Woermann, E., Gans, W., Jacobsson, E., Eriksson, G., Rosen, E. (1987). Activity - Composition Relations of the Magnesiowustite Solid - Solution Series in Equilibrium with Metallic Iron in the Temperature-Range 1050 - 1400-K. *Physics and Chemistry of Minerals*, 14: 492 - 498.
- Steelmaking, T.J.S.f.t.P.o.S.-T.t.C.o. (1988). *Steelmaking Data Source Book*. Gordon and Breach Science Publishers, Montreux.
- Stevenson, D.L. (1990). Fluid dynamics of core formation. In: H.E. Newsom, J. H. Jones (Editors). *Origin of the Earth*. Oxford University Press, New York: 231 - 249.

- Stickels, C.A. and Hucke, E.E. (1964). Measurement of dihedral angles. *Transactions of the Metallurgical Society of Aime*, 230: 795 - 801.
- Sylvester, P.J. and Eggins, S.M. (1997). Analysis of Re, Au, Pd, Pt and Rh in NIST glass certified reference materials and natural basalt glasses by laser ablation ICP-MS. *Geostandard Newsletter: The Journal of Geostandards and Geoanalysis*, 21: 215 - 230.
- Takafuji, N., Hirose, K., Mitome, M. and Bando, Y. (2005). Solubilities of O and Si in liquid iron in equilibrium with (Mg,Fe)SiO<sub>3</sub> perovskite and the light elements in the core. *Geophysical Research Letters*, 32.
- Takafuji, N., Hirose, K., Ono, S., Xu, F. F., Mitome, M., Bando, Y. (2004). Segregation of core melts by permeable flow in the lower mantle. *Earth and Planetary Science Letters*, 224: 249 - 257.
- Terasaki, H., Frost, D.J., Rubie, D.C. and Langenhorst, F. (2005). The effect of oxygen and sulphur on the dihedral angle between Fe-O-S melt and silicate minerals at high pressure: Implications for Martian core formation. *Earth and Planetary Science Letters*, 232: 379-392.
- Terasaki H, Frost DJ, Rubie DC, Langenhorst F. (2007). Interconnectivity of Fe-O-S liquid in polycrystalline silicate perovskite at lower mantle conditions *Physics of the Earth and Planetary Interiors*, 161: 170 - 176.
- Thibault, Y. and Walter, M.J. (1995). The Influence of Pressure and Temperature on the Metal-Silicate Partition-Coefficients of Nickel and Cobalt in a Model-C1 Chondrite and Implications for Metal Segregation in a Deep Magma Ocean. *Geochimica Et Cosmochimica Acta*, 59: 991 - 1002.
- Trønnes, R.G.a.F. and Frost, D.J. (2002). Peridotite melting and mineral - melt partitioning of major and minor elements at 22 - 24.5 GPa. *Earth and Planetary Science Letters*, 197: 117 - 131.
- Utigard, T. (1994). Surface and interfacial - tensions of iron-based systems. *ISIJ International*, 34: 951 - 959.
- Wade, J. and Wood, B.J. (2001). The Earth's 'missing' niobium may be in the core. *Nature*, 409: 75 - 78.
- Wade, J., Wood, B.J. (2005). Core formation and the oxidation state of the Earth. *Earth and Planetary Science Letters*, 236: 78 - 95.
- Wagner, C. (1962). *Thermodynamics of alloys*. Addison-Wesley, Reading, MA.
- Walker, D., Carpenter, M.A. and Hitch, C.M. (1990). Some Simplifications to Multianvil Devices for High - Pressure Experiments. *American Mineralogist*, 75: 1020 - 1028.
- Walte, N.P., Becker J.K., Bons P.D., Rubie D.C., Frost D.J. (2007). Liquid - distribution and attainment of textural equilibrium in a partially - molten crystalline system with a high-dihedral angle liquid phase. *Earth and Planetary Science Letters*. published online: doi:10.1016/j.epsl. 2007.08.003.

- 
- Walter, M.J., Newsom, H.E., Ertel, W. and Holzheid, A. (2000). Siderophile Elements in the Earth and Moon: Metal/Silicate Partitioning and Implications for Core Formation. In: R.M. Canup, Righter, K. (Editor), *Origin of the Earth and Moon*. The University of Arizona space science series, pp. 265 - 289.
- Wänke, H. (1981). Constitution of terrestrial planets. *Philosophical Transactions of the Royal Society of London*, 303: 287 - 302.
- Wasson, J.T. (1985). *Meteorites their record of early solar - system history*. Freeman, New York, 267 pp.
- Wasson, J.T. and Kallemeyn, G.W. (1988). Compositions of Chondrites. *Philosophical Transactions of the Royal Society of London*; Series a; 325: 535 - 544.
- Wetherill, G.W. (1985). Occurrence of Giant Impacts During the Growth of the Terrestrial Planets. *Science*, 228: 877 - 879.
- Wood, B.J., Walter, M.J. and Wade, J. (2006). Accretion of the Earth and segregation of its core. *Nature*, 441: 825 - 833.
- Yin, Q.Z., Jacobsen, S. B., Yamashita, K., Blichert-Toft, J., Telouk, P., Albarede, F (2002). A short timescale for terrestrial planet formation from Hf - W chronometry of meteorites. *Nature*, 418: 949-952.
- Yoshino, T., Walter, M.J. and Katsura, T. (2003). Core formation in planetesimals triggered by permeable flow. *Nature*, 422: 154 - 157.



# Appendix

**Table I: Average compositions of the quenched silicates and metals from the study of chapter 3 - EPMA results (wt%); table continues on the next two pages; footnotes for all at bottom of last table**

silicate	P1-19		P1-21		P1-20		C15-9		C15-10		V307		V312		V334		V310		V337	
	No=29	$\pm 2\sigma^a$	No=30	$\pm 2\sigma$	No=54	$\pm 2\sigma$	No=26	$\pm 2\sigma$	No=26	$\pm 2\sigma$	No=78	$\pm 2\sigma$	No=19	$\pm 2\sigma$	No=40	$\pm 2\sigma$	No=4	$\pm 2\sigma$	No=37	$\pm 2\sigma$
Si	25.26	0.39	24.29	0.55	20.49	0.50	20.21	0.70	18.75	0.55	25.72	0.92	21.14	2.38	22.36	0.89	22.80	0.45	19.92	0.30
Mg	21.31	0.99	20.43	1.57	23.24	1.13	21.58	3.51	20.79	5.04	21.51	0.95	22.43	1.65	20.01	1.18	20.72	0.99	20.76	2.07
Al	2.76	0.28	2.84	0.29	2.17	0.62	2.18	0.59	2.17	0.79	2.50	0.43	5.13	4.00	2.23	0.23	2.37	0.20	1.97	0.39
Ca	3.23	0.25	3.14	0.29	2.27	0.34	2.58	0.79	2.57	1.08	2.91	0.71	2.88	0.61	3.00	0.28	2.77	0.28	2.25	0.46
Fe	0.29	0.12	0.82	0.28	5.60	0.82	1.01	0.02	2.56	0.18	0.23	0.23	0.88	0.56	1.56	0.31	2.77	0.31	4.55	0.24
Co	<0.002*	0.005	<0.003*	0.008	0.013	0.014	<0.003*	0.004	<0.004*	0.006	0.005*	0.014	<0.005*	0.010	<0.003*	0.005	0.009*	0.019	0.009*	0.008
Ni	<0.003*	0.009	<0.003*	0.009	<0.005*	0.012	<0.001*	0.002	<0.002*	0.005	<0.003*	0.011	0.006*	0.016	<0.002*	0.005	<0.003*	0.012	<0.004*	0.006
Ti	0.11	0.02	0.13	0.02	0.10	0.07	1.78	0.45	1.85	0.72	0.11	0.03	0.082	0.018	1.86	0.32	0.13	0.02	1.78	0.36
V	-	-	-	-	-	-	0.80	0.05	1.23	0.10	-	-	-	-	0.51	0.04	-	-	1.00	0.09
Cr	0.017	0.011	0.047	0.016	0.13	0.03	0.60	0.05	0.97	0.18	0.010*	0.018	0.10	0.13	0.38	0.03	0.071	0.027	0.68	0.06
Mn	0.14	0.02	0.13	0.02	0.11	0.03	1.83	0.16	1.84	0.33	0.11	0.03	0.079	0.014	1.65	0.11	0.14	0.03	1.64	0.11
Ta	0.38	0.11	2.88	0.57	2.43	0.35	1.93	0.58	2.07	0.77	0.10	0.17	0.67	0.10	1.60	0.58	2.60	0.52	1.76	0.56
Nb	-	-	-	-	-	-	0.68	0.21	1.49	0.59	-	-	-	-	0.35	0.11	-	-	1.18	0.34
Ga	0.031#	0.066	0.064#	0.089	0.29	0.10	-	-	-	-	0.039#	0.026	0.11	0.04	-	-	0.23	0.03	-	-
In	0.073#	0.019	0.089	0.023	0.15	0.03	-	-	-	-	0.070#	0.057	0.10	0.06	-	-	0.14	0.03	-	-
Zn	0.13	0.01	0.22	0.01	0.45	0.09	-	-	-	-	<0.12	0.05	0.22	0.05	-	-	0.42	0.02	-	-
W	<0.002*	0.007	<0.008*	0.015	<0.006*	0.012	-	-	-	-	-	-	<0.006*	0.020	<0.005*	0.010	<0.005*	0.017	<0.010*	0.020
S	-	-	-	-	-	-	-	-	-	-	-	-	-	-	-	-	-	-	-	-
O calc. <sup>b</sup>	46.87		45.97		43.93		43.08		41.93		47.08		45.15		44.55		44.50		43.28	
Total	100.61		101.07		101.36		98.26		98.22		100.52		98.98		100.06		99.68		100.81	

metal	P1-19		P1-21		P1-20		C15-9		C15-10		V307		V312		V334		V310		V337	
	No=30	$\pm 2\sigma^a$	No=32	$\pm 2\sigma$	No=30	$\pm 2\sigma$	No=35	$\pm 2\sigma$	No=34	$\pm 2\sigma$	No=17	$\pm 2\sigma$	No=37	$\pm 2\sigma$	No=42	$\pm 2\sigma$	No=38	$\pm 2\sigma$	No=35	$\pm 2\sigma$
Si	2.90	0.21	0.19	0.10	<0.001*	0.00	2.07	0.11	0.23	0.08	10.45	1.30	2.06	0.20	<0.13#	0.35	<0.12#	0.14	<0.0002*	0.0011
Fe	83.87	1.45	85.43	3.32	88.17	1.19	89.48	0.94	94.98	0.74	79.29	6.76	86.40	1.58	80.68	2.81	87.21	1.49	87.15	1.15
Co	0.91	0.04	0.85	0.10	1.07	0.07	0.93	0.16	1.08	0.08	0.84	0.15	1.03	0.07	1.05	0.32	0.93	0.07	1.04	0.17
Ni	1.79	0.09	1.53	0.24	1.98	0.19	1.75	0.34	1.81	0.06	1.53	0.31	1.77	0.16	1.77	1.45	1.72	0.22	1.85	0.79
Ti	0.011#	0.014	<0.005*	0.008	0.002*	0.006	<0.004*	0.006	<0.003*	0.004	0.043#	0.097	0.006*	0.012	0.049	0.025	0.006*	0.013	0.014#	0.010
V	-	-	-	-	-	-	1.35	0.01	0.56	0.03	-	-	-	-	2.77	1.03	-	-	1.29	0.27
Cr	0.36	0.03	0.40	0.06	0.10	0.06	1.44	0.02	0.95	0.03	0.33	0.09	0.61	0.09	2.64	1.01	0.29	0.05	1.71	0.40
Mn	0.069	0.025	<0.014*	0.019	<0.001*	0.004	0.19	0.05	0.047	0.014	<0.039#	0.099	0.013*	0.071	0.42	0.10	0.023#	0.035	0.20	0.05
Ta	2.02	1.54	1.37	0.49	<0.008*	0.025	0.14	0.07	<0.012*	0.019	3.43#	7.92	1.16	0.84	0.54	0.22	0.35	0.14	<0.014*	0.024
Nb	-	-	-	-	-	-	1.53	0.34	0.38	0.07	-	-	-	-	3.46	2.22	-	-	0.57	0.55
Ga	2.54	0.28	1.56	0.89	2.05#	1.17	-	-	-	-	1.60	0.13	1.83	0.58	-	-	2.19	0.62	-	-
In	0.85	0.18	0.71	0.16	0.73	0.27	-	-	-	-	0.79	1.11	0.92	0.21	-	-	0.88	0.29	-	-
Zn	0.82	0.06	0.36	0.19	0.10	0.05	-	-	-	-	0.58	0.20	0.52	0.09	-	-	0.26	0.08	-	-
W	0.016*	0.023	0.012*	0.022	0.007*	0.019	-	-	-	-	-	-	0.004*	0.021	0.004*	0.009	<0.025	0.044	<0.079	0.053
S	-	-	-	-	-	-	-	-	-	-	-	-	-	-	-	-	-	-	-	-
Total	96.16 <sup>c</sup>		92.43 <sup>c</sup>		94.22 <sup>c</sup>		98.89		100.05		98.92 <sup>c</sup>		96.33 <sup>c</sup>		93.51 <sup>c</sup>		94.01 <sup>c</sup>		93.92 <sup>c</sup>	

Table I continued

silicate	V309		V311		V346		V366		V365		V367		Z457		Z442		Z469		Z447			
	No=24	$\pm 2\sigma^a$	No=60	$\pm 2\sigma$	No=31	$\pm 2\sigma$	No=26	$\pm 2\sigma$	No=24	$\pm 2\sigma$	No=26	$\pm 2\sigma$	No=31	$\pm 2\sigma$	No=34	$\pm 2\sigma$	No=33	$\pm 2\sigma$	No=14	$\pm 2\sigma$		
Si	19.37	0.57	18.40	0.42	16.98	0.82	16.62	0.80	16.12	0.56	15.93	0.72	20.27	0.97	20.76	1.56	18.78	3.69	20.79	0.89		
Mg	19.52	7.05	20.67	4.41	27.66	23.31	29.07	2.42	29.20	1.39	30.26	1.27	22.32	2.28	24.96	3.95	25.05	7.71	25.36	1.67		
Al	2.65	1.57	2.30	1.01	1.80	7.39	1.52	0.70	1.20	0.18	1.23	0.32	1.91	0.36	2.02	0.21	1.85	0.33	1.80	0.12		
Ca	2.82	1.67	2.59	1.19	2.96	10.76	2.42	1.30	1.75	0.58	1.79	0.70	2.65	0.82	2.58	1.38	1.70	2.45	2.45	0.51		
Fe	9.06	1.07	10.05	1.42	0.74	1.04	0.94	0.26	1.96	0.32	1.05	0.26	7.25	0.66	1.60	0.32	2.34	0.81	2.03	0.22		
Co	0.023	0.024	0.029	0.032	<0.002*	0.004	<0.002*	0.003	<0.002*	0.003	<0.002*	0.003	<0.002*	0.005	0.021	0.017	<0.003*	0.008	0.005*	0.006	0.006*	0.012
Ni	0.006*	0.017	0.008*	0.032	<0.002*	0.004	<0.003*	0.004	<0.002*	0.002	<0.002*	0.005	0.010	0.016	<0.003*	0.009	<0.003*	0.006	<0.004*	0.009		
Ti	0.15	0.09	0.11	0.05	1.81	6.36	1.48	0.65	1.32	0.38	1.21	0.32	0.07	0.02	0.13	0.06	1.54	2.38	0.10	0.04		
V	-	-	-	-	0.59	1.31	0.57	0.14	0.65	0.05	0.52	0.06	-	-	-	-	0.96	0.41	-	-		
Cr	0.13	0.05	0.14	0.06	0.32	0.80	0.32	0.09	0.44	0.04	0.30	0.05	0.13	0.02	0.072	0.016	0.57	0.19	0.084	0.013		
Mn	0.11	0.03	0.13	0.04	1.01	1.76	1.10	0.28	1.11	0.18	0.91	0.14	0.049	0.023	0.090	0.032	1.04	0.56	0.073	0.021		
Ta	2.84	1.69	2.66	1.45	2.11	8.54	1.58	0.78	1.41	0.48	1.39	0.61	1.87	0.79	1.96	1.64	1.36	3.15	1.89	1.00		
Nb	-	-	-	-	0.97	3.88	0.80	0.40	1.04	0.36	0.75	0.32	-	-	-	-	0.93	1.98	-	-		
Ga	0.80	0.44	0.73	0.29	-	-	-	-	-	-	-	-	0.26	0.09	0.049#	0.080	-	-	0.076#	0.105		
In	0.34	0.18	0.30	0.11	-	-	-	-	-	-	-	-	0.12	0.03	0.048#	0.016	-	-	0.060#	0.015		
Zn	0.53	0.05	0.50	0.04	-	-	-	-	-	-	-	-	0.34	0.04	0.19	0.02	-	-	0.20	0.02		
W	<0.006*	0.020	<0.005*	0.017	0.011*	0.041	-	-	-	-	-	-	<0.005*	0.015	<0.005*	0.015	<0.007*	0.013	0.027	0.031		
S	-	-	-	-	-	-	-	-	-	-	-	-	-	-	-	-	-	-	-	-		
O calc. <sup>b</sup>	42.12	-	41.58	-	42.84	-	42.65	-	41.91	-	41.88	-	43.29	-	43.98	-	43.12	-	44.13	-		
Total	100.48	-	100.19	-	99.80	-	99.08	-	98.10	-	97.21	-	100.59	-	98.45	-	99.25	-	99.09	-		

metal	V309		V311		V346		V366		V365		V367		Z457		Z442		Z469		Z447	
	No=46	$\pm 2\sigma^a$	No=40	$\pm 2\sigma$	No=37	$\pm 2\sigma$	No=39	$\pm 2\sigma$	No=33	$\pm 2\sigma$	No=32	$\pm 2\sigma$	No=45	$\pm 2\sigma$	No=18	$\pm 2\sigma$	No=35	$\pm 2\sigma$	No=29	$\pm 2\sigma$
Si	0.022*	0.077	0.016*	0.056	1.36	0.10	1.44	0.07	0.22	0.11	1.64	0.10	0.12*	0.12	4.23	1.02	2.87	0.39	1.39	0.07
Fe	88.31	3.53	89.86	1.78	90.15	2.54	90.03	1.43	94.18	1.05	90.43	1.95	93.61	0.98	88.09	1.09	90.36	2.17	54.37	1.91
Co	1.05	0.11	0.93	0.15	0.97	0.05	0.93	0.02	1.09	0.08	0.93	0.02	1.11	0.07	0.87	0.31	1.04	0.05	0.56	0.03
Ni	1.78	0.36	1.87	0.73	2.03	0.26	1.75	0.07	1.93	0.23	1.72	0.08	2.11	0.13	1.32	0.65	1.99	0.16	1.16	0.08
Ti	0.003*	0.008	<0.003*	0.007	0.016#	0.008	<0.007*	0.009	<0.003*	0.006	<0.008*	0.007	0.001*	0.005	<0.005*	0.007	0.015#	0.007	0.001*	0.004
V	-	-	-	-	1.18	0.19	1.15	0.08	0.55	0.16	1.06	0.21	-	-	-	-	0.56	0.30	-	-
Cr	0.22	1.06	0.091	0.030	1.72	0.15	1.63	0.07	1.14	0.13	1.57	0.13	0.064	0.026	0.26	0.05	1.35	0.19	0.12	0.02
Mn	0.013	0.063	0.002	0.012	0.63	0.07	0.66	0.03	0.28	0.04	0.68	0.06	0.001	0.006	0.064	0.022	0.59	0.07	0.015	0.023
Ta	<0.015*	0.039	0.024*	0.043	0.10#	0.13	0.12	0.08	0.011*	0.02	0.13#	0.15	<0.007*	0.025	0.75#	0.75	0.072#	0.147	<0.008*	0.018
Nb	-	-	-	-	0.99	1.39	1.16	0.71	0.26	0.47	1.14	1.21	-	-	-	-	0.64	1.47	-	-
Ga	1.18#	1.19	0.77#	0.81	-	-	-	-	-	-	-	-	2.18	0.19	2.49	0.17	-	-	5.18	0.19
In	0.60#	0.34	0.48#	0.44	-	-	-	-	-	-	-	-	0.87#	0.69	0.92	0.20	-	-	0.59	0.13
Zn	0.12#	0.31	0.047#	0.033	-	-	-	-	-	-	-	-	0.25	0.04	0.45	0.07	-	-	1.40	0.04
W	<0.026	0.045	<0.016*	0.027	<0.001*	0.004	-	-	-	-	-	-	0.017*	0.025	0.024#	0.030	<0.002*	0.008	35.77	1.93
S	-	-	-	-	-	-	-	-	-	-	-	-	-	-	-	-	-	-	-	-
Total	93.34 <sup>c</sup>	-	94.12 <sup>c</sup>	-	99.15	-	98.88	-	99.66	-	99.32	-	100.34	-	99.47	-	99.48	-	100.56	-

Table I continued

silicate	Z474		Z448		Z551		H2333		H2340		H2347		H2350		S3658	
	No=34	$\pm 2\sigma^a$	No=28	$\pm 2\sigma$	No=61	$\pm 2\sigma$	No=58	$\pm 2\sigma$	No=47	$\pm 2\sigma$	No=48	$\pm 2\sigma$	No=50	$\pm 2\sigma$	No=32	$\pm 2\sigma$
Si	19.08	3.18	20.76	1.22	18.95	0.52	24.12	1.45	22.48	2.77	20.98	0.99	19.28	1.02	22.76	1.92
Mg	23.97	5.52	25.14	2.03	24.49	2.20	22.47	1.93	22.05	1.90	21.03	0.97	19.49	0.96	22.60	2.61
Al	1.63	0.16	1.80	0.30	1.63	0.14	2.37	1.37	2.05	1.51	2.53	0.29	1.87	0.23	1.94	0.37
Ca	1.80	2.07	2.70	0.44	2.07	0.74	3.17	1.13	3.04	1.01	2.64	0.17	2.87	0.08	3.04	0.49
Fe	3.38	1.12	1.85	0.39	2.08	0.30	0.64	0.46	2.78	1.41	6.24	0.73	9.79	0.95	1.91	0.74
Co	0.009*	0.008	0.004*	0.010	0.004*	0.003	<0.003*	0.008	0.007*	0.011	0.021	0.013	0.030	0.014	<0.006*	0.010
Ni	<0.005*	0.007	<0.004*	0.010	0.003*	0.003	<0.005*	0.010	0.009*	0.014	<0.017	0.014	<0.020	0.011	<0.009*	0.020
Ti	1.32	1.03	0.10	0.02	1.49	0.42	0.14	0.03	0.060	0.012	0.057	0.009	0.14	0.01	0.12	0.02
V	0.94	0.28	-	-	0.88	0.07	-	-	-	-	-	-	-	-	-	-
Cr	0.64	0.16	0.068	0.016	0.52	0.04	0.028	0.013	0.28	0.07	0.17	0.03	0.15	0.02	0.13	0.10
Mn	1.16	0.37	0.079	0.025	1.15	0.19	0.066	0.028	0.079	0.029	0.11	0.02	0.05	0.02	0.086	0.020
Ta	1.14	1.40	1.94	0.64	1.58	0.85	0.62	0.75	1.68	1.52	2.82	0.66	3.22	0.69	2.60	1.32
Nb	0.88	1.05	-	-	0.88	0.45	-	-	-	-	-	-	-	-	-	-
Ga	-	-	0.067#	0.074	-	-	0.17	0.11	0.62	0.09	1.23	0.13	1.48	0.12	0.12	0.11
In	-	-	0.056#	0.014	-	-	<0.10#	0.06	0.27	0.04	0.46	0.03	0.64	0.01	0.087#	0.011
Zn	-	-	0.13	0.02	-	-	0.27	0.16	0.41	0.26	0.52	0.08	0.59	0.06	0.17	0.05
W	<0.005*	0.014	0.065	0.081	-	-	<0.003*	0.009	<0.005*	0.011	<0.003*	0.011	0.004*	0.012	0.007*	0.017
S	-	-	-	-	0.029	0.039	-	-	-	-	-	-	-	-	-	-
O calc. <sup>b</sup>	42.78		44.00		42.86		46.19		44.81		44.10		41.90		45.07	
Total	98.75		98.77		98.61		100.36		100.64		102.92		101.54		100.66	

metal	Z474		Z448		Z551		H2333		H2340		H2347		H2350		S3658	
	No=37	$\pm 2\sigma^a$	No=34	$\pm 2\sigma$	No=37	$\pm 2\sigma$	No=33	$\pm 2\sigma$	No=43	$\pm 2\sigma$	No=36	$\pm 2\sigma$	No=32	$\pm 2\sigma$	No=34	$\pm 2\sigma$
Si	1.49	0.21	4.63	0.30	1.08	0.21	3.46	0.76	0.032#	0.137	0.001*	0.010	<0.001*	0.006	4.93	1.71
Fe	89.56	1.55	87.80	0.65	83.36	0.93	80.13	4.30	84.19	3.24	88.21	1.08	89.46	1.01	86.81	4.29
Co	1.04	0.11	0.96	0.11	1.00	0.02	0.98	0.09	1.05	0.26	1.01	0.35	0.96	0.31	1.14	0.79
Ni	2.01	0.20	1.76	0.29	1.90	0.08	1.81	0.29	1.92	1.50	2.02	1.83	1.97	1.51	2.13	1.18
Ti	0.013#	0.004	<0.002*	0.006	0.004*	0.003	0.034	0.011	0.002*	0.007	0.001*	0.005	<0.001*	0.004	<0.002*	0.004
V	0.35	0.16	-	-	0.86	0.04	-	-	-	-	-	-	-	-	-	-
Cr	1.00	0.18	0.26	0.02	1.59	0.08	0.85	0.16	1.75	0.56	0.21	0.13	0.08	0.06	0.31	0.16
Mn	0.39	0.05	0.069	0.018	0.70	0.10	0.27	0.04	0.058	0.022	0.023	0.020	0.002	0.010	0.080	0.043
Ta	<0.017*	0.045	0.25#	0.20	0.14	0.06	3.10	0.61	0.13	0.09	<0.006*	0.016	<0.005*	0.01	0.30#	0.46
Nb	0.32	0.72	-	-	1.25	0.14	-	-	-	-	-	-	-	-	-	-
Ga	-	-	2.39	0.14	-	-	2.22	0.43	0.96#	2.41	0.49#	1.05	0.37#	0.67	2.67	0.89
In	-	-	0.86	0.14	-	-	0.86	0.30	0.46#	0.85	0.30#	0.60	0.27#	0.41	1.06	0.35
Zn	-	-	0.40	0.01	-	-	0.35	0.07	0.11#	0.20	0.040#	0.075	0.031#	0.081	0.32	0.09
W	0.001*	0.006	0.64	0.30	-	-	0.28	0.16	0.45	0.18	<0.020*	0.025	0.018*	0.029	<0.011*	0.025
S	-	-	-	-	7.61	0.97	-	-	-	-	-	-	-	-	-	-
Total	96.19		100.03		99.50		94.35 <sup>c</sup>		91.12 <sup>c</sup>		92.34 <sup>c</sup>		93.17 <sup>c</sup>		99.77	

No= number of analyses; <sup>a</sup> Errors are given as two standard deviations of the respective population <sup>b</sup> Oxygen in silicate calculated by stoichiometry <sup>c</sup> Totals of metals from samples run in graphite capsules are < 100 due to the likely presence of C which was not analyzed \* Conc. close to or below the detection limit # Conc. less certain or overestimated with EPMA

**Table II: EPMA analyses of ferropicrinite from experiments contained in MgO single crystal capsules (wt%)**

	C15-9		C15-10		V346		V366		V365		V367		Z457		Z442		Z447		Z448		Z551		S3658	
wt %	No = 6		No = 5		No = 4		No = 8		No = 8		No = 9		No = 7		No = 9		No = 5		No = 9		No = 8		No = 7	
	$\pm 2\sigma^a$		$\pm 2\sigma$																					
SiO <sub>2</sub>	0.130	0.410	0.067	0.127	0.132	0.266	<0.011*	0.023	0.036	0.075	0.379	1.612	0.123	0.029	0.116	0.023	0.150	0.169	0.086	0.016	0.127	0.113	0.092	0.021
MgO	93.71	5.15	89.07	6.13	93.62	3.99	95.53	3.57	92.53	4.69	94.05	5.00	83.55	1.86	94.83	0.90	94.55	0.26	95.55	0.63	91.76	3.52	95.74	1.36
Al <sub>2</sub> O <sub>3</sub>	1.01	0.34	1.26	0.62	1.70	0.56	0.97	0.37	0.91	0.32	1.03	0.69	1.29	0.05	1.53	0.05	1.40	0.03	1.28	0.14	1.19	0.41	1.23	0.07
CaO	<0.009*	0.006	<0.010*	0.011	0.031	0.010	0.023	0.010	0.025	0.031	0.067	0.230	0.039	0.027	0.037	0.011	0.034	0.010	0.051	0.017	0.019*	0.007	0.041	0.020
FeO	1.27	0.27	4.12	1.41	1.57	0.37	1.41	0.28	3.46	1.08	2.10	0.79	15.99	0.72	3.29	0.47	4.38	0.21	3.71	0.71	3.75	1.43	4.84	1.28
CoO	<0.011*	0.014	0.022	0.012	l.o.d.	0.008	0.006	0.011	0.011*	0.018	0.006*	0.009	0.067	0.014	0.011*	0.013	0.016*	0.016	0.012*	0.020	0.017*	0.013	0.018*	0.027
NiO	<0.010*	0.021	0.016*	0.021	l.o.d.	0.005	l.o.d.	0.005	l.o.d.	0.008	l.o.d.	0.006	0.059	0.030	0.008*	0.017	0.013*	0.011	0.017*	0.021	0.016*	0.018	0.021	0.028
TiO <sub>2</sub>	1.52	1.01	1.54	0.98	0.97	0.44	0.61	0.49	0.58	0.39	0.68	0.56	0.018*	0.01	0.05	0.01	0.04	0.02	0.04	0.01	0.48	0.20	0.03	0.01
V <sub>2</sub> O <sub>3</sub>	1.81	2.39	2.53	1.96	1.66	1.21	1.14	1.44	1.91	1.96	1.27	1.31	-	-	-	-	-	-	-	-	1.58	1.37	-	-
Cr <sub>2</sub> O <sub>3</sub>	1.03	0.61	2.15	1.28	0.81	0.25	0.55	0.39	1.12	0.68	0.61	0.36	0.29	0.03	0.16	0.02	0.18	0.02	0.13	0.02	0.94	0.51	0.23	0.22
MnO	0.874	0.246	0.873	0.124	1.073	0.219	0.777	0.315	0.877	0.304	0.790	0.298	0.052	0.018	0.093	0.022	0.077	0.032	0.071	0.025	1.044	0.320	0.103	0.019
Ta <sub>2</sub> O <sub>5</sub>	0.145	0.152	0.110	0.106	0.053*	0.009	0.035*	0.041	0.041*	0.044	0.046*	0.152	0.042*	0.067	0.070	0.052	0.074	0.047	0.038*	0.070	0.029*	0.020	0.021*	0.070
Nb <sub>2</sub> O <sub>5</sub>	0.088	0.139	0.106	0.083	0.013	0.033	0.008	0.018	0.011	0.019	0.031	0.120	-	-	-	-	-	-	-	-	0.006	0.014	-	-
Ga <sub>2</sub> O <sub>3</sub>	-	-	-	-	-	-	-	-	-	-	-	-	0.209	0.148	0.031*	0.071	0.064*	0.107	0.073	0.112	-	-	0.074	0.108
In <sub>2</sub> O <sub>3</sub>	-	-	-	-	-	-	-	-	-	-	-	-	0.043*	0.008	0.033*	0.008	0.038*	0.007	0.034*	0.007	-	-	0.036*	0.009
ZnO	-	-	-	-	-	-	-	-	-	-	-	-	0.827	0.027	0.457	0.016	0.494	0.015	0.279	0.023	-	-	0.447	0.055
Total	101.62	0.92	101.87	0.42	101.64	0.68	101.07	0.49	101.52	0.52	101.05	0.98	102.60	1.23	100.70	0.52	101.52	0.46	101.37	0.64	100.96	1.05	102.93	0.78

No = number of analyses

<sup>a</sup> Uncertainties are given as two standard errors of the respective population

\* Concentration close to the detection limit

l.o.d. limit of detection

**Table III: Metal-silicate partition coefficients for the study of chapter 3 calculated on mol% basis**

run	Si	Fe	Co	Ni	Ti	V	Cr	Mn	Ta	Nb	Ga	In	Zn													
	±	±	±	±	±	±	±	±	±	±	±	±	±													
P1-19 #	0.108	0.005	270.8	65.4	534.2	1038	488.7	724.9	0.090	0.070	-	-	19.64	7.93	0.475	0.111	4.96	2.47	-	-	77.40	97.77	11.00	2.24	5.80	0.40
P1-21 #	0.0066	0.0023	85.93	20.56	214.3	348.1	418.6	877.5	0.031	0.038	-	-	7.08	2.01	0.086	0.084	0.39	0.13	-	-	20.21	20.70	6.63	1.67	1.35	0.47
P1-20 #	4.1*10 <sup>-5</sup>	0.0001	13.96	0.94	74.76	39.04	362.6	426.6	0.020	0.036	-	-	0.727	0.290	0.005	0.020	0.003	0.006	-	-	6.31	2.57	4.44	1.19	0.197	0.064
C15-9	0.103	0.005	89.54	2.76	352.3	285.2	1345	888	0.0022	0.0017	1.70	0.03	2.42	0.16	0.103	0.014	0.074	0.022	2.27	0.48	-	-	-	-	-	-
C15-10	0.012	0.002	36.71	2.50	300.0	263.4	741.2	656.9	0.0016	0.0012	0.454	0.036	0.961	0.121	0.025	0.005	0.006	0.005	0.253	0.063	-	-	-	-	-	-
V307 #	0.395	0.016	339.7	175.5	159.3	232.7	490.1	943.1	0.376	0.482	-	-	30.74	28.24	0.350	0.504	31.83	49.88	-	-	39.76	13.69	10.99	9.23	4.80	1.36
V312 #	0.090	0.006	90.61	33.06	195.2	234.5	261.0	389.6	0.069	0.082	-	-	5.61	4.29	0.157	0.486	1.60	0.71	-	-	16.00	4.24	8.07	2.91	2.18	0.35
V334 #	0.0048	0.0104	43.25	5.46	310.7	334.2	737.1	1323	0.022	0.013	4.55	1.28	5.88	1.51	0.215	0.036	0.284	0.375	8.24	12.41	-	-	-	-	-	-
V310 #	0.005	0.003	27.01	1.98	86.0	115.4	573.5	1696	0.043	0.059	-	-	3.48	0.93	0.142	0.136	0.116	0.034	-	-	8.30	1.65	5.46	1.36	0.530	0.106
V337 #	8.0*10 <sup>-6</sup>	3.0*10 <sup>-5</sup>	15.97	0.63	91.37	51.00	425.7	494.7	0.0066	0.0030	1.07	0.17	2.09	0.36	0.102	0.019	0.006	0.007	0.405	0.266	-	-	-	-	-	-
V309 #	0.0009	0.0022	7.98	1.18	37.76	27.55	252.9	489.7	0.018	0.031	-	-	1.33	4.50	0.093	0.311	0.004	0.008	-	-	1.21	1.01	1.43	0.84	0.189	0.327
V311 #	0.0007	0.0017	7.55	0.93	27.69	20.20	195.1	493.5	0.023	0.037	-	-	0.55	0.21	0.013	0.054	0.008	0.009	-	-	0.888	0.652	1.36	0.88	0.079	0.036
V346	0.086	0.012	131.2	84.9	475.5	830.3	1146	2475	0.010	0.009	2.14	1.66	5.75	4.76	0.666	0.458	0.052	0.059	1.10	1.30	-	-	-	-	-	-
V366	0.094	0.002	104.3	16.1	614.4	548.0	728.4	617.0	0.0048	0.0035	2.22	0.30	5.49	0.86	0.655	0.094	0.086	0.035	1.58	0.65	-	-	-	-	-	-
V365	0.015	0.004	51.96	4.72	489.4	274.2	990.2	522.0	0.0023	0.0026	0.915	0.143	2.84	0.21	0.272	0.032	0.008	0.008	0.275	0.249	-	-	-	-	-	-
V367	0.111	0.004	93.31	12.22	499.9	642.0	769.2	727.9	0.0071	0.0032	2.20	0.27	5.57	0.50	0.815	0.080	0.105	0.062	1.65	0.96	-	-	-	-	-	-
Z457	0.006	0.003	13.71	0.61	55.77	22.52	225.8	179.6	0.018	0.032	-	-	0.521	0.113	0.031	0.069	0.004	0.007	-	-	8.76	1.50	7.62	3.21	0.768	0.073
Z442	0.213	0.026	57.60	5.82	264.9	298.3	485.9	738.1	0.040	0.031	-	-	3.84	0.56	0.738	0.196	0.398	0.270	-	-	52.68	42.44	19.95	4.25	2.49	0.22
Z469	0.157	0.018	39.83	7.77	205.1	116.9	651.2	644.6	0.010	0.009	0.609	0.238	2.45	0.57	0.586	0.208	0.055	0.090	0.713	1.179	-	-	-	-	-	-
Z447	0.095	0.004	38.22	2.28	139.2	142.0	470.3	570.0	0.018	0.030	-	-	2.05	0.25	0.284	0.228	0.006	0.007	-	-	96.94	67.04	14.08	2.38	9.80	0.54
Z474	0.071	0.030	23.57	9.86	102.6	59.4	367.1	315.9	0.0087	0.0051	0.323	0.147	1.37	0.56	0.301	0.132	0.011	0.016	0.287	0.387	-	-	-	-	-	-
Z448	0.233	0.011	49.34	5.40	225.7	254.9	521.5	779.1	0.020	0.030	-	-	3.94	0.50	0.911	0.186	0.137	0.058	-	-	36.96	20.31	15.99	2.43	3.21	0.23
Z551	0.056	0.005	39.53	2.87	222.3	81.0	547.9	230.1	0.0028	0.0011	0.960	0.052	3.02	0.17	0.605	0.070	0.085	0.030	1.40	0.38	-	-	-	-	-	-
H2333 #	0.128	0.017	111.1	49.1	304.4	533.3	342.0	467.5	0.218	0.065	-	-	54.86	9.07	3.65	1.03	4.48	4.21	-	-	23.64	5.07	3.94	3.24	1.17	0.46
H2340 #	0.0012	0.0036	24.34	8.97	116.2	128.1	168.5	205.6	0.029	0.063	-	-	9.88	1.50	0.597	0.233	0.064	0.052	-	-	2.48	2.23	0.68	1.80	0.212	0.298
H2347 #	4.7*10 <sup>-5</sup>	0.0003	11.57	0.96	39.15	18.88	98.67	81.20	0.021	0.047	-	-	2.01	0.47	0.177	0.106	0.002	0.003	-	-	0.657	0.471	0.270	0.724	0.062	0.080
H2350 #	4.1*10 <sup>-5</sup>	0.0002	7.41	0.50	26.35	9.95	81.20	50.80	0.0056	0.0143	-	-	0.894	0.230	0.034	0.108	0.001	0.002	-	-	0.400	0.242	0.173	0.345	0.042	0.073
S3658	0.223	0.038	46.72	8.93	202.8	192.6	251.5	288.2	0.013	0.019	-	-	2.39	1.06	0.958	0.273	0.119	0.096	-	-	22.92	11.53	12.59	2.24	1.96	0.41

# results from graphite capsules

± Uncertainties determined from error propagation for the calculation of D from the standard deviations of the metal and the silicate concentration

**Table IV: Average composition of the quenched metal melts from the HSE-study of chapter 4 - EPMA results.**

	V364		V363		V347#		V348#		Z544		Z538		Z475		Z484#		Z541		Z505	
wt %	No=42		No=40		No=66		No=49		No=39		No=41		No=44		No=42		No=41		No=29	
	$\pm 2\sigma$																			
Fe	22.03	1.29	36.21	0.17	20.99	3.22	7.02	1.54	19.93	0.39	46.81	0.51	20.18	0.50	6.34	1.70	23.11	0.32	1.09	0.17
Ru	13.38	1.74	11.11	0.15	12.54	0.84	15.39	1.09	13.71	0.32	9.07	0.18	13.13	0.21	15.57	1.38	13.19	0.29	-	-
Rh	14.22	0.31	11.59	0.13	14.96	1.11	17.85	2.23	14.83	0.18	9.46	0.13	15.24	0.15	16.96	0.56	14.03	0.18	28.10	0.37
Pd	13.67	3.05	10.48	0.26	14.22	0.83	13.58	5.35	14.62	0.73	8.74	0.44	13.18	0.55	14.23	4.51	13.45	0.57	-	-
Re	8.44	1.91	6.83	0.18	13.37	3.20	17.34	1.95	7.99	0.36	5.52	0.25	13.76	0.67	17.61	3.84	7.98	0.34	-	-
Ir	14.09	1.66	11.49	0.24	12.37	0.79	15.78	4.98	13.72	0.45	9.38	0.39	12.22	0.40	15.88	2.36	13.60	0.42	-	-
Pt	13.50	1.07	10.93	0.21	12.56	0.29	14.06	0.73	14.35	0.29	9.05	0.25	12.22	0.25	14.06	1.24	13.42	0.26	69.80	0.52
Si	0.0014*	0.011	<0.0015	0.005	0.0051*	0.007	0.0044*	0.004	0.072	0.042	0.419	0.084	0.205	0.042	0.021	0.025	0.264	0.058	0.000	0.000
Cr	0.032	0.018	0.050	0.015	0.020	0.010	0.0079*	0.004	0.029	0.022	0.074	0.020	0.042	0.020	0.010	0.007	0.044	0.014	0.021	0.038
Mn	0.0022*	0.006	0.0031*	0.006	0.0020*	0.000	<0.001	0.002	0.0043*	0.007	0.0074*	0.009	0.0076*	0.008	0.0027*	0.003	0.006*	0.006	0.0019*	0.008
O	-	-	-	-	0.078	0.081	0.419	0.037	-	-	-	-	0.102	0.139	-	-	-	-	-	-
Total	99.38	0.60	98.69	0.45	101.12	0.57	101.44	0.41	99.26	0.63	98.52	0.43	100.29	0.50	100.72	0.59	99.09	0.60	99.02	0.63

# analyses were taken along grids as described in the text

No= number of analyses

Uncertainties are given as two standard deviations for all analyses of a population or of groups of analyses within a grid (see text)

\* Concentration close to the detection limit

**Table V: Average composition of the quenched silicate melts from the HSE-study of chapter 4 - EPMA, LA-ICP-MS and SIMS results; table continues on the next page.**

	<b>V364</b>		<b>V363</b>		<b>V347</b>		<b>V348</b>		<b>Z544</b>											
<b>EPMA</b>	No=49		No=54		No=46		No=50		No=40											
wt %	$\pm 2\sigma$																			
Si	16.79	0.33	18.27	0.48	18.02	0.89	18.10	0.85	21.15	0.48										
Mg	30.57	2.15	29.32	1.92	27.10	4.12	27.95	3.33	23.42	0.82										
Al	1.68	0.74	1.64	0.69	2.47	1.57	2.29	1.42	1.95	0.14										
Ca	2.13	0.89	1.98	0.96	3.23	2.06	2.89	1.69	3.05	0.37										
Fe	4.98	0.73	4.41	0.97	5.65	1.99	4.78	1.83	5.39	0.14										
Ti	0.101	0.039	0.101	0.050	0.137	0.085	0.133	0.077	0.135	0.021										
Cr	0.102	0.016	0.108	0.028	0.126	0.049	0.131	0.054	0.146	0.012										
Mn	0.069	0.012	0.071	0.017	0.090	0.030	0.093	0.033	0.095	0.007										
O calc. <sup>a</sup>	43.15	0.53	43.78	0.57	43.65	0.90	43.76	0.70	44.20	0.23										
Total	99.57	1.10	99.69	0.81	100.47	0.71	100.14	0.55	99.54	0.32										
<b>LA-ICP-MS</b>	No=4		No=4		No=5		No=5		No=4											
ppm	II-2	$\pm\sigma$	N610	$\pm\sigma$	II-2	$\pm\sigma$	N610	$\pm\sigma$	I-2	$\pm\sigma$	N610	$\pm\sigma$	II-2	$\pm\sigma$	N610	$\pm\sigma$				
Ti			967	17			935	4			1358	40			1271	13				
Cr			936	37			969	21			1374	107			1314	78				
Mn			688	13			685	11			1012	63			950	47				
Ru	0.267	0.064			0.064*	0.059			0.723*	0.741			1.63	1.15			0.618	0.045		
Rh	0.888	0.185	0.535	0.125	0.307	0.031	0.188	0.012	2.95	1.92	2.62	2.03	5.00	3.02	3.75	2.15	2.38	0.08	1.911	0.079
Pd	34.6	1.1	36.0	1.9	13.5	1.2	11.04	0.46	16.5	2.5	31.6	3.69	52.2	6.8	88.4	7.4	49.8	4.902	62.74	6.94
Re	1.32	0.07	0.874	0.054	0.163	0.036	0.146	0.037	1.67	0.43	2.66	1.00	8.49	1.76	10.52	2.07	0.816	0.058	0.925	0.061
Ir	Lo.d.				<0.005*	0.008			0.669*	0.596			1.33	1.41			< 0.029*			
Pt	0.940	0.114	0.902	0.099	0.273	0.023	0.224	0.025	1.84	1.25	1.90	1.49	4.09	3.69	3.87	3.34	0.554	0.040	0.599	0.055
<b>SIMS</b>	No=3		No=3		No=4		No=3		No=3											
ppm	% RSD																			
Ru	1.59	40	1.62	44	16.2	103	1.77	20	1.26	10										
Rh	3.29	33	1.97	65	53.6	129	4.70	31	3.57	12										
Pd	61.6	33	34.3	54	72.7	27	37.0	15	30.7	8.6										
Re	3.96	29	1.57	22	13.0	55	7.47	12	2.64	7.7										
Ir	(6.96)	15	(4.94)	21	(< 17.0)	36	(5.71)	13	(5.12)	16										

No= number of analyses

Uncertainties for EPMA analyses are given as two standard deviations of the respective population or of groups of analyses within a grid for the experiments  $\leq 6$  GPa (see text)

Uncertainties for LA-ICP-MS analyses are given as one standard deviation and for SIMS as relative standard deviation (RSD)

<sup>a</sup> Oxygen in silicate calculated by stoichiometry

\* Concentration close to the detection limit; Lo.d. = limit of detection

() for Ir concentrations from SIMS analyses: close to or below the detection limit, erroneous concentrations are produced (see text)

II-2 standardisation based on the HSE doped glass II-2 of this study; I-2 standardisation based on the HSE doped glass I-2 of this study; N610 standardisation based on NIST 610 glass

Table V continued

	<b>Z538</b>		<b>Z475</b>		<b>Z484</b>		<b>Z541</b>		<b>Z505</b>											
<b>EPMA</b>	No=75		No=30		No=43		No=34		No=11											
wt %	$\pm 2\sigma$																			
Si	20.62	1.11	20.59	0.93	21.08	0.80	20.31	0.80	22.18	1.32										
Mg	23.93	1.94	25.47	1.74	24.79	1.53	24.74	1.24	23.90	3.47										
Al	1.96	0.19	1.76	0.16	1.87	0.11	1.96	0.07	2.46	3.04										
Ca	2.68	0.80	2.37	0.69	2.59	0.58	2.60	0.39	3.37	1.35										
Fe	5.23	0.76	5.08	0.56	4.36	0.26	4.76	0.29	1.45	0.52										
Ti	0.124	0.068	0.111	0.060	0.120	0.029	0.109	0.031	0.106	0.054										
Cr	0.129	0.022	0.126	0.020	0.136	0.013	0.125	0.011	0.232	0.148										
Mn	0.080	0.017	0.077	0.015	0.090	0.011	0.076	0.011	0.094	0.034										
O calc. <sup>a</sup>	43.73	0.63	44.36	0.66	44.45	0.28	43.72	0.48	45.16	1.02										
Total	98.49	1.01	99.95	1.49	99.48	0.42	98.40	0.68	98.95	0.46										
<b>LA-ICP-MS</b>	No=4		No=4		No=6		No=4		No=5											
ppm	II-2	$\pm\sigma$	N610	$\pm\sigma$	I-2	$\pm\sigma$	N610	$\pm\sigma$	II-2	$\pm\sigma$	N610	$\pm\sigma$	I-2	$\pm\sigma$	N610	$\pm\sigma$				
Ti			1254	26			1067	18			1122	5			999	62				
Cr			1419	51			1278	40			1353	29			2187	631				
Mn			872	18			764	23			871	20			899	16				
Ru	0.038*	0.054			4.66	3.12			5.36	1.55			1.09	0.06						
Rh	0.452	0.073	0.298	0.037	14.5	3.6	9.78	2.61	17.6	3.8	11.0	2.6	4.62	0.21	4.33	0.19	45.7	6.7	30.8	3.0
Pd	20.9	0.6	25.7	0.6	92.1	14.5	140	22	183	11	247	15	82.3	4.5	113	5				
Re	0.073	0.020	0.054	0.013	6.17	1.36	7.57	1.63	20.2	4.0	21.5	4.7	0.978	0.046	1.24	0.09				
Ir	l.o.d.				2.84	3.96			2.85	3.03			0.117	0.033						
Pt	0.424	0.123	0.485	0.151	7.95	6.86	5.95	5.16	6.73	4.32	5.14	3.37	2.36	0.33	2.65	0.37	7.51	1.30	6.22	0.78
<b>SIMS</b>	No=3		No=3		No=3		No=2													
ppm	% RSD		% RSD		% RSD		% RSD													
Ru	1.47	20			6.35	7.9			6.30	12			3.35	19			-			
Rh	2.65	22			23.9	15			18.7	2.7			10.6	17			90.63			
Pd	29.3	0.11			146	21			150	19			59.3	2.1			-			
Re	1.53	20			6.54	8.6			21.3	20			3.04	9.9			-			
Ir	(6.10)	9.5			(7.00)	36			(6.57)	16			(6.35)	4.9			-			

No= number of analyses

Uncertainties for EPMA analyses are given as two standard deviations of the respective population

Uncertainties for LA-ICP-MS analyses are given as one standard deviation and for SIMS as relative standard deviation (RSD)

<sup>a</sup> Oxygen in silicate calculated by stoichiometry

\* Concentration close to the detection limit; l.o.d. = limit of detection

() Ir concentrations from SIMS analyses: close to or below the detection limit, erroneous values are produced (see text)

II-2 standardisation based on the HSE doped glass II-2 of this study; I-2 standardisation based on the HSE doped glass I-2 of this study; N610 standardisation based on NIST 610 glass

**Table VI: EPMA analyses of ferropericlasite from experiments of the HSE-study of chapter 4 (wt%)**

	V364		V363		V347		V348		Z544		Z538		Z475		Z484		Z541	
wt %	No = 30		No = 24		No = 16		No = 13		No = 27		No = 30		No = 9		No = 15		No = 32	
	$\pm 2\sigma^a$		$\pm 2\sigma$															
SiO <sub>2</sub>	0.012*	0.027	0.046	0.241	0.037	0.047	0.051	0.057	0.114	0.058	0.094	0.074	0.144	0.057	0.109	0.056	0.097	0.058
MgO	92.58	2.09	92.36	2.75	88.76	0.68	90.46	1.57	86.71	1.47	87.18	1.36	88.78	1.34	89.45	0.59	89.11	0.86
Al <sub>2</sub> O <sub>3</sub>	0.766	0.203	0.915	0.362	1.37	0.08	1.37	0.25	1.34	0.16	1.41	0.21	1.36	0.09	1.45	0.06	1.47	0.15
CaO	0.022	0.016	0.022	0.016	0.020*	0.022	0.024	0.019	0.027	0.020	0.028	0.018	0.039	0.022	0.030	0.016	0.032	0.015
FeO	5.86	1.77	6.29	2.12	9.05	0.36	7.53	1.00	11.28	1.21	10.84	1.16	9.23	0.10	8.40	0.16	9.26	0.58
TiO <sub>2</sub>	0.014*	0.014	0.027	0.023	0.024*	0.012	0.016*	0.018	0.023*	0.011	0.028	0.016	0.021*	0.007	0.016*	0.012	0.021*	0.018
Cr <sub>2</sub> O <sub>3</sub>	0.297	0.258	0.221	0.230	0.518	0.033	0.653	0.240	0.392	0.109	0.300	0.060	0.273	0.020	0.362	0.026	0.297	0.036
MnO	0.051	0.018	0.050	0.027	0.073	0.007	0.076	0.015	0.089	0.013	0.076	0.010	0.077	0.007	0.085	0.007	0.074	0.012
Total	99.61	0.46	99.93	0.27	99.85	0.67	100.18	0.90	99.97	0.39	99.96	0.67	99.93	1.46	99.90	0.68	100.36	0.63

No = number of analyses

<sup>a</sup> Uncertainties are given as two standard errors of the respective population

\* Concentration close to or below the detection limit

**Table VII: Metal-silicate partition coefficients for the HSE-study of chapter 4 calculated on mol % basis**

	P (GPa)	T (°C)	log $f_{O_2}$ ( $\Delta$ IW)	Ru	$\pm$	Rh	$\pm$	Pd	$\pm$	Re	$\pm$	Ir	$\pm$	Pt	$\pm$
V364	3.5	2500	-0.16	2.4*10 <sup>+6</sup>	6.1*10 <sup>+5</sup>	7.6*10 <sup>+5</sup>	1.6*10 <sup>+5</sup>	9.4*10 <sup>+3</sup>	1.0*10 <sup>+3</sup>	3.1*10 <sup>+5</sup>	4.1*10 <sup>+4</sup>			6.9*10 <sup>+5</sup>	8.4*10 <sup>+4</sup>
V363	6	2150	-1.07	7.4*10 <sup>+6</sup>	6.8*10 <sup>+6</sup>	1.6*10 <sup>+6</sup>	1.6*10 <sup>+5</sup>	1.7*10 <sup>+4</sup>	1.4*10 <sup>+3</sup>	1.8*10 <sup>+6</sup>	3.9*10 <sup>+5</sup>	5.4*10 <sup>+7</sup>	9.3*10 <sup>+7</sup>	1.7*10 <sup>+6</sup>	1.5*10 <sup>+5</sup>
V347	6	2150	0.45	8.4*10 <sup>+5</sup>	8.8*10 <sup>+5</sup>	2.3*10 <sup>+5</sup>	1.5*10 <sup>+5</sup>	2.0*10 <sup>+4</sup>	3.1*10 <sup>+3</sup>	3.8*10 <sup>+5</sup>	1.1*10 <sup>+5</sup>	4.9*10 <sup>+5</sup>	4.1*10 <sup>+5</sup>	3.2*10 <sup>+5</sup>	2.2*10 <sup>+5</sup>
V348	6	2150	2.78	5.2*10 <sup>+5</sup>	3.7*10 <sup>+5</sup>	2.0*10 <sup>+5</sup>	1.2*10 <sup>+5</sup>	6.9*10 <sup>+3</sup>	1.4*10 <sup>+3</sup>	1.1*10 <sup>+5</sup>	2.5*10 <sup>+4</sup>	3.3*10 <sup>+5</sup>	3.5*10 <sup>+5</sup>	1.9*10 <sup>+5</sup>	1.7*10 <sup>+5</sup>
Z544	18	2200	0.60	1.1*10 <sup>+6</sup>	7.8*10 <sup>+4</sup>	3.0*10 <sup>+5</sup>	1.1*10 <sup>+4</sup>	7.0*10 <sup>+3</sup>	7.2*10 <sup>+2</sup>	4.7*10 <sup>+5</sup>	3.4*10 <sup>+4</sup>	1.2*10 <sup>+7</sup>	2.2*10 <sup>+5</sup>	1.2*10 <sup>+6</sup>	9.4*10 <sup>+4</sup>
Z538	18	2300	-1.22	8.9*10 <sup>+6</sup>	1.3*10 <sup>+7</sup>	7.8*10 <sup>+5</sup>	1.3*10 <sup>+5</sup>	7.8*10 <sup>+3</sup>	3.0*10 <sup>+2</sup>	2.8*10 <sup>+6</sup>	7.9*10 <sup>+5</sup>			7.9*10 <sup>+5</sup>	2.3*10 <sup>+5</sup>
Z475	18	2300	0.42	1.3*10 <sup>+5</sup>	9.0*10 <sup>+4</sup>	5.0*10 <sup>+4</sup>	1.2*10 <sup>+4</sup>	3.4*10 <sup>+3</sup>	5.4*10 <sup>+2</sup>	1.1*10 <sup>+5</sup>	2.4*10 <sup>+4</sup>	1.0*10 <sup>+5</sup>	1.4*10 <sup>+5</sup>	7.3*10 <sup>+4</sup>	6.3*10 <sup>+4</sup>
Z484	18	2300	2.74	1.7*10 <sup>+5</sup>	4.9*10 <sup>+4</sup>	5.4*10 <sup>+4</sup>	1.2*10 <sup>+4</sup>	2.2*10 <sup>+3</sup>	3.1*10 <sup>+2</sup>	5.0*10 <sup>+4</sup>	1.2*10 <sup>+4</sup>	1.6*10 <sup>+5</sup>	1.7*10 <sup>+5</sup>	1.2*10 <sup>+5</sup>	7.6*10 <sup>+4</sup>
Z541	18	2400	0.00	5.6*10 <sup>+5</sup>	2.9*10 <sup>+4</sup>	1.4*10 <sup>+5</sup>	7.1*10 <sup>+3</sup>	3.8*10 <sup>+3</sup>	2.4*10 <sup>+2</sup>	3.8*10 <sup>+5</sup>	1.9*10 <sup>+4</sup>	2.7*10 <sup>+6</sup>	7.4*10 <sup>+5</sup>	2.6*10 <sup>+5</sup>	3.7*10 <sup>+4</sup>
Z505	18	2200	4.33			4.5*10 <sup>+4</sup>	7.1*10 <sup>+3</sup>							6.8*10 <sup>+5</sup>	1.3*10 <sup>+5</sup>

$\pm$  Uncertainties determined from error propagation for the calculation of D from the standard deviations of the metal and the silicate concentration

Data based on experimental results without corrections for metal activities





Hiermit erkläre ich, daß ich die vorliegende Arbeit selbständig verfaßt und keine anderen als die von mir angegebenen Quellen und Hilfsmittel benutzt habe.

Ferner erkläre ich, daß ich nicht anderweitig mit oder ohne Erfolg versucht habe, eine Dissertation einzureichen und keine gleichartige Doktorprüfung an einer anderen Hochschule endgültig nicht bestanden habe

Bayreuth, Februar 2008

Ute Mann